Pulsed Laser Deposition and Characterisation of ZnO and Aluminium-doped ZnO Nanostructures on Silicon and Flexible Plastic Substrates

Saikumar Inguva **B.Sc., M.Sc.**

Thesis Submitted for the Award of PhD

School of Physical Sciences

Dublin City University

Principal Supervisor
Dr. Jean-Paul Mosnier

Supervisor
Prof. Enda McGlynn

January 2016

Declaration

I hereby certify that this material, which I now submit for assessment on the programme of study leading to the award of PhD is entirely my own work, that I have exercised reasonable care to ensure that the work is original, and does not to the best of my knowledge breach any law of copyright, and has not been taken from the work of others save and to the extent that such work has been cited and acknowledged within the text of my work.

Signed: _____ ID No. : 11212319

Date: _____

Acknowledgements

First and foremost, I would like to thank my supervisor Dr. Jean-Paul Mosnier for giving me the opportunity to pursue PhD studies at DCU. My sincere thanks to him for his guidance, endless support, suggestions and encouragement throughout my PhD. Also, my thanks to him for allowing me to use the pulsed laser deposition (PLD) facilities and various characterisation techniques. Thanks a million Jean-Paul for everything you have done for me. It has really meant to me a lot.

I would also like to thank my supervisor Prof. Enda McGlynn for his constant support, advice and encouragement. Many more thanks Enda for allowing me to use your laboratory facilities, especially photoluminescence instruments. Your advice, especially on 3.331 eV luminescence in ZnO was incredible. Thanks a lot Enda for everything you have done for me. I'm sure the knowledge that I gained with JP and Enda shall go a long way to fulfill my dreams in my research career. Thanks again both of you. I also thank Prof. Patrick McNally (School of Electronic Engineering, DCU) for being a member of my supervisory panel.

I would like to extend my thanks to all the academic staff of School of Physical Sciences, DCU. In particular, thanks to Dr. Tony Cafolla for helping me with the AFM measurements. Many thanks to Dr. Brendan Twamley (School of Chemistry, DCU) for his assistance with the FE-SEM measurement. Many thanks to Liz O'Connor (INSPIRE and STEP Research Administrator) and Lisa Peyton for their help on administrative stuff. Thanks to technical staff of the School: Ray Murphy, Des Lavelle, Pat Wogan and Alan Hughes for their help whenever I needed technical assistance during my course.

I would also like to thank our collaborators Dr. Enrico Marsili (Nanyang Technological University, Singapore), Mr. Fidal Kumar and Prof. T.S. Chandra (Indian Institute of Technology Madras, Chennai, India), Dr. Satheesh Krishnamurthy (Open University, UK), Mr. Sandeep Kumar Marka and Dr. V.V.S.S. Srikanth (University of Hyderabad, India), Dr. Monica Epifanio (DCU) and Dr. Michael Kitching (DCU) for their help, advice and suggestions.

I would further like to thank my seniors Dr. Eanna McCarthy, Dr. James Connolly and Dr. Conor McLoughlin for introducing me the world of PLD and ZnO. Special thanks to Dr. Rajani K Vijayaraghavan (DCU) for her continuous help, suggestions and support during the course of study. Thanks a lot to Dr. Daragh Byrne for motivating me and sharing his valuable suggestions. Thanks to Dr. Seamus Garry for his assistance with SEM whenever I

was stuck. Thanks to Dr. Rajesh, Dr. Gurusharan, and Dr. Lalit for their encouragement and support.

Many more thanks to my colleague Ciarán Gray for his suggestions, discussions, assistance and encouragement; Ciarán, I had a very good time with your company. Thanks to Jennifer Gaughran for providing the Zeonor plastic sheets. I would like to thank all my fellow postgrads (past and present) for their great company.

Thanks extended to my housemates and colleagues: Sharath, Mithun, Mahendar (UL), Lakshmi Narayan, Venkatesh Kannan and Venkatesh Selvaraju for their encouragement and support, and keeping a healthy and studious atmosphere in the house. Many thanks to my best friends Balakrishna (Spain), Vinay (India) and Mahesh (India) for their emotional support.

Acknowledgement would be incomplete without thanking my lovely family. Many more thanks to my parents: Krishna Murthy (dad) and Indira (mom), brothers: Narasimha Murthy and Venkateshwarlu, and sisters in-law: Harini and Kavya. My special thanks to my grandmother Bhanumathi (late) for her invaluable love and care. Thanks to Amith Kumar, my brother, for his countless support. Thanks to my family friends/relatives: Rajesh, Chaitanya, Pavan and Santhosh for their support. Thanks to god "Shirdi Sai Baba" for caring for me and bringing me to this stage.

Last but not least, my sincere thanks to my funding body INSPIRE (Integrated Nanoscience Platform for Ireland). Without their financial support this work would not have been possible.

"*This work funded by INSPIRE was conducted under the framework of the Irish Government's Programme for Research in Third Level Institutions Cycle 5, National Development Plan 2007-2013 with the assistance of the European Regional Development Fund*".

Contents

List of Acronyms

Atomic Force Microscopy…….. AFM

Atomic Layer Deposition……....ALD

Aluminium……Al

Al-doped ZnO…….....AZO

Argon…….....Ar

Carbothermal Reduction…….CTR

Carbon felt……CF

Copper…….....Cu

Cyclo-Olefin Polymer……..COP

Dielectric Barrier Discharge……DBD

Donor Acceptor Pair……....DAP

Donor Bound Exciton…….....DBX

Deep Donor Bound Exciton……....DD

Dublin City University…….DCU

Energy Dispersive X-ray Spectroscopy……..EDX

Face-Centred Cubic……...FCC

Field Emission Scanning Electron Microscope…...FE-SEM

Full Width at Half Maximum.....FWHM

Free Exciton……..FX

Gallium Nitride…….GaN

Ga-doped ZnO……..GZO

Gold……...Au

Hexagonal Close Packed……...HCP

Hydrogen……...H

High Resolution Transmission Electron Microscopy….HR-TEM

Indium……In

In-doped ZnO…….....IZO

Indium-Gallium doped ZnO…….....IGZO

Indium Tin Oxide…….....ITO

Longitudinal Optical……..LO

Mass Flow Controller…….....MFC

milliTorr…….mTorr

Near Band Edge…….NBE

Nanosphere Lithography…….....NSL

Oxygen……...O

Photoluminescence…….....PL

Photomultiplier Tube…….PMT

Polyethylene Terephthalate…….....PET

Polyethylene Naphtalate…….....PEN

Polycarbonate……..PC

Polymethyl Methacrylate…….....PMMA

Polymide…….....PI

Pulsed Laser Deposition…….....PLD

Scanning Electron Microscopy……..SEM

Selective Area Electron Diffraction.....SAED

Silicon…….Si

Transmission Election Microscopy…...TEM

Transparent Conductive Oxide…….....TCO

Two Electron Satellite……...TES

Vapour Liquid Solid…….....VLS

Vapour Phase Transport……VPT

Water Contact Angle……WCA

X-ray Diffraction……..XRD

Zero Phonon Line……ZPL

Zinc Oxide……....ZnO

List of Figures: Abbreviated titles Page

List of Tables

Publications

Saikumar Inguva, Sandeep Kumar Marka, Rajani K. Vijayaraghavan, Enda McGlynn, Vadali V.S.S. Srikanth and Jean-Paul Mosnier, "Crystalline ZnO/Amorphous ZnO Core/Shell Nanorods: Self-Organized Growth, Structure, and Novel Luminescence", ***Journal of Physical Chemistry C*** 119 (2015) 4848−4855.

Saikumar Inguva, Rajani K. Vijayaraghavan, Enda McGlynn and Jean-Paul Mosnier, "Highly transparent and reproducible nanocrystalline ZnO and AZO thin films grown by room temperature pulsed-laser deposition on flexible Zeonor plastic substrates", ***Materials Research Express*** 2 (2015) 096401.

Monica Epifanio, **Saikumar Inguva**, Michael Kitching, Jean-Paul Mosnier and Enrico Marsili, "Effects of atmospheric air plasma treatment of graphite and carbon felt electrodes on the anodic current from *Shewanella* attached cells", ***Bioelectrochemistry*** 106 (2015) 186-193.

Saikumar Inguva, Ciarán Gray, Enda McGlynn and Jean-Paul Mosnier, "Origin of the 3.331 eV emission in ZnO nanorods: comparison of vapour phase transport and pulsed-laser deposited grown nanorods", ***Journal of Luminescence*** (under review).

Fidal V T K, **Saikumar Inguva**, Satheesh Krishnamurthy, Enrico Marsili, Jean-Paul Mosnier and Chandra T S, "Electrochemical interaction of glucose oxidase immobilized on the surface of nanostructured zinc oxide and aluminum-doped zinc oxide (Al-ZnO) thin films", ***Sensors and Actuators B*** (under review).

Manuscripts in Preparation

Saikumar Inguva, Enda McGlynn and Jean-Paul Mosnier," The strong effect of oxygen growth pressure on the structure and properties of ZnO and AZO thin films grown by room temperature pulsed laser deposition on flexible Zeonor plastic substrates", in preparation for Journal of Materials Chemistry C.

Saikumar Inguva, Rajani K. Vijayaraghavan, Sandeep Kumar Marka, Enda McGlynn and Jean-Paul Mosnier, "Laterally interconnected core/shell ZnO nanorod architectures", in preparation for RSC Advances.

Saikumar Inguva, Enda McGlynn and Jean-Paul Mosnier, "Ageing effect study of the ZnO and AZO thin films grown by room temperature pulsed-laser deposition on flexible Zeonor plastic substrates", in preparation for Thin Solid Films.

Conferences

Saikumar Inguva, Rajani K. Vijayaraghavan, Enda McGlynn and Jean-Paul Mosnier, "Highly transparent and conductive ZnO and AZO thin films grown by room temperature pulsed laser deposition on flexible Zeonor plastic substrates". Poster presentation in EMRS fall meeting, Warsaw, Poland, 15^{th} -18^{th} September 2015.

Saikumar Inguva, Ciarán Gray**,** Enda McGlynn and Jean-Paul Mosnier, "High optical quality of vertically aligned ZnO nanorods grown by catalyst-free vapor phase transport on pulsed-laser deposited ZnO seed layers". Poster presentation in EMRS fall meeting, Warsaw, Poland, 15^{th} -18^{th} September 2015.

Saikumar Inguva, R K Vijayaraghavan, James Connolly, Enda McGlynn and Jean-Paul Mosnier. "Highly transparent ZnO and AZO thin films pulsed laser deposited on flexible Zeonor plastic substrates at room temperature". Poster presentation in EMRS fall meeting, Warsaw, Poland, 15^{th} -19^{th} September 2014 **(Received the best poster presentation award).**

Saikumar Inguva, Sandeep Kumar Marka, Rajani K. Vijayaraghavan, Enda McGlynn, V.V.S.S. Srikanth and Jean-Paul Mosnier. "Catalyst free ZnO core-shell nanorods: growth, structural characterizations and 3.331 eV photoluminescence properties". Oral presentation in EMRS fall meeting, Warsaw, Poland, 15^{th}-19^{th} September 2014.

Saikumar Inguva, Sandeep Kumar Marka, Rajani K. Vijayaraghavan, Enda McGlynn, Vadali.V.S.S. Srikanth, J.P. Mosnier, "Crystalline ZnO/Amorphous ZnO Core/Shell Nanorods: Self-Organized Growth, Structure and 3.331 eV Luminescence". Poster presentation in BOC poster competition at School of Physical Sciences, Dublin City University, Ireland, 26th February 2015 (**Received the best poster presentation award)**.

Saikumar Inguva, Sandeep Kumar Marka, Rajani K. Vijayaraghavan, Enda McGlynn, Vadali.V.S.S. Srikanth, J.P. Mosnier, "Crystalline ZnO/Amorphous ZnO Core/Shell Nanorods: Self-Organized Growth, Structure and 3.331 eV Luminescence". Poster presentation in IOP Ireland spring meeting at Clarion Hotel, Cork, Ireland, 28th March 2015.

Saikumar Inguva, Rajani K. Vijayaraghavan, Enda McGlynn and Jean-Paul Mosnier, "Highly transparent ZnO and AZO thin films pulsed laser deposited on flexible Zeonor plastic substrates at room temperature". Poster presentation in Intel Ireland research conference at science gallery, Dublin, Ireland, 18th November 2014.

Fidal V T K, Satheesh Krishnamurthy, Enrico Marsili, James Connolly, **Saikumar Inguva**, Jean-Paul Mosnier, Chandra T S, "Improved performance of GOx/transparent conducting ZnO/metal doped ZnO electrode by Nafion entrapment". Poster presentation in EMRS spring meeting, Strasbourg, France, 28-30th May 2013.

Saikumar Inguva, Eanna McCarthy, Enda McGlynn and Jean-Paul Mosnier, "Effect of gas pressure during buffer growth on the morphologies of ZnO nanorods grown by pulsed-laser deposition on Si (100) substrates". Poster presentation at School of Physical Sciences, Dublin City University, Ireland, 31st May 2013.

Abstract

Saikumar Inguva

Pulsed Laser Deposition and Characterisation of ZnO and Aluminium-doped ZnO Nanostructures on Silicon and Flexible Plastic Substrates

We have developed recipes for the catalyst-free growth of upstanding/vertically aligned ZnO nanorods featuring core/shell or interconnected core/shell architectures on ZnO-seeded Si (100) substrates using the pulsed laser deposition (PLD) technique. The structural, morphological and luminescent properties of these ZnO nanorod samples were established. A ZnO emission band at 3.331 eV was observed in the core/shell and interconnected core/shell nanorod architectures and its origin linked to the defects observed at the crystalline/amorphous interface of the core/shell structure. This particular defect PL emission appears to be a new observation for ZnO.

We have grown vertically aligned ZnO nanorods on PLD prepared ZnO-seeded Si substrates by catalyst-free vapour phase transport (VPT). The nanorods featured excellent optical properties and a coverage density higher than previously published data. The structural, morphological and luminescent properties of the seed layers and nanorods were inter-compared. Importantly, we also compared the near band edge emission of such VPT-and PLD-deposits, with a focus on the identification of the origin of the emission feature at 3.331 eV.

We have researched the room temperature PLD growth of highly transparent and conductive ZnO and Al-doped ZnO (AZO) nanocrystalline thin films on flexible Zeonor plastic substrates. The trends for the growth rate, surface morphology, hydrophobicity and the structural, optical and electrical properties of 65 nm - 420 nm thick ZnO/AZO films grown on Zeonor substrates were analysed as a function of oxygen growth pressure (1-300 mTorr). The as-grown films showed highly reproducible deposition behaviour, and featured high transmittance, low-electrical resistance, optical smoothness, low residual stress, and hydrophobicity.

The results presented in this thesis are discussed in the context of prospective and suitable applications.

Chapter 1

Review of the Fields and Motivations for the Thesis Work

Semiconductors play a ubiquitous role in our day-to-day life by the virtue of their many commercial applications. This demands to do research on their development. In this regard, Silicon (Si) is the most popular semiconductor in scientific research and technology. Other semiconductors that have been investigated, e.g. gallium nitride (GaN), gallium arsenide (GaAs), zinc oxide (ZnO) and zinc selenide (ZnSe). Among them, ZnO is a promising candidate and has attracted great attention due to the abundant sources of this raw material along with its excellent material properties that includes simple nanostructure fabrication.

This chapter provides the background information on, and applications of, the topics covered in this thesis. We review the field, and demonstrate our motivations and the goals of the thesis. We then provide an outline of the thesis with a brief description of the individual chapters.

1.1 ZnO based core/shell nanorods: Motivation

Core/shell architectures enable the tailoring of novel properties via modification of the functionality, charge or reactivity of the nanostructure surface [1-4]. They are also observed to have improved physical and chemical properties [1]. In particular, the enhancement of the luminescent properties of one-dimensional nanostructures can be achieved [4]. These are the reasons why core/shell nanostructures have attracted attention for the past few years. Core/shell nanostructures are made up of a variety of materials including metals (Ni-core/Ag-shell) [5], semiconductors (ZnO/ZnS, ZnO/Ag_2S, ZnO/CuS) [1-3], hydroxides ($Ln(OH)_3/SiO_2$) [6], and organic materials (Polypyrrole/Poly(N-vinylcarbazole)) [7]. They have been attracting significant attention for applications in several interdisciplinary fields such as sensing, multi-enzyme bio-catalysis, drug delivery and photonics [8], for example.

In this regard, ZnO, a semiconductor with a wide direct band gap (3.37 eV) and a large free exciton binding energy of 60 meV, has been used successfully in core/shell architectures due to its excellent material (optoelectronic, piezoelectric, biocompatibility) properties [9-11] to include simple nanostructuring. With greater details of the ZnO based core/shell nanostructures and their applications, we now review the previous works. In terms of sensor based applications, Si et al. [12] have fabricated Fe_2O_3/ZnO core/shell nanorods for cyclohexane, ethanol and acetone gas sensors while Hwang et al. [13] have fabricated ZnO/SnO_2 core/shell nanowires for NO_2 and C_2H_5OH gas sensors. Huang and Lin [14] have also fabricated ZnO/In_2O_3 core/shell nanorods for hydrogen sensors. In terms of photovoltaic applications, Schrier et al. [15] have grown ZnO/ZnS, ZnO/ZnTe core/shell nanowires while Greene et al. [16] have grown ZnO/TiO_2 core/shell nanorods. Kanmani and Ramachandran [17] have also fabricated TiO_2/ZnO core/shell nanomaterials for photovoltaic applications. Furthermore, Wang et al. [18] have also fabricated

ZnO/TiO_2 core/shell nanorods. In terms of supercapacitor applications, Li et al. [19] have prepared ZnO/MoO_3 core/shell nanocables while Yang et al. [20] have prepared hydrogenated ZnO based core/shell nanocables. In terms of energy storage applications, Xia et al. [21] have synthesised ZnO/NiO core/shell nanowires. In this context, Wang et al. [22] have reported crystalline ZnO/amorphous Bi_2O_3 core/shell nanorods and inorganic/organic (i.e. ZnO/ polyaniline (PANI)) core/shell nanotubes. Furthermore, Tang et al. [23] and Trejo et al. [24] have synthesised Zn/ZnO core/shell architectures. Also, Zhou et al. [25] have reported ZnO quantum dot based $ZnO/Zn(OH)_2$ core/shell architectures. Similarly, Richters et al. [26] and Chen et al. [27] have produced ZnO/Al_2O_3 core/shell nanowires and nanorods, respectively.

We now review briefly the growth methods used for the production of core/shell nanostructures. The core/shell nanostructures are typically fabricated as part of complex multi-step processes. In the first step, the nanostructure core is fabricated, followed by the growth of the shell region in a second step, with several intermediate operations and possibly a change of growth method being implemented between these two steps. For example, Greene et al. [16] have prepared ZnO nanorod cores in a two-step aqueous process and subsequently fabricated a TiO_2 shell by atomic layer deposition (ALD). Also, Huang et al. [14] have prepared the ZnO core and In_2O_3 shell by an aqueous chemical process and a combination of sputtering and thermal oxidation methods, respectively. Additionally, other growth methods were used such as hydrolysis by Si et al. [12] and Kanmani et al. [17], electro-chemical by Li et al. [19], and pulsed laser deposition (PLD) by Li et al. [4] and Kaydashev et al. [28]. Of particular interest for the present work, we note the PLD works of Kaydashev et al. [28] and Li et al. [4] who prepared $ZnO/Zn_{0.9}Mn_{0.1}O$ and ZnO/Er_2O_3 core/shell nanorods using multi-step growth processes in Ar and/or O_2 ambient pressures with the aid of an Au catalyst, respectively.

On the basis of the reported works, our goal for the present work is to reduce the complexity of these multi-step processes, which were used previously, to produce catalyst-free ZnO based core/shell nanorods. In this work [29], we grow for the first time, self-organised crystalline ZnO/amorphous ZnO core/shell nanorods on Si (100) wafers by PLD in a two stage process, without using a metal catalyst seed and without the need for a separate growth stage for the shell region. We also

investigate the structural, morphological and optical properties of the as-grown core/shell nanorod deposit and the relationship of the latter to the unique defect structure associated with the core/shell architecture. The details are discussed in Chapter 4.1.

1.2 ZnO nanorods: Motivation

Vertically aligned ZnO nanostructures (1D) have been of great interest for many years due to applications in optoelectronic devices such as light emitting diodes [30,31], nanolasers [32], solar cells [33], chemical and gas sensors [34,35], field emission devices [36,37] and schottky diodes [38]. Furthermore, ZnO nanorods have also been used for biosensors [39-41]. A recent review on ZnO nanostructure-based biosensors has been reported in refs [42,43]. Because of the biocompatibility properties of ZnO, it has also been used for anti-bacterial activities [44,45]. As mentioned earlier, ZnO has exciting material properties with a high optical gain* (300 cm^{-1}) [46]. These features are favourable for laser processes. Low-dimensional ZnO single crystals are able to reduce the laser threshold via the quantum size effect [46]. The above stated features drive considerable interest in the growth of ZnO based nanostructures such as nanorods, nanowires and nanobelts.

1.2.1 ZnO-seeded Si substrates

Silicon (Si) is a commonly used substrate due to its high melting point that allows high processing temperatures during deposition and results in good conductive/electrical properties [4,13,15,29,36,46-50]. However, direct growth of ZnO nanorods or nanowires on a Si substrate is not possible as ZnO does not readily nucleate on the Si surface. In this regard, a metal catalyst, e.g. Au-coated Si has been used [51]. However, due to a large mismatch of 40.1 % between the ZnO and Si lattices [48], the as-grown ZnO nanorods tended to grow with poor alignment. Later on, a thin ZnO film used as a seed layer on Si was suitable to grow highly vertically aligned ZnO nanorods [29,36,46-50,52-54].

*Optical gain describes the optical amplification in the material, this is associated with stimulated emission of the light (photons) created by the electrons and holes recombination.

This is because the ZnO seed layer helps to form nucleation sites that initiate nanorod growth, and also it provides a crystalline substrate with a perfect lattice match for the ZnO nanorod growth. In this work, we used Si (100) wafers as substrate.

1.2.2 ZnO seed layers grown by PLD on Si substrates

Li et al. [48,49] have reported a detailed study of the growth of ZnO nanorods by vapour phase transport (VPT) on ZnO seed layers grown by various techniques such as PLD, direct current (DC) reactive sputtering, radiofrequency (RF) sputtering and thermal oxidation methods. Jie et al. [54] have reported the synthesis and optical properties of ZnO nanorods by VPT on PLD prepared ZnO seed layers. Zhao et al. [50] have reported VPT grown ZnO nanorods on ZnO seed layers prepared by electron beam evaporation. Rajendra Kumar et al. [36] have reported VPT-grown ZnO nanorods on PLD-grown ZnO seed layers and studied their effects on field emission properties. Garry et al. [55] have reported ZnO nanorod arrays by VPT on PLD-grown ZnO seed layers using nanosphere lithography (NSL) patterns, with and without a Au catalyst. However, a drawback associated with lithography techniques is the low deposition temperature. On the whole, PLD-prepared ZnO seed layers are considered to be the best choice for the growth of high density, highly textured and high optical quality of vertically aligned ZnO nanorods, as observed by Li et al. [48] and Jie et al. [54].

1.2.3 ZnO nanorods grown by PLD on ZnO-seeded Si substrates

ZnO nanorods were grown using the PLD technique on PLD deposited ZnO seed layers by a few workers. For example, Sun et al. have grown ZnO nanorods [56-58], nanowires [59] and nanotubes [60] by PLD on PLD-prepared ZnO seed layers. The morphologies of such nanorods/nanowires/nanowalls are highly dependent on background gas pressure during deposition. For example, Tien et al. [61] and Zhang et al. [62] have studied the effects of the ambient pressure of the oxygen/argon gas mixture on the morphology of the ZnO nanostructures on ZnO-coated sapphire substrates. Their studies showed a transition from ZnO nanowalls to ZnO nanowires/nanorods morphology with a variation of background gas pressure from 150 to 500 mTorr in ref [61], and from 20 to 175 Torr in ref [62]. Premkumar

et al. [63] have grown ZnO nanorods and nanowalls by PLD on GaN, Al_2O_3 and Si substrates while Liu et al. [64] have grown ZnO nanorods on Si and sapphire substrates. Li et al. [65] and Choi et al. [66] have also grown ZnO nanorods and brush-shaped ZnO hetero nanorods by PLD, respectively.

1.2.4 ZnO nanorods grown by VPT on ZnO seeded Si substrates

There are only a few reports of VPT-grown ZnO nanorods on PLD-prepared ZnO seed layers. Li et al. [48,49], Jie et al. [54], Rajendra Kumar et al. [36], and Garry et al. [55] have previously produced VPT-grown ZnO nanorods on PLD-prepared ZnO seed layers without a metal catalyst.

In order to understand the growth of high quality ZnO nanorods on ZnO seed layers, the crystalline, surface morphology and optical properties of both the ZnO seed layers and ZnO nanorods need to be studied. To the best of our knowledge, this type of work has not been reported previously. In this thesis, (i) we grow high optical quality and high density of vertically aligned ZnO nanorods by a catalyst-free VPT technique on the catalyst-free PLD-grown ZnO seed layers. (ii) For the first time, we systematically study and inter-compare the structural, morphological and optical properties of the PLD-grown ZnO seed layers, PLD-grown ZnO nanorods and VPT-grown ZnO nanorods. (iii) Importantly, we further investigate the origin of the 3.331 eV emission band in ZnO seen in the PLD-grown nanorod samples, by comparing the PL emissions seen from PLD- and VPT-grown nanorod samples. The results and details are given in section 4.3.

1.3 ZnO and AZO thin films on plastics: Motivation

Deposition of transparent conductive oxide (TCO) films on thin plastic flexible substrates is of significant interest in research and current technological developments. This is due to the need for such material systems in novel applications of transparent electronics where flexibility has become a key factor. Plastic substrates feature advantageous characteristics including light weight, compactness, impact resistance as well as low-cost and, thus, supersede glass substrates in certain applications.

1.3.1 ZnO-based TCOs on flexible Zeonor plastics

In recent years, deposition of ZnO-based TCOs on flexible plastic substrates has attracted much attention due to the wide range of applications of such materials in flexible flat panel displays [67], solar cells [68], organic light emitting diodes [69], and thin film transistors [70,71], for example.

ZnO and Al-doped ZnO (AZO) are well-known semiconductor oxide materials for thin film deposition and generally produce films with excellent optical, e.g. high transparency [72], and electrical, e.g. n-type conductivity properties [73,74]. These materials also exhibit long-term environmental stability [75] and bio-compatibility properties [11]. There exists a body of work on the deposition and properties of thin films of ZnO, AZO and the related materials IGZO (indium- gallium ZnO), IZO (ZnO:In) and GZO (ZnO:Ga), on plastic substrates such as polyethylene terephthalate (PET) [68,71,76-80], polyethylene naphtalate (PEN) [70], polycarbonate (PC) [81], polymethyl methacrylate (PMMA or Perspex) [82], polymide (PI) [69,83], polyester [84] and cyclo-olefin polymer (COP) [85,86].

In this research, we use for the first time [87] Zeonor® -a proprietary brand of COP plastics [88]- hereafter referred to as Zeonor, as a substrate for the deposition of ZnO and AZO thin films. Zeonor is the material of choice for many applications in microfluidics [89], bio-diagnostics [90] and biosensors [91], as well as in stringent optics applications such as high density DVDs, liquid crystal displays and plastic optical fibers [88,92]. These and other state-of-the-art devices may variously require the deposition of electrical contacts and/or high-quality optical coatings that could potentially be achieved with ZnO and AZO thin films. Zeonor has unique features compared to other plastic materials [88]; notably, its water absorption of less than 0.01% is significantly smaller than that of PC (0.2%), PMMA (0.3%) and PET (0.01 to 1.5%) [85,88,92]. Thus, outgassing and water absorption effects in a vacuum environment are minimised, enabling the direct deposition of materials on Zeonor without the need for buffer or barrier layers.

Deposition on Zeonor plastic requires substrates at low or room temperatures, this is because the glass transition* temperature of Zeonor is close to 100 ^{o}C [88]. PLD appears a highly suitable and versatile preparation technique to meet this demanding challenge. Furthermore, due to high-energetic, on the order of or > 1 eV [76], plasma particles produced during deposition in the PLD chamber, the materials can crystallise even at low/room temperatures. Indeed, several works have reported the production of high-quality crystalline ZnO/AZO films on amorphous or plastic substrates using PLD at room/low temperatures, e.g. [76, 82,93,94]. PLD at room temperature (RT) is, thus, the growth technique that we use in the present work to grow ZnO and AZO films on Zeonor plastic substrates. More details on the PLD growth technique are provided in section 2.2.

The growth rate, surface morphology, hydrophobicity and the structural, optical and electrical properties of as-grown films with thicknesses ~ 65 nm - 420 nm were recorded for oxygen growth pressures between 1 and 300 mTorr. Films with high reproducibility, excellent crystallinity, high optical transparency and good conductivity were obtained. We also performed an ageing study on selected samples. The details are given in sections- 5.1, 5.2 and 5.3.

1.4 General objectives of this work

Based on this background information and the reviews of the fields, we state our aims and goals:

- To reduce the complexity of the multi-step and multi growth processes used previously for the production of core/shell nanorods. To produce ZnO core/shell architectures by PLD using a two-stage process, without the aid of any metal catalyst.
- To produce high optical quality and high-density vertically aligned ZnO nanorods on PLD grown ZnO seed layers.

*The glass transition in amorphous materials is the reversible transition from a hard and brittle state (glass state) into a molten, rubber-like, state as the temperature is increased.

- To use PLD to grow reproducible, high-quality ZnO and AZO nanocrystalline thin films on flexible Zeonor plastic substrates at room temperature, and reveal the dependency of the growth rates, the microstructure and the surface, structural, optical and electrical properties of ZnO and AZO thin films of different thicknesses on the oxygen ambient pressure.
- To use PLD to grow high quality ZnO and AZO nanostructured films on polycarbonate plastic substrates for the investigation of glucose oxidase-based bio-sensing application. This work is presented in Appendix A.
- To investigate the effects of atmospheric air plasma treatment of polished graphite and unpolished carbon felt electrodes on their surface roughness and hydrophobicity and the current output from electrochemically active *S. loihica* PV-4 biofilms for bio-fuel cell applications. This work is presented in Appendix B.

1.5 Thesis Outline

This thesis comprises seven chapters. We give a brief description of the contents of each of the chapters.

Chapter 1

This chapter provides the background information on, and applications of, the topics covered in the thesis. The reviews of the fields justify our motivation for the research and the various goals of the thesis.

Chapter 2

This chapter describes the general properties of the ZnO material including the crystal and electronic structures. We provide background on the operating principles, and experimental descriptions of both the nanostructures growth and air plasma apparatus used in this work.

Chapter 3

This chapter describes the various characterisation techniques that were used in this work to study the surface morphology and material properties of the as-grown samples. The principles of operation and equipment setup of the techniques are also presented.

Chapter 4

This chapter describes the growth and characterisation of unique crystalline-ZnO/amorphous-ZnO core/shell nanorods. These self-organised core/shell architectures are prepared by a catalyst-free PLD technique on ZnO-seeded Si (100) substrates. The structural, morphological and luminescent properties of the ZnO nanorod samples are established. A ZnO emission band at 3.331eV is revealed in the core/shell architecture and its origin is linked to the observed defects at the crystalline/amorphous interface of the core/shell structure.

This chapter also presents the catalyst free-PLD growth and characterisation of interconnected architectures based ZnO core/shell nanorods on ZnO-seeded Si (100) substrates, and notably their optical properties.

This chapter also describes the growth and characterisation of high optical quality and high density of vertically aligned ZnO nanorods by a catalyst-free VPT technique on catalyst free PLD-grown ZnO seed layers. This work also compares the structural, morphological and optical properties of the PLD-grown ZnO seed layers, PLD-grown ZnO nanorods, and VPT-grown ZnO nanorods.

Chapter 5

This chapter describes the growth and characterisation of highly transparent and conductive ZnO and Al-doped ZnO (AZO) nanocrystalline thin films on flexible Zeonor plastic substrates. These films are reproducibly grown using PLD at room temperature. This chapter shows the effects of oxygen in a selected pressure range on the growth rate, surface morphology, hydrophobicity and the structural, optical and electrical properties of films having different thicknesses. The pressure range explored should correspond with observable changes in the film properties as it is in

the range where nanostructuring should occur. This chapter also presents an ageing study on selected samples.

Chapter 6

This last chapter summarises the works and results discussed in the thesis, as well as suggestions for possible future applications for the works.

Appendix A

This section presents the growth and characterisation of ZnO and AZO nanostructured films on polycarbonate (PC) plastic substrates. The performance (measured as part of a collaborative work) of the nanostructured ZnO and AZO films prepared on PC substrates as part of a glucose oxidase (GOx)-based biosensor application is presented.

Appendix B

This section investigates the effects of atmospheric air plasma treatment on surface roughness, hydrophobicity and the current output from attached *S. loihica* PV-4 cells on polished graphite, and carbon felt electrodes. This collaborative work demonstrated a low-cost, scalable and user friendly route to increase the current output in bio-electrochemical systems based on atmospheric air plasma treatments.

1.6 References

[1] Y. F Zhu, A. H. Fan, W. Z. Shen, A general chemical conversion route to synthesize various ZnO-based core/shell structures, *J. Phys. Chem. C* 112 (2008) 10402-10406.

[2] S. K. Panda, A. Dev, S. Chaudhuri, Fabrication and luminescent properties of c-axis oriented ZnO-ZnS core-shell and ZnS nanorod arrays by sulfidation of aligned ZnO nanorod arrays, *J. Phys. Chem. C* 111 (2007) 5039-5043.

[3] T. Gao, Q. Li, T. Wang, Sonochemical synthesis, optical properties, and electrical properties of core/shell-type ZnO nanorod/CdS nanoparticle composites. *Chem. Mater.* 17 (2005) 887-892.

[4] S. Z. Li, C.L. Gan, H. Cai, C.L. Yuan, J. Guo, P.S. Lee, J. Ma, Enhanced photoluminescence of ZnO/Er_2O_3 core-shell structure nanorods synthesized by pulsed laser deposition, *Appl. Phys. Lett. 90* (2007) 263106.

[5] C.-C. Lee, D.-H. Chen, Large-scale synthesis of Ni-Ag core-shell nanoparticles with magnetic, optical and anti-oxidation properties, *Nanotechnology* 17 (2006) 3094-3099.

[6] Y.-S. Lin, Y. Hung, H.-Y. Lin, Y.-H. Tseng, Y.F. Chen, C.-Y. Mou, Photonic crystals from monodisperse lanthanide-hydroxide-at-silica core/shell colloidal spheres, *Adv. Mater.* 19 (2007) 577-580.

[7] J. Jang, Y. Nam, H. Yoon, Fabrication of polypyrrole-poly(n-vinylcarbazole) core-shell nanoparticles with excellent electrical and optical properties, *Adv. Mater.* 17 (2005) 1382-1386.

[8] F. Caruso, Nanoengineering of particle surfaces, *Adv. Mater.* 13 (2001) 11-22.

[9] Z.L. Wang, Novel nanostructures of ZnO for nanoscale photonics, optoelectronics, piezoelectricity, and sensing, *Appl.Phys. A* 88 (2007) 7-15.

[10] Z.L. Wang, J. Song, Piezoelectric nanogenerators based on zinc oxide nanowire arrays, *Science* 312 (2006) 242-246.

[11] Y. Liu, M. Zhong, G. Shan, Y. Li, B. Huang, G. Yang, Biocompatible ZnO/Au nanocomposites for ultrasensitive DNA detection using resonance Raman scattering. *J. Phys. Chem. B* 112 (2008) 6484-6489.

[12] S. Si, C. Li, X. Wang, Q. Peng, Y. Li, Fe_2O_3/ZnO core-shell nanorods for gas sensors, *Sensors Actuat. B-Chem.* 119 (2006) 52-56.

[13] I.-S. Hwang, S.-J. Kim, J.-K. Choi, J. Choi, H. Ji, G.-T. Kim, G. Cao, J.-H. Lee, Synthesis and gas sensing characteristics of highly crystalline ZnO–SnO_2 core–shell nanowires, *Sensors Actuat. B-Chem.* 148 (2010) 595-600.

[14] B.-J. Huang, J.-C. Lin, Core-shell structure of zinc oxide/indium oxide nanorod based hydrogen sensors, *Sensors Actuat. B-Chem.* 174 (2012) 389-393.

[15] J. Schrier, D.O. Demchenko, L.W. Wang, Optical properties of ZnO/ZnS and ZnO/ZnTe heterostructures for photovoltaic applications, *Nano Lett.* 7 (2007) 2377-2382.

[16] L.E. Greene, M. Law, B.D. Yuhas, P.Yang, ZnO-TiO_2 core-shell nanorod/P3HT solar cells, *J. Phys. Chem. C* 111 (2007) 18451-18456.

[17] S.S. Kanmani, K. Ramachandran, Synthesis and characterization of TiO_2/ZnO core/shell nanomaterials for solar cell applications, *Renewable Energy* 43(2012) 149-156.

[18] M. Wang, C. Huang, Y. Cao, Q. Yu, W. Guo, Q. Huang, Y. Liu, Z. Huang, J. Huang, H. Wang, Z. Deng, The effects of shell characteristics on the current-voltage behaviors of dye-sensitized solar cells based on ZnO/TiO_2 core/shell arrays, *Appl. Phys. Lett.* 94 (2009) 263506.

[19] G.R. Li, Z.-L. Wang, F.-L. Zheng, Y.-N. Ou, Y.-X. Tong, ZnO@MoO_3 core/shell nanocables: facile electrochemical synthesis and enhanced supercapacitor performances, *J. Mater. Chem.* 21 (2011) 4217-4221.

[20] P. Yang, X. Xiao, Y. Li, Y. Ding, P. Qiang, X. Tan, W. Mai, Z. Lin, W. Wu, T. Li, H. Jin, P. Liu, J. Zhou, C.P. Wong, Z.L. Wang, Hydrogenated ZnO Core-Shell Nanocables for Flexible Supercapacitors and Self-Powered Systems, *ACS Nano* 7 (2013) 2617-2626.

[21] X. Xia, J. Tu, Y. Zhang, X. Wang, C. Gu, X.-B. Zhao, H.J. Fan, High-Quality Metal Oxide Core/Shell Nanowire Arrays on Conductive Substrates for Electrochemical Energy Storage, *ACS Nano* 6 (2012) 5531-5538.

[22] Z.-L. Wang, R. Guo, G.-R. Li, L.-X. Ding, Y.-N. Ou, Y.-X. Tong, Controllable synthesis of ZnO-based core/shell nanorods and core/shell nanotubes, *RSC Adv.* 1 (2011) 48-51.

[23] D.-M. Tang, G. Liu, F. Li, J. Tan, C. Liu, G.Q. Lu, H.-M. Cheng, Synthesis and Photoelectrochemical Property of Urchin-like Zn/ZnO Core-Shell Structures, *J. Phys. Chem. C* 113 (2009) 11035-11040.

[24] M. Trejo, P. Santiago, H. Sobral, L. Rendon, U. Pal, Synthesis and Growth Mechanism of One-Dimensional Zn/ZnO Core-Shell Nanostructures in Low-Temperature Hydrothermal Process, *Cryst. Growth Des.* 9 (2009) 3024-3030.

[25] H. Zhou, H. Alves, D.M. Hofmann, W. Kriegseis, B.K. Meyer, G. Kaczmarczyk, A. Hoffmann, Behind the weak excitonic emission of ZnO quantum dots: ZnO/$Zn(OH)_2$ core-shell structure, *Appl. Phys. Lett.* 80 (2002) 210-212.

[26] J.-P. Richters, T. Voss, D.S. Kim, R. Scholz, M. Zacharias, Enhanced surface-excitonic emission in ZnO/Al2O3 core–shell nanowires, *Nanotechnology* 19 (2008) 305202.

[27] C.Y. Chen, C.A. Lin, M.J. Chen, G.R. Lin, J.H. He, ZnO/Al_2O_3 core–shell nanorod arrays: growth, structural characterization, and luminescent properties, *Nanotechnology* 20 (2009) 185605.

[28] V.E. Kaydashev, E.M. Kaidashev, M. Peres, T. Monteiro, M.R. Correia, N.A. Sobolev, L.C. Alves, N. Franco, E. Alves, Structural and optical properties of $Zn_{0.9}Mn_{0.1}O$/ZnO core-shell nanowires designed by pulsed laser deposition, *J. Appl. Phys.* 106 (2009) 093501.

[29] S. Inguva, S.K. Marka, R.K. Vijayaraghavan, E. McGlynn, Vadali V. S. S. Srikanth, J.-P. Mosnier, Crystalline ZnO/amorphous ZnO core/shell nanorods: Self-organized growth, structure and novel luminescence, *J. Phys. Chem. C* 119 (2015) 4848-4855.

[30] J.C.D. Faria, A.J. Campbell, M.A. McLachlan, ZnO Nanorod Arrays as Electron Injection Layers for Efficient Organic Light Emitting Diodes, *Adv. Funct. Mater.* 25 (2015) 4657-4663.

[31] Y. Ryu, T.-S. Lee, J.A. Lubguban, H.W. White, B.-J. Kim, Y.-S. Park, C.-J. Youn, Next generation of oxide photonic devices: ZnO-based ultraviolet light emitting diodes, *Appl. Phys. Lett.* 88 (2006) 241108.

[32] Y.-H. Chou, B.-T. Chou, C.-K. Chiang, Y.-Y. Lai, C.-T. Yang, H. Li, T.-R. Lin, C.-C. Lin, H.-C. Kuo, S.-C. Wang, T.-C. Lu, Ultrastrong Mode Confinement in ZnO Surface Plasmon Nanolasers, *ACS Nano* 9 (2015) 3978-3983.

[33] Y. Dou, F. Wu, C. Mao, L. Fang, S. Guo, M. Zhou, Enhanced photovoltaic performance of ZnO nanorod-based dye-sensitized solar cells by using Ga doped ZnO seed layer, *J. Alloys Compounds* 633 (2015) 408-414.

[34] S. Santra, A. De Luca, S. Bhaumik, S.Z. Ali, F. Udrea, J.W. Gardner, S.K. Ray, P.K. Guha, Dip pen nanolithography-deposited zinc oxide nanorods on a CMOS MEMS platform for ethanol sensing, *RSC Adv.* 5 (2015) 47609.

[35] M. Cittadini, M. Sturaro, M. Guglielmi, A. Resmini, I.G. Tredici, U. Anselmi-Tamburini, P. Koshy, C.C. Sorrell, A. Martucci, ZnO nanorods grown on ZnO sol–gel seed films: Characteristics and optical gas-sensing properties, *Sensors Actuat. B-Chem.* 213 (2015) 493-500.

[36] R.T. Rajendra Kumar, E. McGlynn, C. McLoughlin, S. Chakrabarti, R.C. Smith, J.D. Carey, J.P. Mosnier, M.O. Henry, Control of ZnO nanorod array density by Zn supersaturation variation and effects on field emission, *Nanotechnology* 18 (2007) 215704.

[37] S Garry, É McCarthy, J.P. Mosnier, E McGlynn, Influence of ZnO nanowire array morphology on field emission characteristics, *Nanotechnology* 25 (2014) 135604.

[38] Z. Yuan, Low-Temperature Growth of Well-Aligned ZnO Nanorod Arrays by Chemical Bath Deposition for Schottky Diode Application, *J. Electron Mater.* 44 (2015) 1187-1191.

[39] R. Ahmad, N. Tripathy, J.-H. Park, Y.-B. Hahn, A comprehensive biosensor integrated with a ZnO nanorod FET array for selective detection of glucose, cholesterol and urea, *Chem. Comm.* 51 (2015) 11968-11971.

[40] Z. Kang, Y. Gu, X. Yan, Z. Bai, Y. Liu, S. Liu, X. Zhang, Z. Zhang, X. Zhang, Y. Zhang, Enhanced photoelectrochemical property of ZnO nanorods array synthesized on reduced graphene oxide for self-powered biosensing application, *Biosens. Bioelectron.* 64 (2015) 499-504.

[41] Z. Kang, X. Yan, Y. Wang, Z. Bai, Y. Liu, Z. Zhang, P. Lin, X. Zhang, H. Yuan, X. Zhang, Y. Zhang, Electronic Structure Engineering of Cu_2O Film/ZnO Nanorods Array All-Oxide p-n Heterostructure for Enhanced Photoelectrochemical Property and Self-powered Biosensing Application, *Scientific Reports* 5 (2015) 7882.

[42] S.K. Arya, S. Saha, J.E. Ramirez-Vick, V. Gupta, S. Bhansali, S.P. Singh, Recent advances in ZnO nanostructures and thin films for biosensor applications: review, *Anal. Chim. Acta.* 737 (2012) 1-21.

[43] Y. Zhang, Z. Kang, X. Yan, Q. Liao, ZnO nanostructures in enzyme biosensors, *Sci. China Mater.* 58 (2015) 60-76.

[44] K.H. Tam, A.B. Djurišić, C.M.N. Chan, Y.Y. Xi, C.W. Tse, Y.H. Leung, W.K. Chan, F.C.C. Leung, D.W.T. Au, Antibacterial activity of ZnO nanorods prepared by a hydrothermal method, *Thin Solid Films* 516 (2008) 6167-6174.

[45] T.O. Okyay, R.K. Bala, H. N. Nguyen, R. Atalay, Y. Bayam, D.F. Rodrigues, Antibacterial properties and mechanisms of toxicity of sonochemically grown ZnO nanorods, *RSC Adv.* 5 (2015) 2568-2575.

[46] D.C. Kim, B.H. Kong, H.K. Cho, D.J. Park, J.Y. Lee, Effects of buffer layer thickness on growth and properties of ZnO nanorods grown by metalorganic chemical vapour deposition, *Nanotechnology* 18 (2007) 015603.

[47] D. Byrne, E. McGlynn, J. Cullen, M.O. Henry, A catalyst-free and facile route to periodically ordered and c-axis aligned ZnO nanorod arrays on diverse substrates, *Nanoscale* 3 (2011) 1675-1682.

[48] C. Li, G. Fang, J. Li, L. Ai, B. Dong, X. Zhao, Effect of seed layer on structural properties of ZnO nanorod arrays grown by vapor-phase transport, *J. Phys. Chem. C* 112 (2008) 990-995.

[49] C. Li, G. Fang, Q. Fu, F. Su, G. Li, X. Wu, X. Zhao, Effect of substrate temperature on the growth and photoluminescence properties of vertically aligned ZnO nanostructures, *J. Cryst. Growth.* 292 (2006) 19-25.

[50] D. Zhao, C. Andreazza, P. Andreazza, J. Ma, Y. Liu, D. Shen, Buffer layer effect on ZnO nanorods growth alignment, *Chem. Phys. lett.* 408 (2005) 335-338.

[51] R.T.R. Kumar, E. McGlynn, M. Biswas, R. Saunders, G. Trolliard, B. Soulestin, J. Duclere, J.P. Mosnier, M.O. Henry, Growth of ZnO nanostructures on Au-coated Si: Influence of growth temperature on growth mechanism and morphology, *J. Appl. Phys.* 104 (2008) 084309.

[52] D.J. Park, D.C. Kim, J.Y. Lee, H.K. Cho, Synthesis and microstructural characterization of growth direction controlled ZnO nanorods using a buffer layer, *Nanotechnology* 17 (2006) 5238-5243.

[53] J. Song, S. Lim, Effect of seed layer on the growth of ZnO nanorods, *J. Phys. Chem. C* 111 (2007) 596-600.

[54] J. Jie, G. Wang, Y. Chen, X. Han, Q. Wang, B. Xu, J. Hou, Synthesis and optical properties of well-aligned ZnO nanorod array on an undoped ZnO film, *Appl. Phys. Lett.* 86 (2005) 031909.

[55] S. Garry, E. McCarthy, J.P. Mosnier, E. McGlynn, Control of ZnO nanowire arrays by nanosphere lithography (NSL) on laser-produced ZnO substrates, *Appl. Surf. Sci.* 257 (2011) 5159-5162.

[56] Y. Sun, G.M. Fuge, M.N.R. Ashfold, Growth of aligned ZnO nanorod arrays by catalyst-free pulsed laser deposition methods, *Chem. Phys. Lett.* 396 (2004) 21-26.

[57] Y. Sun, R.P. Doherty, J.L. Warren, M.N.R. Ashfold, Effect of incident fluence on the growth of ZnO nanorods by pulsed excimer laser deposition, *Chem. Phys. Lett.* 447 (2007) 257-262.

[58] Y. Sun, G.M. Fuge, M.N.R. Ashfold, Growth mechanisms for ZnO nanorods formed by pulsed laser deposition, *Superlattice Microst.* 39 (2006) 33-40.

[59] Y. Sun, N.A. Fox, G.M. Fuge, M.N.R. Ashfold, Toward a Single ZnO Nanowire Homojunction, *J. Phys. Chem. C* 114 (2010) 21338-21341.

[60] Y. Sun, G.M. Fuge, N.A. Fox, D.J. Riley, M.N. R. Ashfold, *Adv. Mater.* 17 (2005) 2477-2481.

[61] L. C. Tien, S. J. Pearton, D. P. Norton, F. Ren, Synthesis and microstructure of vertically aligned ZnO nanowires grown by high-pressure-assisted pulsed-laser deposition, *J. Mater. Sci*. 43 (2008) 6925-6932.

[62] P. Zhang, G.D. Zhou, H.B. Gong, H.Y. Xu, D. Nakamura, T. Okada, H.B. Zeng, B.Q. Cao, Pressure-Induced Growth Evolution of Different ZnO Nanostructures by a Pulsed Laser Ablation Method, *Sci. Adv. Mater.* 4 (2012) 455-462.

[63] T. Premkumar, Y.S. Zhou, Y.F. Lu, K. Baskar, Optical and Field-Emission Properties of ZnO Nanostructures Deposited Using High-Pressure Pulsed Laser Deposition, *ACS Appl. Mater. Interfaces* 2 (2010) 2863-2869.

[64] Z.W. Liu, C.K. Ong, T. Yu, Z.X. Shen, Catalyst-free pulsed-laser-deposited ZnO nanorods and their room-temperature photoluminescence properties, *Appl. Phys. Lett.* 88 (2006) 053110.

[65] Q. Li, K. Gao, Z. Hu, W. Yu, N. Xu, J. Sun, J. Wu, Photoluminescence and Lasing Properties of Catalyst-Free ZnO Nanorod Arrays Fabricated by Pulsed Laser Deposition, *J. Phys. Chem. C* 116 (2012) 2330-2335.

[66] J. Choi, H. Ji, O.T. Tambunan, I.-S. Hwang, H.-S. Woo, J.-H. Lee, B.W. Lee, C. Liu, S.J. Rhee, C.U. Jung, G.-T. Kim, Brush-Shaped ZnO Heteronanorods Synthesized Using Thermal-Assisted Pulsed Laser Deposition, *ACS Appl. Mater. Interfaces* 3 (2011) 4682-4688.

[67] J. Lee, P. Lee, H.B. Lee, S. Hong, I. Lee, J. Yeo, S.S. Lee, T.-S. Kim, D. Lee, S.H. Ko, Room-Temperature Nanosoldering of a Very Long Metal Nanowire Network by Conducting-Polymer-Assisted Joining for a Flexible Touch-Panel Application, *Adv. Funct. Mater.* 23 (2013) 4171-4176.

[68] G.-J. Chang, S.-Y. Lin, J.-J. Wu, Room-temperature chemical integration of ZnO nanoarchitectures on plastic substrates for flexible dye-sensitized solar cells, *Nanoscale* 6 (2014)1329-1334.

[69] J.-S. Park, T.-W. Kim, D. Stryakhilev, J.-S. Lee, S.-G. An, Y.-S. Pyo, D.-B. Lee, Y.G. Mo, D.-U. Jin, H.K. Chuang, Flexible full color organic light-emitting

diode display on polyimide plastic substrate driven by amorphous indium gallium zinc oxide thin-film transistors, *Appl. Phys. Lett.* 95 **(**2009) 013503.

[70] Y.H. Hwang, J.-S. Seo, J.M. Yun, H. Park, S. Yang, S.-H.K Park, B.-S. Bae, An 'aqueous route' for the fabrication of low-temperature-processable oxide flexible transparent thin-film transistors on plastic substrates, *NPG Asia Mater.* 5 (2013) e45.

[71] K. Nomura, H. Ohta, A. Takagi, T. Kamiya, M. Hirano, H. Hosono, Room-temperature fabrication of transparent flexible thin-film transistors using amorphous oxide semiconductors, *Nature* 432 (2004) 488-492.

[72] H. Hagendorfer, K. Lienau, S. Nishiwaki, C.M. Fella, L. Kranz, A.R. Uhl, D. Jaeger, L. Luo, C. Gretener, S. Buecheler, Y.E. Romanyuk, A.N. Tiwari, Highly Transparent and Conductive ZnO: Al Thin Films from a Low Temperature Aqueous Solution Approach, *Adv. Mater.* 26 **(**2014) 632-636.

[73] J.G. Lu, Z.Z. Ye, Y.J. Zeng, L.P. Zhu, L. Wang, J. Yuan, B.H. Zhao, Q.L. Liang, Structural, optical, and electrical properties of (Zn,Al)O films over a wide range of compositions, *J. Appl. Phys.* 100 (2006) 073714.

[74] J.G. Lu, S. Fujita, T. Kawaharamura, H. Nishinaka, Y. Kamada, T. Ohshima, Z.Z.Ye, Y.J. Zeng, Y.Z. Zhang, L.P. Zhu, H.P. He, B.H. Zhao, Carrier concentration dependence of band gap shift in n-type ZnO:Al films, *J. Appl. Phys.* 101 (2007) 083705.

[75] D.H. Zhang, T.L. Yang, J. Ma, Q.P. Wang, R.W. Gao, H.L. Ma, Preparation of transparent conducting ZnO:Al films on polymer substrates by r.f. magnetron sputtering, *Appl. Surf. Sci.* 158 (2000) 43-48.

[76] G. Socol, M. Socol, N. Stefan, E. Axente, G. Popescu-Pelin, D. Craciun, L. Duta, C.N. Mihailescu, I.N. Mihailescu, A. Stanculescu, D. Visan, V. Sava, A.C. Galca, C.R. Luculescu, V. Craciun, Pulsed laser deposition of transparent conductive oxide thin films on flexible substrates, *Appl. Surf. Sci.* 260 (2012) 42-46.

[77] K.A. Sierros, D.A. Banerjee, N.J. Morris, D.R. Cairns, I. Kortidis, G. Kiriakidis, Mechanical properties of ZnO thin films deposited on polyester substrates used in flexible device applications, *Thin Solid Films* 519 (2010) 325-330.

[78] R.-Y. Yang, M.-H. Weng, C.-T. Pan, C.-M. Hsiung, C.-C. Huang, Low-temperature deposited ZnO thin films on the flexible substrate by cathodic vacuum arc technology, *Appl. Surf. Sci.* 257 (2011) 7119-7122.

[79] D. Han, W. Wang, J. Cai, L. Wang, Y. Ren, Y. Wang, Z. Shengdong, Flexible Thin-Film Transistors on Plastic Substrate at Room Temperature, *J. Nanosci. Nanotechnol.* 13 (2013) 5154-5157.

[80] D. Han, C. Zhuofa, N. Zhao, W. Wang, F. Huang, S. Zhang, X. Zhang, Y. Wang, Flexible aluminum-doped zinc-oxide thin-film transistor fabricated on plastic substrates, *Proc. SPIE USA* 8987 (2014) 89871L (doi: 10.1117/12.2044554).

[81] L. Gong, J. Lu, Z. Ye, Transparent and conductive Ga-doped ZnO films grown by RF magnetron sputtering on polycarbonate substrates, *Sol. Energy Mater. Sol. Cells* 94 (2010) 937-941.

[82] J. Connolly, A. Jain, G. Pastorella, S. Krishnamurthy, J.-P Mosnier, E. Marsili, Zinc oxide and indium tin oxide thin films for the growth and characterization of Shewanella loihica PV-4 electroactive biofilms, *Virulence* 2 (2011) 479-482.

[83] M. Matsumura, R.P. Camata, Pulsed laser deposition and photoluminescence measurements of ZnO thin films on flexible polyimide substrates, *Thin Solid Films* 476 (2005) 317-321.

[84] E. Fortunato, P. Nunes, D. Costa, D. Brida, I. Ferreira, R. Martins, Characterization of aluminium doped zinc oxide thin films deposited on polymeric substrates, *Vacuum* 64 (2002) 233-236.

[85] A. Miyake, T. Yamada, H. Makino, N. Yamamoto, T. Yamamoto, Effect of substrate temperature on structural, electrical and optical properties of Ga-doped ZnO films on cyclo olefin polymer substrate by ion plating deposition, *Thin Solid Films* 517 (2008) 1037-1041.

[86] J.-P. Kim, J.-S. Bae, T.-E. Hong, M.-S. Won, J.-H. Yoon, B.-S. Lee, H.-J. Lee, Optical and electrical properties of ZnO films, codoped with Al and Ga deposited at room temperature by an RF sputtering method, *Thin Solid Films* 518 (2010) 6179-6183.

[87] S. Inguva, R.K. Vijayaraghavan, E. McGlynn, J.-P. Mosnier, Highly transparent and reproducible nanocrystalline ZnO and AZO thin films grown by room temperature pulsed-laser deposition on flexible Zeonor plastic substrates, *Mater. Res. Express* 2 (2015) 096401.

[88] Web reference: Zeon Corporation, Available at: www.zeon.co.jp (last accessed 2nd May 2015).

[89] S. Laib, B.D. MacCraith, Immobilization of biomolecules on cyclo olefin polymer supports, *Anal. Chem.*79 (2007) 6264-6270.

[90] R.P. Gandhiraman, C. Volcke, V. Gubala, C. Doyle, L. Basabe-Desmonts, C. Dotzler, M.F. Toney, M. Iacono, R.I. Nooney, S. Daniels, B. James, D.E. Williams, High efficiency amine functionalization of cycloolefin polymer surfaces for biodiagnostics, *J. Mater. Chem.* 20 (2010) 4116-4127.

[91] C. Volcke, R.P. Gandhiraman, V. Gubala, J. Raj, Th. Cummins, G. Fonder, R.I. Nooney, Z. Mekhalif, G. Herzog, S. Daniels, D.W.M. Arrigan, A.A. Cafolla, D.E. Williams, Reactive amine surfaces for biosensor applications, prepared by plasma-enhanced chemical vapour modification of polyolefin materials, *Biosens. Bioelectron.* 25 (2010)1875-1880.

[92] K. Obuchi, M. Komatsu, K. Minami, High performance optical materials cyclo olefin polymer ZEONEX, *Proc. SPIE USA* 6671 (2007) 66711I (doi:10.1117/12.749910).

[93] K. Matsubara, P. Fons, K. Iwata, A. Yamada, S. Niki, Room-temperature deposition of Al-doped ZnO films by oxygen radical-assisted pulsed laser deposition, *Thin Solid Films* 422 (2002)176-179.

[94] J.-P. Mosnier, R.J. O'Haire, E. McGlynn, M.O. Henry, S.J. McDonnell, M.A. Boyle, K.G. McGuigan**,** ZnO films grown by pulsed-laser deposition on soda lime glass substrates for the ultraviolet inactivation of Staphylococcus epidermidis biofilms, *Sci. Technol. Adv. Mater.* 10 (2009) 045003.

Chapter 2

Background on Materials and Growth Methods

2.1 Materials (ZnO) properties

In this section, we describe the general properties of the ZnO material including crystal structure and electronic structure.

Among the functional oxide materials, ZnO is the most promising candidate and has attracted great attention due to its excellent material (optoelectronic and piezoelectric etc.) properties [1,2]. ZnO has a direct band-gap of 3.37 eV at room temperature. Compared to other wide band-gap semiconductors, especially its main competitor GaN, it has the following advantages.

(i) ZnO has a larger free exciton binding energy of 60 meV (much higher than that of GaN's 25 meV) which is advantageous for efficient emission at room temperature for lasers and UV-emitters [3].

(ii) ZnO is relatively cheap and abundant. It is available in large area single crystals (~ 2 inch), which enables homoepitaxy and also makes ZnO devices scalable for commercialisation [4,5].

(iii) ZnO has better radiation hardness (with ~ 1.5 MeV high energy electron irridation) characteristics than GaN (~1 MeV) and GaAs (~ 1 MeV) [5]. ZnO has useful features including bio-compatibility [6,7], and its nanostructure fabrication is relatively simple.

(iv) ZnO can be deposited at room/low-temperatures [8].

(v) Because of intrinsic and extrinsic defects/impurities, which lead to energy levels within the ZnO bandgap corresponding to emissions at a range of different wavelengths, ZnO can emit across the visible spectrum [9,10], which is a key advantage for white light LEDs.

ZnO has many applications in optoelectronic devices such as light emitting diodes [10-12], solar cells [13], transparent conductive oxides (TCO) [14], chemical and gas sensors [15,16], field effect transistors [17], Schottky diodes [18], and also in surface acoustic wave devices [19].

2.1.1 Crystal structure

ZnO is a II-VI compound semiconductor. In normal conditions such as standard temperature and pressures, it has a hexagonal-shaped wurtzite crystal structure. But, it also exists in the cubic rock salt and cubic zinc-blende forms [20-22]. In ZnO crystal structure, each Zn ion is surrounded by four oxygen ions, and vice versa. The structure is in the shape of a tetrahedral configuration as shown in Figure 2.1 (a). The unit cell structure is shown in Figure 2.1 (b). The lattice parameters are $a = b = 0.32498$ nm and $c = 0.52066$ nm. The volume of the ZnO unit cell with a wurtzite structure is 23.8×10^{-3} nm^3 [22].

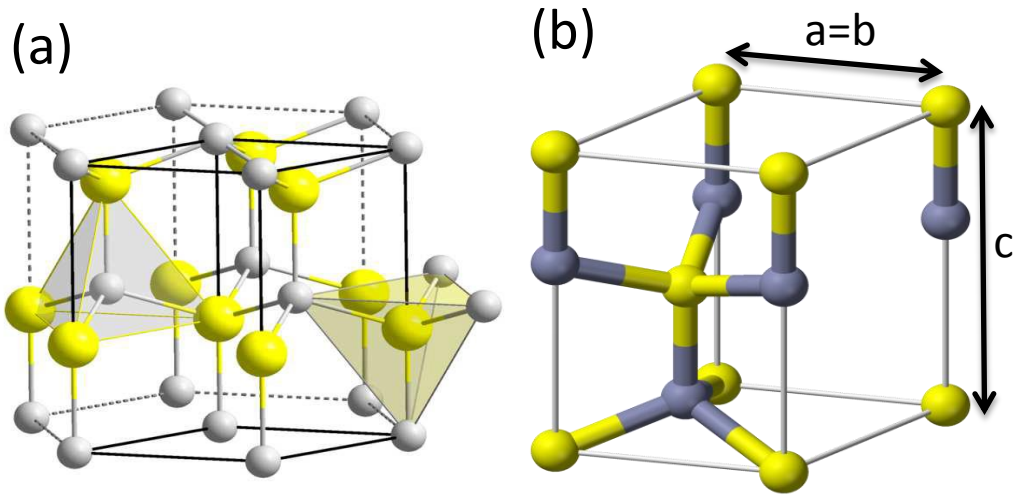

Figure 2.1: (a) The wurtzite crystal structure of ZnO (b) the unit cell of wurtzite structured ZnO (Ref. [23]). The Zn^{2+} and O^{2-} ions in grey and yellow colours, respectively.

The principal planes of the ZnO hexagonal (wurtzite) structure are shown in Figure 2.2. Using Miller-Bravais four index notation, *a*-plane and *m*-plane are denoted by (11-20) and (10-10), respectively. The *a*-plane and *m*-planes are parallel to the *c*-axis and are non-polar planes. However, *c*-plane consists of alternative positively Zn (0001) and negatively charged O (000-1) planes. Hence, the *c*-plane is a polar plane. The *r*-plane and *R*-planes are semi-polar planes and are denoted by (10-11) and (10-12), respectively. There is only a very little information available in the literature on these *r*- and *R*-planes, which is due to difficulties in epitaxial growth of those planes [24].

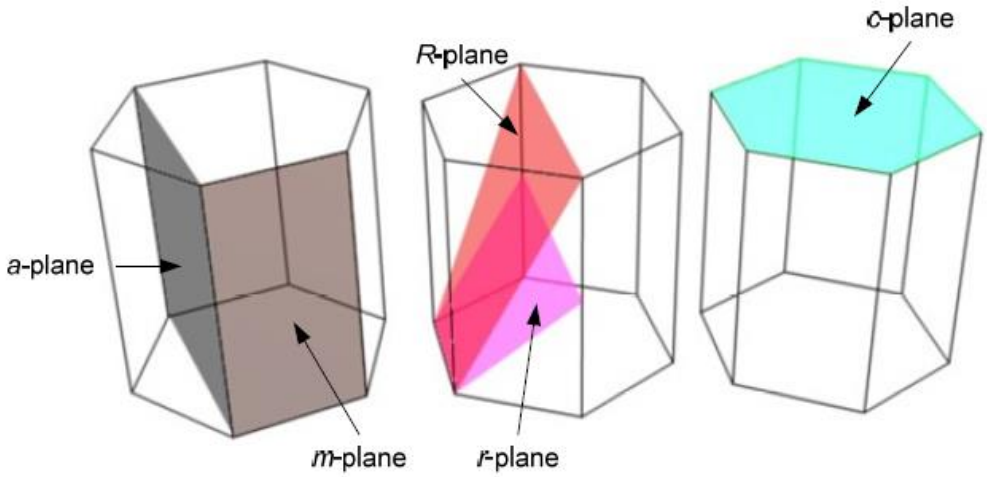

Figure 2.2: Showing the various crystal planes of the ZnO hexagonal structure (Ref [25]).

Al-doped ZnO (AZO) material has improved electrical properties compared to ZnO, due to the increase in free carrier concentration as Al is an *n*-type dopant. In recent years, AZO has been considered a better choice to replace indium tin oxide (ITO). In AZO crystal structure, Al^{+3} ions substitute Zn^{+2} ions [25]. The further details on the comparisons of the structural, optical and electrical properties between ZnO and AZO films are presented in Chapter 5.

2.1.2 Electronic structure

Zinc (Zn) metal has the outer shell electronic configuration of $3d^{10}\ 4s^2$ while oxygen (O) has the outer shell electronic configuration of $2s^2\ 2p^4$. Since 'O' has a greater electronegativity than 'Zn', this enables to draw the outer shell electrons of Zn 4s shell into unequal bonds with O. A complete band structure of ZnO has been a mystery for several decades. This is because of the lack of correlation between theoretical calculations and experimental data. Experimental evidence suggests that the 3d electrons of Zn have an influence on the valence band electrons of Zn and O such as Zn-4s and O-2p [26,27]. Additionally, hybrid orbitals strongly influence the Zn-4s and O-2p electrons. Figure 2.3 shows the schematic presentation of the ZnO band structure with the band gap in between O^{2-} 2p valence band and Zn^{2+} 4s conduction band states.

ZnO is a direct wide band gap semiconductor with a band gap of 3.37 eV at room temperature. This implies that the conduction band minimum and valence band maximum are positioned in phase at the same location. Therefore, their wave functions or *k*-vector values are the same. The conduction band is primarily composed of empty Zn^{2+} 4s electrons associated with Γ_7 symmetry while the valence band is composed from the occupied O^{2-} 2p electrons. As shown in Figure 2.3, *p*-type orbitals are split by the hexagonal crystal field and spin-orbit coupling into three bands labelled as A,B and C with symmetries Γ_7, Γ_9 and Γ_7, respectively. The holes formed in the A valence band are referred to as light holes. Whereas, the holes formed in the B and C valence bands are referred to as heavy holes and spin orbit spin-off band holes, respectively.

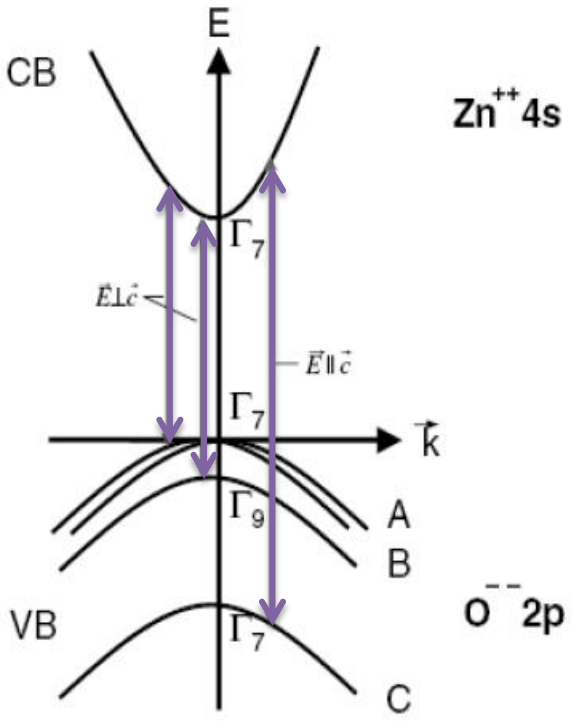

Figure 2.3: Schematic representation of the ZnO electronic band structure [28].

ZnO is an *n*-type intrinsic semiconductor. The origin of this behaviour remained a mystery for many years. Previously it was believed that the native defects in ZnO such as Zn interstitials and O vacancies were the main reasons for the *n*-type conductivity [26,29,30]. However, it was later suggested that hydrogen (H) was the source for the *n*-type conductivity in ZnO. Hydrogen is amphoteric in most of the semiconductors, which means that it is found as H^+ in *p*-type and H^- in *n*-type semiconductors. In ZnO, the H^+ state is found and therefore hydrogen acts as a donor [26]. Additionally, some reports also suggest that intrinsic defects play a minor role in the *n*-type conductivity [29,30] and show that hydrogen incorporation is the prime cause for this *n*-type conductivity. The *n*-type conductivity of ZnO can be further increased by doping with aluminum (Al), gallium (Ga) and indium (In). This is because of the increase in free electron carrier concentration. In this work, we have used only Al-doped ZnO (2 wt% Al_2O_3 component equivalent to 3 at% Al). A detailed review report for the optical and electrical properties of ZnO can be found in ref [26].

P-type ZnO still remains an issue due to its unstable behaviour. However, *p*-type ZnO has been reported by many groups with a few different dopants, e.g.

copper (Cu), antimony (Sb), gallium (Ga) and nitrogen (N) [31-37]. The ultimate success of the above works for the *p-n* junction-based devices still needs to be studied properly in terms of their stability. This may lead to the future commercialisation of those devices.

2.2 Growth techniques

In this section, we describe the growth techniques such as pulsed laser deposition (PLD) and vapor phase transport (VPT) used in this work. These details include the introduction, background and principles of those techniques. PLD is the most extensively used growth technique in this work, while VPT is used for one application only.

2.2.1 General presentation and basic principles of PLD

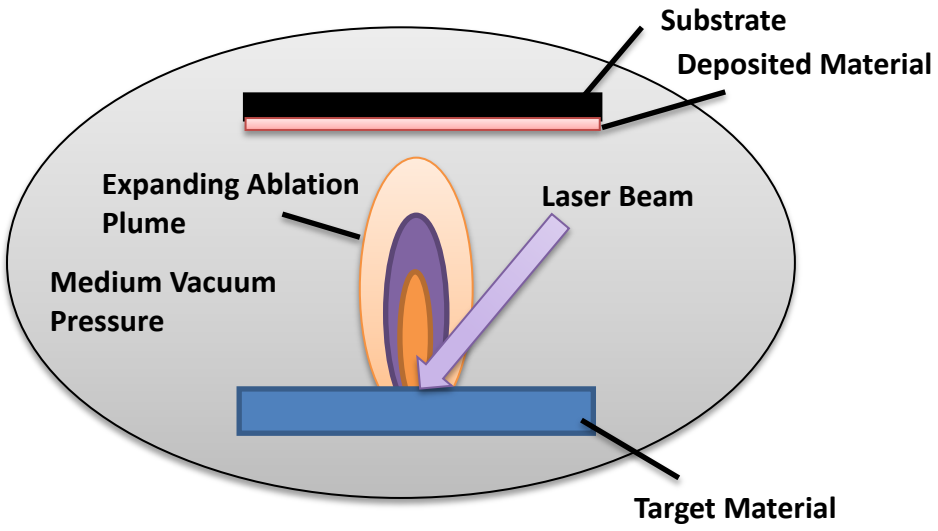

Figure 2.4: Schematic representation of the ablation plasma production in the PLD apparatus.

PLD is a well-established epitaxial material deposition technique [38-40]. In PLD, when the laser pulse is focused on a material target with a suitable fluence, it generates a plasma plume. This plasma then expands through the low-pressure background gas in the PLD chamber and re-condenses on the substrate. This is the fundamental scheme of the PLD technique.

When a pulsed laser is focused on the target material with a high energy density (fluence, e.g. 2 J/cm^2), the electromagnetic energy is ultimately converted into thermal energy through various electronic excitation and collision processes [40]. This leads to a rise of the surface temperature above the vapourisation temperature which allows the evaporation of the source material (target). The duration of this process is very short and less than the laser pulse duration (e.g. 6 ns). So, the remaining of the laser pulse will be absorbed by the evaporated target material close to the surface of the target. Typically, the absorbed energy is high and concentrated enough to break the bonds in the material and create an ionised ablation plasma. The minimum laser fluence (energy per unit area) required to create plasma is called the ablation threshold. For ZnO, the nanosecond laser ablation threshold is observed to be ~ 0.23-0.47 J/cm^2 [41]. The produced plasma starts to expand in a forward direction and perpendicular to the target due to the pressure gradient at the target surface. During the ablation plasma expansion, the high energetic plasma neutral or ionised atoms and molecules collide with the background gas, get electronic excited and emit photons in the decay. As a result, it produces the characteristic luminous plasma called a plasma plume. This ablation plume consists of a mixture of energetic species such as atomic and molecular ions, electrons, and clusters. They have temperatures in a range of 10^3-10^4 K, kinetic energy (~ 1 eV), velocity (~ 10^6 cm/s) and the plasma particle densities are of the order of 10^{18} cm^{-3}. The gas pressure in the chamber affects the mean free path of the ablated species in the plume. Therefore, the control of the background gas pressure is a key parameter to modify the kinetic energy of the ablated species. In this regard, at high gas pressures the kinetic energy of the ablated species is low due to high density of the gas molecules, which slows down the ablated species.

Depending on the substrate temperature during growth, the plume species will arrange on the substrate following different growth modes. The various growth modes and detailed growth kinetics were established using reflection high-energy electron diffraction (RHEED), see a review in ref [39]. In brief, the growth modes depend on the surface energy of the substrate ($\delta_{substrate}$), surface energy of the film (δ_{film}), and energy of the substrate film interface (δ_{sf}).

- If $\delta_{substrate} > \delta_{film} + \delta_{sf,}$ then the growth mode is called layer-by-layer or Frank Van der Merwe growth. In this mode, the formation of new layers only begins when the previous layer is completed. This mode can lead to high quality uniform films.
- If $\delta_{substrate} < \delta_{film} + \delta_{sf,}$ then the growth mode is called 3D island or Volmer Weber growth. In this mode, the deposited material nucleates and forms 3D islands. This growth mode can lead to polycrystalline films.
- A combination of the above two modes leads to the Stranski Krastanov growth mode: the intial uniform layer growth is followed by 3D island growth.

Film growth using PLD depends on several important deposition parameters including substrate deposition temperature, oxygen deposition pressures, and the distance between target and substrate. Films properties will also depend on the number of laser shots, the laser frequency/repetition rate, and laser fluence on target. We now briefly discuss the effects of these parameters on the structure and properties of the material being deposited.

- Effect of substrate deposition temperature: Substrate deposition temperature is a key growth parameter that affects the crystallinity (due to the effect of increased surface diffusion with increased substrate temperature) of the material and, hence, affects the other material properties. For example, the electrical conductivity and optical transmittance of the TCO film will increase as the substrate temperature increases. This can be explained by an increase in grain size of the films with increasing substrate temperature [39].
- Effect of oxygen deposition pressure: Background gas (e.g. oxygen in this work) pressure also affects the surface morphology and opto-electronic properties significantly. This is because an increase in oxygen pressure reduces the kinetic energy of the ablated species due to the inelastic collisions between oxygen gas molecules and plume species. In this thesis (chapter 5), we have extensively investigated the effects of oxygen pressure as a function of film thickness for the ZnO and AZO thin films grown on Zeonor substrates.

- Effect of target-substrate distance: Background gas pressure and target-substrate distance are interrelated growth parameters. As the background gas pressure increases the ejected plume dimensions decrease, due to the "confining" effect of the collisions between gas molecules and ablated species (just discussed above). For given laser fluence and background oxygen pressure, there exists an optimal target-substrate distance L (typically a few cm's) for which congruent, i.e. preserved stoichiometry, deposition occurs [40, 42, 43]. For target-substrate distances much larger or much smaller than L, the deposition rate becomes much smaller than the optimal deposition rate (see below) [42].
- Effect of number of laser shots: Film thickness increases with the number of laser shots. This increase in thickness affects the optical and electrical properties as the film structure becomes closer to that of the bulk material.
- Effect of the laser repetition rate: An increase of the laser repetition rate increases the amount of ablated species reaching the substrate. As a result more nanoparticles transport to and condense on the substrate allowing the growth of high density nanowires/nanorods [43].
- Effect of laser fluence: High laser fluence increases the energy of the ablated species. This means that the species can transfer more efficiently the background gas to the substrate for better crystalline quality [39,40].

Some of the advantages of PLD are listed below.

(i) PLD can be carried out even at room temperature [44].

(ii) PLD can produce crystalline deposits even at low temperatures due to the - presence of high energetic ionised species in the plasma produced by the laser [44].

(iii) PLD can deposit multi-layers using multi-material targets, which is very useful for device fabrication [45].

(iv) PLD can produce films of varying thicknesses, ranging from nano scale to micro scale, by varying the number of laser shots.

(v) The PLD deposition rate is relatively high compared to other deposition techniques, and ideally of the order of 1 Å/pulse [42].

There are a few drawbacks also associated with the PLD technique. The most important ones are: (i) Slight difficulty to produce uniform films or nanostructures. However improved uniformity can be achieved with a systematic rotation of the targets and substrates during deposition. (ii) Problems associated with large scale production [42,46].

2.2.1.1 PLD apparatus

The standard PLD apparatus is shown in Figures 2.5(a, b). The system consists of a main 50 L stainless-steel chamber, where the deposition takes place. A 4 L stainless-steel load lock chamber is connected to the main chamber through a gate valve. These two chambers are maintained under high vacuum (~ 3×10^{-5} mTorr or 3.9×10^{-6} Pa), independent of each other, using turbomolecular vacuum pumps. This allows loading and unloading the samples into the main chamber through the load-lock chamber, without breaking vacuum in the main chamber. The vacuum pumps are cooled by a continuous flow of water. The main chamber is pumped with a turbomolecular pump (Pfeiffer TMU 521P) and with an oil free backing pump (MVP 055). The load-lock chamber is also pumped with a turbomolecular pump (TMU 071) and with an oil-free backing pump (MVP 015). The main chamber is able to reach a vacuum of ~ 1×10^{-5} mTorr from the atmospheric pressure in 24 hrs. Whereas, the backing pump is able to reach a vacuum of ~ 5×10^{-5} mTorr from atmospheric pressure in the same 24 hrs duration. In this work, oxygen gas (99.999% purity) was used during the deposition as a background gas. Oxygen gas pressure/flow rate can be controlled by a mass flow controller (MFC) and by varying the speed of turbomolecular vacuum pump. Dry nitrogen gas is used for venting the main and load-lock chambers to the atmospheric pressure.

The target-substrate distance was kept constant at 5 cm in our experiments. The ZnO target was purchased from PI-KEM being a 99.999% pure sintered ceramic disk of 2.54 cm diameter and 1 cm height. The aluminum-doped ZnO (AZO) target was also used with a 2 wt% Al_2O_3 component equivalent to 3 at% Al. The substrates used were Silicon (Si) (100) and plastics such as Zeonor and polycarbonate. The cleaning procedures of the substrates prior to deposition are discussed in the respective Chapters 4 and 5.

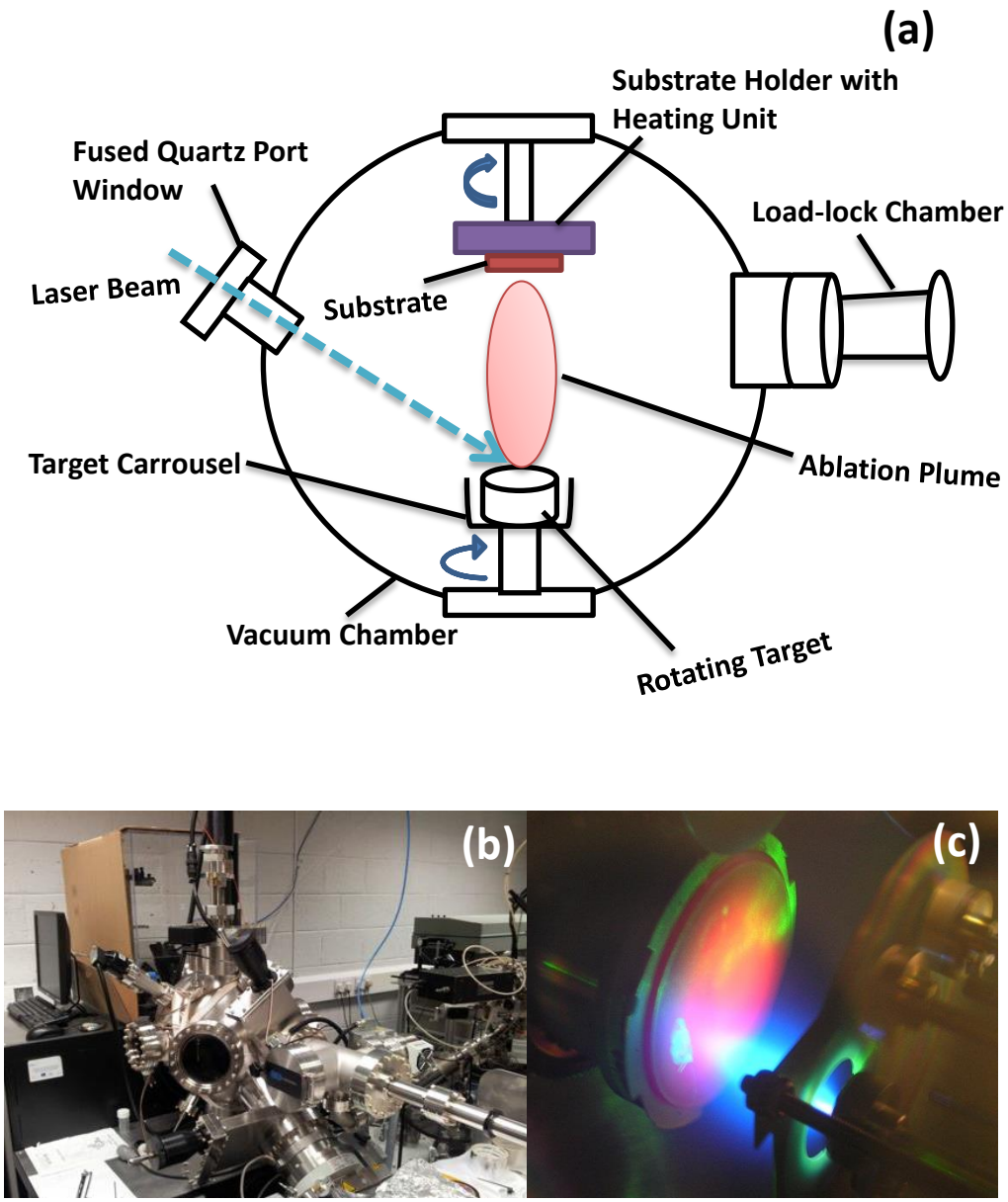

Figure 2.5: (a) Showing typical representation and (b) photograph of PLD apparatus, and (c) the photographic view of plasma produced during the deposition.

To maintain the uniform deposition across the substrate, the substrate and target can be rotated by a computer-controlled motor. The sample holder in the main chamber is equipped with a heater coil and it is capable of reaching the maximum temperature of ~ 1050 ^{o}C. The heater coil temperatures can be measured by a thermocouple and it displays the reading using a digital control unit. The whole heating system can be controlled by a computer [46].

The PLD apparatus is equipped with a high-power, Q-switched, and frequency-quadrupled Continuum Powerlite Precision II Nd:YAG Laser. This laser has a fundamental wavelength of 1060 nm. This is then quadrupled by two harmonic crystals to emit an output wavelength of 266 nm. The repetition rate, pulse width and energy of the laser were 10 Hz, 6 ns and 150 mJ, respectively. The laser beam was imaged with the help of a single biconvex lens to form a spot of ~ 4 mm diameter on the target surface to produce an average fluence of ~ 2.0 J/cm^2. The laser beam was focused on the target at an incident angle of 45°. Values of 1.5 W, 25 MW and 2×10^8 Wcm^{-2} were, thus, realised for the average power (pulse energy/periodic time), peak power (pulse energy/pulse width) and power density (peak power/surface area), respectively, for all the growths in this series of experiments [47].

2.2.2 Vapour phase transport (VPT)

We have used the vapour phase transport (VPT) growth technique to grow catalyst-free ZnO nanorods on PLD prepared catalyst free ZnO seed layers. A metal catalyst (e.g. Au) coated Si substrate has been used to grow ZnO nanorods [48,49] directly on Si, but the lattice mismatch between Si (and any native oxide present) and ZnO is a significant issue that results in a disordered/unaligned nanorod growth. Therefore, a ZnO seed/buffer layer on Si as a substrate ensures energetically favourable nucleation sites to initiate the growth, and also provides textured crystalline substrates with a perfect lattice match for the ZnO nanorod growth on the ZnO seed layers. The ZnO seed/buffer layers can be grown directly on Si substrates without catalyst [50] and also can be grown with the aid of Au catalyst [51]. As mentioned earlier, in our research we have used a catalyst free PLD technique to grow ZnO seed layers on Si substrates.

In VPT, a mixture of ZnO and carbon (in the form of graphite powder) is heated up and this creates a Zn vapour source. This vapour is then transported on to the substrate or ZnO seed layers, where it condenses or oxidises. In detail, the evaporated ZnO and carbon mixture reacts to form carbon monoxide and zinc vapour. This reaction is called carbothermal reduction and hence this growth technique is also called carbothermal reduction VPT. This zinc vapour is then

condensed at the nucleation points close to the surface and reacts with residual oxygen in the furnace tube and condenses into ZnO at the nucleation point.

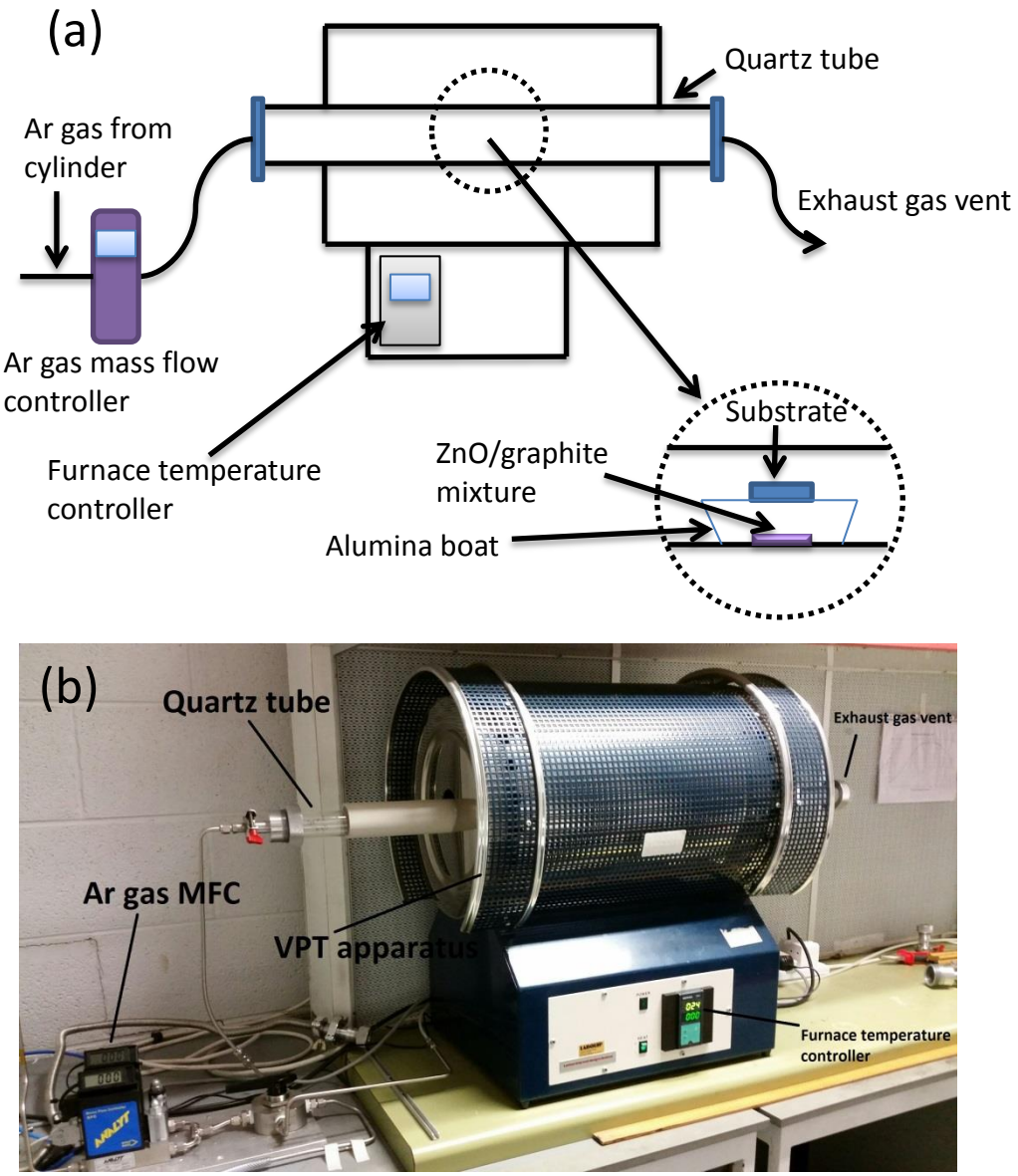

Figure 2.6: (a) Schematic diagram of the VPT apparatus with furnace setup and (b) the photographic image of the same apparatus set up.

The carbothermal and subsequent oxidation reactions are shown below [51] (where ‘s’ is solid state and ‘g’ is gaseous state). At the growth temperatures used in this thesis the dominant secondary product of the carbothermal reduction is CO, at lower temperatures it can be CO_2.

$$ZnO(s) + C(s) \rightarrow Zn(g) + CO(g)$$
$$Zn(g) + ½\ O_2(g) \rightarrow ZnO(s).$$

Figure 2.6 (a) and (b) shows schematic representation and photographic view of the VPT apparatus. VPT growth was conducted in a quartz tube with a length of 115 cm and an internal diameter of 37 mm. The quartz tube was positioned in a single temperature zone of a horizontal tube furnace (Lenton Thermal Designs), with a uniform supply of high purity (99.999%) Ar gas flow controlled by an Analyt GFC 17 mass flow controller (MFC). High purity graphite power (99.9999%; 60 mg) and ZnO (99.9995%; 60 mg) powders were carefully weighed and then mixed and ground using a mortar and pestel for a few minutes until a homogeneous mixture is obtained. This mixture was then loaded and spread carefully over a 2 cm length in the middle of an alumina boat. The ZnO coated Si substrate was placed directly above the mixture (ZnO seed layers facing down) on the boat. This was arranged using supports of two thin strips of Si pieces. The alumina boat was then carefully loaded into the middle of the quartz tube. The quartz tube was sealed using tube caps and a 90 sccm (standard cubic centimeter per minute) flow of high purity Ar flow was used to purge the tube for 5-10 min. After this step, the furnace was heated up to 900 ^{o}C using a temperature controller and growth took place over a period of one hour. The furnace was then cooled for several hours to reach a temperature of ~ 300 ^{o}C. The Ar flow was stopped before unloading the alumina boat from the quartz tube. Finally, ZnO nanorod sample was collected from the alumina boat and then characterised.

2.3 References

[1] Z.L. Wang, Novel nanostructures of ZnO for nanoscale photonics, optoelectronics, piezoelectricity, and sensing, *Appl. Phys. A* 88 (2007) 7-15.

[2] Z.L. Wang, J. Song, Piezoelectric nanogenerators based on zinc oxide nanowire arrays, *Science* 312 (2006) 242-246.

[3] S.K. Das, F. Güell, C. Gray, P.K. Das, R. Grunwald, E. McGlynn, ZnO nanorods for efficient third harmonic UV generation: erratum, *Opt. Mater. Express* 4 (2014) 1243-1243.

[4] A. Tsukazaki, M. Kubota, A. Ohtomo, T. Onuma, K. Ohtani, H. Ohno, S.F. Chichibu, M. Kawasaki, Blue light-emitting diode based on ZnO, *Jpn. J. Appl. Phys.* 44 (2005) L643.

[5] D.C. Look, Recent advances in ZnO materials and devices, *Mater. Sci. Eng. B* 80 (2001) 383-387.

[6] Y. Liu, M. Zhong, G. Shan, Y. Li, B. Huang, G. Yang, Biocompatible ZnO/Au nanocomposites for ultrasensitive DNA detection using resonance Raman scattering, *J. Phys. Chem. B* 112 (2008) 6484-6489.

[7] P.W. Sadik, S.J. Pearton, D.P. Norton, E. Lambers, F. Ren, Functionalizing Zn- and O-terminated ZnO with thiols, *J. Appl. Phys.* 101 (2007) 104514.

[8] R.Y. Yang, M.H. Weng, C.T. Pan, C.M. Hsiung, C.C. Huang, Low-temperature deposited ZnO thin films on the flexible substrate by cathodic vacuum arc technology, *Appl. Surf. Sci.* 257 (2011) 7119-7122.

[9] C.H. Ahn, Y.Y. Kim, D.C. Kim, S.K. Mohanta, H.K. Cho, A comparative analysis of deep level emission in ZnO layers deposited by various methods, *J. Appl. Phys.* 105 (2009) 13502.

[10] W. Liu, S.L. Gu, J.D. Ye, S.M. Zhu, S.M. Liu, X. Zhou, R. Zhang, Y. Shi, Y.D. Zheng, Y. Hang, C.L. Zhang, Blue-yellow ZnO homostructural light-emitting diode realized by metalorganic chemical vapor deposition technique, *Appl. Phys. Lett.* 88 (2006) 092101.

[11] Y. Ryu, T.S. Lee, J.A. Lubguban, H.W. White, B.J. Kim, Y.S. Park, C.J. Youn, Next generation of oxide photonic devices: ZnO-based ultraviolet light emitting diodes, *Appl. Phys. Lett.* 88 (2006) 1108.

[12] D.C. Look, B. Claflin, Y.I. Alivov, S.J. Park, The future of ZnO light emitters, *Phys. Stat. Sol.* A 201 (2004) 2203-2212.

[13] M. McCune, W. Zhang, Y. Deng, High efficiency dye-sensitized solar cells based on three-dimensional multilayered ZnO nanowire arrays with “caterpillar-like” structure, *Nano lett.* 12 (2012) 3656-3662.

[14] G. Socol, M. Socol, N. Stefan, E. Axente, G. Popescu-Pelin, D. Craciun, L. Duta, C.N. Mihailescu, I.N. Mihailescu, A. Stanculescu, D. Visan, V. Sava, A.C. Galca, C.R. Luculescu, V. Craciun, Pulsed laser deposition of transparent conductive oxide thin films on flexible substrates, *Appl. Surf. Sci.* 260 (2012) 42-46.

[15] Z. Fan, D. Wang, P.C. Chang, W.Y. Tseng, J.G. Lu, ZnO nanowire field-effect transistor and oxygen sensing property, *Appl. Phys. Lett.* 85 (2004) 5923-5925.

[16] Q. Wan, Q.H. Li, Y.J. Chen, T.H. Wang, X.L. He, J.P. Li, C.L. Lin, Fabrication and ethanol sensing characteristics of ZnO nanowire gas sensors, *Appl. Phys. Lett.* 84 (2004) 3654-3656.

[17] Y. Shao, J. Yoon, H. Kim, T. Lee, W. Lu, Temperature Dependence of Electron Transport in ZnO Nanowire Field Effect Transistors, *Electron Devices, IEEE Transactions on.* 61 (2014) 625-630.

[18] A. Dey, A. Layek, A. Roychowdhury, M. Das, J. Datta, S. Middya, D. Das, P.P. Ray, Investigation of charge transport properties in less defective nanostructured ZnO based Schottky diode, *RSC Adv.* 5 (2015) 36560-36567.

[19] E.B. Magnusson, B.H. Williams, R. Manenti, M.S. Nam, A. Nersisyan, M.J. Peterer, A. Ardavan, P.J. Leek, Surface acoustic wave devices on bulk ZnO crystals at low temperature, *Appl. Phys. Lett.* 106 (2015) 063509.

[20] W.L. Bragg, J.A. Darbyshire, The structure of thin films of certain metallic oxides, *T. Faraday Soc.* 28 (1932) 522-529.

[21] L.P. Snedeker, A.S. Risbud, O. Masala, J.P. Zhang, R. Seshadri, Organic phase conversion of bulk (wurtzite) ZnO to nanophase (wurtzite and zinc blende) ZnO, *Solid State Sci.* 7 (2005) 1500-1505.

[22] S. Desgreniers, High-density phases of ZnO: Structural and compressive parameters, *Phys. Rev. B* 58 (1998) 14102.

[23] Web reference: https://en.wikipedia.org/wiki/File:Wurtzite-unit-cell-3D-balls.png (last accessed on 15th June, 2015).

[24] R. Aggarwal, H. Zhou, C. Jin, J. Narayan, R.J. Narayan, Semipolar r-plane ZnO films on Si (100) substrates: Thin film epitaxy and optical properties, *J. Appl. Phys.* 107 (2010) 113530.

[25] D. Byrne, PhD thesis on "*The growth and characterisation of ordered arrays of zinc oxide nanostructures and optical studies of defects in zinc oxide*", DCU, (2012).

[26] Ü Özgür, Ya.I. Alivov, C. Liu, A. Teke, M.A. Reshchikov, S. Doğan, V. Avrutin, S.J. Cho, H. Morkoc, A comprehensive review of ZnO materials and devices, *J. Appl. Phys.* 98 (2005) 041301.

[27] R.T. Girard, O. Tjernberg, G. Chiaia, S. Söderholm, U.O. Karlsson, C. Wigren, H. Nylen, I. Lindau, Electronic structure of ZnO (0001) studied by angle-resolved photoelectron spectroscopy, *Surf. Sci.* 373 (1997) 409-417.

[28] C. Klingshirn, ZnO: From basics towards applications, *phys. stat. soli. B* 244 (2007) 3027-3073.

[29] D.C. Look, D.C. Reynolds, J.R. Sizelove, R.L. Jones, C.W. Litton, G. Cantwell, W.C. Harsch, Electrical properties of bulk ZnO, *Solid. State. Commun.* 105 (1998) 399-401.

[30] K. Vanheusden, C.H. Seager, W.L. Warren, D.R. Tallant, J.A. Voigt, Correlation between photoluminescence and oxygen vacancies in ZnO phosphors, *Appl. Phys. Lett.* 68 (1996) 403-405.

[31] J.B. Kim, D. Byun, S.Y. Ie, D.H. Park, W.K. Choi, J.W. Choi, B. Angadi, Cu-doped ZnO-based p–n hetero-junction light emitting diode, *Semicond. Sci. Tech.* 23 (2008) 095004.

[32] C.H. Park, S.B. Zhang, S.H. Wei, Origin of p-type doping difficulty in ZnO: The impurity perspective, *Phys. Rev. B* 66 (2002) 073202.

[33] F.X. Xiu, Z. Yang, L.J. Mandalapu, D.T. Zhao, J.L. Liu, W.P. Beyermann, High-mobility Sb-doped p-type ZnO by molecular-beam epitaxy, *Appl. Phys. Lett.* 87 (2005) 152101-152101.

[34] C.H. Zang, D.M. Zhang, C.J. Tang, S.J. Fang, Z.J. Zong, Y.X. Yang, C.H. Zhao, Y.S. Zhang, Optical properties of a ZnO/P nanostructure fabricated by a chemical vapor deposition method, *J. Phys. Chem. C* 113 (2009) 18527-18530.

[35] M. Joseph, H. Tabata, T. Kawai, p-type electrical conduction in ZnO thin films by Ga and N codoping, *Jpn. J. Appl. Phys.* 38 (1999) L1205.

[36] D.C. Look, D.C. Reynolds, C.W. Litton, R.L. Jones, D.B. Eason, G. Cantwell, Characterization of homoepitaxial p-type ZnO grown by molecular beam epitaxy, *Appl. Phys. Lett.* 81 (2002) 1830-1832.

[37] X. Fang, J. Li, D. Zhao, D. Shen, B. Li, X. Wang, Phosphorus-doped p-type ZnO nanorods and ZnO nanorod p−n homojunction LED fabricated by hydrothermal method, *J. Phys. Chem. C* 113 (2009) 21208-21212.

[38] M. Lorenz, M.S.R. Rao, 25 years of pulsed laser deposition, *J. Phys. D:Appl.Phys.* 47 (2014) 030301.

[39] R. Eason, Eds., *Pulsed Laser Deposition of Thin films: Applications-Led growth of Functional Materials*, (2007), Wiley: Hoboken, NJ.

[40] D.B. Chrisey, G.K. Hubier, Eds., *Pulsed Laser Deposition of Thin Films*, (1994), Wiley: USA.

[41] D. Canteli, S. Fernandez, C. Molpeceres, I. Torres, J.J. Gandía, Nanosecond laser ablation processes in aluminum-doped zinc-oxide for photovoltaic devices, *Appl. Surf. Sci.* 258 (2012) 9447– 9451.

[42] J.M. Dekkers, PhD thesis on "*Transparent Conducting Oxides on Polymeric Substrates by Pulsed Laser Deposition*", University of Twente, (2007).

[43] R. Guo, J. Nishimura, M. Matsumoto, M. Higashihata, D. Nakamura, T. Okada, Density-controlled growth of ZnO nanowires via nanoparticle-assisted pulsed-laser deposition and their optical properties, *Jpn. J. Appl. Phys.* 47 (2008) 741-745.

[44] Y. Liu, L. Zhao, J. Lian, Al-doped ZnO films by pulsed laser deposition at room temperature, *Vacuum* 81 (2006) 18-21.

[45] M. Lorenz, E.M. Kaidashev, A. Rahm, Th. Nobis, J. Lenzner, G. Wagner, D. Spemann, H. Hochmuth, M. Grundmann, Mg_x Zn_{1-x} O (0 <x< 0.2) nanowire arrays on sapphire grown by high-pressure pulsed-laser deposition, *Appl. Phys. Lett.* 86 (2005)143113.

[46] E. McCarthy, PhD thesis on "Growth of zinc oxide nanowires for field emission application", DCU, (2013).

[47] J.P. Mosnier, R.J. O'Haire, E. McGlynn, M.O. Henry, S.J. McDonnell, M.A. Boyle, K.G. McGuigan, ZnO films grown by pulsed-laser deposition on soda lime glass substrates for the ultraviolet inactivation of Staphylococcus epidermidis biofilms, *Sci. Tech. Adv. Mater.* 10 (2009) 045003.

[48] Z. Zhu, T.L. Chen, Y. Gu, J. Warren, R.M. Osgood Jr., Zinc oxide nanowires grown by vapor-phase transport using selected metal catalysts: a comparative study, *Chem. Mater.* 17 (2005) 4227-4234.

[49] R.T. Rajendra Kumar, E. McGlynn, M. Biswas, R. Saunders, G. Trolliard, B. Soulestin, J.R. Duclere, J.P. Mosnier, M.O. Henry, Growth of ZnO nanostructures on Au-coated Si: Influence of growth temperature on growth mechanism and morphology, *J. Appl. Phys.* 104 (2008) 084309.

[50] R.T. Rajendra Kumar, E. McGlynn, C. McLoughlin, S. Chakrabarti, R.C. Smith, J.D. Carey, J.P. Mosnier, M.O. Henry, Control of ZnO nanorod array density by Zn supersaturation variation and effects on field emission, *Nanotechnology* 18 (2007) 215704.

[51] S. Garry, E. McCarthy, J.P. Mosnier, E. McGlynn, Control of ZnO nanowire arrays by nanosphere lithography (NSL) on laser-produced ZnO substrates, *Appl. Surf. Sci.* 257 (2011) 5159-5162.

Chapter 3

Characterisation Techniques and Principles

A wide selection of characterisation techniques were used to study the surface morphology and material properties of the as-grown samples. The schematic chart-representation of the various characterisations is shown in Figure 3.1. Scanning electron microscopy (SEM), atomic force microscopy (AFM) and transmission electron microscopy (TEM) were used to study the surface morphology of the samples. The structural properties were studied by 2θ-ω and pole figure scans of x-ray diffraction (XRD), and Raman spectroscopy. Optical properties were studied by UV-visible transmission and low-temperature photoluminescence (PL) spectra. Electrical properties were studied by Van der Pauw/Four point probe and Hall effect instruments. Hydrophobicity properties were studied by water contact angle (WCA) instruments. A brief introduction, the principles of operation and the actual equipment setup for the various characterisation techniques are detailed in the following sections.

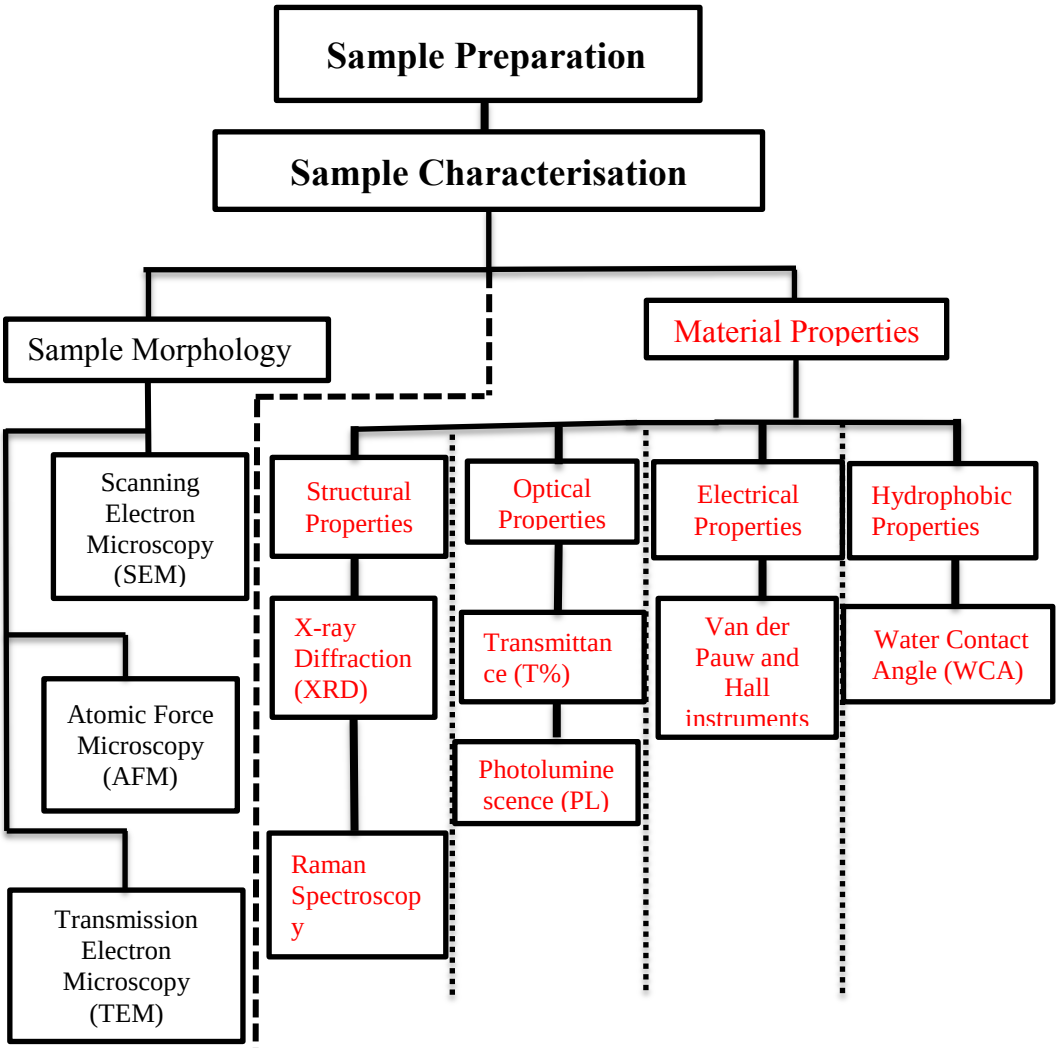

Figure 3.1: The schematic chart representation showing the various characterisation techniques that were used to study the surface morphology and material properties of the samples.

3.1 Dektak profilometry

Dektak profilometry (D150) from Veeco (currently trading as Bruker) is a surface profilometer that measure surface topography, step size (i.e. thickness), and surface roughness using stylus profilometry technology. It has 3D mapping capability, repeatability down to 4 Å which is the industry's standard for lowest noise. There are other techniques to measure thickness, some of which require having a physical contact with the sample surface, while others are purely optical-based, e.g. ellipsometry. Profilometry is an easy method to measure film thickness. A typical view of a contact profilometer is represented in Figure 3.2. It consists of a

stylus that can be moved in X,Y and Z-axes. The stylus is positioned on the surface of the sample as shown in Figure 3.2 and it is controlled by computer software. The process can be observed by a CCD camera. When the stylus is brought to contact with the surface, then moved laterally across the surface. This is measured as the change in vertical heights as a function of horizontal distances. The recorded readings can be plotted as a height profile of the surface.

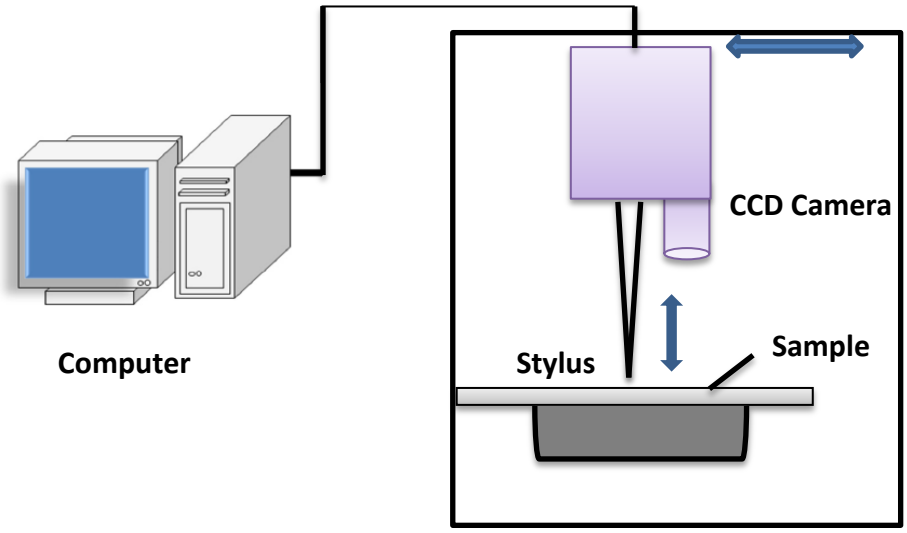

Figure 3.2: Schematic representation of the profilometry set up.

We have used Dektak profilometry to measure the thicknesses of our ZnO and AZO thin films grown on Zeonor plastic substrates. Our samples (ZnO and AZO thin films on Zeonor substrates) have a mask on one side and thin films on the other side. So, the thickness was measured using the step-height from the profilometry. Glass cover slips were used as masks in this work. The photograph of the profilometry is shown in Figure 3.3 (a). The microscopy image in Figure 3.3 (b) shows the mask part and thin film parts of the sample. The stylus and its reflection can be seen in Figure 3.3 (b). The thickness was measured from the step height as shown in Figure 3.3 (c), as an example. The tangent drawn on profile (Figure 3.3 (c)) was taken as a reference to measure the accurate step height or thickness of the sample. Several step heights were measured for each sample and the standard deviation of those values was taken as an error bar length.

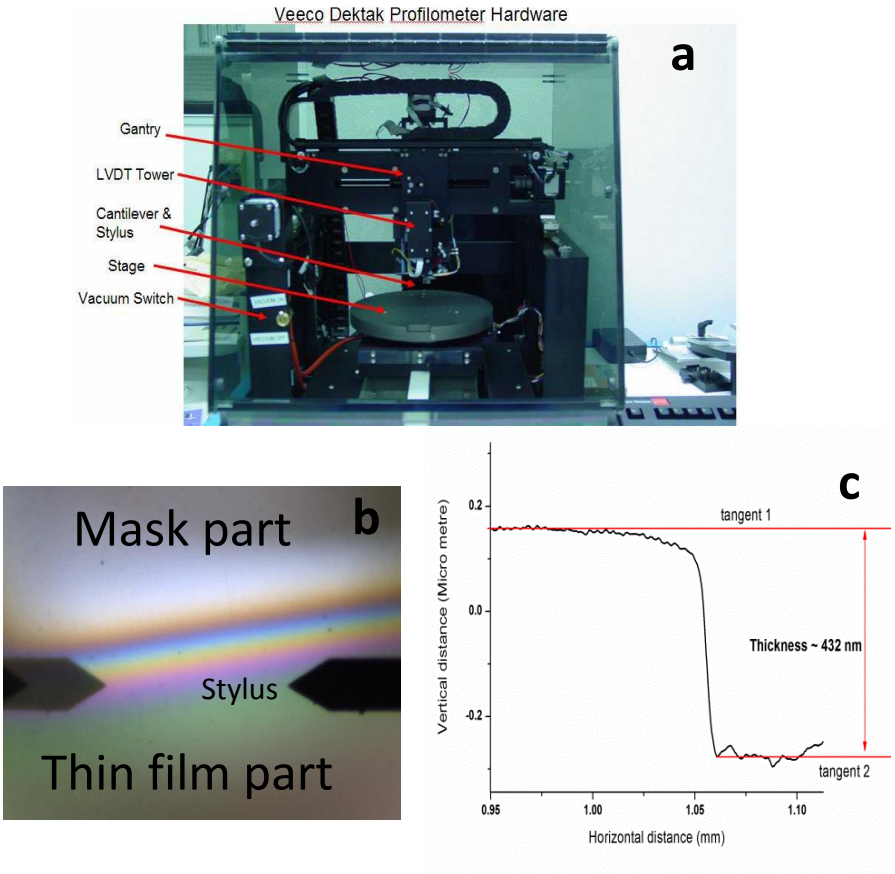

Figure 3.3: (a) Photograph of Dektak profilometry with various parts, (b) the microscope image for the step and (c) step height (or thickness) of the films measured using Dektak profilometry.

3.2 X-Ray diffraction (XRD)

3.2.1 2θ-ω scans

XRD (Bruker AXS D8 advance diffractometer) was used in this work to investigate the crystalline quality, presence of lattice planes and orientation of growth in the ZnO samples (thin films and nanorods). The structural characteristics were investigated by θ-2θ (or 2θ-ω) and rocking curve scans. Sample holder was positioned in x, y and z-directions, and then the circular motion was optimised by θ and φ in the XRD apparatus (Figure 3.4(a)). After the x, y, z, θ and φ direction alignments, XRD θ-2θ scan was performed with a fixed angle of X-ray source, in which the sample holder gradually rotated with an angle "θ" while the X-ray detector rotated by an angle "2θ". The further analyses of the observed XRD θ-2θ peaks was performed by a rocking curve scan, where the X-ray source and the detector were held static, while the sample holder was rotated around the θ-value for the peak.

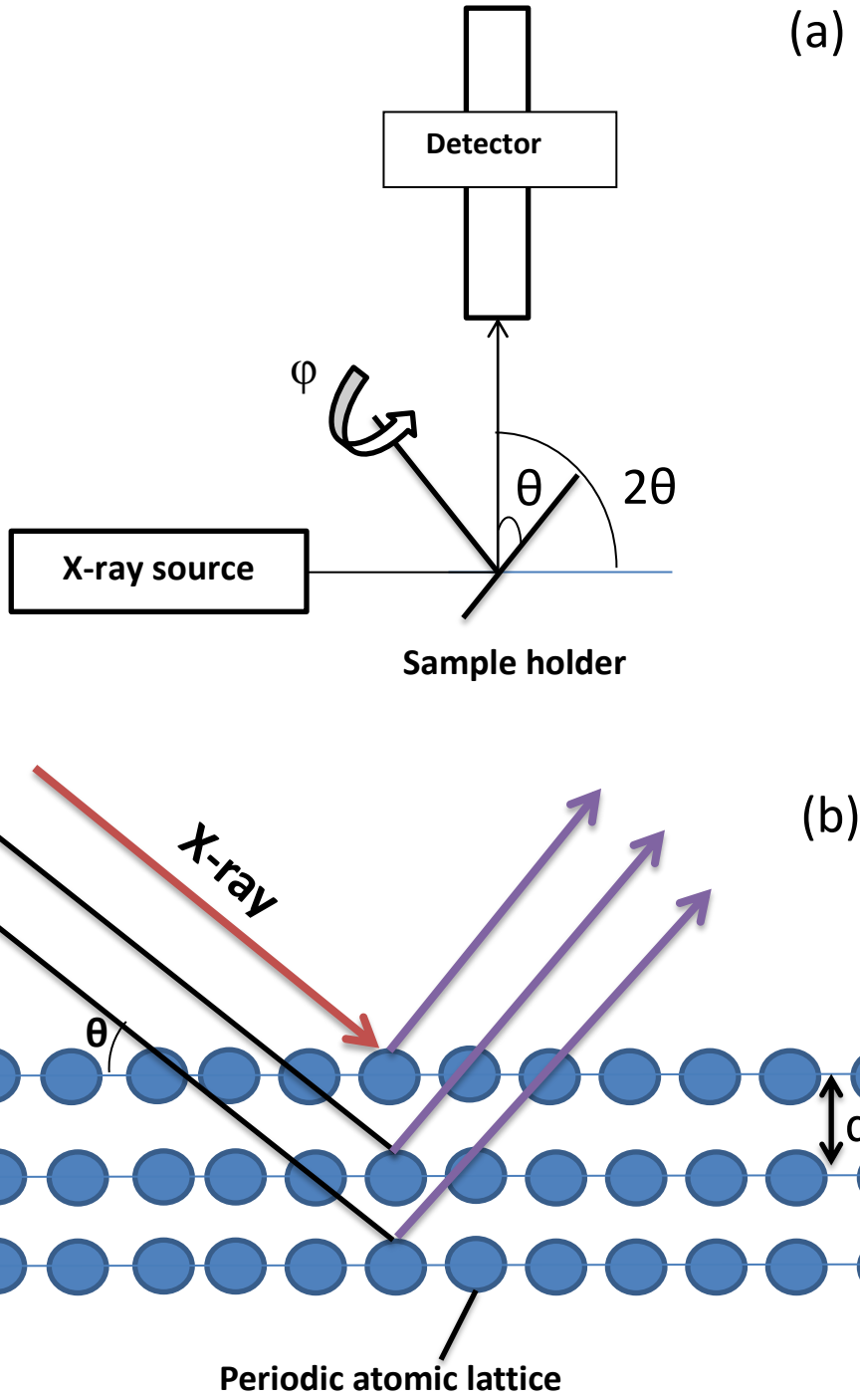

Figure 3.4: (a) Schematic representation of XRD apparatus, (b) Bragg's diffraction of X-rays by atomic planes of the sample.

XRD is a characterisation technique, which is used to measure the crystalline quality or texture of the materials. Generally, when an X-ray beam is incident on a material, the incident X-rays are either absorbed or scattered by the material. The XRD technique works only for the scattered X-ray waves. Scattering can be either

elastic or inelastic. The scattered inelastic waves (or Compton scattered waves) from different electrons do not interfere with each other because there is no phase relationship between the incident and the scattered waves. Hence, no crystallographic information can be revealed from the inelastic scattered X-rays. However, the elastic scattered waves are partially coherent and can interfere with the incident waves under certain conditions. Therefore, the crystallographic information can be obtained only from the elastic scattered waves. The condition for constructive interference is discussed below.

As discussed, when X-rays are incident on a crystal, the rays reflected by the atomic planes of the crystal can interfere because of their path and phase differences. The condition for the constructive interference is given by following equation. This is known as Bragg's Law [1]. A typical representation of the interaction of the X-rays with the periodic atomic lattice is shown in Figure 3.4 (b).

$$2d_{hkl}\sin\theta_n = n\lambda \qquad \text{(Eq. 3.1)}$$

Here, λ = 1.5425 Å is the wavelength of the Cu K_α line: is average over $K_{\alpha1}$ and $K_{\alpha2}$ components (radiation lines). θ_n is the Bragg angle, *n* is the order of reflection (e.g. *n*=1,2,3 etc.), and d_{hkl} is the spacing between consecutive atomic planes (e.g. d_{002}, d_{101} etc.). For hexagonal wurtzite structure of ZnO, the lattice spacing can be calculated from the following equation 3.2, ref [2].

$$\frac{1}{d^2{}_{hkl}} = \frac{4}{3}\left(\frac{h^2+hk+k^2}{a^2}\right) + \frac{l^2}{c^2} \qquad \text{(Eq. 3.2)}$$

Where, *a* and *c* are the lattice constants of the unit cell.

For (002) plane, $d_{002} = \frac{c}{2}$ and

For (100) plane, $d_{100} = 0.86 \times a$.

We use the (002) peak FWHM values and 2θ angular positions to estimate the samples crystallite size and residual stress, respectively. The average crystallite size D can be calculated using Scherrer equation [3]

$$D = \frac{0.9\lambda}{\beta_{hkl}\cos\theta_B} \qquad \text{(Eq. 3.3)}$$

where λ = 0.15425 nm is the wavelength of the Cu K_α line, θ_B is the Bragg angle and $\beta_{hkl} = \sqrt{\left(\beta_{hkl}^{meas}\right)^2 - \left(\beta_{hkl}^{instr}\right)^2}$ (in radian) is the 2θ FWHM of the ZnO (002) peak after removal of the instrumental broadening, assuming Gaussian line profiles.

The residual stress (σ) in the ZnO film plane is proportional to the strain along the *c*-axis in the biaxial strain model. Maniv et al. [4] have derived a formula to express σ in the biaxial strain model:

$$\sigma = -4.54 \times 10^{11} \frac{(c - c_0)}{c_0} \text{ Nm}^{-2} \qquad \text{(Eq. 3.4)}$$

where c and c_0 are the c-axes length of the strained and relaxed ZnO crystal, respectively. This is the expression we have used in this work.

3.2.2 Pole figure scans

We have also performed pole figure experiments on some of our thin films and nanorod samples to obtain more crystallographic information. A pole figure is a stereographic projection. For a selected set of crystal planes, it provides a stereographic projection of the variation of pole density with pole concentration as a function of pole orientation.

In order to understand the pole figure results, we give a simple explanation here with an example. Suppose there are 3 grains in a metal cubic sheet. The orientation of these grains can be known from Laue methods. The orientation of all the grains can be explained by plotting a stereographic projection of the (100) poles. The projection plane is parallel to metal sheet plane. Pole figure stereographic images depend on the distribution of grains. If the grains are distributed randomly, the poles are then distributed uniformly on a stereographic projection. This is shown in Figure 3.5 (a). But, if the grains are oriented in a preferred direction then the pole will tend to cluster by forming only at a few particular places. This behaviour is represented in Figure 3.5 (b). This is called cubic texture and it reveals the texture behaviour of the metal sheet [5,6]. Figure 3.5 (a) and (b) are 2D stereographic projections.

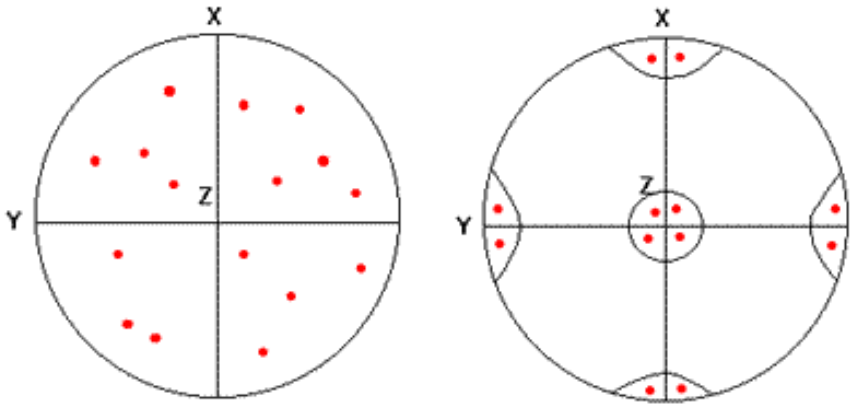

Figure 3.5: (a) (100) Pole figures without texture and (b) (100) Pole figures with texture.

Pole figure experiments were performed as part of a collaboration with the School of Electronic Engineering, DCU. A Jordan Valley BEDE-D1 XRD instrument was used for the pole figure experiments.

3.3 Atomic force microscopy (AFM)

AFM is a scanning probe microscope that depends on force interaction between a small probe (or tip) and the surface of the material. In certain conditions, instrument resolution can reach atomic scale [7]. In AFM instruments, a laser is focused on the surface of a small cantilever. The focused laser spot is reflected on the mirror towards a photodiode detector [8]. The cantilever is mounted on a piezo crystal, which is in a tripod configuration. This allows the cantilever to move freely in x, y and z-directions. A vacuum chuck is used to mount the sample on the sample holder during the scan. A schematic view and photograph of AFM apparatus are shown in Figures 3.6 (a) and (b).

AFM instruments can operate in three distinct modes: contact mode, dynamic mode and tapping mode. However, the mode of operation is decided based on the sample nature. For example, contact mode is often not suitable for soft, smooth and delicate samples. In this work, we have used the AFM instrument in tapping mode. In tapping mode, the cantilever oscillates close to its resonance frequency and is then brought close to the surface. The cantilever taps on the surface (or has intermittent

contact with the surface). In tapping mode, the cantilever is relatively contamination-free as compared with the contact mode [8].

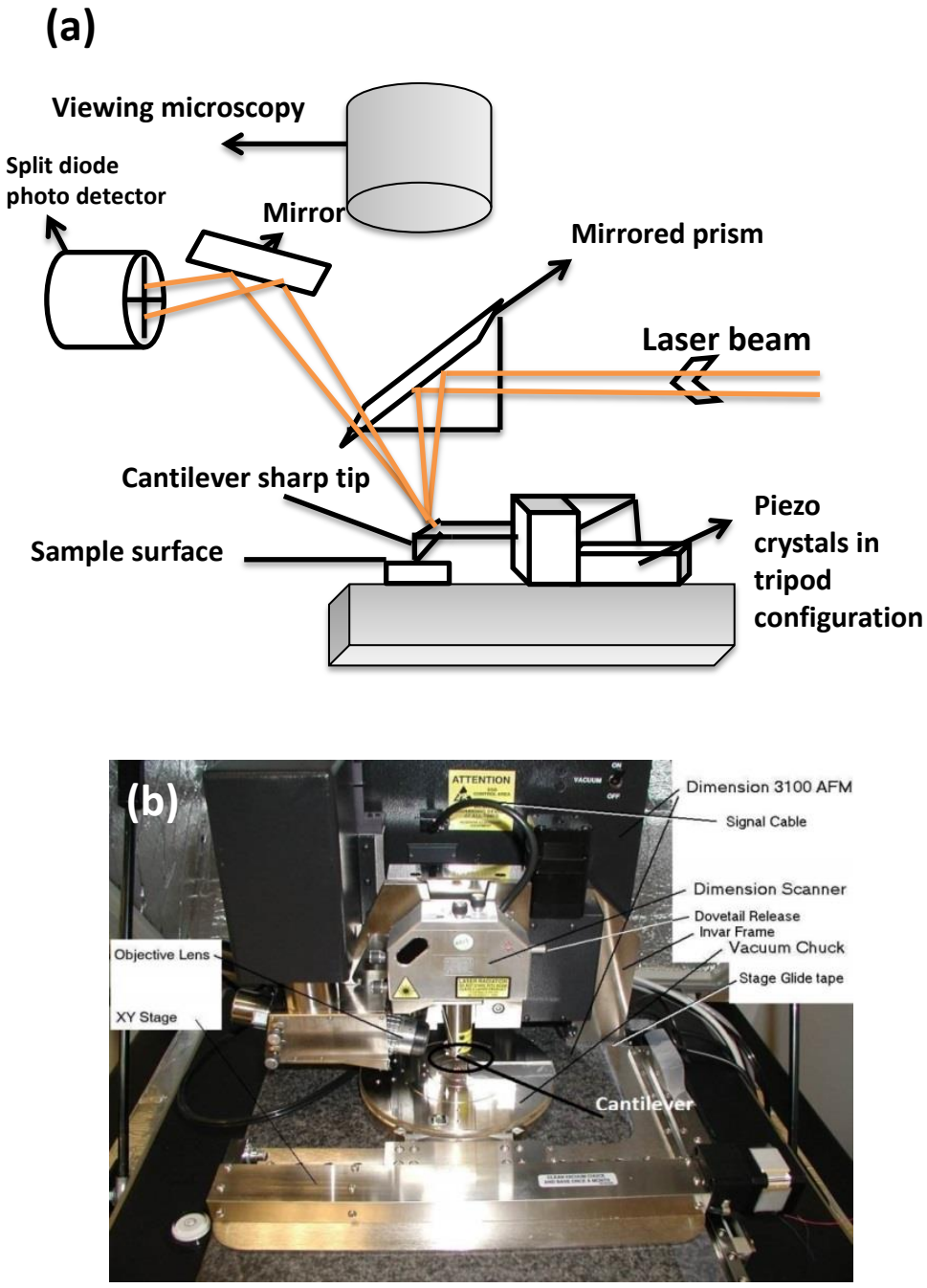

Figure 3.6: (a) Schematic representation of a typical AFM instrument, (b) photograph of AFM apparatus (Ref. [9]).

To investigate surface morphology and surface roughness, AFM (Veeco dimension 3100 controlled by a nanoscope IIIa controller, digital instruments) was used. The instrument was operated in tapping mode using standard aluminium-

coated silicon AFM probe (Tap 300Al-G, Budget sensors) with a force constant of 40 N/m. The collected data was analysed by WSXM software to calculate grain size and rms roughness of the samples [10].

3.4 Scanning electron microscopy (SEM)

SEM was used to study the morphology of the samples. In SEM, a high energy beam of electrons is incident on the sample that is examined. The interactions between electrons and the surface of sample may be an elastic or inelastic scattering process. These interactions cause the emission of the secondary electrons, backscattered electrons, Auger electrons, characteristic X-rays, and cathodoluminescence emission. The possible interactions are shown in Figure 3.7. The mode of operation of SEM depends on the mode of interaction of the electron beam with the surface of the samples being analysed. Some modes give information about the morphology, while others reveal information about the material properties of the samples. Thus, SEM can be operated in multiple modes depending on the information required about the samples. For SEM instruments, the operation electron acceleration voltage is normally between 5-25 kV.

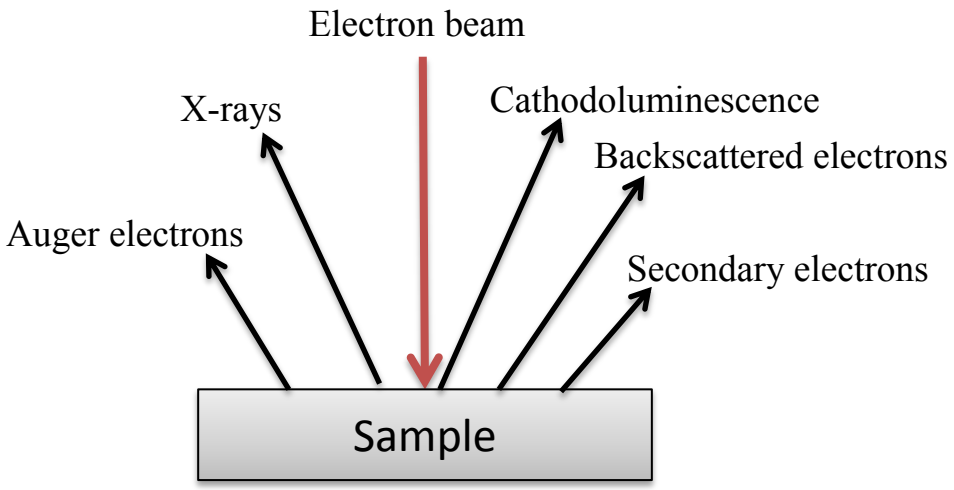

Figure 3.7: Schematic representation of the electron beam interaction with the sample.

In elastic collisions, the elastically scattered electrons are the ones that are deflected away from the surface of the sample and are known as backscattered

electrons. The amount of backscattering is highly dependent on the mass of the element being examined. Thus, the higher the mass the higher the number of back scattered electrons. This can be used to identify different compositions of the materials under investigated. Circular detectors are suitablely placed to detect the backscattered electrons through an aperture (see Figure 3.8 (a)).

On the other hand, in inelastic scattering the incident electron beam knocks out the electrons in the outer shell of the atoms of the examined material. The ejected electrons from the atoms are known as secondary electrons, and have low energies about $\leq$ 50 eV. As these secondary electrons have low energies, they play a significant role in visualising the topography of the samples. The ejected secondary electrons are accelerated to a sufficient energy that can activate a scintillator. Further, the emitted light is then amplified using a photomultiplier tube and converted into a digital image. Secondary electron detectors can be used to create high quality images with a large depth of field because of the number of secondary electrons emitted from the surface. The number of emitted secondary electrons significantly increases as the angle between the surface normal and incoming electron beam increases. This leads to a contrast based on the angle of tilt that is used during the final image.

The ejected electrons during the interactions may also possibly lead to a second detectable signal. Some of the secondary electrons emitted leave behind an inner shell hole. These holes recombine with electrons. The energy difference between the inner and outer orbital shells of the atoms causes the energy emission in the form of X-rays. The energies of the emitted X-rays characterise the binding energies of the orbitals present. This is known as energy dispersive X-ray spectroscopy (EDX), which works if a dispersive or energy-resolving device is present such as a multichannel analyser as shown in Figure 3.8 (b). EDX provides the stoichiometry information of the composite material under examination.

The schematic representation of the typical SEM apparatus is shown in Figure 3.8 (a) and (b). The SEM system used in this work has two column chambers under vacuum. The lower chamber may be brought to atmosphere without breaking vacuum, and the other chamber using a differential vacuum pumping system. At this

atmospheric pressure state, the samples are mounted in the lower chamber. The top column contains an electron gun or electron source, which can be either a tungsten filament (a hot cathode) that acts as a thermionic emitter or a cold cathode emitter that uses a field emission source. An SEM apparatus normally uses thermionic emitters, whereas a Field Emission SEM (FE-SEM) instrument uses field emitters. The electrons emitted from the electron gun are additionally accelerated by the anode. A series of magnetic lenses and apertures are used to focus the electron beam in a column as shown in Figure 3.8 (a). A condenser lens is used to adjust the spot size and beam current, and an objective lens is used to adjust the focus.

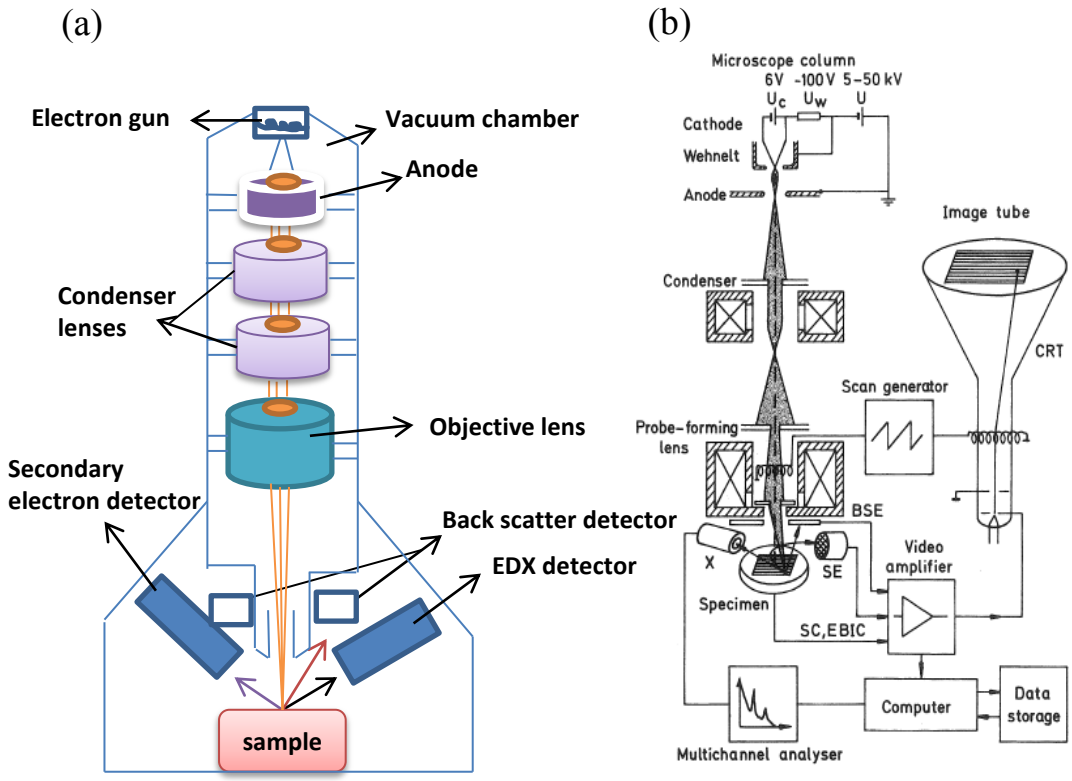

Figure 3.8: (a) Schematic diagram of the main components of a typical SEM system, (b) a detailed diagram showing the secondary electron (SE) and backscattered electron (BSE) detectors and the associated electronics (Ref. [11]).

In this work, SEM characterisation was performed using a Carl-Zeiss EVO series model SEM, fitted with secondary electron, backscattered electron and EDX detectors. Additionally, for high resolution purposes a FE-SEM (Hitachi S5500) was

also used. The FE-SEM instrument based characterisations were performed at laboratories of the School of Chemical Sciences, DCU.

3.5 Transmission electron microscopy (TEM)

In order to further characterise the individual nanostructures (here nanorods), we have also used TEM in this work. TEM is a microscopy technique in which an electron beam of high energy is transmitted through an ultra-thin (~ 100 nm) sample. An image is formed of the electrons that were transmitted after interaction with the sample. For this purpose, electrostatic lenses are used to focus and magnify the image of the transmitted electron beam recorded on a phosphor screen or a specially adapted CCD camera. TEM instrument operates at an electron acceleration voltage in between 100 kV and 300 kV [12]. Similar to SEM, either a thermionic emission source or a field emission source is used to produce the electron beam in TEM.

There are various modes of operation for the TEM. They depend on the information that is required from the sample being examined. The different modes of operation in TEM are scanning transmission electron microscopy (STEM), dark field TEM (DF-TEM), bright field TEM (BF-TEM), selected area electron diffraction (SAED), high resolution TEM (HR-TEM), and electron energy loss spectroscopy (EELS). In this work, we have used HR-TEM and SAED operation modes. These two modes of operation are discussed below in a greater detail.

(i) High resolution TEM (HR-TEM)

HR-TEM image reveals the information about the individual planes of the crystal structure for sample being studied. HR-TEM is a powerful tool to study the crystalline properties of nanostructured materials. The high-energy electron beam acts as an electron wave (from de Broglie's wave-particle duality) in the TEM apparatus. When an electron wave interacts with crystallographic structure of the sample, it creates an interference pattern from the elastically scattered electrons. The combined information obtained by transmitting an electron beam through the sample and the interference pattern reveals the crystal structure of the sample. Distribution, grain boundaries, structural defects, dislocations, stacking faults in the material can also be identified by HR-TEM.

(ii) Selective area electron diffraction (SAED)

SAED is another technique that reveals crystallographic information on the sample. As mentioned above, an electron beam acts as an electron wave when it interacts with a crystalline sample. In this regard, the regular crystal structure of the sample acts as a diffraction grating to the electron wave. Hence, the scattering of the electrons takes place at different angles. Using the adjustment for the dark field mode of the TEM apparatus, the pattern of the scattered electrons will be observed as a diffraction pattern. This diffraction pattern is similar to XRD and it reveals the crystallographic information of the sample being examined. However, XRD is a bulk characterisation, which covers a whole area (~ 80 mm^2) of the sample while SAED focusses on a small area (~ few 10's of nm^2) of the sample. Since high energetic and narrow electron beams are used in SAED, it allows to obtain the crystallographic properties of the individual features in a high resolution image of the sample to be studied.

In this work, TEM experiments were performed (Instrument model: FEI Technai G^2 S – Twin, operating voltage of 200 kV) by our collaborators at the University of Hyderabad, Hyderabad, India.

3.6 Water contact angle (WCA)

Contact angle instruments were used to investigate the degree of hydrophobicity of the ZnO and AZO thin films. A commercial FTA (First Ten Angstroms USA) 200, contact angle instrument was used. A schematic representation of the WCA apparatus is illustrated in Figure 3.9 (a). FTA 32 software was used to control the water drop flow rates of the instrument between 0.05 – 125 μL/s. In this work, we used a flow rate 1.5 μL/s.

Contact angle works on the principle of Young's equation (Eq. 3.5 shown below), which relates interaction among the liquid, solid and vapour phases [13]. The schematic representation of these quantities is shown in Figure 3.9 (b). The typical parts of the contact angle analyser are shown in photograph form of Figure 3.9 (c). Pure (HPLC grade) water was used for all the WCA experiments. The syringe needle tip was placed 2 mm above the film surface. A water droplet can be

imaged by the camera and analysed by computer software. Generally, if water contact angle is less than 90° the surface of the material is considered to be "hydrophilic", and if the contact angle value is more than 90° then the surface is considered to be "hydrophobic".

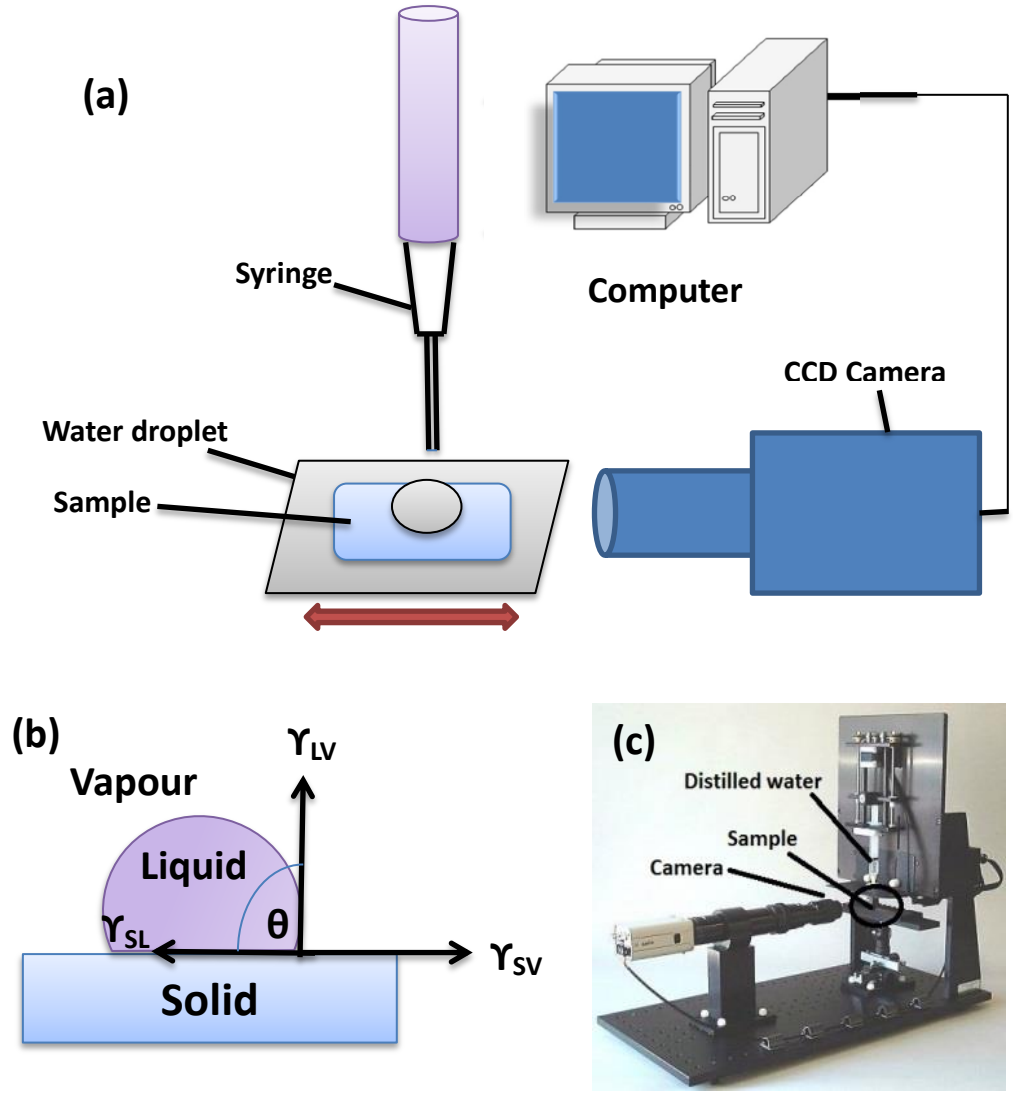

Figure 3.9: (a) A schematic representation of WCA apparatus, (b) showing the quantities in Young's equation and (c) photographic view of the contact angle instruments used in this work.

$$\Upsilon_{SV} = \Upsilon_{SL} + \Upsilon_{LV} \cos\theta \qquad \text{(Eq. 3.5)}$$

Where θ is contact angle, Υ_{SL} is the solid/liquid interfacial free energy, Υ_{SV} is the solid surface free energy and Υ_{LV} is the liquid surface free energy. If θ=90°, $\Upsilon_{SV} = \Upsilon_{SL}$ and If θ=0°, then $\Upsilon_{SV} = \Upsilon_{SL} + \Upsilon_{LV}$.

3.7 UV-visible spectrophotometer

UV-visible spectrophotometer (Varian CARY 50 scan) was used in this work to measure the optical transmittance of the samples (ZnO and AZO thin films on Zeonor plastics). It can measure optical transmission spectra in a wavelength range of 300 nm - 1100 nm. As shown Figure 3.10, a beam of light comes from the source. Afterwards, the light beam passes through a monochromator and is then incident on a sample. The transmitted light through the sample is collected by a detector. The collected data was analysed by the Scan software.

When monochromatic radiation of intensity I_o is directed at the sample, absorption takes place. After absorption, if the resultant intensity is I, then the amount of transmittance is defined as $T = \frac{I}{I_o}$. This is also called Beer-Lambert law [14] and equation 3.6 is shown below.

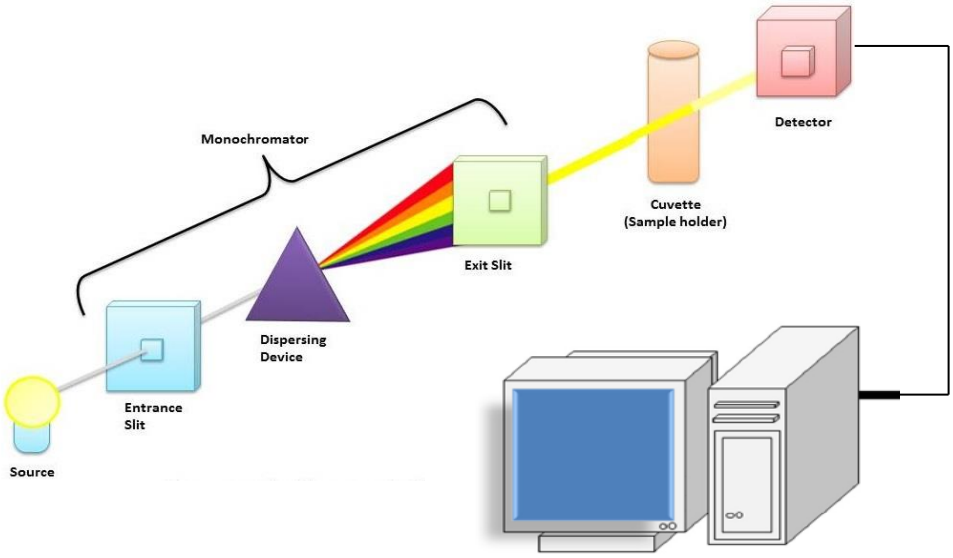

Figure 3.10: Schematic diagram of the optical setup for UV-visible spectrophotometer (Ref. [15]). A reference beam is used in our experiments to set a baseline correction for the removal of the transparent substrate absorption.

$$T = \frac{I}{I_o} = e^{-\mu x} \qquad \text{(Eq. 3.6)}$$

Where μ is the linear absorption coefficient and x is the thickness of the sample.

3.8 Low temperature photoluminescence

Photoluminescence (PL) is a powerful, non-destructive technique to analyse the electronic properties of semiconductor materials. Generally, it involves absorption of photons to excite the electrons from the valence band to the conduction band. Since the excited state electrons are unstable and their life time is about 10^{-9} sec, they decay back to the ground state through electron-hole recombination. During this process the excited carriers first thermalise to the lowest available energies, either at the band edges or in available defect levels, on a timescale of a few picoseonds, and then emit energy in the form of light, on a timescale of nanoseconds, with a wavelength corresponding to the energy difference between the two states. PL relies on the creation of an electron-hole pair in the material during the interaction process with the light source (here the light source is typically a laser). When an electron jumps into the conduction band, it leaves a hole in the valence band. The creation of mobile holes in the valence band and electrons in the conduction band are crucial aspects of the PL technique. At low temperatures the electron-hole pair can form a bound state due to their mutual Coulombic attraction, known as an exciton, and hence the low temperature PL technique depends on the exciton features. At higher temperatures the exciton is thermally dissociated and the PL is determined by the independent electron and hole properties. The temperature at which exciton dissociation occurs is determined by the exciton binding energy (60 meV in ZnO).

ZnO is a direct band gap semiconductor material; this means that the crystal momentum value is the same for both the extrema of the valence and conduction bands. In this case, an electron and a hole can recombine in a radiative process involving only one photon and is a highly efficient process. The energy of the emitted photon will be the same as the energy difference between the valence and conduction band extrema. However, in indirect band gap materials the crystal momentum is not the same for both the valence and conduction bands. Hence, particles such as phonons are involved, in order to conserve the crystal momentum in indirect band gap materials. The emitted photon energies are affected by the loss or gain of energy from phonons and also the recombination probability is reduced in such materials because of the less probable three body recombination process (photon, phonon and carriers). Hence direct band gap materials are more efficient

optical emitters. Figure 3.11 shows a schematic representation of excitation and recombination processes in direct and indirect band gap semiconductors.

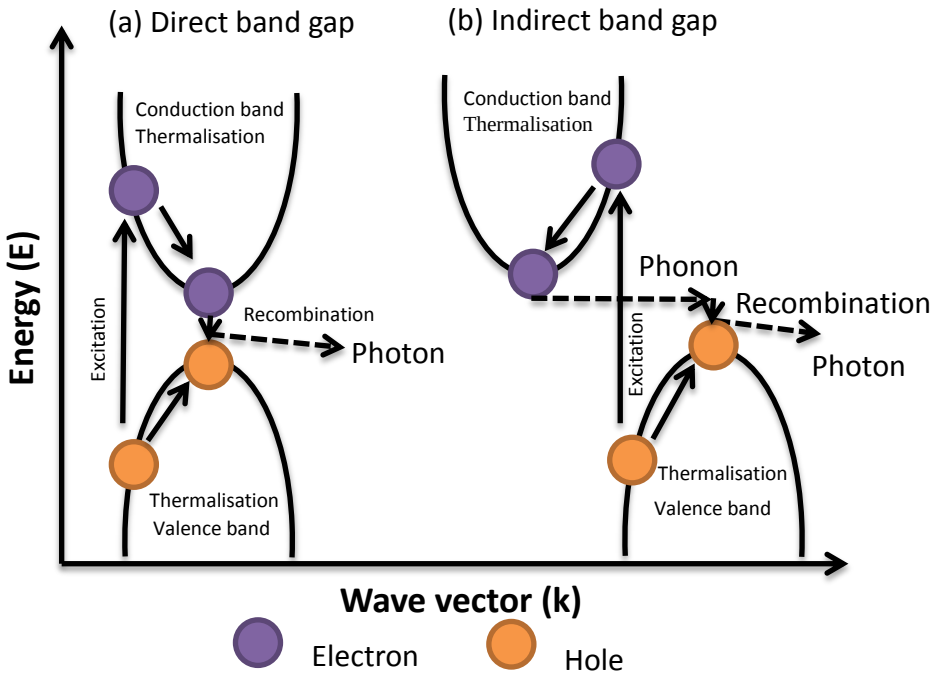

Figure 3.11: Diagram showing excitation and recombination process in (a) direct and (b) indirect band gap semiconductors.

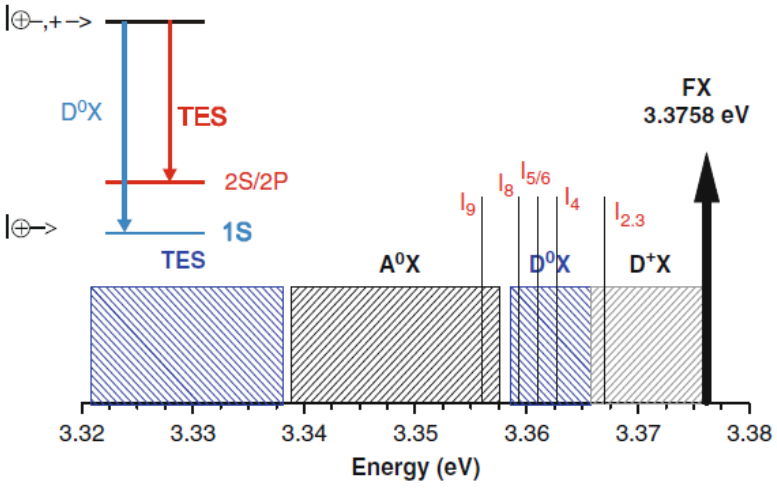

Figure 3.12: Schematic representation of main types of bound excitons in the band edge region for ZnO (Ref. [16]).

In pure materials, the excitons are free to move through the crystal structure. Therefore, these freely moving excitons are called free excitons (FE). When impurity atoms such as donors or acceptors or other defects are present, the excitons can be

trapped at these sites with characteristic localization energies. These trapped excitons are referred to as bound excitons (BE) and they are very useful features to study defects and impurities in the crystal structure, since the energy emitted when the electron and hole of the exciton recombine has a specific value for a particular defect/impurity species due to the characteristic exciton localization energy. PL provides a method to study the defects and impurities in the material and their characteristic effects on the electronic states. Defects in the crystal lattice of the material can be point defects and impurities as well as extended defects such as dislocations, stacking faults and grain boundaries. By careful analysis of the PL spectrum, defects and impurities can in some cases be identified.

Excitons may bind at acceptor sites ($A^{O}X$), donor sites ($D^{O}X$) and ionised donor sites ($D^{+}X$). Additionally, if a material contains both donors and acceptors then it is possible for donor-acceptor recombination transitions (DAP) to emit photons [17]. Two electron satellites (TES) are also possible if a $D^{O}X$ bound exciton recombines and leaves the donor atom in either a 2s or 2p excited state. Furthermore, when the exciton recombines, some of the energy can go into the release of a phonon (or multiple phonons). These features are known as phonon replicas, and the most common of such features in ZnO are associated with the creation of longitudinal optical (LO) phonons. Figure 3.12 shows the main types of bound exciton emissions that exist in the near band edge region for ZnO.

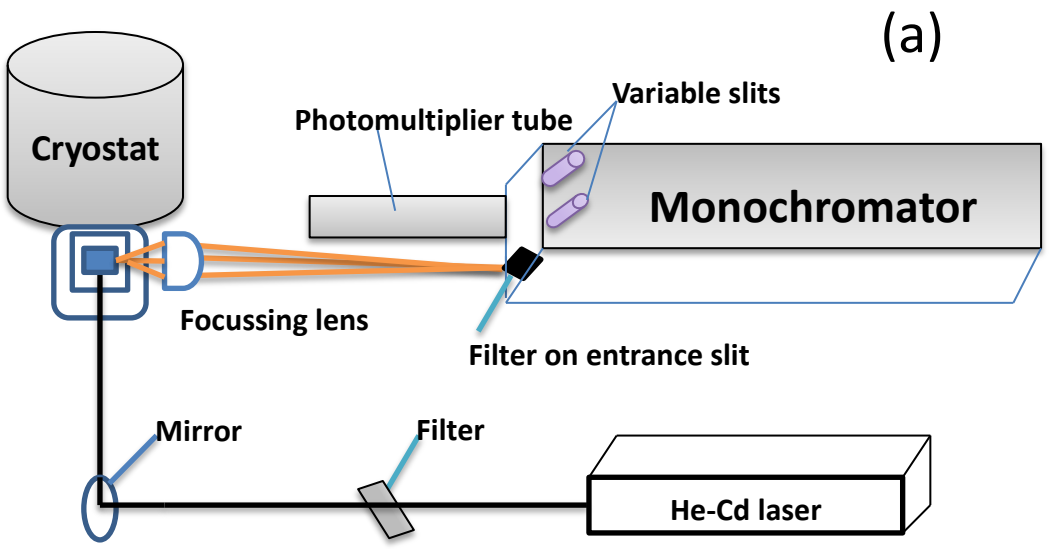

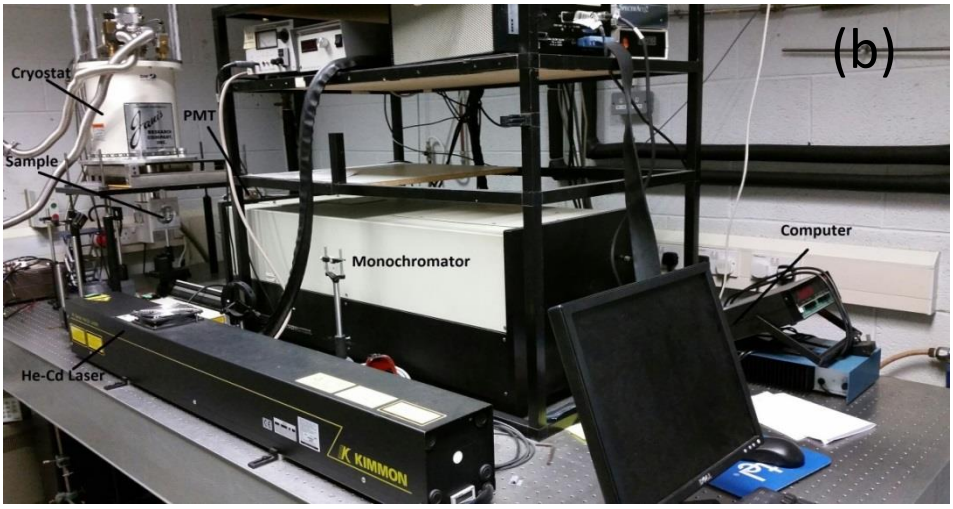

Figure 3.13: (a) Schematic representation of the optical setup used for low-temperature PL apparatus with the SPEX monochromator and (b) Photograph of the same apparatus.

Low-temperature PL (at 13 K) spectra were recorded (with 1 m model SPEX 1704 monochromator) using 325 nm He-Cd laser excitation. A schematic representation and photographic view of the PL apparatus is shown in Figure 3.13 (a) and (b), respectively. All samples were loaded in a cryostat, which can lower sample temperatures to 10 K-13 K using a closed cycle helium gas refrigerator. The PL detection equipment consists of a cooled photomultiplier tube (Hamamatsu model R3310-02) with single photon detection and the monochromator contained a grating blazed* at 330 nm (ISA model 510-05). The laser beam was focused on to the sample using a series of mirrors. The sample was placed in the cryostat at an angle of 45˚ to the incident laser beam. The emitted light from the sample was carefully collected using focusing lenses, and then directed towards the entrance of the monochromator through a grating slit, and using a long wavelength pass filter to remove short wavelength laser plasma emission features. The spectrum is then acquired by the computer-controlled monochromator, and analysed using software. The scan time needed for particular samples can be controlled by the slit width and the step size used during the scan.

*A blazed grating is a special diffraction grating, optimised to achieve maximum reflection effiency at a certain wavelength. In a blazed grating, the grooves are inclined to the flat surface by an angle for which the direction of maximum reflectance is identical to the angle of diffraction for a given angle of incidence.

In this work, some of the PL scans were performed in the presence of a Hg-lamp providing reference spectral lines for wavelength calibration purposes. The measured wavelengths were corrected for the index of refraction of air.

3.9 Raman spectroscopy

When a monochromatic light source (the light source is usually a laser) interacts with a sample, the scattered photons are observed. The frequency of the scattered photons can be either identical with, or higher or lower, than the original light frequency. This is because of the nature of the interaction between the incident light and the sample and is called the Raman effect. This frequency shift of the re-emitted photons can reveal information on the vibrational, rotational and other low-frequency excitations of the sample. Raman spectroscopy can be used for the study of solids, liquids and gases.

The Raman effect is based on the effect of molecular deformations (due to phonons or other excitations) on the polarizability of the sample (α). The laser beam creates an oscillating electromagnetic wave in the sample with an electrical vector E. This creates an induced electrical dipole moment $P = \alpha E$. Certain deformations of the lattice due to phonons (so-called Raman active modes, whose properties can be understood using the symmetry characteristics of the lattice and the modes) modulates the polarizability at the phonon characteristic frequency υ_m. The net effect in the classical view is a molecule with a dipole oscillating with 3 frequency components, specifically i) Rayleigh scattering, ii) Stokes scattering and (iii) anti-Stokes scattering [18].

i) Rayleigh scattering- The scattered photon has the same frequency as the original incident photon. This interaction is called Rayleigh (or elastic) scattering.

ii) Stokes scattering- The scattered photon has a reduced frequency ($\upsilon_o - \upsilon_m$). This is called Stokes scattering.

iii) Anti-stokes scattering- The frequency of the scattered photon is increased to $\upsilon_o + \upsilon_m$. This is called anti-Stokes scattering.

Raman scattering (especially in solids) induces the transistions in atoms/molecules of the sample. These transistions can be rotational, vibrational, and electronic. Sometimes these transistions may have a combination of the above. A detailed study of the Raman spectroscopy for solids has been reviewed by Devine and Adar [19]. Also, a comprehensive review of Raman spectroscopy for ZnO can be seen in ref [16].

A Raman spectroscopy system typically consists of an excitation source i.e. laser, sample illumination system and light collection optics, filter or spectrophotometer, and a detector (CCD or PMT). In this work, Raman spectra were measured at room temperature using a Jobin Yvon Horiba LabRAM 800 spectrometer with a 488 nm Ar^+ laser as the excitation source, focused through an 100× microscope objective. In this work, Raman measurements were used to understand the lattice defects present in the interconnected nanorod samples. Raman experiments were performed as part of a collaboration with the School of Electronic Engineering, DCU.

3.10 Van der Pauw and Hall effect experiments

3.10.1 Van der Pauw/Four-point probe: Resistivity measurement

The four point probe method provides an accurate measurement of electrical resistivity via specific current-voltage measurements. This is a technique to measure the sheet resistance and bulk resistivity of thin films of known thicknesses. The input voltage can be set in between 20-200 mV, the corresponding current is then automatically recorded by the software controlling the instrument. This technique was first developed by Van der Pauw and Leo [20].

As shown in Figure 3.14, the current source is applied to the contacts 1 and 2 (I_{12}) and then the voltage measured across the contacts 4 and 3 (V_{43}). Similarly, the current source is then applied to the contacts 1 and 4 (I_{14}) and the voltage (V_{23}) measured.

The sheet resistance is given by

$$R_s = \frac{\Pi}{2.\ln(2)}\left[\frac{V_{43}}{I_{12}} + \frac{V_{23}}{I_{14}}\right].F(Q) \quad (\Omega/\text{sq}) \quad \text{(Eq. 3.7)}$$

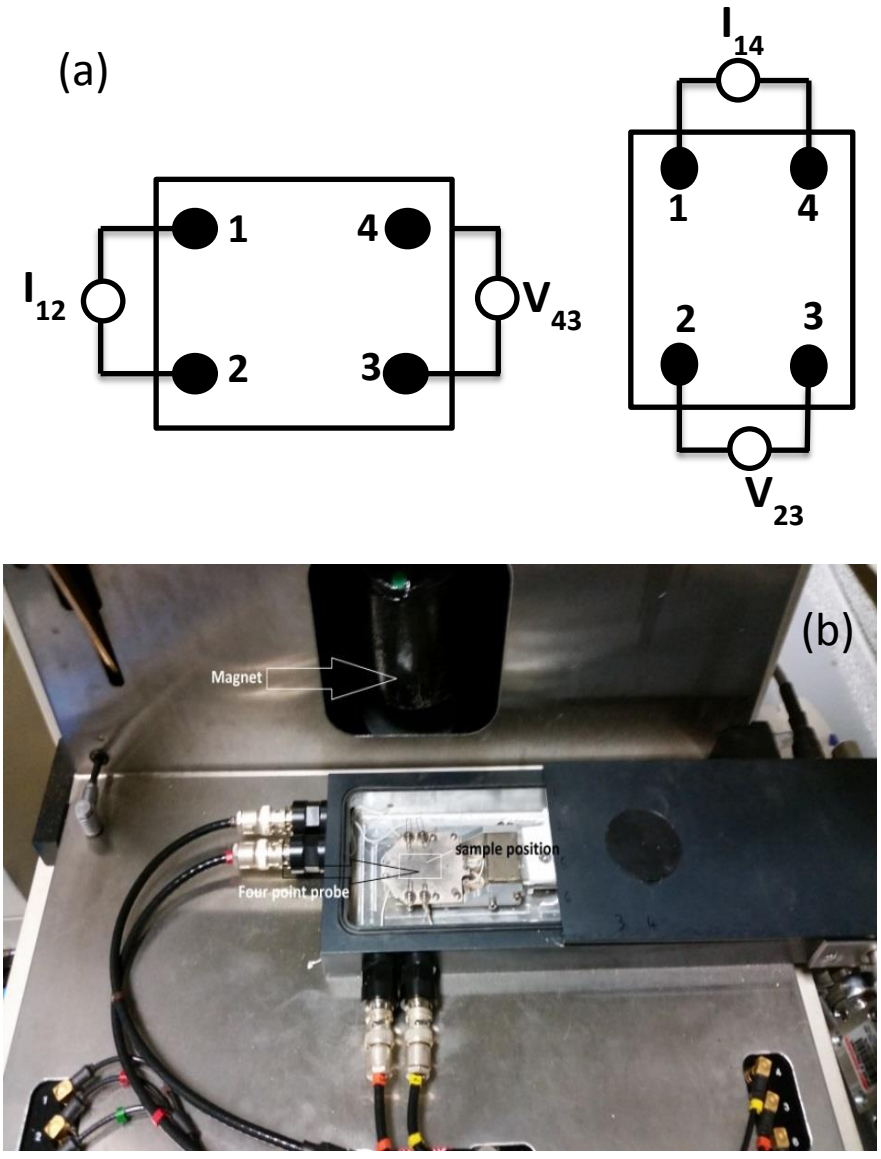

Figure 3.14: (a) Principle diagram for the four point probe method of resistivity measurements, (b) shows the photograph of the typical parts of the instruments such as four point probes and the sample position (magnet is used for Hall effect measurements).

Where, Q and F are the symmetry and correction factors respectively. F is a correction factor for geometrical asymmetry. It is not related to material anisotropy or inhomogeneity and it is a function of symmetry factor Q.

Symmetry factor Q is defined as $Q=\frac{V_{43}.\ I_{14}}{I_{12}.V_{23}}$ (Eq. 3.8)

For known thickness, resistivity can be measured using

$\rho = R_s\ t$ (Ω cm) (Eq. 3.9)

3.10.2 Hall effect experiment

Once the resistivity measurements are carried out, we perform Hall effect measurements. The apparatus is the same as used for four-point probe measurements. We measure the Hall mobility, Hall coefficient and carrier concentration of the samples. In 1879, E. H. Hall discovered this effect. He observed that when an electrical current passes through a sample located in a magnetic field, a potential (voltage difference) develops in a perpendicular direction to both the electric and magnetic fields, proportionally to the electric and magnetic field strength. In a semiconductor material, when a magnetic field B_z is applied in a direction perpendicular to the direction of applied electric field $E_{x,}$ a transverse field is then developed perpendicular to the both E_x and B_z, i.e. along y-direction. This is shown in Figure 3.15. Suppose that the mobile charges are positive with charge q and move along the slab in x-axis with a drift velocity V_x. Thus, the magnitude of the magnetic force on a given mobile charge q is given by $qV_x B_z$. In a steady state, the force created by magnetic field is balanced by the force created by electric field.

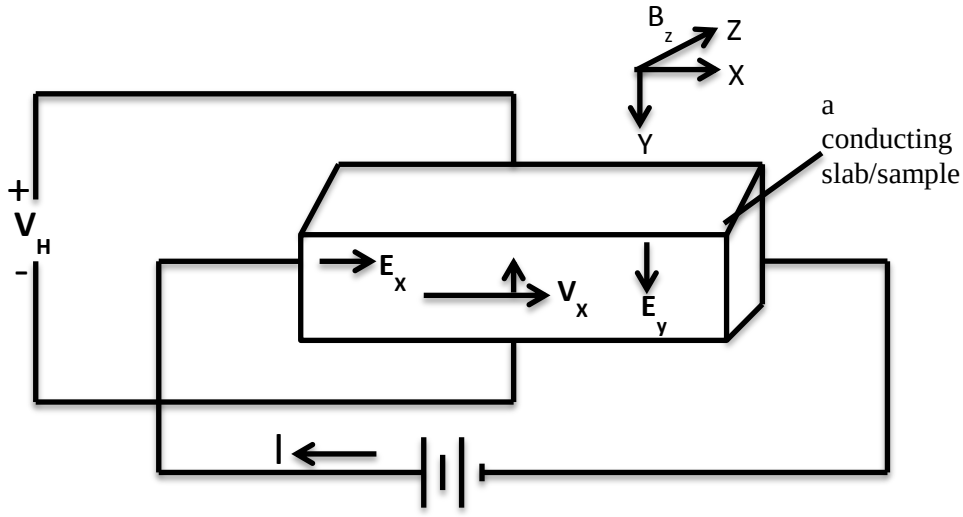

Figure 3.15: The visual representation of the Hall effect measurement set up.

Therefore, the equation is given by

$$qE_y = qV_x B_z \qquad \text{(Eq. 3.10)}$$

Hole current density is defined as

$$J_{p.x} = V_x qp \qquad \text{(Eq. 3.11)}$$

Where $J_{p.x}$ is the hole current density, q is the charge and p is the hole concentration.

$$\text{Thus, } E_y = R_H J_{p.x} B_z \qquad \text{(Eq. 3.12)}$$

Where R_H is the Hall coefficient and is given by $R_H = 1/qp$.

Suppose the charge carriers are electrons, then the $R_H = -1/qn$.

The carrier concentration can be obtained from

$$N = 1/(q.R_H)\ \ cm^{-3} \qquad \text{(Eq. 3.13)}$$

The Hall mobility is given by

$$\mu_H = R_H \sigma \qquad \text{(Eq. 3.14)}$$

where σ is the conductivity and $\sigma = 1/\rho$.

These measurements indicate the type of charge carriers in the material. If the sign for the Hall coefficient value is negative then the material is considered n-type conductive. If the sign for Hall coefficient value is positive then the material is p-type conductive. A review on Hall effect and its application is seen in ref [21]. In this work, we used Van der Pauw method/Hall effect apparatus with model-Accent HL5500 instruments.

3.11 References

[1] J. Rousseau, *Basic Crystallography*, (1998), Sussex: John Wiley & Son Ltd.

[2] H. Morkoç, Ü. Özgür, *Zinc Oxide- Fundamentals, Materials and Device Technology*, (2009), Wiley: Germany.

[3]V.D. Mote, Y. Purushotham, B.N. Dole, Williamson-Hall analysis in estimation of lattice strain in nanometer-sized ZnO particles, *J. Theoretical Appl. Phys.* 6 (2012)1-8.

[4] S. Maniv, W.D. Westwood, E. Colombini, Pressure and angle of incidence effects in reactive planar magnetron sputtered ZnO layers, *J. Vac. Sci. Technol.* 20 **(**1982) 162-170.

[5] B.D. Cullity and S.R. Stock, *Elements of X-Ray Diffraction,* 3rd edition, (2001), Prentice Hall: New Jersey, Chapter 14, pp 404-406.

[6] V. Randle, O. Engler, Introduction to texture analysis: Macrotexture, microtexture, and orientation mapping, (2000), CRC press: USA.

[7] Y. Chung, *Practical Guide to Surface Science and Spectroscopy,* (2001), Academic Press: London.

[8] S.N. Magonov and M. Whangbo, *Surface Analysis with STM and AFM: Experimental and Theoretical Aspects of Image Analysis*, (2008), John Wiley & Sons Ltd: Germany.

[9] Web ref: http://www.asmicro.com/Equipment/Identifying_NanoScope.htm, Advanced Surface Microscopy Inc,. (last accessed on 11th June 2015).

[10] I. Horcas, R. Fernández, J. Gomez-Rodriguez, J. Colchero, J. Gómez-Herrero, A. Baro, WSXM: a software for scanning probe microscopy and a tool for nanotechnology, *Rev. Sci. Instrum.* 78 (2007) 013705.

[11] L. Reimer, *Scanning Electron Microscopy: Physics of Image Formation and Microanalysis*, (2013), Springer: Berlin.

[12] D. Byrne, PhD thesis on "*the growth and characterisation of ordered arrays of zinc oxide nanostructures and optical studies of defects in zinc oxide*", DCU, (2012).

[13] L.R. White, On deviations from Young's equation, Journal of the Chemical Society, *Faraday Transactions.1: Phys. Chem. Condensed Phases*, 73 (1977) 390-398.

[14] D. Swinehart, The Beer-Lambert law, *J. Chem. Educ.* 39 (1962) 333.

[15] Web ref: http://namrataheda.blogspot.ie/2013/07/spectrophotometry-part-2-uv-visible.html (last accessed on 11th June 2015).

[16] C.F. Klingshirn, B.K. Meyer, A. Waag, A. Hoffmann, J. Geurts, *Zinc Oxide, from fundamental properties towards novel applications*, (2010), Springer: Berlin, Chapter 7, pp171 or pp 23-31.

[17] P.K. Basu, *Theory of Optical Processes in Semiconductors: Bulk and Microstructures*,(1997),Oxford University Press: Oxford.

[18] J. R. Ferraro and K. Nakamoto, *Introductory Raman Spectroscopy*, (1994), Academic Press: London; Boston, MA.

[19] T. M. Devine and F. Adar, Raman Spectroscopy of Solids, *Characterization of Materials*, (2012) 1067–1104, doi: 10.1002/0471266965.com060.pub2.

[20] Van der Pauw, Leo J, A Method of Measuring Specific Resistivity and Hall Effect of Discs of Arbitrary Shape, *Philips Research Reports* 13 (1958) 1-9.

[21] C.L. Chien, C.R. Westgate, *The Hall effect and its application*,(1980), Springer: New York.

Chapter 4

Growth and Characterisation of ZnO-based Core/Shell Nanorods on ZnO-Seeded Si Substrates

In section 4.1, we focus on the growth and characterisation of unique crystalline-ZnO/amorphous-ZnO core/shell nanorods. These self-organised core/shell architectures are prepared by catalyst-free PLD on ZnO-seeded Si (100) substrates. The structural, morphological and luminescent properties of these samples are established. A ZnO emission band at 3.331eV is revealed in the core/shell architecture and its origin linked to the observed defects at the crystalline/amorphous interface of the core/shell structure. This particular defect PL emission appears to be a new observation for ZnO. In section 4.2, we present the catalyst free-PLD growth and characterisation of ZnO interconnected architectures on ZnO-seeded Si (100) substrates. In section 4.3, we present the growth and characterisation of the high optical quality of vertically aligned ZnO nanorods by catalyst-free VPT technique on PLD grown ZnO seed layers. It also includes a

comparison between the structural, morphological and optical properties of the PLD grown ZnO seed layers, the VPT grown ZnO nanorods and the PLD grown ZnO nanorods.

4.1 Crystalline-ZnO/amorphous-ZnO core/shell nanorods

4.1.1 Growth details

ZnO/ZnO core/shell nanorods (here onwards sample is labelled as ZnO/ZnO core/shell, this is because core is crystalline ZnO and shell is amorphous ZnO, see section 4.1.2.2 below for more details) were grown using a standard PLD apparatus equipped with a high-power, Q-switched, frequency-quadrupled, Nd:YAG laser. The laser specifications and other growth parameters of the PLD system were discussed earlier in Chapter 3. Here we present the growth details of the core/shell nanorods. The target-substrate distance was kept constant at 5 cm. Cleaved 1 cm × 2 cm pieces of Si (100) wafers were used as substrates. Prior to deposition, the substrates were degreased/cleaned for 15 minutes in an ultrasonic bath filled with acetone/isopropyl alcohol. Silver paste was used to mount substrates on the substrate holder in the deposition chamber. Before deposition, the substrates were heated to 900 °C using a heater coil for 30 minutes for the purpose of surface cleaning e.g. removal/vapourisation of hydrocarbon contaminants and then cooled down to 450 °C. The rationale for using these growth parameters (substrate temperatures and oxygen pressures) is based on our previous investigations. For example, we found that a 450 °C growth temperature for the seed layer provides a better crystalline substrate compared with the 100 °C and 300 °C growths.

The fabrication of the ZnO/ZnO core/shell nanorods involved two stages [1]. The first stage was the preparation of a thin ZnO seed or buffer layer. The seed layer of thickness around 120 nm (5000 laser shots) was deposited at a substrate temperature of 450 °C in an ambient O_2 pressure of 100 mTorr. Following deposition of the seed layer, the substrate temperature was increased to 700 °C at a rate of 12 °C /minute, then left at this temperature for 5 minutes, and finally cooled down to 150 °C at a rate of 9 °C/minute. The second stage involved the preparation of the core/shell nanorods. The ZnO seed/substrate temperature was initially raised to 800 °C at a rate of 7 °C/minute. The ZnO/ZnO core/shell nanorods were then

grown at this temperature in a 600 mTorr O_2 pressure and left in these conditions for 5 minutes. After this period, the substrate temperature was cooled down to 150 °C at a rate of 9 °C/minute. The actual deposition time of the core/shell nanorods was about 2 hrs (40,000 laser shots), excluding the sequence of heating and cooling phases to pre- and post-growth. The full length of the core/shell nanorod obtained in these conditions was around 1 μm**.** Five growths using the same conditions and sequences were performed over a two week period. The same core/shell nanorod architecture was obtained in each case and is thus fully reproducible. From the viewpoint of the growths, we conclude that the overall sequence of specific heating and cooling phases used in this work has allowed us to achieve self-organised core/shell architecture, without the need for a separate growth step for the shell region. The self-organisation of ZnO nanostructures is a known feature [2]. Also, to the best of our knowledge, similar growths of ZnO nanorods [3,4] carried out in similar pressure conditions, all lead to a simple nanorod structure, i.e. without a shell. Thus, we can conclude that the series of substrate temperatures for the given deposition rate used in this PLD work should be the important parameter influencing the growth mode and kinetics [5] that lead to the formation of the core/shell architecture.

The structural characteristics were investigated by 2θ-ω, and pole figure X-ray diffraction scans, respectively. The surface morphologies and nanostructures were studied by scanning electron microscopy (SEM) and field emission SEM (FE-SEM), transmission electron microscopy (TEM) at an operating voltage of 200 kV. High resolution TEM (HR-TEM) and selective area electron diffraction (SAED) were studied using the same TEM apparatus. Low-temperature photoluminescence (PL) spectra were recorded using a 325 nm He-Cd laser excitation.

4.1.2 Results and discussions

4.1.2.1 Structural properties

Figure 4.1 shows the 2θ-ω XRD scan, on a logarithmic scale, for ZnO/ZnO core/shell nanorods grown by PLD and similar data from a ZnO single-crystal wafer. The ZnO/ZnO core/shell nanorods show a dominant (002) reflection at $2\theta \approx 34.40^{o}$ and a weaker (004) reflection at $2\theta \approx 72.62^{o}$. The origin of the weaker or impurity

features is also mentioned in the figure caption. No other ZnO-related peaks are observable. The intensity of the PLD-deposited ZnO (002) reflection is around a million counts. The ZnO/ZnO core/shell nanorods grown by PLD on Si (100) substrates are clearly highly textured and oriented with their *c*-axes normal to the substrate surface. We note that previous studies of Rajendra Kumar et al. [6], McCarthy et al. [7], and Wan et al. [8] showed the similar XRD data (including the identification of the weaker/impurity peaks) for their ZnO nanorod or thin film samples grown on Si substrates. Here, we have compared our ZnO/ZnO core/shell nanorods with normal ZnO nanorods. This is because there have been no reports published on ZnO/ZnO homo-material (i.e. same material in both core and shell regions) based core/shell nanorods. In this regard, we believe that ZnO nanorods are the suitable materials for comparisons with our ZnO/ZnO core/shell nanorods. Indeed, these comparsions can be allowed as XRD is a bulk characterisation technique.

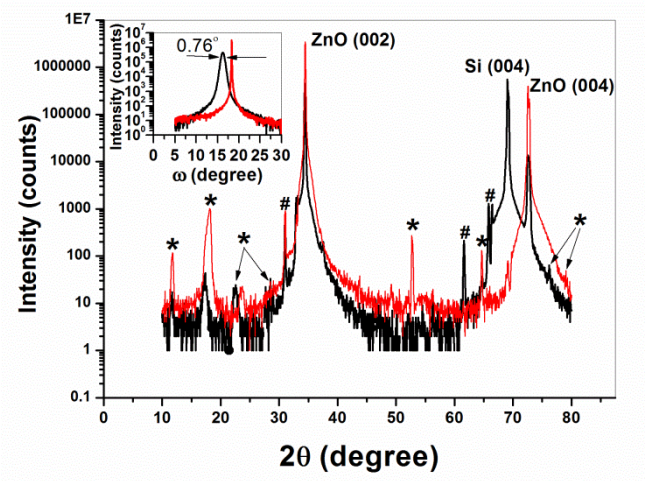

Figure 4.1: 2θ-ω (or 2θ-θ) XRD scans for ZnO/ZnO core/shell nanorods (black line) and a ZnO single crystal wafer (red line) (The features marked '*' are due to the adhesive mounting tape used. The features marked '#' are due to Cu K_β and tungsten L_α radiations from the x-ray tube, the latter due to contamination). The inset shows the rocking curve scans from the two samples around the ZnO (002) peak position.

For comparison, we have measured a 2θ-ω XRD scan using *c*-plane terminated ZnO single crystal wafer of thickness 0.5 mm (Tokyo Denpa) using the same conditions. The measured 2θ value for the ZnO single crystal (002) reflection is ≈

34.45º, almost identical to the value for our nanorods (≈ 34.40º). We have also measured the FWHM of the ZnO (002) reflection for the PLD-deposited ZnO, and used these 2θ and FWHM values to calculate the *c*-axis lattice spacing and crystallite size (more accurately the out-of-plane coherence length), using Bragg's law and the Scherrer equation corrected for instrumental broadening, respectively (we use the weighted average value of the wavelengths of Cu $K_{\alpha 1}$ and Cu $K_{\alpha 2}$ radiation lines for the x-ray wavelength in all calculations, i.e. λ = 1.5425 Å). The details of the calculation are discussed earlier in Chapter 3 and also see a previous article [9] for more details. The PLD-deposited ZnO (002) reflection FWHM, *c*-axis lattice spacing, and crystallite size values are 0.198º, 5.216 Å, and 75.31 nm, respectively. The *c*-axis lattice spacing value is comparable with the value calculated for the ZnO single crystal wafer (5.207 Å). We note that the value of the lattice spacing (*c*) obtained from the aforementioned single crystal value of 2θ = 34.45º matches the published ZnO *c*-axis lattice spacing of 5.20690 Å (JCPDS card number 36-1451).

The inset of Figure 4.1 shows the rocking curve for the (002) reflection from the ZnO/ZnO core/shell nanorods sample (black line) and for the (002) reflection from the ZnO single crystal wafer (red line). The rocking curve of the ZnO/ZnO core/shell nanorods sample has a FWHM of 0.76º which is notably smaller than the data on samples of similar type reported previously for ZnO nanorods. For example, FWHM of rocking curve values are ~ 2º in ref [6], ~ 2.3º in ref [7], and ~ 6.3º in ref [10]. This, together with the 2θ-ω data, indicates excellent crystallite alignment and texture. We note that, as expected, the FWHM of the rocking curve for the ZnO single crystal wafer is much narrower, essentially limited by the instrument broadening (< 0.1º). Since no catalyst was used as a seed in our synthesis, no other materials or crystalline phases are identified in the XRD data. In conclusion, the XRD analyses confirm that the ZnO/ZnO core/shell nanorod deposit grown by PLD on Si (100) substrates is well-aligned with excellent *c*-axis orientation normal to the substrate surface.

XRD pole figure analyses were also used to undertake a more detailed investigation of the texture and in-plane orientation of the ZnO/ZnO core/shell nanorods. Pole figures of the (002), (101) and (102) planes were measured at 2θ values of 34.5°, 36.5° and 47.5°, respectively (Figure 4.2). Figure 4.2 (a) shows a

narrow and intense (002) pole figure centered at Ψ=0 indicating the growth of the core/shell nanorods with their vertical axes along the substrate normal. Figures 4.2 (b) and (c) show rotationally (circularly) symmetric (101) and (102) pole figures at Ψ angle values of ~ 62.7° and ~ 42.9°, respectively. The latter are very close to the value of the angles between the ZnO (101)/(002) and (102)/(002) planes, as expected from the known crystallographic structure of ZnO [11,12]. Teki et al. [11] have observed the angles between ZnO (101)/(002) and (102)/(002) planes at ~ 61° and ~ 43°, respectively. The intense spots at Ψ = 45° on the (102) pole figure, indicated in Figure 4.2 (c), are due to the (220) planes of the Si substrate, and seen previously [11]. The pole figure data confirm that the PLD grown ZnO/ZnO core/shell nanorods are well textured with excellent vertical orientation along the *c*-axis and also show the complete absence of any in-plane orientation, i.e. the absence of epitaxy, on the substrate.

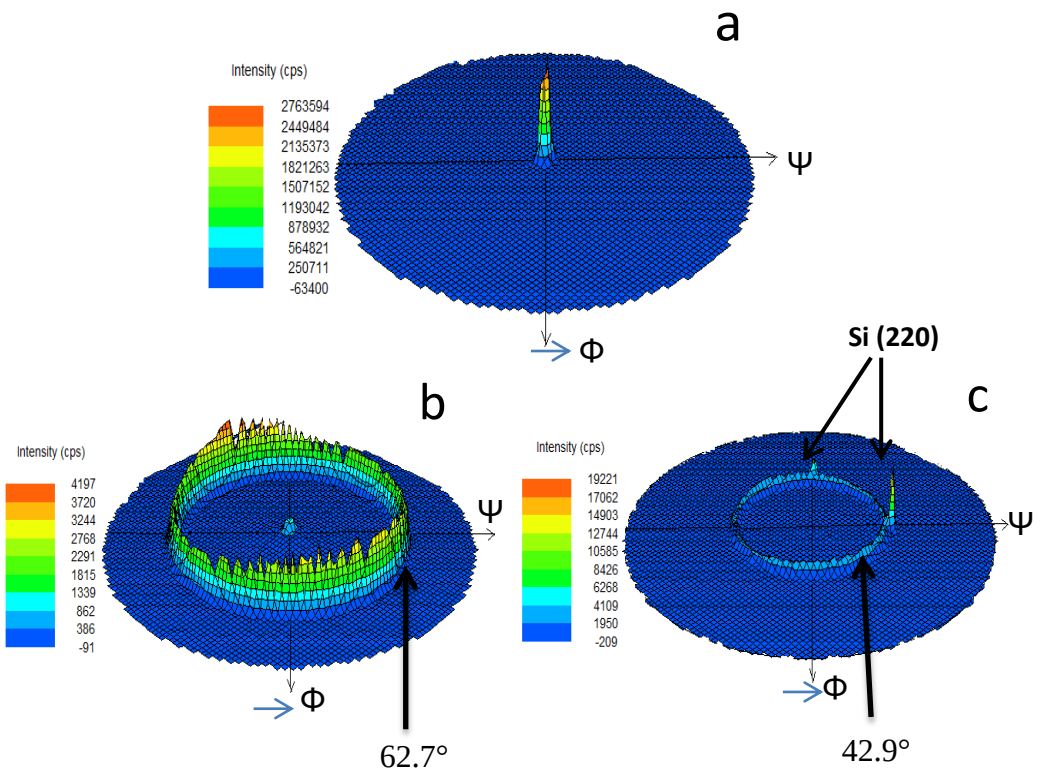

Figure 4.2: XRD pole figures for the (a) (002), (b) (101) and (c) (102) ZnO planes, respectively, in ZnO/ZnO core/shell nanorods grown by PLD.

4.1.2.2 Surface morphology and nanostructuring

The surface morphologies of the core/shell nanorod deposits were studied using SEM, FE-SEM, and TEM. Figures 4.3(a), (b) and (d) show FE-SEM images, and Figure 4.3(c) shows SEM images, taken at various tilt angles. These images show that the core/shell nanorods have almost conical terminations with rounded or blunt tips. Figure 4.3 also strongly supports the conclusions from XRD (2θ-ω and x-ray pole figures) analysis concerning preferred *c*-axis orientation and the absence of in-plane epitaxial ordering. The SEM and FE-SEM images of Figure 4.3 allow us to conclude that the core/shell nanorods are densely packed, with a uniform morphology.

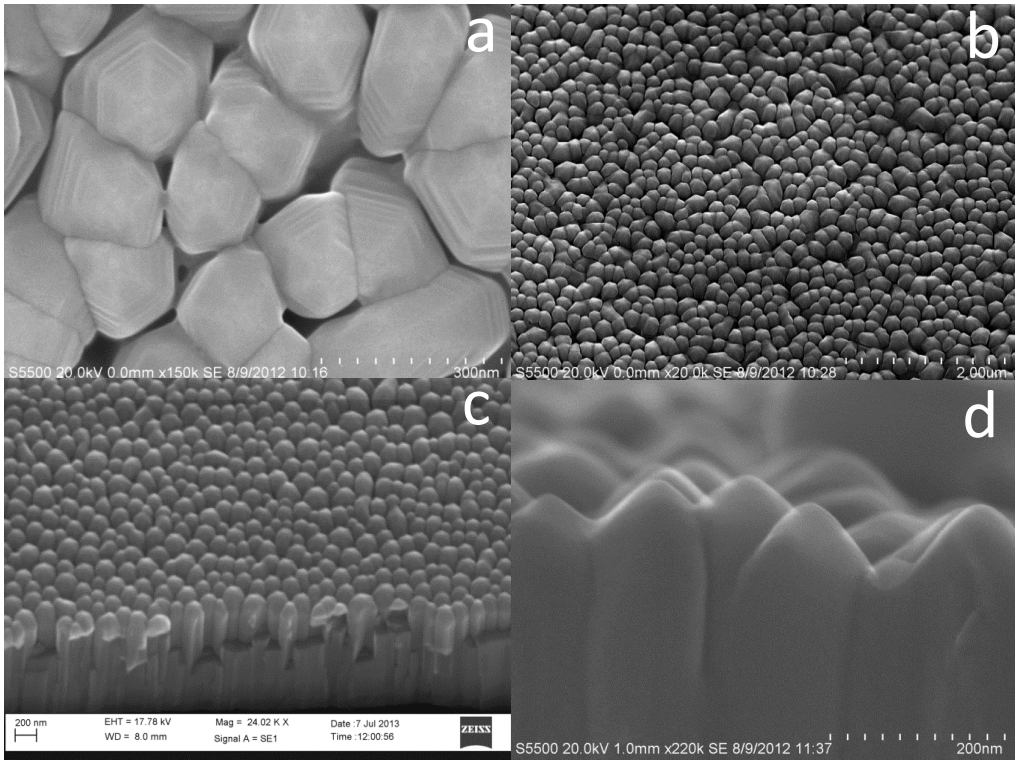

Figure 4.3: Field emission SEM (a), (b) and (d) and SEM (c) images of ZnO/ZnO core/shell nanorods grown by PLD at (a) 0º tilt (plane view), (b) 20º tilt, (c) 30º tilt, and (d) 85º tilt angles.

Significant insights into the core/shell nanorods structure were revealed using TEM and HR-TEM analyses. Regions of the samples containing hundreds of ZnO/ZnO core/shell nanorods were peeled off from the Si (100) substrate using a surgical blade and mounted on the 300 mesh size TEM grid for analysis. Figure 4.4

(a) and (b-d) show TEM and HR-TEM images of the core/shell nanorods, respectively. The images in Figures 4.4 (a) and (b) show that the nanorods have a core/shell structure with a crystalline (cr) core and an amorphous (am) shell. We now use the "cr-ZnO/am-ZnO core/shell" terminology to accurately refer to the established structure of the nanorods. Further detailed investigations were made at different locations of a specific core/shell nanorod, indicated by the circled regions marked 'b, c and d' in Figure 4.4 (a), corresponding to the images shown in Figure 4.4 (b), (c) and (d). The inset of Figure 4.4 (b) shows a HR-TEM image at the core/shell boundary region of the cr-ZnO/am-ZnO core/shell nanorods. These data confirm in greater detail the core/shell structure. A line (for a visual impression) was drawn as a guide to the eye in Figure 4.4 (b) to show the crystalline core and amorphous shell regions.

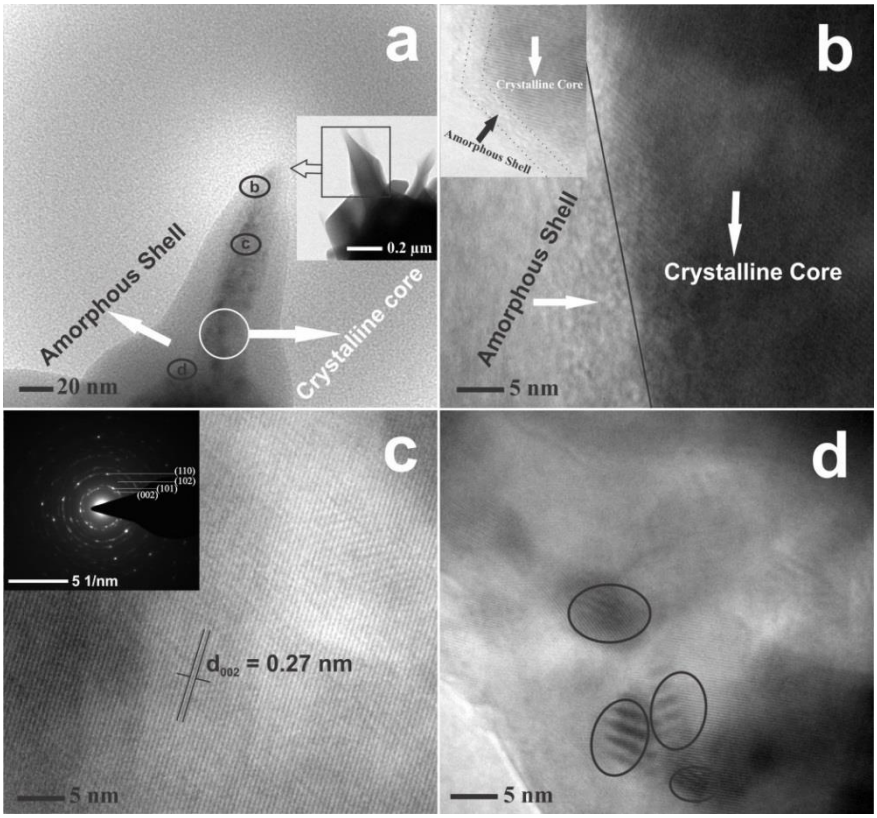

Figure 4.4: TEM, HR-TEM and SAED images of cr-ZnO/am-ZnO core/shell nanorods grown by PLD; (a): TEM image of a core/shell nanorod; (b): crystalline core and amorphous shell boundary region of a nanorod in the area indicated by circle b in (a); (c): HR-TEM image for the core-part of a core/shell nanorod in the area indicated by circle c in (a); (d): Identified Moiré fringes in the area indicated by circle d in (a). Inset of (c) shows SAED pattern of the area shown in (c). These images were collected at various tilts of the nanorods.

The cr-core/am-shell structure can be at least partially explained by the combination of several plausible factors such as the rate of material deposition prevailing in the PLD apparatus at the 800 °C substrate temperature, shadowing effects due the compact nanorod distribution and the final cooling rate. All of these factors may contribute to prevent the adatom diffusion necessary to find an equilibrium lattice site in the crystalline growth directions perpendicular to the c-axis. Additionally, we note that such cr-core/am-shell structures have also been produced serendipitously in previous works using different growth methods [13-17].

The HR-TEM image of the core part of the core/shell nanorods (indicated by circled region c in Figure 4.4 (a)) is represented in Figure 4.4 (c) and the observed lattice spacing from HR-TEM (0.27 nm) is in good agreement with that obtained from the XRD data above, see Figure 4.1(0.26 nm). The selected area electron diffraction (SAED) pattern was collected using a 200 nm aperture and is shown in the inset of Figure 4.4 (c). The ring pattern in SAED indicates the field of view contains polycrystalline material. The indexed (002), (101), (102) and (110) diffraction peaks belong to the pure ZnO phase and provide information complementary to the XRD pole figure data above. The HR-TEM data also allows us to identify specific regions at the interface between the crystalline core and amorphous shell, indicated by the round circles (from the circled region d of Figure 4.4 (a)) in Figures 4.4 (d) which display clear evidence of Moiré fringes at the boundary. Li et al. identified no Moiré patterns in their HR-TEM data from PLD grown ZnO/Er_2O_3 core/shell nanorods, because their Er_2O_3 shell region was polycrystalline [18]. Overall, the TEM and HR-TEM data clearly show that cr-ZnO/am-ZnO core/shell nanorods grown by PLD on Si (100) substrates have a core/shell structure (with a crystalline core and an amorphous shell) with Moiré fringes identified at the boundary region where structural defects are expected, which may well be associated with the core/shell boundary interface region.

4.1.2.3 Optical properties

Because of intrinsic and extrinsic defects/impurities, which lead to a range of donor/acceptor levels within the bandgap, ZnO can emit right across the visible spectrum, as well as in the near UV [19,20]. This is a key advantage for devices such as white light LEDs. However, the absence of stable and high Hall mobility p-type

material [21] remains the major obstacle for the development of large scale LEDs and laser diodes, and this, in turn, is due to the nature of the defect population in the material itself. In this regard, it remains of crucial importance to understand the defect population in this material, and a powerful tool for the study of such defects is their PL emission.

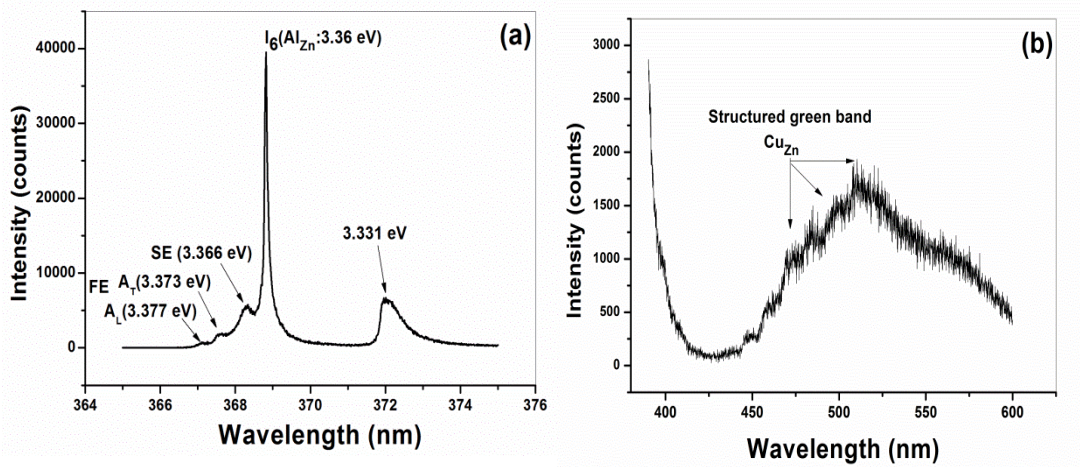

Figure 4.5: Low temperature (13 K) PL spectra of cr-ZnO/am-ZnO core/shell nanorods (a) near band-edge region showing emission band at 3.331 eV and (b) visible region showing structured green band emission.

Figure 4.5 shows a typical low-temperature (13 K) PL spectrum of the cr-ZnO/am-ZnO core/shell nanorods produced in this work. Figure 4.5 (a) reveals a strong I_6 line at 3.36 eV, which is generally attributed to Al impurities, as well as a surface exciton (labelled SE) at 3.366 eV, and free exciton emission (labelled FE) at 3.377 eV (A_L: longitudinal free exciton-polariton) and 3.373 eV (A_T: transverse free exciton-polariton). Interestingly, an additional broad emission at 3.331 eV was also consistently observed in the low-temperature PL spectra of these samples. Defect-related emissions in the energy region 3.31 eV to 3.35 eV have been observed in various ZnO structures including bulk, single crystals, micro-/nano-crystals, heterostructures, quantum dots, 1D structures (nanorods and nanowires) and also in p-type ZnO [22-27], and there are a number of reports of emission at, or very close to 3.331 eV [28-42]. However, as we describe below, the 3.331 eV emission seen in the present work in these cr-ZnO/am-ZnO core/shell nanorods grown on ZnO buffer layers/Si (100) substrates by PLD, has considerably different features and thus seems to have a different origin compared to the emissions at this energy reported by

others. In a number of cases the emissions listed above have been associated with structural defects in ZnO crystals [22,23,25]. We note that, in previous articles, the emission lines observed at 3.3328 eV and 3.3363 eV in a ZnO single crystals are labelled as Y_0 and Y_1, respectively [23]. Furthermore the feature at 3.3328 eV (Y_0) is also labelled in some publications as a DBX (donor bound exciton) [43], and as a DD (deep donor bound exciton), emission [24,44]. The emission at 3.331 eV observed in this work is considerably broader (FWHM ~ 1.75 meV) than the emissions at or close to 3.331 eV observed in these other works (FWHM~ 0.5 meV and 0.2 meV) [22,23], as well as displaying a clearly asymmetric line shape not seen in these other works. In the particular case of the Y/DD lines we also note that the thermal activation energies of the Y/DD emissions are very small and the features are strongly quenched with increasing temperature and are not seen above 20K, which is completely at odds with the 3.331 eV emission observed in our samples, which survives to much higher temperatures (> 100 K), as described below. These various differences lead us to conclude that the 3.331 eV emission we observe has a different origin compared to the emissions at this energy reported by others. Deep level visible emission was also observed from the cr-ZnO/am-ZnO core/shell nanorods, as shown in Figure 4.5 (b) where the structured green band, due to Cu impurities, is clearly observed [45].

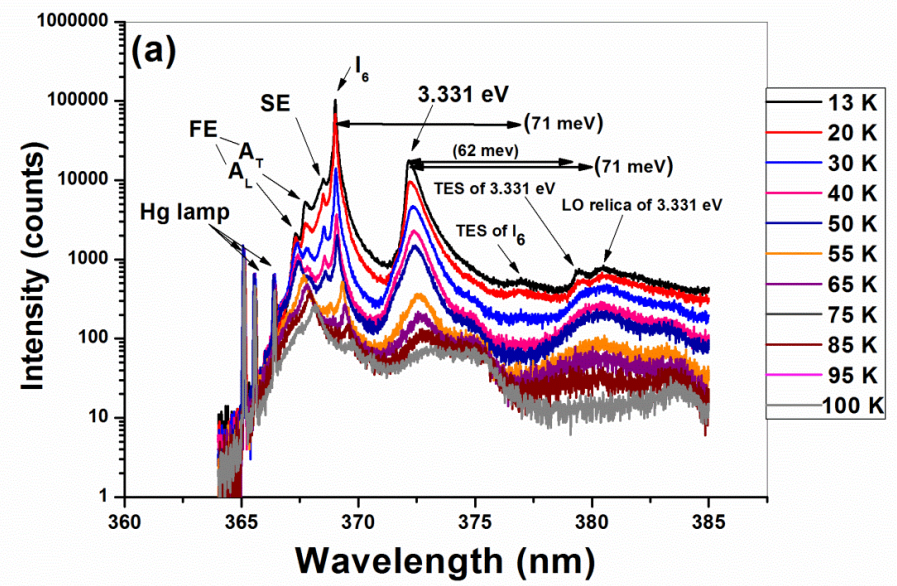

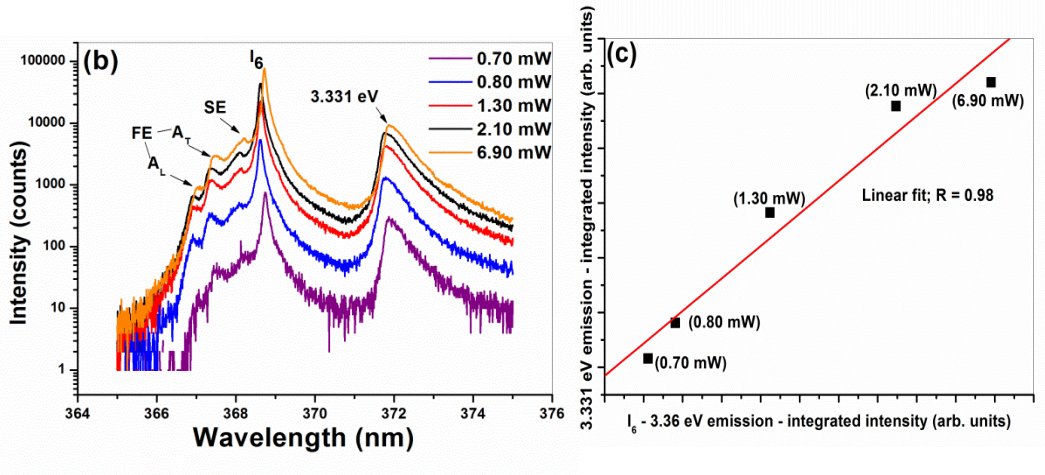

Figure 4.6: (a) Dependence of PL emission from cr-ZnO/am-ZnO core/shell nanorods on cryostat temperature, (b) Dependence of PL emission from cr-ZnO/am-ZnO core/shell nanorods on laser excitation power at constant cryostat temperature of 13 K and (c) Linear correlation between the integrated intensities of the I_6 (3.36 eV) and 3.331 eV emission bands for the various laser powers used in this work.

The 3.331 eV emission was further investigated by varying temperature and laser excitation power. Figure 4.6 (a) shows temperature dependent PL spectra from 13 K to 100 K. We observed that as temperature increases the surface and shallow bound exciton emissions quench rapidly. It is clear that the initially strong I_6 line reduces in intensity much faster compared to the 3.331 eV band. The 3.331 eV band can still be clearly seen at a temperature of 100 K and this behaviour implies involvement of deeply bound constituents, either an electron or a hole or both. Generally, two electron satellite (TES) and longitudinal optical (LO) replicas of the line are located in a region 30 - 70 meV from the parent emissions. However, since the 3.331 eV band still remains visible at a temperature of 100 K where the shallow bound exciton emission has been quenched, it is not due to a TES of the shallow bound exciton emission. We note that TES of the dominant I_6 line, and the TES and an LO replica of the 3.331 eV emission are also observed in Figure 4.6 (a). These temperature dependent PL studies enable us to conclude that the 3.331 eV emission is stable up to 100 K and therefore it is neither a shallow bound exciton, nor a TES or phonon replica of a shallower bound exciton transition, and is therefore the zero phonon line associated with the recombination of deeply bound carriers at a defect in the material. The present findings show that most of the previously published

assignments of the origin of the 3.331 eV emission as a TES band are likely to be erroneous [28-42].

We have also varied the laser excitation power (using neutral density filters), at a fixed cryostat temperature of 13 K, as shown in Figure 4.6(b). The 3.331 eV band remains visible and its shape largely unchanged with varying power of the laser. Slight laser heating effects can just be distinguished at the highest laser power of 6.90 mW, where a small redshift in emission is seen across the entire near band-edge region. It is however clearly observed in Figure 4.6(c) that the 3.331 eV band scales in a similar manner to the I_6 shallow bound exciton emission with varying laser excitation power, even at the highest laser powers. This clearly demonstrates that the 3.331 eV emission is associated with a single electron-hole recombination, rather than a bi-exciton or other multi-electron-hole pair crystal excitation, and the slight effects of laser heating at the highest laser power do not in any way affect this conclusion.

Based on the general similarity in emission energy of the 3.331 eV band to that seen for other structural defect-related UV emissions [22,23,25,28-42], and the simultaneous presence of structural defects at the irregular boundary region of our core/shell nanorods, as revealed by HR-TEM data above (Figure 4.4 (d)), we propose that the origin of the 3.331 eV band is recombination of electron-hole pairs localised at a range of structural defects associated with the core/shell boundary interface region. This assignment is based on: (i) the demonstrated presence of structural defects at the boundary region of the core/shell nanorods, as shown by HR-TEM, in samples which exhibit this 3.331 eV band emission, (ii) the deeper spectral position of the emission, similar to PL emissions from other structural defects in ZnO, which is also consistent with the temperature stability of the emission, and (iii) the expected presence of structural defects with slightly different environments at the core/shell boundary region which explains both the relatively large line-width of the 3.331 eV emission as well as the quite distinct asymmetric line profile, since the slightly differing structural defect environments give rise to slight changes in emission energy from individual defects (i.e. inhomogeneous broadening), and the ensemble yields the broad and asymmetric emission band observed in measurements. This assignment is discussed further in sections 4.2 and 4.3 below, and the additional

measurements and analysis contained in those sections supports and strengthens this assignment.

4.1.3 Conclusions

We have grown, for the first time, self-organised cr-ZnO/am-ZnO core/shell nanorods on Si (100) wafers by PLD, without using a metal catalyst seed and without the need for a separate growth stage for the shell region. This was achieved by using a specific sequence of heating and cooling phases pre- and post-deposition. The deposits were characterised using x-ray diffraction, electron microscopies and photoluminescence. The characterisation studies showed that the nanorods are highly textured with their *c*-axis oriented normal to, but without epitaxial in-plane ordering on, the substrate surface. The nanorods have conical terminations with rounded/blunt tips. They present unique core/shell architecture with a crystalline core and an amorphous shell while structural defects feature in the region of the core/shell boundary interface. The samples exhibit an emission band at 3.331 eV in their low-temperature photoluminescence spectrum. This emission arises from a single electron-hole pair recombination involving deeply bound constituents likely associated with the structural defects at the core/shell boundary interface region.

4.2 Interconnected cr-ZnO/am-ZnO core/shell nanorods

There are some reports on ZnO interconnected nanorods in the literature. For example, Gao et al. [46] have reported three-dimensional interconnected network of ZnO nanowires and nanorods grown by a high temperature solid–vapor deposition (also called as vapour phase transport) process on Al_2O_3 or Si (110) substrates. Breedon et al. [47] have reported the interconnected ZnO nanowires grown by hydrothermal aqueous synthesis on spray pyrolysis deposited ZnO seeded glass substrates. Yu et al. [48] have reported the interconnected network based ZnO nanostructures grown by aqueous solution method on MOCVD prepared cracked-GaN seeded Si (111) substrates. Yin et al. [49] have reported ZnO interconnected nanowall networks on ZnO/Si substrates by thermal evaporation of metallic Zn powder at low temperature. Also, Rahmani et al. [50] have reported interconnected ZnO nanowires by a hydrothermal method on spray pyrolysis prepared ZnO seeded glass substrates. Furthermore, Ranjith et al. [51] have also reported interconnected ZnO nanowires by a solution growth method on spray pyrolysis prepared ZnO seeded glass substrates. On the basis of the reported works, our goal for the present work is to reduce the complexity of these multi-step processes (including a change of growth method being implemented between the growth steps), which were used previously, to produce interconnected ZnO nanorods. The ZnO morphology in the above reported works is completely different from our present interconnected nanorods because our interconnected nanorods have core/shell architectures. These were grown by PLD on a PLD prepared ZnO seeded Si (100) substrates.

4.2.1 Growth details

ZnO/ZnO core/shell interconnected nanorods were grown using the same PLD apparatus in identical growth conditions as in the previous work (see section 4.1), except for a laser energy of 110 mJ. Four growths (over a two week) using the same conditions and sequences were performed and the same interconnected based core/shell nanorod architecture was obtained in each case. It is thus fully reproducible.

The structural characteristics were investigated by 2θ-ω x-ray diffraction scans (XRD). The surface morphologies and nanostructures were studied by scanning

electron microscopy (SEM) and transmission electron microscopy (TEM). Low-temperature photoluminescence (PL) spectra were recorded using a 325 nm He-Cd laser excitation. Raman spectra were measured using Ar^+ laser excitation at 488 nm. The electrical properties were also studied by four point probe/Hall effect instruments.

4.2.2 Results and discussions

4.2.2.1 Structural properties

Figure 4.7 shows the 2θ-ω XRD scan, on a log scale, for interconnected ZnO/ZnO core/shell nanorods grown by PLD and similar data from a ZnO single-crystal wafer. The interconnected nanorod sample shows a dominant (002) reflection at 2θ ≈ 34.53º and a weaker (004) reflection at 2θ ≈ 72.74º. The intensity of the ZnO (002) reflection for the same nanorod sample is around a million counts. No other ZnO related peaks were observed in our XRD experiments. We note that the reason behind the annealing of this interconnected core/shell nanorod sample is discussed in the optical properties (see section 4.2.2.3). We also note that there is no significant change observed with the annealing of the interconnected core/shell nanorod samples in terms of their structural properties (see black and blue lines in Figure 4.7).

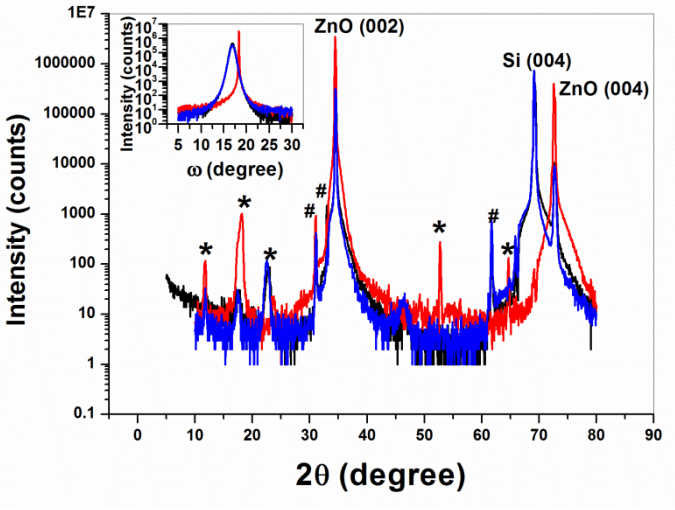

Figure 4.7: 2θ-ω XRD scans for the interconnected ZnO/ZnO core/shell nanorods (black line), annealed interconnected core/shell nanorods (blue lines) and a ZnO single crystal wafer (red line) (The features marked '*' are impurity lines. The features marked '#' are due to Cu K_β and tungsten L_α radiations from the x-ray tube, the latter due to contamination).

The inset shows the rocking curve scans from the two samples around the ZnO (002) peak position.

The FWHM, *c*-axis lattice spacing and crystallite size values for the (002) reflection of the interconnected nanorod sample are 0.205º, 0.519 nm and 38.74 nm, respectively. The above stated crystallite size value was measured from Scherrer equation (Eq 3.3) considering the correction factor for instrumental broadening. For comparison, we have measured a 2θ-ω XRD scan using *c*-plane terminated ZnO single crystal wafer of thickness 0.5 mm (Tokyo Denpa) using the same conditions. We note that the *c*-axis lattice spacing values of our interconnected nanorod sample (i.e. 0.519 nm) is in a good agreement with the ZnO wafer (i.e. 0.520 nm) values. We also note that the *c*-axis lattice spacing (i.e. 0.519 nm) of interconnected core/shell nanorods reported here is also close to previously reported (see section 4.1.2.1) core/shell nanorods (i.e. 0.5216 nm), but that there is some evidence of strain in these laterally interconnected nanostructures. This slight strain may be due to the effect of the lateral interconnections, since the morphology is no longer that of free standing, separated nanorods (see section 4.2.2.2 below). The crystallite size value for interconnected core/shell nanorod sample (38.74 nm) is observed to be small compared with normal core/shell nanorods, as reported previously (75.31 nm). This indicates that interconnection morphology affects the crystallite size and hence the crystallinity of the nanorods.

The inset of Figure 4.7 shows the rocking curve (RC) for the (002) reflection from the interconnected ZnO/ZnO core/shell nanorods sample (black line) and the same reflection from the ZnO single crystal wafer (red line). The FWHM of the RC for the interconnected nanorods is about 0.86º, which is comparatively larger than the previously (see section 4.1.2.1) reported core/shell nanorods (i.e. 0.76º). However, we note that the FWHM of RC reported in this work is much smaller than the previously reported values for ZnO nanorods [6,7,10]. Overall, the XRD analyses confirm that the interconnected ZnO/ZnO core/shell nanorods are well-aligned with *c*-axis orientation, however, their crystalline quality is less than that of the core/shell nanorods of section 4.1.2.1.

4.2.2.2 Surface morphology and nanostructuring

The surface morphologies of the interconnected ZnO/ZnO core/shell nanorods are studied by SEM and TEM. Figure 4.8 shows the interconnected nanorods captured at various tilt angles. It is clearly seen that the nanorods are interconnected with one another, and this interconnection behaviour also appears to be uniform across the sample. The length of interconnection junction was measured to be in a range of ~ 120-160 nm and the height of the nanorod was measured at about 1 μm. Figure 4.8 (d) shows that the nanorods have almost conical terminations with rounded or blunt tips, which is similar to the previously reported (see section 4.1.2.2) core/shell nanorods. Furthermore, SEM images show that the nanorods are densely packed with a uniform morphology. Overall, the SEM images confirm the vertical orientation of the nanorods, which supports our previous arguments from the XRD analyses.

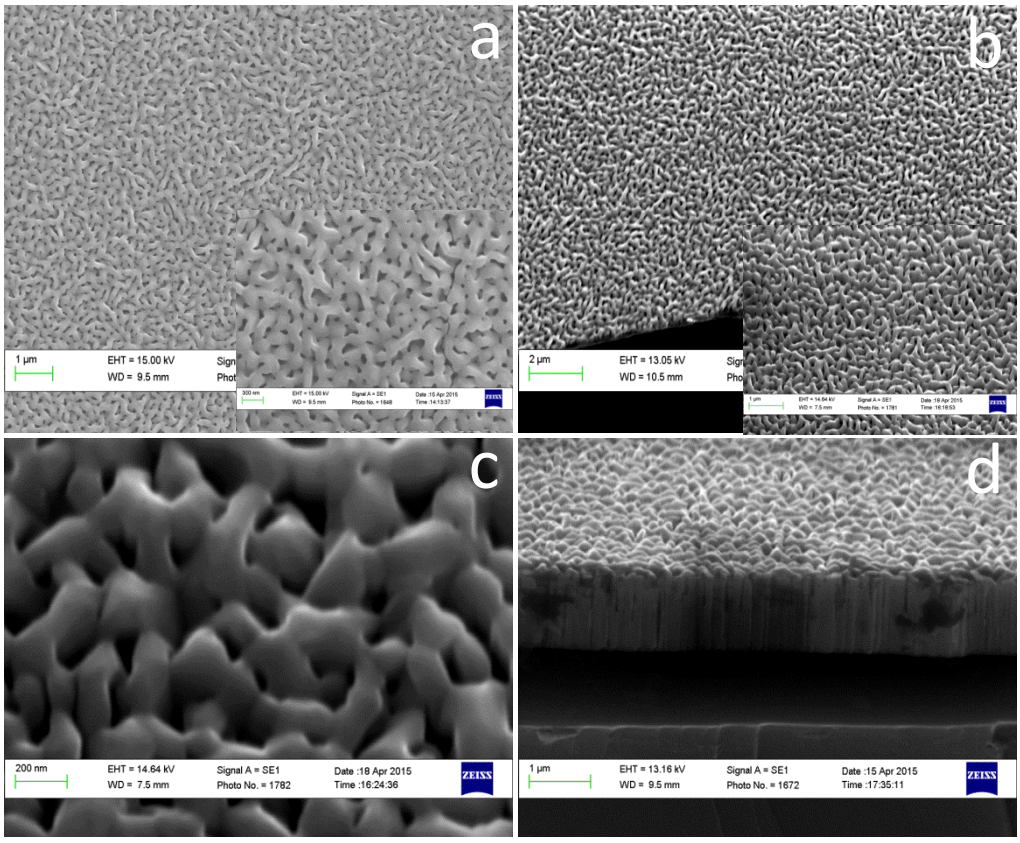

Figure 4.8: SEM images of the interconnected ZnO/ZnO core/shell nanorods grown by PLD at (a) 0º tilt (plane view), (b) 30º tilt, (c) an enlarged view of (b) at 30º tilt, and (d) 70º tilt angles. The insets of (a) and (b) showing enlarged views of the same images.

Greater details of the interconnected core/shell nanorods structure were revealed using TEM and HR-TEM. Regions of the samples containing hundreds of ZnO/ZnO core/shell interconnected nanorods were peeled off from the Si (100) substrate using a surgical blade and mounted on the 300 mesh size TEM grid for analysis. Figure 4.9 (a) and (c) show the TEM images, and (b) shows the HR-TEM images of the interconnected core/shell nanorods. The images (a), (b) and (c) show the crystalline (cr)-core/amorphous (am)-shell architectures of the interconnected nanorods. Figure 4.9 (b) further confirms this cr-ZnO/am-ZnO core/shell architecture of the interconnected nanorods by HR-TEM analyses, where high crystallinity behaviour in the core region and an amorphous nature in the shell region were observed.

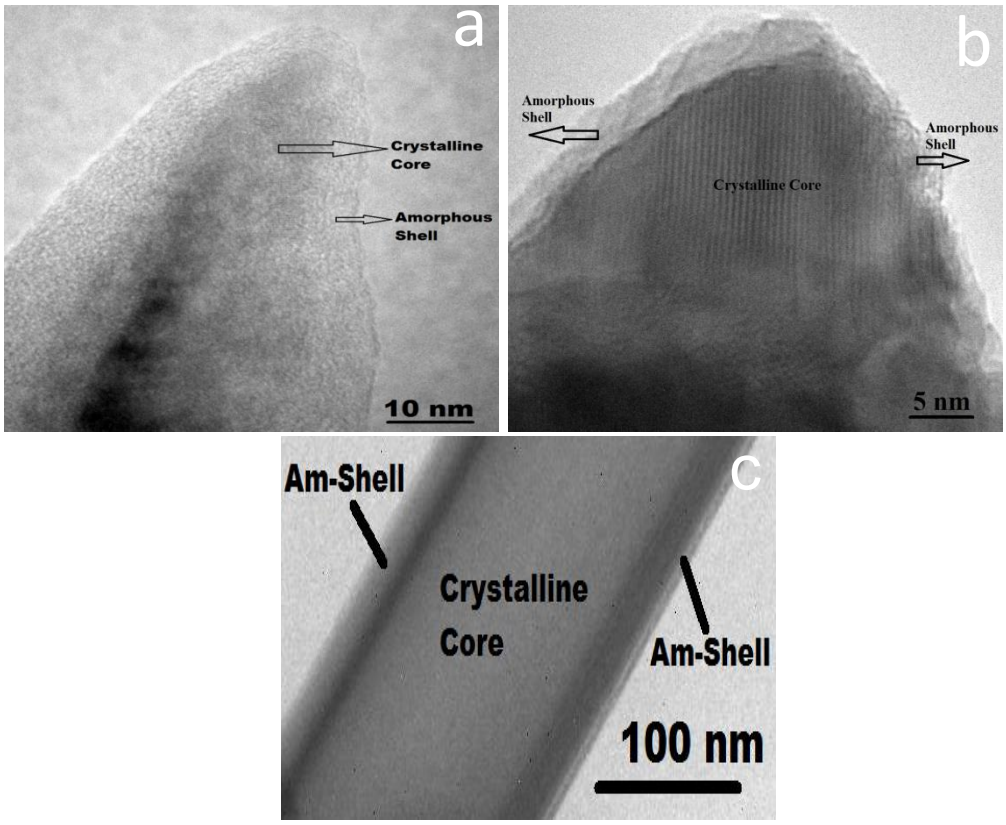

Figure 4.9: TEM and HR-TEM images of the interconnected cr-ZnO/am-ZnO core/shell nanorods grown by PLD; (a): TEM image of an interconnected core/shell nanorod at the top surface; (b): HR-TEM image showing crystalline core and amorphous shell architecture of a nanorod; (c): TEM image showing the core/shell architecture of the nanorod in a broader view at the middle of the nanorod.

The reasons for the cr-core and am-shell architecture were explained previously in terms of the heating and cooling sequences used in the nanorod growth. We believe that the laser energy (i.e. 110 mJ, but no change in spot size) used for growth of the interconnected core/shell nanorods plays an important role for this interconnection behaviour. Indeed, the previous studies of Wang et al. [52] have observed a significant effect of the laser energy on the nanorods morphology. In our work, we propose the following explanation for the observed interconnected morphology. As a decrease in laser energy reduces the kinetic energy of the ablated species, they will not have sufficient energy to find their correct lattice sites as soon as the heating has stopped. As a result, they will form ZnO material at random places, notably in between the nanorods, leading to the observed interconnected morphology. More detailed work, using TEM for example, is required to fully understand the interconnection behaviour.

4.2.2.3 Optical properties

The normalised low-temperature PL spectra for the interconnected cr-ZnO/am-ZnO core/shell nanorods show a free exciton (FE), surface exciton (SE) and a strong I_6 bound exciton (BX) line observed at 3.372 eV, 3.367 eV and 3.361 eV, respectively. Additionally, the emission at 3.331 eV is also seen identically to the previously reported (see section 4.1.2.3) cr-ZnO/am-ZnO core/shell nanorods. In our previous studies, reported in section 4.1 above and also in ref [1], we have investigated this 3.331 eV emission using HR-TEM, cryostat temperature and laser power dependent PL and we proposed that the origin of the 3.331 eV band is due to electron-hole recombination at structural defects associated with the core/shell boundary interface region. Since the interconnected cr-ZnO/am-ZnO core/shell nanorods reported in this section also show the same emission as well as a similar defective core/shell boundary interface region, these data further confirmed the origin of the 3.331 eV band (see Figure 4.9 and 4.10). In this section, we undertake further investigations on this emission by (i) thermal annealing of the deposited sample and (ii) Raman studies. The interconnected core/shell nanorod sample was placed in a quartz tube for the annealing at 500 °C. The duration for the annealing was about 1 hr in atmospheric air. The normalised low-temperature PL for the annealed sample was measured and the results show in Figure 4.10. This study reveals that the intensity of the 3.331 eV emission is slightly enhanced with

annealing, but that no major differences are observed with this level of annealing. It is unlikely that such low temperature anneals cause significant changes to the crystal structure of the deposit.

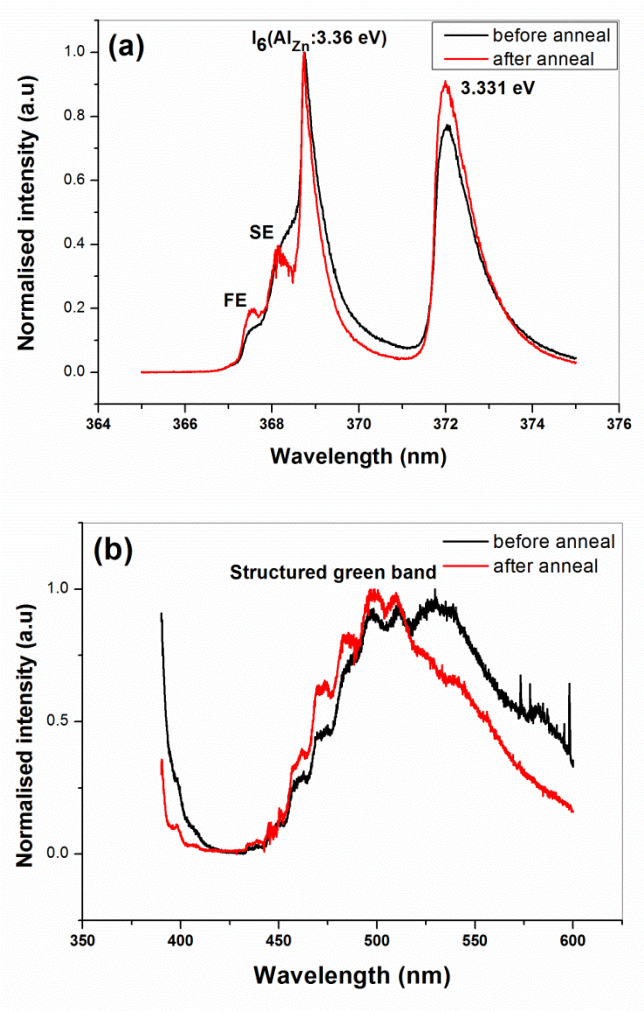

Figure 4.10: Normalised low temperature (13 K) PL spectra of the interconnected cr-ZnO/am-ZnO core/shell nanorods; (a): near band-edge region showing free exciton, surface exciton and 3.331 eV emission before anneal (black lines) and after anneal (red lines), and (b): visible region showing structured green band emission for before anneal (black lines) and after anneal (red lines).

In the visible region, the structured green band is seen in Figure 4.10 (b) indicating Cu impurities present in the ZnO nanorod samples. After the annealing, the intensity of structured green band is also slightly enhanced. We have also analysed the surface morphology of these annealed interconnected nanorods using SEM. These images are shown in Figure 4.11. These SEM images of annealed

nanorod samples show the same interconnected architecture as the previous (Figure 4.8). The totality of these data (XRD, SEM and PL) shows that thermal annealing has not affected significantly the structure, surface morphology and the luminescent properties of the interconnected nanorods.

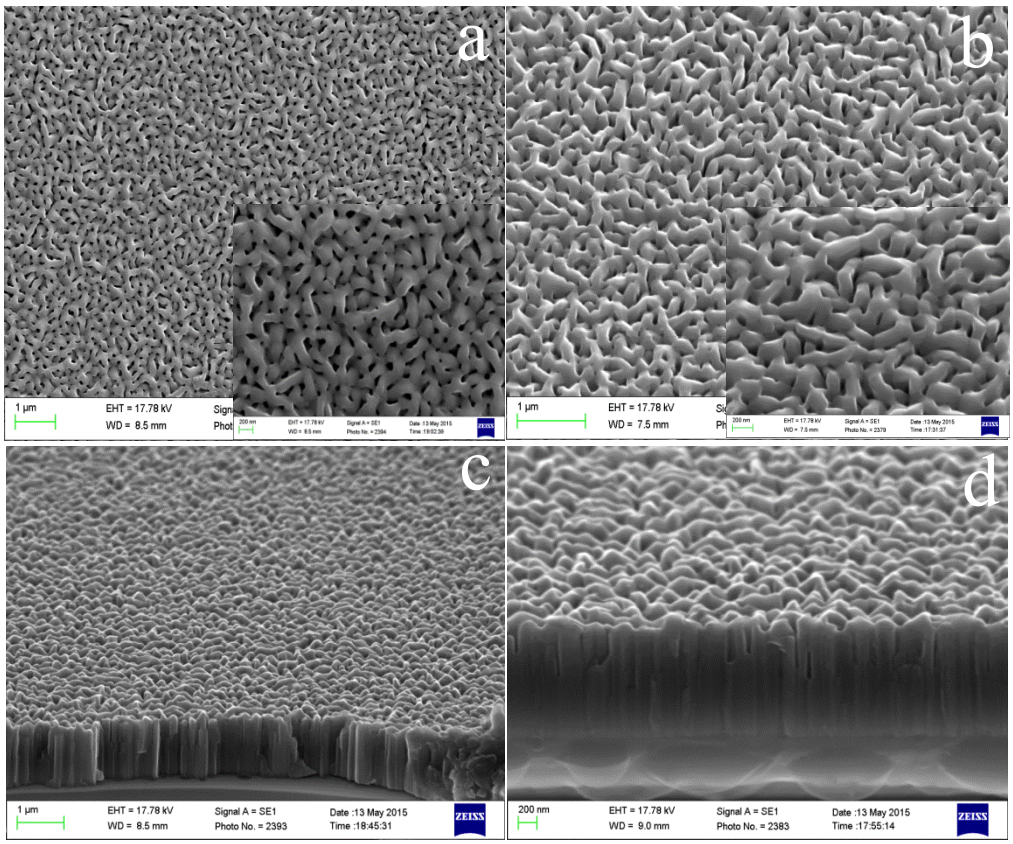

Figure 4.11: SEM morphology of the interconnected cr-ZnO/am-ZnO core/shell nanorods after annealing. a) 0º tilt (plane view), (b) 30º tilt, (c) and (d) 70º tilt angles. The insets of (a) and (b) showing enlarged views of the same images.

4.2.2.4 Raman scattering studies

Raman analyses of the interconnected cr-ZnO/am-ZnO core/shell nanorods (for both unannealed and annealed samples) were performed to obtain additional information on the samples. Calibration of the spectrometer was performed using a Silicon (100) standard sample with a strong Raman line at 520.07 cm^{-1} (Figure 4.12 (c)) and the laser spot size used was ~ 1 µm. Strong and sharp bands around 98 and 437 cm^{-1} were observed in the Raman spectra for both the unannealed and annealed nanorod samples (Figure 4.12 (a)). These bands are attributed to the non-polar E_2

vibrational modes corresponding to the wurtzite phase of ZnO [53-55]. The E_2 (low) mode is associated with the vibration of the heavy Zn sub-lattice, while the E_2 (high) mode involves mostly the oxygen atoms [56]. Additionally, two other weak lines, attributed to the A_1(TO) (~ 376 cm^{-1}) mode, which has polar symmetry, and the E_{2High}-E_{2Low} (~ 330 cm^{-1}) mode, a second order non-polar E_2 symmetry mode, were also observed [57,58].

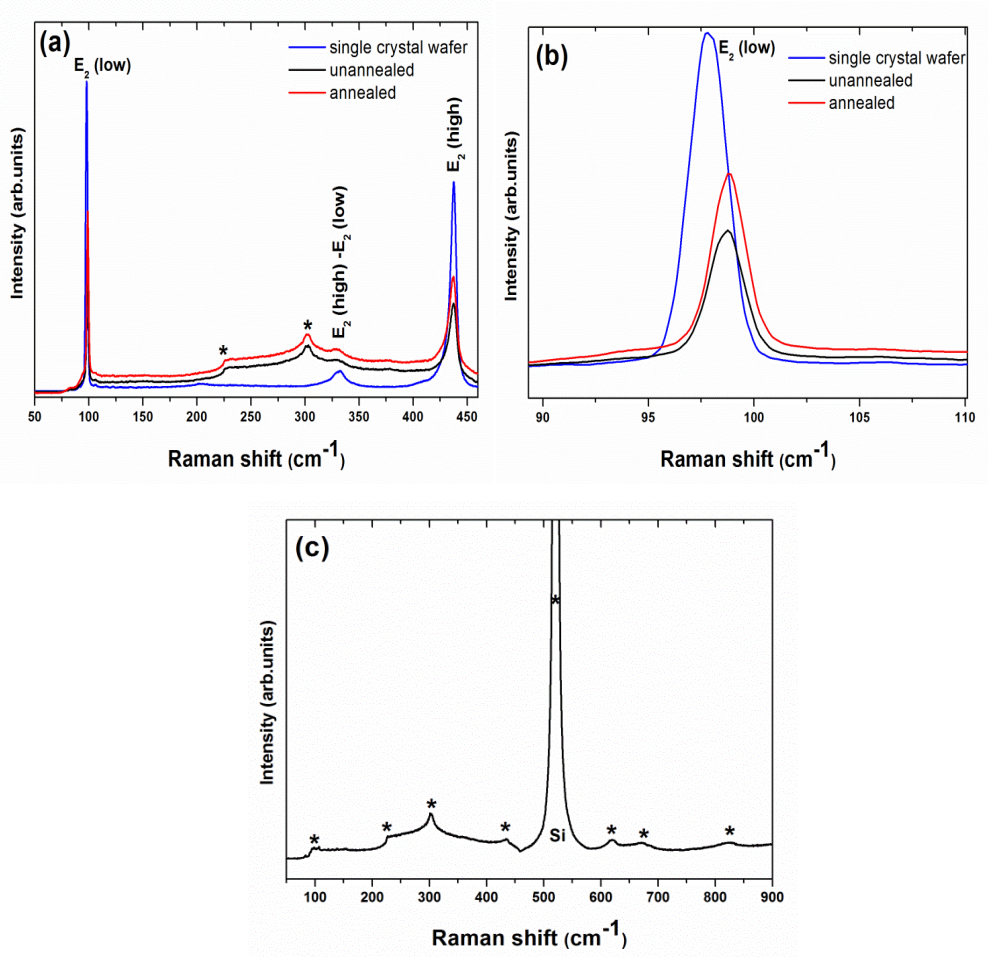

Figure 4.12: Raman spectra in a range 50-450 cm^{-1} for the (a) interconnected cr-ZnO/am-ZnO core/shell nanorods (unannealed sample-black lines and annealed sample-red lines) and a ZnO single crystal wafer (blue lines); (b) an enlarged view of E_2 (low) Raman band for the three samples; (c) Raman spectrum for Si standard sample, showing Si related strong and weak Raman bands in a range 50-900 cm^{-1} marked with '*' features.

For comparison purposes, we have also measured a Raman spectrum for a *c*-axis oriented ZnO single crystal wafer. In order to understand the stress in the interconnected nanorods sample, the E_2(high) mode of the sample was compared

with that of the wafer sample, as this mode is sensitive only to stress [59]. The FWHM and position of the E_2 (high) mode of both the samples were found by fitting using Lorentzian function. A slight red shift (0.5 cm^{-1}) (a clear view of the data is not shown) accompanied by an increase in the FWHM (from 6.1 cm^{-1} to 8.6 cm^{-1}) of the E_2 (high) band of the interconnected nanorods sample with respect to the bulk wafer was observed, which is attributed to the presence of tensile stress in the sample [59], consistent with the XRD data shown earlier. In addition to that a slight blue shift of E_2 (low) band of ~ 1 cm^{-1} was also observed for the nanorod samples compared with the single crystal wafer (Figure 4.12 (b)), which may attributed to the defects in the sample [60]. We note that the Raman data analyses are currently in progress. Overall, Raman studies confirm the wurtzite phase of the interconnected cr-ZnO/am-ZnO core/shell nanorods.

4.2.2.5 Electrical properties

Since our core/shell nanorods are interconnected, we have performed four point probe/Hall electrical measurements in order to investigate the electrical properties of this sample.

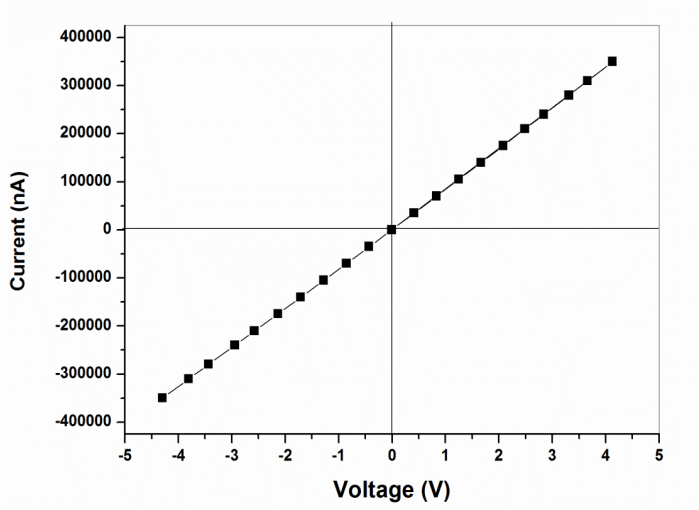

Figure 4.13: I-V curve for the *n*-type interconnected cr-ZnO/am-ZnO core/shell nanorods showing a good ohmic behaviour.

The linear behaviour of the I-V curve shows that the interconnected nanorods have ohmic behaviour. The resistivity, Hall mobility, and electron carrier

concentration of the nanorods were measured to be ~ 1.95 × 10^2 Ω cm, ~ 22 cm^2/V-s and ~ 2.14 ×10^{14} cm^{-3}. This large resistivity value can be expected for the nanorod morphology as observed by Lee et al. [61] for similar morphologies. The large resistivity value could also be explained in terms of high oxygen pressure (600 mTorr) used for the growth. If oxygen pressure is high (corresponding to less kinetic energy of the ablated species) during deposition, then it decreases the number of oxygen vacancies. This further allows decreasing the carrier concentration and hence increases the resistivity (see discussions in Chapter 5 for more details). We note that, after the annealing at 500 °C, the resistivity value was reduced to ~ 8.25×10^1 Ω cm (decreased by a factor of two), Hall mobility was reduced by a small amount to ~ 21 cm^2/V-s, and the carrier concentration was increased to 2.18×10^{15} cm^{-3}. The slight improvement in conductivity upon annealing could possible be correlated with a partial improvement of the crystallinity for those samples (see section 4.2.2.1).

4.2.3 Conclusions

We have grown, an interconnected architecture of crystalline ZnO/amorphous ZnO core/shell nanorods by catalyst-free PLD on ZnO seeded Si (100) substrates. XRD showed that these interconnected core/shell nanorods are well-aligned with *c*-axis orientation. The SEM images showed that the nanorods have interconnected architectures with a uniform morphology. The nanorods have conical terminations of rounded/blunt tips. TEM and HR-TEM studies revealed that these nanorods have crystalline ZnO/amorphous ZnO core/shell architectures. In terms of optical properties, the low-temperature PL showed the same emission at 3.331 eV seen in the PL spectra of the normal cr-ZnO/am-ZnO core/shell nanorods. The intensity of this emission was slightly enhanced after the thermal annealing at 500 °C, without a change of morphology. Raman studies showed the strong Raman bands at ~ 98 and 437 cm^{-1}, which are attributed to the non-polar E_2 vibrational modes corresponding to wurtzite ZnO. Electrical studies showed the *n*-type material with ohmic behaviour. The resistivity and Hall mobility values are ~ 1.95 × 10^2 Ω cm and ~ 22 cm^2/V-s, respectively. The conductivity was further partially improved for the annealed sample.

4.3 Origin of the 3.331 eV emission in ZnO nanorods: comparison of vapour phase transport and pulsed laser deposition grown nanorods

The utilisation of ZnO nanorods in optoelectronic devices is ultimately determined by the optical quality of the nanorods [62]. Thus, an understanding of the different optically-active defects which contribute to the near-UV band edge photoluminescence (PL) in ZnO and its nanostructures and the relationship of these defects to the nanostructure morphology is key to the choice of the optimum deposition methods and conditions for a particular application. In this work, we have grown ZnO nanorods by catalyst-free VPT and catalyst-free PLD, with the aim of further elucidating the origin of the 3.331 eV defect emission [1]. The near band edge PL spectra of the nanorods grown by either PLD or VPT show that the 3.331 eV emission is present in the former and completely absent in the latter. These data are considered together with SEM data and provide strong support for the assignment of the origin of the 3.331 eV emission to structural defects at the nanorod interface region.

4.3.1 Growth details

4.3.1.1 ZnO seed layer formation

ZnO seed layers were first prepared by PLD on Si (100) substrates for both the VPT and PLD nanorod depositions. Prior to deposition, Si substrates were cleaned by ultrasonication firstly in acetone and then in isopropanol for 15 min each. The details of the seed layer growth have been given in previous section 4.1.1.

4.3.1.2 VPT nanorod growth

ZnO nanorods were grown by VPT on these ZnO-seeded Si substrates at 900 °C using an Ar gas flow rate of 90 sccm for 1 hour. The temperature ramping of the furnace was varied between 25 and 50 °C/min until 900 °C. 60 mg of high purity graphite powder and 60 mg of ZnO powder were ground together for a few minutes until a homogeneous mixture was obtained. This mixture was then loaded and spread carefully over a 2 cm length in the middle of an alumina boat and the substrate suspended above it. This boat was then loaded into the furnace for the nanorod

growth [6,63]. Further details concerning the VPT growth process are discussed earlier in section 2.2.2.

4.3.1.3 PLD nanorod growth

ZnO nanorods were also grown by PLD on ZnO seeded Si substrates. Prior to nanorod deposition, the seed layers were annealed to 800 °C for 110 min. The ZnO nanorods were then grown at this substrate temperature in a 600 mTorr oxygen pressure using 40,000 laser shots for the deposition over a period of ~ 2 hrs. The details of the PLD nanorod growth are presented earlier in section 4.1.1.

4.3.2 Results and discussions

4.3.2.1 Structural properties

XRD data (2θ-ω scans) from PLD-grown ZnO seed layers, VPT-grown ZnO nanorods and PLD-grown ZnO nanorods in addition to data from a *c*-plane terminated ZnO single crystal wafer (Tokyo Denpa) of thickness 0.5 mm are shown in Fig 4.14. All the deposited material shows a dominant ZnO (002) reflection at 2θ ≈ 34.5º. Since the XRD data shown in Fig 4.14 is plotted on log scale, a weak ZnO (004) reflection was also observed at 2θ ≈ 72.80º in both the seed layer and nanorod samples (shown in the right hand side inset). No other ZnO-related diffraction peaks were observed, which indicates a high degree of texture (vertical orientation) for all the deposited materials. No other deposited material or crystalline phases were observed in the XRD data. A number of other reflections, due either to the Si substrates [64] or impurities in the x-ray tube, are indicated in the figure and explained in the figure caption.

As mentioned above, a ZnO single crystal wafer was also measured with the same apparatus and its ZnO (002) reflection was observed at 2θ ≈ 34.45º. The (002) reflection full width at half maximum (FWHM), *c*-axis lattice spacing and out-of-plane coherence length (crystallite size, from the Scherrer equation) were measured for the PLD-grown ZnO seed layer (0.225º, 0.520 nm and 35.30 nm, respectively), the VPT-grown ZnO nanorods (0.208º, 0.519 nm and 38.11 nm, respectively) and the PLD-grown ZnO nanorods (0.198°, 0.521 nm, and 75.31 nm, respectively). The crystallinity of the nanorods is improved compared to the seed layers. The value of *c*-axis lattice spacing for VPT- and/or PLD-grown ZnO nanorods is in excellent

agreement with the value determined from the data from the ZnO wafer (i.e. 0.521 nm).

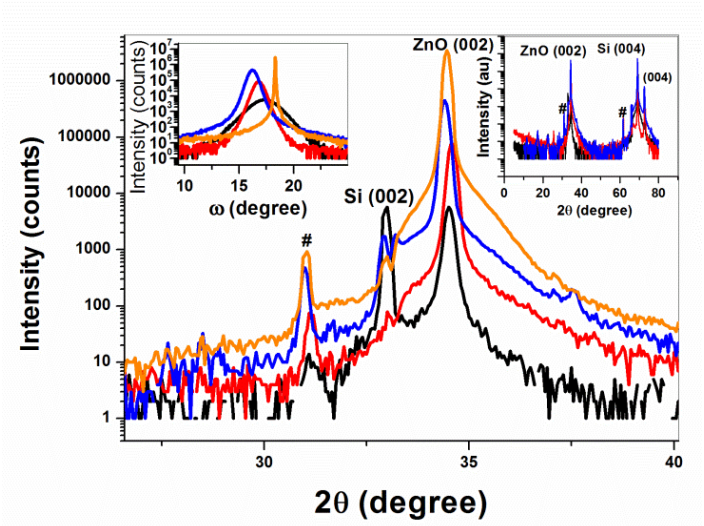

Figure 4.14: 2θ−ω XRD data for PLD-grown ZnO seed layers (black line), VPT-grown ZnO nanorods (red line), PLD-grown ZnO nanorods (blue line) and a ZnO wafer (orange line). The features marked with # are due to Cu K_β and tungsten L_α radiation from the X-ray tube, with the latter due to contamination. The left hand side inset shows the rocking curve (RC) data from the four samples around the ZnO (002) peak position. The right hand side inset shows the 2θ−ω data for the deposited samples over a broader 2θ angular range. Both insets use the same colours as in the main figure.

The left hand side inset of Fig 4.14 shows rocking curve (RC) data for the (002) reflection of the PLD-grown ZnO seed layers, VPT-grown ZnO nanorods, PLD-grown ZnO nanorods and the ZnO wafer. The FWHM of the RCs for the PLD-grown ZnO seed layers, VPT-grown ZnO nanorods and PLD-grown ZnO nanorods are 2.16º, 0.84º and 0.76º, respectively. We note that our FWHM value for the RC for VPT-ZnO nanorods is much smaller compared to reports of similar VPT-grown samples from Rajendra Kumar et al. and Li et al. who find FWHM values of ~ 2-2.8º and ~ 1.5º, respectively [6,65] and are comparable (albeit slightly larger than) the values for our PLD-grown ZnO nanorods. These data further indicate the highly textured nature (with *c*-axis orientation) of the nanorod deposits and the high crystalline quality of these materials.

4.3.2.2 Surface morphologies and nanostructuring

Figure 4.15 shows the morphologies of the PLD-grown ZnO seed layers (a), VPT-grown ZnO nanorods (b-d) and PLD-grown ZnO nanorods (e-f). The PLD-grown ZnO seed layer appears smooth and continuous. PLD-grown ZnO seed layers have been reported to be excellent substrates for the growth of high quality nanorods by Jie et al. [10] and Li et al. [65]. Fig 4.15(b) shows VPT-grown ZnO nanorods at a 30º tilt view while the inset shows a plan view of the same nanorods. Fig 4.15(c) shows a higher magnification view of the individual VPT-grown nanorod morphology at the same 30º tilt view while the Fig 4.15(d) shows a 70º tilt view of these nanorods. These data show that the VPT-grown nanorods have excellent *c*-axis orientation normal to the substrate surface, which correlates well with the XRD analysis discussed above.

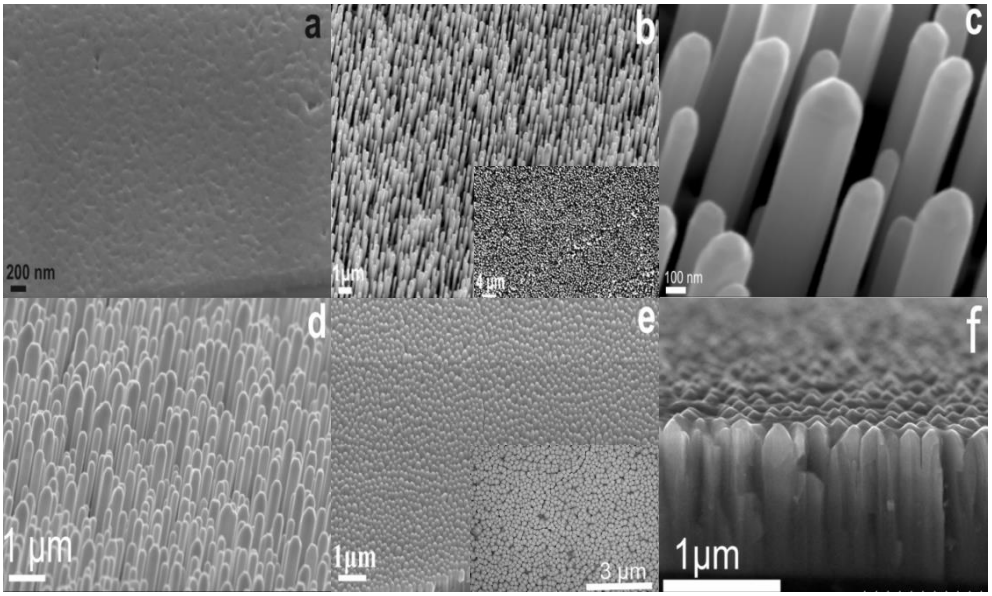

Figure 4.15: SEM data from the (a) PLD-grown ZnO seed layers at 30º tilt view, (b) VPT-grown ZnO nanorods at 30º tilt view, (c) an enlarged view of (b), and (d) the same VPT-grown ZnO nanorods at 70º tilt view, (e) PLD-grown ZnO nanorods at 30º tilt view, (f) the same PLD-grown ZnO nanorods at 80º tilt view. The inset of (b) shows a plan view of (b) with a smaller magnification scale while the inset of (e) shows a plan view of (e).

Figure 4.15(c) in particular shows that the VPT-grown nanorods are well separated (typically by some 100's of nm) and show smooth, facetted top and side surfaces, indicative of the underlying hexagonal crystalline symmetry. Previous

TEM studies [66-68] carried out in this laboratory of VPT grown ZnO nanorods have shown that VPT-grown nanorods synthesized under similar conditions have smooth surfaces and are crystalline throughout, consistent with the SEM data in Fig 4.15. SEM data from PLD-grown ZnO nanorods at 30º tilt view is shown in Fig 4.15(e) while the inset shows a top view of the same nanorods. Fig 4.15(f) shows an 85º tilt view of these PLD-grown ZnO nanorods. Although an identical PLD-grown ZnO seed layer was used for the growth of both VPT- and PLD-ZnO nanorods, the PLD-grown ZnO nanorods are very closely packed and the nanorod surfaces appear rougher (from a visual impression), which is likely due to both the underlying crystalline core/amorphous shell nature of these nanostructures, as revealed by previous TEM studies [1], as well as proximity effects from neighbouring nanorods contacting each other during growth. Again the data show that the PLD-grown nanorods have excellent *c*-axis orientation normal to the substrate surface.

The lengths and widths of the VPT-grown ZnO nanorods were extracted using 'Image J' software [69] and are in the range of 1.5 - 2 μm and ~ 175 - 200 nm, respectively. The same quantities for the PLD-grown ZnO nanorods are in the range of 0.9 - 1.2 μm and ~ 135 - 200 nm, respectively. The surface coverage density of the VPT-grown ZnO nanorods was measured to be ~ 18 per μm^2 (based on a count of ~ 75 nanorods in a 4 μm^2 region) and ~ 28 per μm^2 for the PLD-grown ZnO nanorods (based on a count of ~ 113 nanorods in a 4 μm^2 region). The density value for the VPT nanorod sample shows somewhat larger value than in previous works (8 per μm^2 and 12 per μm^2), e.g. [6,65].

4.3.2.3 Optical properties

Figure 4.16(a) shows the near band edge emission region for all the deposited samples, which is dominated by the I_6 bound exciton (BX) line at 3.36 eV in all cases, which is attributed to Al impurities, as well as the surface exciton (SE) and free excitons (FE) for the three samples, which can be seen in the inset of Fig 4.16(a). FWHM values of the I_6 BX for the PLD-grown ZnO seed layers, VPT-grown ZnO nanorods and PLD-grown ZnO nanorods are 2.062 meV, 1.994 meV and 1.437 meV, respectively indicating the high optical quality of these samples. Two electron satellite (TES) and longitudinal optical (LO) phonon replicas are normally observed in the highest optical quality materials and are located in the spectral region

~ 30-70 meV from the parent emissions. Such features are clearly seen for VPT-grown ZnO nanorods, we observe the TES of the I_6 line at 3.320 eV and its two LO replicas, TES 1LO and TES 2LO, at 3.251 eV and 3.182 eV, respectively. The LO replicas of the BX emission, such as BX-1LO, BX-2LO and BX-3LO are also clearly seen for the VPT-grown ZnO nanorods at 3.290 eV, 3.217 eV and 3.145 eV, respectively, and less clearly for the PLD-grown materials. The LO replicas in all cases are spaced ~ 72 meV apart, characteristic of the ZnO crystal. The PL intensity from the VPT-grown ZnO nanorods is much greater than both the PLD-grown ZnO seed layer and the PLD-grown nanorods in both the near band edge and visible spectral regions (the latter shown in Fig 4.16(b)).

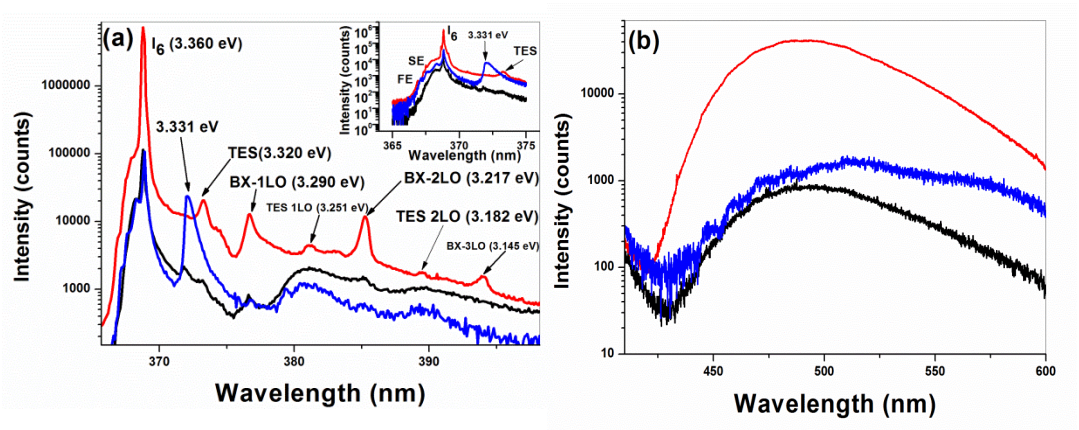

Figure 4.16: Low-temperature (13 K) PL spectra of PLD-grown ZnO seed layers (black lines), VPT-grown ZnO nanorods (red lines) and PLD-grown ZnO nanorods (blue lines): (a) near band edge region, (b) visible region. Inset of (a) shows magnified view of surface exciton (SE) and free exciton (FE) spectral region.

In the case of PLD-grown ZnO nanorods, a defect-related emission at 3.331 eV and its TES and LO replicas were also seen, as discussed in sections 4.1 and 4.2 above. These are not present in either the PLD-grown seed layer or the VPT-grown nanorod emissions. The intensity of the 3.331 eV emission is comparable to the BX emission in the same sample. The present study allows us to make comparisons with ZnO nanorod deposits grown by VPT, as well as with continuous ZnO film deposits. We assigned the origin of this spectral feature to structural defects at the nanorod interface region based on the data in section 4.1 and 4.2 above, and also in ref [1].

The present work adds considerable weight to this assignment since the feature is not seen in the continuous film deposited by PLD at similar temperatures, nor it is seen in the VPT-grown nanorods also deposited at similar temperatures. The latter are well separated and display smooth, facetted surfaces, indicative of a crystalline interface boundary. The emission is only seen from PLD-grown ZnO nanorods which are closely packed and whose surfaces appear rough and irregular due to the underlying core-shell architecture and proximity effects from neighbouring nanorods [1].

The totality of data from our present measurements allows us to confidently assign the 3.331 eV emission to recombination of electron-hole pairs localised at a range of structural defects with slightly different environments at the core/shell boundary region giving rise to a relatively large and asymmetric inhomogeneously broadened line. Our data show that the appearance of this feature is intimately linked to the presence of an inhomogeneous interface at a nanorod core/shell boundary region, and that the absence of interfaces (in continuous films such as the PLD-grown seed layer) or their replacement by smooth, facetted ones (in the VPT-grown sample) leads to the complete disappearance of this feature.

4.3.3 Conclusions

We have successfully grown ZnO nanorods by both VPT and PLD on PLD-grown ZnO seed layers and have studied their structural, morphological and luminescent properties as well as that of the underlying PLD-grown ZnO seed layers. XRD studies show that the VPT-grown and PLD-grown ZnO nanorods, as well as the PLD-grown seed layers are highly textured with *c*-axis orientation normal to the substrate plane. SEM images confirm this and further show that the VPT-grown ZnO nanorods are well separated with the nanorods spaced by distances of 100's nm, with smoothly facetted top and side surfaces while PLD-grown ZnO nanorods are densely packed and show rough surfaces by comparison. Low temperature PL from all samples shows a dominant I_6 BX line, along with SE and FE emission in the near band edge region, while the VPT-grown nanorods clearly show TES and TES LO phonon replicas as well as LO replicas of the I_6 BX. These data reflect the high optical quality of the deposited materials, in particular for the case of VPT-grown

ZnO nanorods. In the near band edge spectrum from PLD-grown ZnO nanorods, a defect related emission was observed at 3.331 eV, which was not seen for either the PLD-grown seed layer or VPT-grown nanorod samples. Overall, the present report allows us to confidently assign the 3.331 eV emission to recombination at structural defects at the core/shell boundary region, and shows that the presence of an inhomogeneous interface at a nanorod core/shell boundary is crucial to the observation of this emission feature. Hence, the present work contributes to the understanding of the different optically-active defects related to the near-UV band edge photoluminescence (PL) in ZnO nanostructures and the relationship of these defects to the nanostructure morphology, which is crucial to the choice of the optimum growth parameters when targeting a particular application.

4.4 References

[1] S. Inguva, S.K. Marka, R.K. Vijayaraghavan, E. McGlynn, Vadali V. S. S. Srikanth, J.-P. Mosnier, Crystalline ZnO/amorphous ZnO core/shell nanorods: Self-organized growth, structure and novel luminescence, *J. Phys. Chem. C* 119 (2015) 4848-4855.

[2] C.F. Klingshirn, B.K. Meyer, A. Waag, A. Hoffmann, J. Geurts, In *Zinc Oxide-From Fundamental Properties Towards Novel Applications;* R. Hull, C. Jagadish, R. M. Osgood, J. Parisi, Z. Wang, H. Warlimount, Eds.; Springer: Berlin, 120 (2010) Chapter 3, pp 66-67.

[3] L.C. Tien, S.J. Pearton, D.P. Norton, F. Ren, Synthesis and microstructure of vertically aligned ZnO nanowires grown by high-pressure-assisted pulsed-laser deposition, *J. Mater. Sci.* 43 (2008) 6925-6932.

[4] M. Willander, O. Nur, Q.X. Zhao, L.L. Yang, M. Lorenz, B.Q. Cao, J.Z. Perez, C. Czekalla, G. Zimmermann, M. Grundmann, A. Bakin, A. Behrends, M. Al-Suleiman, A. El-Shaer, A.C. Mofor, B. Postels, A. Waag, N. Boukos, A. Travlos, H.S. Kwack, J. Guinard, D.L.S. Dang, Zinc oxide nanorod based photonic devices: recent progress in growth, light emitting diodes and lasers, *Nanotechnology* 20 (2009) 332001.

[5] R. Eason, Ed.; *Pulsed Laser Deposition of Thin films: Applications-led growth of Functional Materials;* Wiley: Hoboken, NJ, (2007) Chapter 8, pp 177-180 and Chapter 12, pp 268-282.

[6] R.T. Rajendra Kumar, E. McGlynn, C. McLoughlin, S. Chakrabarti, R.C. Smith, J.D. Carey, J.P. Mosnier, M.O. Henry, Control of ZnO nanorod array density by Zn supersaturation variation and effects on field emission, *Nanotechnology* 18 (2007) 215704.

[7] E. McCarthy, R.T. Rajendra Kumar, B. Doggett, S. Chakrabarti, R.J. O'Haire, S.B. Newcomb, J.P. Mosnier, M.O. Henry, E. McGlynn, Effects of the crystallite mosaic spread on integrated peak intensities in 2 theta-omega measurements of highly crystallographically textured ZnO thin films, *J. Phys. D: Appl. Phys*. 44 (2011) 375401.

[8] W. Wan, L. Zhu, L. Hu, G. Chen, W. Mi, Z. Ye, Investigation of morphology evolution of Cu-ZnO nanorod arrays and enhancement of ferromagnetism by codoping with N, *Phys. Lett. A* 378 (2014) 2763-2767.

[9] V.D. Mote, Y. Purushotham, B. N. Dole, Williamson-Hall Analysis in Estimation of Laticce Strain in Nanometer-Sized ZnO Particles, *J. Theor. Appl. Phys.* 6 (2012) 1-8.

[10] J. Jie, G. Wang, Y. Chen, X. Han, Q. Wang, B. Xu, J. Hou, Synthesis and optical properties of well-aligned ZnO nanorod array on an undoped ZnO film, *Appl. Phys. Lett.* 86 (2005) 031909.

[11] R. Teki, T.C. Parker, H. Li, N. Koratkar, T. Lu, S. Lee, Low temperature synthesis of single crystalline ZnO nanorods by oblique angle deposition. *Thin Solid Films* 516 (2008) 4993-4996.

[12] H. Morkoç, Ü. Özgür, In *Zinc Oxide-Fundamentals, Materials and Device Technology;* Wiley-VCH: Germany, (2009) Chapter-1 and 2.

[13] M. Wang, C. Huang, Y. Cao, Q. Yu, W. Guo, Q. Huang, Y. Liu, Z. Huang, J. Huang, H. Wang, Z. Deng, The effects of shell characteristics on the current-voltage behaviors of dye-sensitized solar cells based on ZnO/TiO_2 core/shell arrays, *Appl. Phys. Lett.* 94 (2009) 263506.

[14] P. Yang, X. Xiao, Y. Li, Y. Ding, P. Qiang, X. Tan, W. Mai, Z. Lin, W. Wu, T. Li, H. Jin, P. Liu, J. Zhou, C.P. Wong, Z.L. Wang, Hydrogenated ZnO Core-Shell Nanocables for Flexible Supercapacitors and Self-Powered Systems, *ACS Nano* 7 (2013) 2617-2626.

[15] X. Xia, J. Tu, Y. Zhang, X. Wang, C. Gu, X. Zhao, H.J. Fan, High-Quality Metal Oxide Core/Shell Nanowire Arrays on Conductive Substrates for Electrochemical Energy Storage, *ACS Nano* 6 (2012) 5531-5538.

[16] Z. Wang, R. Guo, G. Li, L. Ding, Y. Ou, Y. Tong, Controllable synthesis of ZnO-based core/shell nanorods and core/shell nanotubes, *RSC Adv.* 1 (2011) 48-51.

[17] H. Zhou, H. Alves, D. Hofmann, W. Kriegseis, B. Meyer, G. Kaczmarczyk, A. Hoffmann, Behind the weak excitonic emission of ZnO quantum dots: ZnO/$Zn(OH)_2$ core-shell structure, *Appl. Phys. Lett.* 80 (2002) 210-212.

[18] S.Z. Li, C.L. Gan, H. Cai, C.L. Yuan, J. Guo, P.S. Lee, J. Ma, Enhanced photoluminescence of ZnO/Er_2O_3 core-shell structure nanorods synthesized by pulsed laser deposition, *Appl. Phys. Lett.* **2007**, *90*, 263106.

[19] A. Djurisic, Y. Leung, K. Tam, L. Ding, W. Ge, H. Chen, S. Gwo, Green, yellow, and orange defect emission from ZnO nanostructures: Influence of excitation wavelength, *Appl. Phys. Lett.* 88 (2006) 103107.

[20] W. Liu, S. Gu, J. Ye, S. Zhu, S. Liu, X. Zhou, R. Zhang, Y. Shi, Y. Zheng, Y. Hang, C. Zhang, Blue-yellow ZnO homostructural light-emitting diode realized by metalorganic chemical vapor deposition technique, *Appl. Phys. Lett.* 88 (2006) 092101.

[21] D.C. Look, B. Claflin, Y. Alivov, S. Park, The future of ZnO light emitters, *phys. stat. sol. A* 201 (2004) 2203-2212.

[22] M. Schirra, R. Schneider, A. Reiser, G.M. Prinz, M. Feneberg, J. Biskupek, U. Kaiser, C.E. Krill, K. Thonke, R. Sauer, Stacking fault related 3.31-eV luminescence at 130-meV acceptors in zinc oxide, *Phys. Rev. B* 77 (2008) 125215.

[23] M.R. Wagner, G. Callsen, J.S. Reparaz, J.-H. Schulze, R. Kirste, M. Cobet, I. A. Ostapenko, S. Rodt, C. Nenstiel, M. Kaiser, A. Hoffmann, A.V. Rodina, M.R. Phillips, S. Lautenschlaeger, S. Eisermann, B.K. Meyer, Bound excitons in ZnO: Structural defect complexes versus shallow impurity centers, *Phys. Rev. B* 84 (2011) 035313.

[24] K. Johnston, M.O. Henry, D. McCabe, E. McGlynn, M. Dietrich, E. Alves, M. Xia, Identification of donor-related impurities in ZnO using photoluminescence and radiotracer techniques, *Phys. Rev. B* 73 (2006) 165212.

[25] H. Alves, D. Pfisterer, A. Zeuner, T. Riemann, J. Christen, D.M. Hofmann, B.K. Meyer, Optical investigations on excitons bound to impurities and dislocations in ZnO, *Opt. Mater.* 23 (2003) 33-37.

[26] J.G. Reynolds, C.L. Reynolds Jr., A. Mohanta, J.F. Muth, J.E. Rowe, H.O. Everitt, D.E. Aspnes, Shallow acceptor complexes in p-type ZnO, *Appl. Phys. Lett.* 102 (2013) 152114.

[27] M. Lange, J. Zippel, G. Benndorf, C. Czekalla, H. Hochmuth, M. Lorenz, M. Grundmann, Temperature dependence of localization effects of excitons in $ZnO/Cd_xZn_{1-x}O/ZnO$ double heterostructures, *J. Vac. Sci. Technol. B* 27 (2009) 1741-1745.

[28] L. Schneider, S. V. Zaitsev, G. Bacher, W. Jin and M. Winterer, Recombination dynamics in ZnO nanoparticles produced by chemical vapor synthesis, *J. Appl. Phys.* 102 (2007) 023524.

[29] V. Khranovskyy, R. Minikayev, S. Trushkin, G. Lashkarev, V. Lazorenko, U. Grossnerc, W. Paszkowiczb, A. Suchocki, B. G. Svensson, R. Yakimov, Improvement of ZnO thin film properties by application of ZnO buffer layers, *J. Cryst. Growth* 308 (2007) 93-98.

[30] F. Li, L. Wang, J. Dai, Y. Pu, W. Fang, F. Jiang, Photoluminescence observations of hydrogen incorporation and outdiffusion in ZnO thin films, *J. Luminescence* 124 (2007) 162-166.

[31] J. S. Park, S. K. Hong, T. Minegishi, I. H. Im, S. H. Park, T. Hanada, J. H. Chang, M. W. Cho, T. Yao, The high quality ZnO growth on c-Al_2O_3 substrate with Cr_2O_3 buffer layer using plasma-assisted molecular beam epitaxy, *Appl. Surf. Sci.* 254 (2008) 7786-7789.

[32] J. S. Park, J. H. Chang, T. Minegishi, H. J. Lee, S.H. Park, I. H. Im, T. Handa, S. K. Hong, M. W. Cho, T. Yao, Growth of Polarity-Controlled ZnO Films on (0001) Al_2O_3, *J. Electron. Mater.* 37 (2008) 736-742.

[33] A. N. Gruzintsev, A. N. Red'kin, E. E. Yakimov, C. Barthou, Edge Luminescence of ZnO Nanorods on High-Intensity Optical Excitation, *Semiconductors* 42 (2008) 1092-1097.

[34] J. W. Sun, Y. M. Lu, Y. C. Liu, D. Z. Shen, Z. Z. Zhang, B. H. Li, J. Y. Zhang, B.Yao, D. X. Zhao, X. W. Fan, Excitonic electroluminescence from ZnO-based heterojunction light emitting diodes, *J. Phys. D: Appl. Phys.* 41 (2008) 155103.

[35] T. Voss,C. Bekeny, J. Gutowski, R. Tena-Zaera, J. Elias, C. Lévy-Clément, I. Mora-Seró, J. Bisquert, Localized versus delocalized states: Photoluminescence from electrochemically synthesized ZnO nanowires, *J. Appl. Phys.* 106 (2009) 054304.

[36] J. K. Dangbegnon, K. Talla, K. T. Roro, J. R. Botha, Metalorganic chemical vapor deposition of ZnO:N using NO as dopant, *Physica B* 404 (2009) 4419-4421.

[37] S. S. Kurbanov, Kh. T. Igamberdiev, T. W. Kang, The UV-laser induced heating effect on photoluminescence from ZnO nanocrystals deposited on different

substrates, *J. Phys. D: Appl. Phys.* 43 (2010) 115401.

[38] S. K. Goswami, B. W. Lee, E. Oh, M. S. Islam, Effect of Precursors on Optical and Structural Properties of ZnO Nanorods Synthesized by Sonochemical Method, *J. Korean Physical Society* 59 (2011) 2313-2317.

[39] K. Johnston, J. Cullen, M. O. Henry, E. McGlynn, M. Stachura, Evidence for As lattice location and Ge bound exciton luminescence in ZnO implanted with ^{73}As and ^{73}Ge, *Phys. Rev. B* 83 (2011) 125205.

[40] S. Yang, C. C. Kuo, W.-R. Liu, B. H. Lin, H.-C. Hsu, C.-H. Hsu, W. F. Hsieh, Photoluminescence associated with basal stacking faults in c-plane ZnO epitaxial film grown by atomic layer deposition, *Appl. Phys. Lett.* 100 (2012) 101907.

[41] V. Sh. Yalishev, Y. S. Kim, X. L. Deng, B. H. Park, Sh. U. Yuldashev, Study of the photoluminescence emission line at 3.33 eV in ZnO films, *J. Appl. Phys.* 112 (2012) 013528.

[42] S. Guillemin, V. Consonni, B. Masenelli, G. Bremond, Extended-Defect-Related Photoluminescence Line at 3.33 eV in Nanostructured ZnO Thin Films, *Appl. Phys. Express* 6 (2013) 111101.

[43] B.K. Meyer, H. Alves, D.M. Hofmann, W. Kriegseis, D. Forster, F. Bertram, J. Christen, A. Hoffmann, M. Strassburg, M. Dworzak, U. Haboeck, A. Rodina, Bound exciton and donor-acceptor pair recombinations in ZnO, *phys. stat. sol. B* 241 (2004) 231-260.

[44] A. Schildknecht, R. Sauer, K. Thonke, Donor-related defect states in ZnO substrate material, *Physica B:Condens.Matter.* 340 (2003) 205-209.

[45] D. Byrne, F. Herklotz, M.O. Henry, E. McGlynn, Unambiguous identification of the role of a single Cu atom in the ZnO structured green band, *J. Phys.:Condens. Matter.* 24 (2012) 215802.

[46] P. X. Gao, C. S. Lao, W. L. Hughes, Z. L. Wang, Three-dimensional interconnected nanowire networks of ZnO, *Chem. Phys. Lett.* 408 (2005) 174-178.

[47] M. Breedon, M. B. Rahmani, S. -H. Keshmiri, W. Wlodarski, K. Kalantar-zadeh, Aqueous synthesis of interconnected ZnO nanowires using spray pyrolysis deposited seed layers, *Mater. Lett.* 64 (2010) 291-294.

[48] N. Yua, D. Deng, D. Yang, Y. Wang, T. Yang, ZnO interconnected network nanostructures grown on cracked GaN by the aqueous solution method, *J. Alloy. Compd.* 505 (2010) L27-L30.

[49] Z. Yin, N. Chen, R. Dai, L. Liu, X. Zhang, X. Wang, J. Wu, C. Chai, on the formation of well-aligned ZnO nanowalls networks by catalyst-free thermal evaporation method, *J. Cryst. Growth* 305 (2007) 296-301.

[50] M. B. Rahmani, M. Breedon, D. Lau, J. L. Campbell, A. Moafi, D. G. McCulloch, W. Wlodarski, K. Kalantar-Zadeh, Gas sensing properties of Interconnected ZnO nanowires, *Sensor Lett.* 9 (2011) 929-935.

[51] K. S. Ranjith, R. Geethu, K. P. Vijayakumar, R. T. Rajendrakumar, Control of interconnected ZnO nanowires to vertically aligned ZnO nanorod arrays by tailoring the underlying spray deposited ZnO seed layer, *Mater. Res. Bull.* 60 (2014) 584-588.

[52] Y. Wang, PhD thesis on "Self-Assembled Nanorods and Nanowires from Oxide Functional Materials Grown by Pulsed Laser Deposition", University of Birmingham, UK, 2014, pp. 169-181.

[53] V. Gupta, P. Bhattacharya, Yu. I. Yuzuk, K. Sreenivas, R.S. Katiyar, Optical phonon modes in ZnO nanorods on Si prepared by pulsed laser deposition, *J. Cryst. Growth* 287 (2006) 39-43.

[54] D. Polsongkram, P. Chamninok, S. Pukird, L. Chow, O. Lupan, G. Chai, H. Khallaf, S. Park, A. Schulte, Effect of synthesis conditions on the growth of ZnO nanorods via hydrothermal method, *Physica B* 403 (2008) 3713-3717.

[55] L. Liao, H. B. Lu, J. C. Li, H. He, D. F. Wang, D. J. Fu, and C. Liu, W. F. Zhang, Size Dependence of Gas Sensitivity of ZnO Nanorods, *J. Phys. Chem. C* 111 (2007) 1900-1903.

[56] Ü. Özgür, Ya. I. Alivov, C. Liu, A. Teke, M. A. Reshchikov, S. Doğan, V. Avrutin, S.-J. Cho, H. Morkoç, A comprehensive review of ZnO materials and devices, *J. Appl. Phys.* 98 (2005) 041301.

[57] K. A. Alim, V. A. Fonoberov, A. A. Balandin, Origin of the optical phonon frequency shifts in ZnO quantum dots, *Appl. Phys. Lett.* 86 (2005) 053103.

[58] L. -L. Xing, C. -H. Ma, Z. -H. Chen, Y. -J. Chen, X. -Y. Xue, High gas sensing performance of one-step-synthesized Pd–ZnO nanoflowers due to surface reactions and modifications, *Nanotechnology* 22 (2011) 215501.

[59] A. -J. Cheng, Y. Tzeng, H. Xu, S. Alur, Y. Wang, M. Park, T. -h. Wu, C. Shannon, D. -J. Kim, D. Wang, Raman analysis of longitudinal optical phonon-plasmon coupled modes of aligned ZnO nanorods, *J. Appl. Phys.* 105 (2009) 073104.

[60] N. Rana, S. Chand, A. K. Gathania, Band gap engineering of ZnO by doping with Mg, *Phys. Scr.* 90 (2015) 085502.

[61] J.H. Lee, C.-Y. Chou, Z. Bi, C.-F. Tsai, H. Wang, Growth-controlled surface roughness in Al-doped ZnO as transparent conducting oxide, Nanotechnology 20 (2009) 395704.

[62] A.B. Djurisic, A.M.C. Ng, X.Y. Chen, ZnO nanostructures for optoelectronics: Material properties and device applications, *Prog. Quant. Electron.* 34 (2010) 191-259.

[63] D. Byrne, E. McGlynn, J. Cullen, M.O. Henry, A catalyst-free and facile route to periodically ordered and c-axis aligned ZnO nanorod arrays on diverse substrates, *Nanoscale* 3 (2011) 1675-1682.

[64] B.-H. Hwang, Calculation and measurement of all (002) multiple diffraction peaks from a (001) silicon wafer, *J. Phys. D: Appl. Phys.* 34 (2001) 2469-2474.

[65] C. Li, G. Fang, J. Li, L. Ai, B. Dong, X. Zhao, Effect of seed layer on structural properties of ZnO nanorod arrays grown by vapor-phase transport, *J. Phys. Chem. C* 112 (2008) 990-995.

[66] C. Li, G. Fang, Q. Fu, F. Su, G. Li, X. Wu, X. Zhao, Effect of substrate temperature on the growth and photoluminescence properties of vertically aligned ZnO nanostructures, *J. Cryst. Growth.* 292 (2006) 19-25.

[67] D. Zhao, C. Andreazza, P. Andreazza, J. Ma, Y. Liu, D. Shen, Buffer layer effect on ZnO nanorods growth alignment, *Chem. Phys. lett.* 408 (2005) 335-338.

[68] D. Byrne, R.F. Allah, T. Ben, D.G. Robledo, B. Twamley, M.O. Henry, E. McGlynn, Study of Morphological and Related Properties of Aligned Zinc Oxide Nanorods Grown by Vapor Phase Transport on Chemical Bath Deposited Buffer Layers, *Cryst. Growth Des.* 11 (2011) 5378-5386.

[69] C.A. Schneider, W.S. Rasband, K.W. Eliceiri, NIH Image to Image J: 25 years of image analysis, *Nat. Methods* 9 (2012) 671-675.

Chapter 5

ZnO and AZO Nanocrystalline Thin Films on Flexible Zeonor Plastic Substrates

In this chapter, we present the properties of high quality ZnO and AZO nanostructured films deposited on flexible Zeonor plastic substrates. On Zeonor substrates, we systematically study the effects of oxygen growth pressure in a selected pressure range (1-300 mTorr) on the growth rate, surface morphology, hydrophobicity and the structural, optical and electrical properties of films having different thicknesses. We divide the pressure range into two regions: The high oxygen growth pressure region (75-300 mTorr) and low oxygen growth pressure region (1-75 mTorr). We note that the pressure range explored should correspond with observable changes in the film properties as it is in the range where nanostructuring should occur.

5.1 High oxygen growth pressures: 75-300 mTorr

The ZnO and AZO thin films were grown by room temperature PLD. We now recall briefly the aspects of ZnO thin film formation relevant to the present work. PLD growth of ZnO thin film is typically carried out in an ambient oxygen pressure, the value of which largely determines the prevalent growth mode, e.g. layer-by-layer. In the 1 –75/100 mTorr (~ 0.1 –7.5/10 Pa) range continuous thin film growth occurs, while upward of 100's mTorr (> 50 Pa) so-called high-pressure PLD-, film nanostructuring [1] is generally observed with concomitant changes in the microstructure and optoelectronic properties. Such pressure-dependent studies were carried out by Zhu et al. [2] and Gondoni et al. [3,4] using the PLD of ZnO and AZO on glass and sapphire substrates, respectively. During film growth (at a given ambient pressure), the polar ZnO material will undergo significant lattice re-organisation due to defect formation and defect/atomic diffusion, formation of a depletion layer, crystal grain formation and densification. These effects will be reflected in the variations of the film properties with film thickness. For example, Zhu et al. [5] studied the change of the crystallinity, microstructure and surface morphology of ZnO thin films of various thicknesses prepared by PLD on glass; while Guillen and Herrero [6] conducted a similar study for AZO films of various thicknesses deposited on glass at room temperature by DC sputtering. Finally, all growth parameters being equal, comparison of the properties of ZnO and AZO films will tell the specific effects of doping by aluminium substitution on the zinc lattice sites [7].

Based on these considerations, the aims of the present work [8] were to: (i) Use PLD to grow reproducible, high-quality ZnO and AZO thin films on flexible plastic Zeonor substrates at room temperature. (ii) Reveal the dependency of the growth rates, the microstructure and the surface, structural, optical and electrical properties of ZnO and AZO thin films of different thickness on the oxygen ambient pressure. In the rest of this section, we provide the necessary experimental details. We then present and discuss the results on thin film properties and associated deposition ambient/oxygen pressure and film thickness trends. Also, we have broadly reviewed the literature relevant to this work. Finally, we propose applications suitable for the range of film properties obtained in the work.

5.1.1 Growth details

All the films were grown in a standard PLD apparatus equipped with a high-power, Q-switched, frequency-quadrupled, Nd:YAG laser. The laser specifications and growth parameters are mentioned earlier in Chapter 2.2. Sheets of 1.2 mm thick 1060R Zeonor [9] cut into 1 cm × 2 cm rectangles were used as substrate. A gentle clean of the bare substrate surfaces with isopropyl alcohol was applied and then dried with nitrogen gas. The Zeonor substrates were mounted and kept at the deposition chamber base pressure of 3×10^{-5} mTorr (3.9×10^{-6} Pa) for about an hour prior to deposition. Growths were carried out in ambient oxygen (deposition) pressures of 75 mTorr (10 Pa), 150 mTorr (20 Pa) and 300 mTorr (40 Pa). From previous literature, see ref. [1] and references therein, in this relatively wide range of deposition pressures, the film growth should span over the transition from 2D layer-by-layer to 3D nanostructuring modes. All the growths were carried out at room temperature (RT) and all the samples characterised as-grown, without post-growth high temperature anneal. The details of the growth parameters of the samples produced in this work are given in Table 5.1.

Film thickness was measured using a Dektak profilometer. Surface morphology was studied by atomic force microscopy (AFM) in tapping mode. The AFM images were acquired by scanning areas of dimensions 5 μm × 5 μm with a fixed resolution of 512 pixels × 512 pixels. The AFM measurements were repeated several times at three randomly chosen locations of every sample with no remarkable differences found between these locations. The water contact angle (WCA) was measured with the help of a computer-controlled WCA commercial instrument implementing the sessile drop technique. In all the WCA experiments, high-purity HPLC grade water was used and released at a flow rate of 1.5 μL/s from a needle tip 2 mm above the film surface. The quoted WCA values are the average of typically ten measurements on different locations over the surface of the sample and the error bars represent the corresponding standard deviations. Structural characteristics were investigated by x-ray diffraction (XRD) using 2θ-ω and pole figure scans, respectively. Optical transmittance spectra were measured using a double-beam UV-vis spectrophotometer, while low-temperature photoluminescence spectra were recorded with a 1 m focal length monochromator following a 325 nm He-Cd laser

excitation. Electrical properties were measured with a commercial 4-point probe/Hall effect apparatus. The experimental uncertainties or statistical errors associated with all these measurements are recorded, where possible, as error bars on the relevant tables and graphs shown in the following.

	Sam-ple label	No. of laser shots	Oxygen pressure (mTorr)	Thickness ±error (nm)	2θ (deg)	*c*-parameter (nm)	FWHM (deg)	Resistivity (10^3 × Ω cm)
ZnO	Z1	5000	75	85±10	34.25	0.5238	0.39	462
	Z2	10000	75	169±22	34.27	0.5235	0.42	17
	Z3	20000	75	340±18	34.34	0.5225	0.44	452
	Z4	5000	150	92±23	34.21	0.5244	0.38	0.15
	Z5	10000	150	190±37	34.23	0.5240	0.41	0.49
	Z6	20000	150	382±74	34.24	0.5240	0.43	17
	Z7	5000	300	97±23	34.21	0.5243	0.38	0.83
	Z8	10000	300	209±43	34.27	0.5235	0.41	22
	Z9	20000	300	422±6	34.26	0.5236	0.41	1.8
AZO	A1	5000	75	67±17	34.34	0.5224	0.52	0.49
	A2	10000	75	131±13	34.40	0.5216	0.52	2.0
	A3	20000	75	263±28	34.45	0.5208	0.49	2.1
	A4	5000	150	74±23	34.40	0.5216	0.49	0.39
	A5	10000	150	140±10	34.48	0.5204	0.49	0.97
	A6	20000	150	289±7	34.46	0.5207	0.46	0.75
	A7	5000	300	86±26	34.48	0.5204	0.70	6.9
	A8	10000	300	199±54	34.48	0.5204	0.66	11
	A9	20000	300	415±4	34.52	0.5198	0.64	21

Table 5.1: Experimental parameters (number of laser shots and oxygen growth pressure) used for the pulsed-laser deposition of ZnO and AZO films on Zeonor substrates. The resulting thickness, 2θ angular position, FWHM of the (002) Bragg reflection, value of the *c*-axis length and resistivity are given for each film. "Z" indicates ZnO films and "A" indicates AZO films.

5.1.2 Results and discussions

5.1.2.1 Thickness measurements and growth rate studies

From Table 5.1, we see that the range of film thicknesses considered in this work is 74–422 nm. Thus, all the films are optically thin and quantum confinement effects are not expected to play any role in the physics underlying their properties. Fig 5.1 shows the variations of the ZnO and AZO films thickness with the number of laser shots for the three oxygen deposition pressures of 75, 150 and 300 mTorr. For all the samples and growth conditions used, film thickness closely fits a linear

function of the number of laser shots (correlation coefficient (R) ~ 1 for the six graphs of Fig 5.1). From the laser repetition rate of 10 Hz and the slope of each plot, the growth rates are obtained with minimum and maximum values of 0.13 nm/s and 0.22 nm/s respectively.

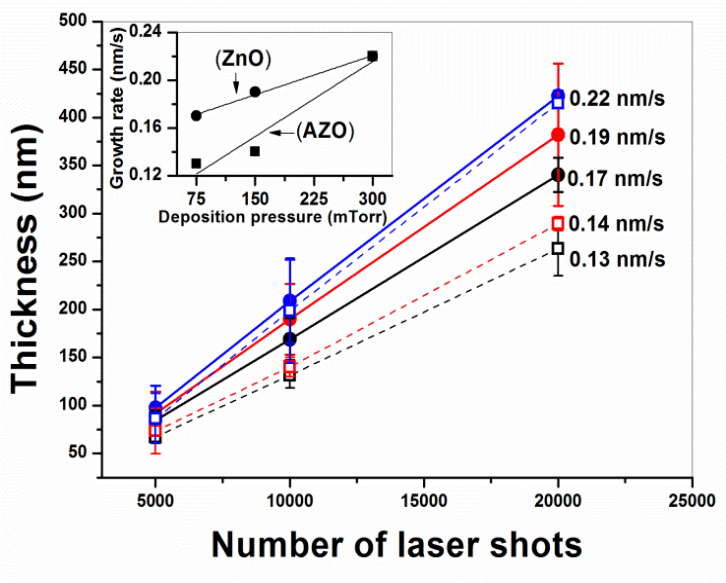

Figure 5.1: Thickness of ZnO (closed symbols, solid lines) and AZO (open symbols, broken lines) thin films, grown by pulsed-laser deposition, on Zeonor substrates as a function of the number of laser shots (repetition rate 10 Hz) for oxygen ambient pressures of 75 (black), 150 (red) and 300 mTorr (blue). The inset shows the corresponding ZnO and AZO film growth rates (nm/s) as a function of oxygen pressure (mTorr).

From the inset of Fig 5.1, where the growth rates are plotted as a function of deposition pressure, we see that the ZnO and AZO film growth rates increase linearly with increasing oxygen deposition pressure at the rates of 2.2×10^{-3} nm/s/10 mTorr and 4.2×10^{-3} nm/s/10 mTorr, respectively. The growth rates have equalised at 300 mTorr oxygen pressure while the AZO growth rate is about 25% lower than that of ZnO for the lower pressures. The lower growth rates for AZO can be explained by a very high chemical affinity of aluminium with oxygen, which reduces their growth rate. From these observations showing linear dependences, we can conclude that similar growth mechanisms leading to optically thin (compared with the wavelength of light) ZnO and AZO films prevail in the range of experimental parameters notably the 75 – 300 mTorr pressure range used. The consistency of growth rates shows that

the thin films of ZnO and AZO can be reproduced when grown on Zeonor substrates by PLD.

5.1.2.2 Surface morphology studies

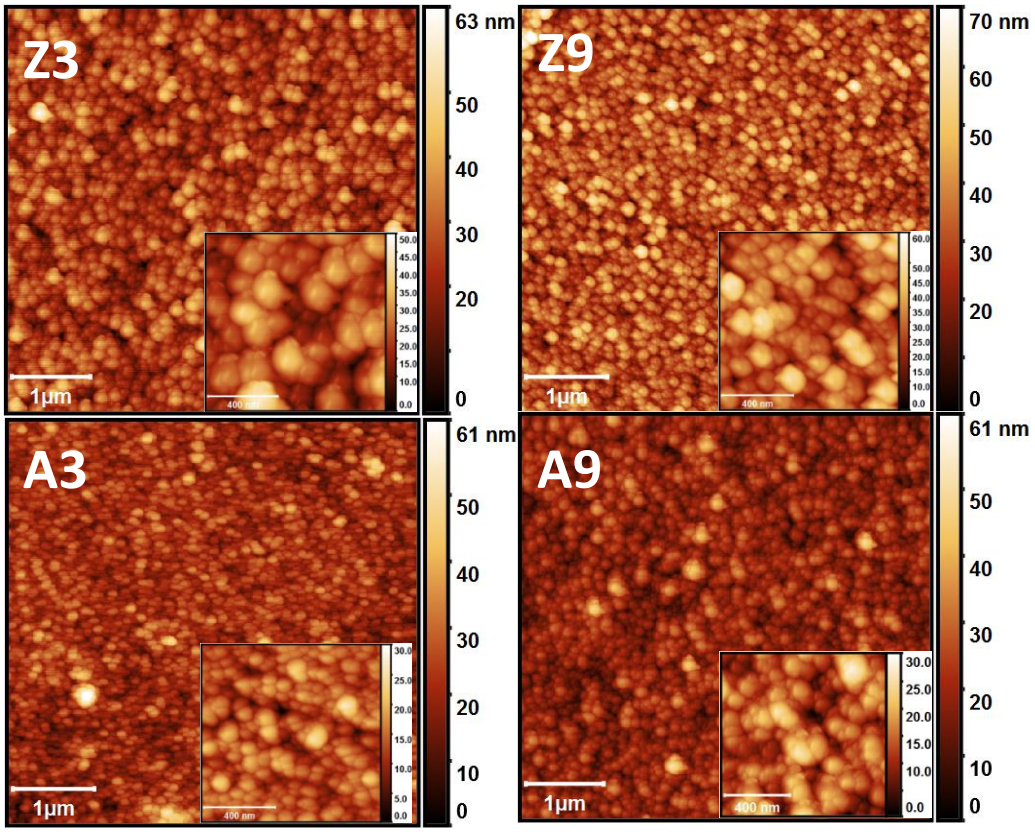

Figure 5.2: AFM images showing the typical surface topography of a selection of ZnO (upper row) and AZO (lower row) films obtained in this work (samples Z3, Z9, A3 and A9). The films were grown by PLD on Zeonor substrates using 20,000 laser shots at ambient oxygen pressures of 75 mTorr (left-hand column) and 300 mTorr (right-hand column). The insets show the same surfaces on a more magnified scale to reveal the finer details of the nanostructured grains. All the scale bars in the insets are 400 nm.

Fig 5.2 shows AFM images of the surface of the thickest ZnO (Z3 and Z9) and AZO (A3 and A9) samples as typical examples. The insets of Fig 5.2 show that the ZnO and AZO films present similar microstructures, for the two growth pressures of 75 and 300 mTorr, in the form of nanostructured, pea-shaped, grains with typical lateral sizes in the range 50 – 200 nm. Similar nanostructured ZnO deposits have been observed in comparable PLD experiments by many authors [10-

13] and also in the laser ablation of silicon [14]. The underlying physical mechanisms have been explained for ZnO in the works of Okada and Kawashima [10] and Hartanto et al. [11]. In short, ZnO nano-clusters of various sizes are initially condensed in the expanding ablation plume and transported to and captured on the substrate. If the substrate is cold and amorphous, as is the case in our work, the nanoparticles have very limited surface diffusion and crystal growth is minimal. The next ablation plume will then build up another patchy layer of similarly shaped nanoparticles and so on. In the case of a high-temperature (and possibly crystalline) substrate, the initial nanoclusters will diffuse rapidly forming a wetting nucleation layer onto which crystalline ZnO nanorods can subsequently grow in a 3D growth mode [13,15]. Relevant to the present work are the fundamental aspects of the synthesis of silicon nanoclusters by conventional PLD discussed by Marine et al. [14] and the work by Jensen [16] on the growth of nanostructures by cluster deposition. From our low-oxygen pressure study (see section 5.2 below), we can conclude that, all other conditions being equal, the transition to 2D film growth on Zeonor substrate will occur at oxygen pressures lower than 75 mTorr. Overall, the AFM observations and their analyses are consistent with the conclusion, drawn at the end of the previous section, of a similar growth mechanism in the investigated pressure range. On the micrometer length scale (main parts of Fig 5.2), no particular organization of the nanostructures can be distinguished and they appear randomly distributed over the observed surface area. All the films surfaces were found to be identically smooth, devoid of cracks, fracture lines or delaminations.

We have estimated the values of the average nanostructure lateral grain size and root mean square (rms) roughness R_q for every sample with the help of imaging processing software (WSXM). The results are plotted in Fig 5.3. The AFM grain sizes typically range from 75 nm (ZnO) – 90 nm (AZO) for the thinner films to values of 180 nm (ZnO) – 140 nm (AZO) for the thicker films. They are also seen to increase in almost linear fashion with increasing film thickness. The grain size data for the ZnO films show a weak dependency on the oxygen pressure with a pattern of lower pressures producing larger nanostructure grain sizes in films of roughly equal thickness being discernable. Whereas, the AZO grain size values appear almost insensitive to the oxygen pressure within the 75 – 300 mTorr range. The ZnO films show a wider dispersion of grain sizes with varying ambient pressure and, on the

whole, nanostructure grain sizes are larger by a few 10's of nm for the ZnO films at equal pressure compared with AZO films.

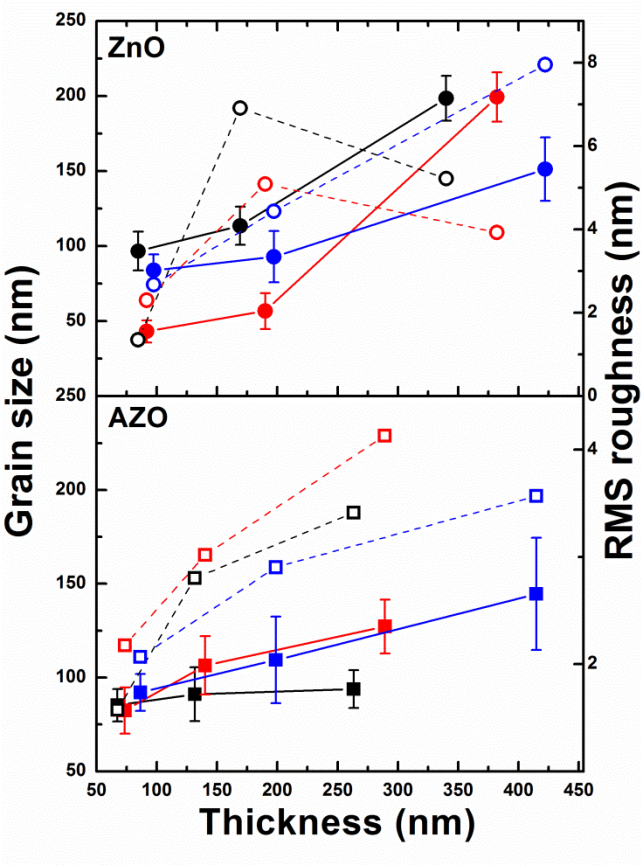

Figure 5.3: Grain size (closed symbols, solid lines) and rms roughness R_q (open symbols, dashed lines) as a function of film thickness for ZnO and AZO thin films deposited by pulsed-laser on Zeonor substrates at ambient oxygen pressures of 75 (black), 150 (red) and 300 mTorr (blue).

Overall the data of Fig 5.3 show that the ZnO film morphology results from interplay between ambient pressure and film thickness effects. According to the growth model presented earlier, for thicker films, the ZnO nanoparticles deposited at a later stage will be captured by a nanostructured ZnO film allowing for better nanocrystal growth leading to larger grains at the lower pressure of 75 mTorr. For AZO, the role of the aluminium dopant in the film growth and lattice reconstruction seems significant to the extent that it appears to shadow the role of the oxygen pressure in the range used. Our experimental observations on grain sizes are generally comparable with previous works on ZnO and AZO nanostructured films deposited on COP and other plastic substrates, e.g. [17,18,19]. The RT PLD work of

Gondoni et al. [3,4], in particular, showing that AZO growth on glass becomes granular for oxygen pressures greater than 10 Pa (77 mTorr) supports our findings and the basic model of nanocluster plume formation.

The rms (R_q) surface roughness of the films is represented on the right vertical axes of Fig 5.3 with different scales for ZnO and AZO. Overall, the trends are similar for the ZnO and AZO films and follow the linear behaviour observed for the nanostructure grain size. The thinner films have R_q values of 1-2 nm, while for the thicker films this is in the range 4-8 nm with the bare Zeonor 1060R surface measured at 0.5 nm [20]. Therefore, all the films are optically smooth* for near-normal incidence illumination. Overall, the surface rms roughness increases close to linearly with oxygen pressure for both the ZnO and AZO films. AZO films of comparable thickness have very similar surface roughness, irrespective of the oxygen pressure, while for ZnO films they are more dispersed. Overall, the ZnO films appear to be rougher by several nm compared with the AZO films in the pressure range used in the work. This is consistent with our observations on grain size as discussed above. The rms surface roughness values of typically a few nanometers reported here compare favourably with those reported in the quoted previous works [2,6,17,18,19]. In particular, we have retrieved the observations by Zhu et al. of an increase in ZnO film rms roughness with an increase in both the oxygen pressure [2] and the film thickness [5]. We have pointed out the importance of a smooth surface for reliable device performance and enhanced lifetime. For example, Han et al. [21] have successfully fabricated AZO TFT's on PET substrates quoting a rms roughness of 1.36 nm, while Connolly et al. [22] have reported the successful deposition of ZnO films on Perspex flexible substrates with a rms roughness of 2.2 nm for use as electrodes in a biofuel cell. The typical roughness of ~ 2 nm for the ZnO and AZO thinner films produced here would thus seem advantageous for similar devices fabricated on flexible Zeonor substrates.

*According to Rayleigh criterion: $d < \lambda/(8\cos\theta)$, where d is surface roughness (rms), λ is incident illumination wavelength, and θ is angle of incidence of the illumination.

5.1.2.3 Water contact angle (WCA) studies

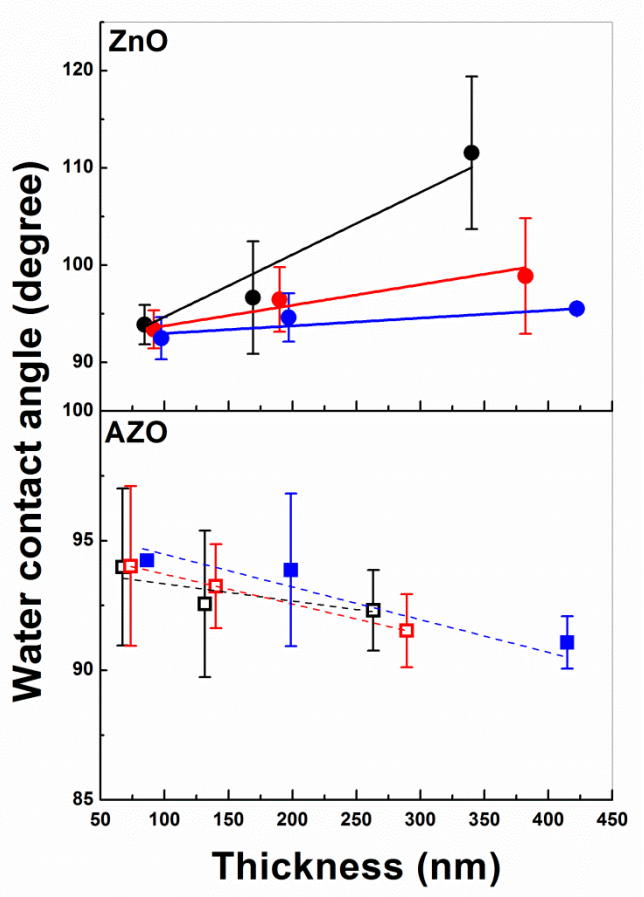

Figure 5.4: Water contact angle as a function of film thickness for ZnO and AZO thin films deposited by pulsed-laser on Zeonor substrates at ambient oxygen pressures of 75 (black), 150 (red) and 300 mTorr (blue).

The wettability of the nanostructured ZnO and AZO thin films was assessed from the variation of the water contact angle (WCA) value with film thickness as shown in Fig 5.4. The size of some of the error bars in this figure reflects the large variations of several degrees which were occasionally found between successive measurements on the same sample. This is compatible with the high sensitivity of the ZnO surface wettability on both exposure to near ultraviolet radiation [23] and chemical contamination [24]. A WCA of 92.0° has been measured for the bare 1060R Zeonor surface, which is therefore hydrophobic [9,20]. Overall, it is seen that the main effect of ZnO and AZO thin film deposition is to increase the hydrophobicity of the Zeonor surface. However, the ZnO and AZO films show

marked differences in this regard when considering the thickness and pressure dependences. For the ZnO films, it is seen that the WCA increases with thickness at all pressures, but the rate of increase is inversely proportional to the oxygen pressure. Indeed, for a 75 mTorr deposition pressure, the ZnO WCA is seen to increase to a maximum value of about 110° for the 340 nm film, while it increases only to about 95° for the 422 nm film deposited at 300 mTorr. For the AZO films, the general trend is a slight decrease of the WCA as a function of film thickness, from about 94° to slightly less than 92° and almost within the error bar, while there appears to be little sensitivity of this decrease on the ambient oxygen pressure. The WCA data of Fig 5.4 can be correlated with the microstructure data of Fig 5.3. The larger WCA values for the thicker ZnO films correspond with the larger nanostructure sizes and rms surface roughnesses observed at the 75 mTorr pressure while the aforementioned lack of sensitivity of the rms roughness on the film thickness and deposition pressure is also seen in the WCA trends for AZO. This is indicative of a lower surface energy for the rougher surfaces which, thus, exhibit larger contact angles [25]. The present results confirm the work of Subedi et al. [26] showing a WCA greater for ZnO than for AZO films and that of Sun et al. [23] reporting the dependence of the ZnO surface wettability on its surface morphology.

5.1.2.4 Structural properties

Fig 5.5 shows the out-of-plane 2θ-ω xrd angular scans measured in the 2θ ≈ 32º-38º range for all the ZnO and AZO samples. All these scans showed a single dominant (002) peak with a weak (101) peak appearing for some of the AZO samples. More extended angular scans also include the broad Zeonor substrate peak at 2θ ≈ 16º as shown in the inset (Z3 sample). These data show that all the ZnO and AZO thin films deposited on Zeonor substrates by PLD have the wurtzite crystalline structure and are highly textured with *c*-axis orientation, i.e. the hexagonal (002) plane (basal plane) lies parallel to the plane of the substrate. The AZO material has a more polycrystalline structure in the thicker films with some grains showing the (101) plane (facet) lying parallel to the substrate plane. It is observed from Fig 5.5 that the (002) peaks are more intense and narrower for ZnO than AZO films of comparable thickness.

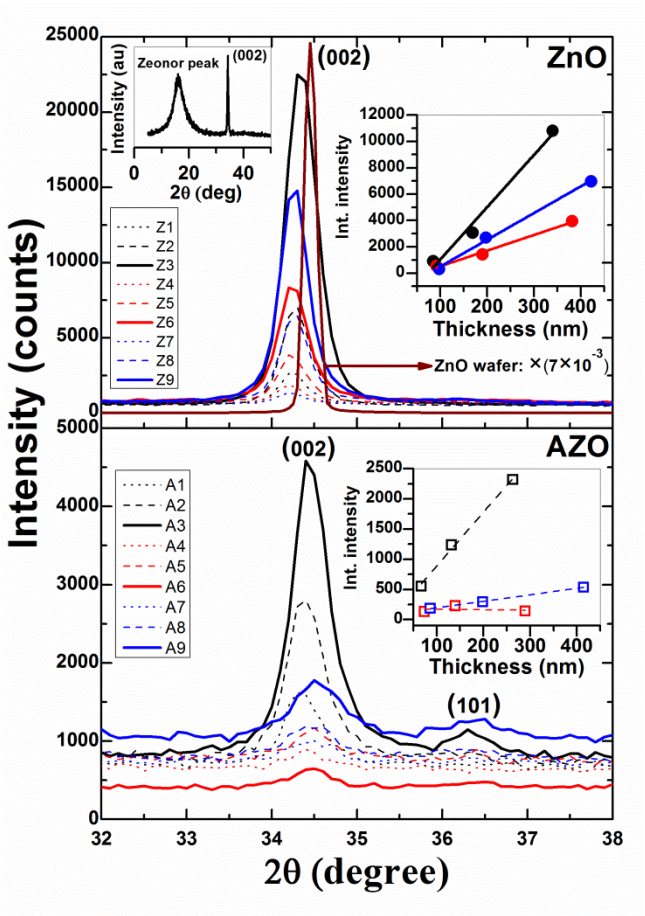

Figure 5.5: 2θ-ω XRD scans for ZnO and AZO thin films deposited by pulsed-laser on Zeonor substrates with 5000 (dotted lines), 10000 (dashed lines) and 20000 (solid lines) laser shots at ambient oxygen pressures of 75 (black), 150 (red) and 300 mTorr (blue). The insets show: (top left) an extended angular range including the amorphous Zeonor diffraction and wurtzite ZnO (002) diffraction peaks; (top and bottom right) the integrated intensities of the (002) peaks as a function of film thickness for the various oxygen pressures used in this work.

In order to establish the effect of oxygen pressure on crystalline quality, the integrated intensity of the (002) peaks was plotted as a function of film thickness for the various growth pressures used in this work. The plots are shown in the insets of Fig 5.5 with added linear trend lines: The effect of pressure on crystalline quality can be assessed by reading the graph along a vertical line of constant film thickness. It is seen that for both the ZnO and AZO films crystalline quality is significantly better at the oxygen pressure of 75 mTorr, while for the AZO films crystalline quality appears less sensitive to oxygen pressure being almost pressure-independent at 150 and 300

mTorr. This is also true for both the ZnO and AZO films of thickness less than or equal to 100 nm. From Fig 5.3 (AFM data), we note that for these films the lateral grain size is of the same order as the thickness. Thus, the films crystalline structure is likely to be initially dominated by the unfavourable interface between the cold amorphous Zeonor surface and the ZnO and AZO nanocrystals. Further film growth atop ZnO or AZO material will then favour better lattice reconstruction minimising surface energy by favouring *c*-axis orientation. This accounts for the general increase of crystalline quality with thickness seen in the inset of Fig 5.5. For AZO, the point defects introduced by the aluminium dopant will also play a role in this regard as the thickness increases (see pole figure data below). The complete set of data of Fig 5.5 points to the enhanced crystalline quality of the ZnO material compared to the AZO material in films grown on thin amorphous Zeonor plastic substrates at room temperature.

(a) Crystallite size studies

The 2θ angular position and full width at half maximum (FWHM) of the (002) peak as well as the *c*-axis length are given in Table 5.1 for all the samples. For reference, we have also measured a *c*-axis oriented ZnO single-crystal wafer of thickness 0.5 mm (Tokyo Denpa) with the same apparatus (shown in Fig 5.5 with scaled down intensity). The measured 2θ value for this wafer sample is about 34.45º. We use the (002) peak FWHM values and 2θ angular positions to estimate the samples crystallite size and residual stress, respectively, The average crystallite size (D) can be calculated [27] using Scherrer equation $D = \frac{0.9\lambda}{\beta_{hkl}\cos\theta_B}$, where λ = 0.15425 nm is the wavelength of the Cu K_α line, θ_B is the Bragg angle and $\beta_{hkl} = \sqrt{\left(\beta_{hkl}^{meas}\right)^2 - \left(\beta_{hkl}^{instr}\right)^2}$ is the 2θ FWHM of the ZnO (002) peak after removal of the instrumental broadening assuming Gaussian line profiles. The instrumental contribution is estimated from the value of the 2θ FWHM for the (002) peak of the single-crystalline ZnO wafer measured at 0.167º. This assumes an essentially infinite "crystallite" size for the ZnO wafer sample. The corresponding graphs are shown in Fig 5.6 from which we see that crystallite sizes are in the ranges 20 – 25 nm and 12 – 18 nm for the ZnO and AZO films, respectively. Overall, the larger D values observed for the ZnO samples are further evidence of the better crystalline quality of

the ZnO compared to the AZO material. The small variations of *D* observed with oxygen pressure and sample thickness in the measured ranges appear not significant being roughly within or just outside of the error bars (relative error of about 5% on *D* for the strongest peak of Fig 5.5).

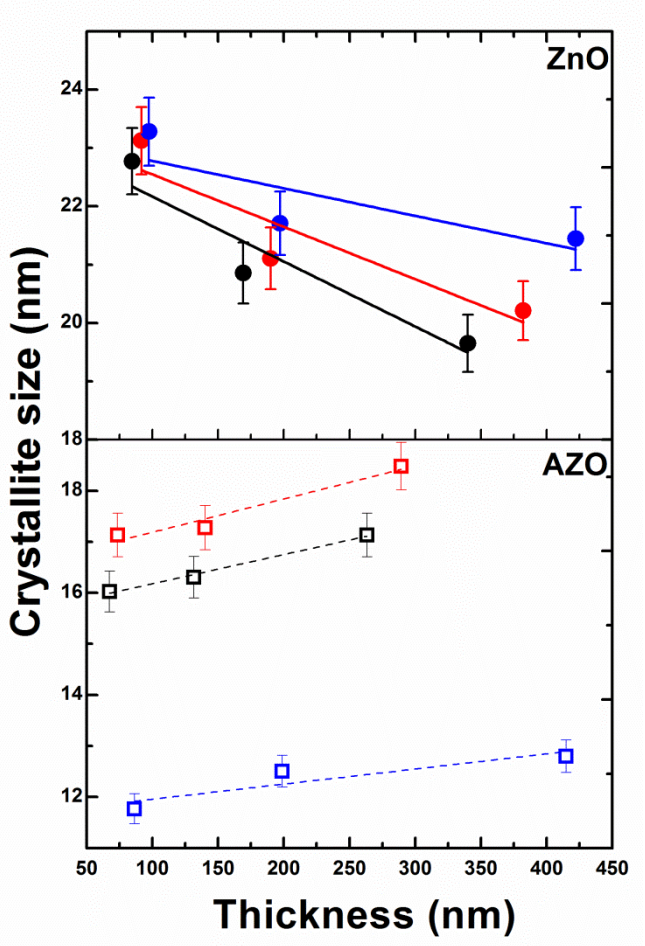

Figure 5.6: Crystallite size as a function of film thickness for ZnO and AZO thin films deposited by pulsed-laser on Zeonor substrates at ambient oxygen pressures of 75 (black), 150 (red) and 300 mTorr (blue).

The present as-grown crystallite size values are similar to literature values obtained in comparable experimental conditions, with additional temperature anneals applied by some of the authors. Zhu et al. [5] report values of 15 and 25 nm for 50 and 225 nm thick ZnO films, respectively, grown at an oxygen pressure of 12 Pa (~100 mTorr) on glass substrates heated at 350 °C. In the present case of Zeonor substrates, the increase in crystallite size with ZnO film thickness seen in [5] is not retrieved, while the same increase with oxygen pressure reported in [2] is broadly

confirmed here. A mean crystallite size of about 23 nm for ~ 250 nm thick AZO films grown on a PET substrate at RT and oxygen pressure of 0.4 Pa (3 mTorr) is reported in refs [6,28], while this is around 10 nm for 500 nm thick AZO films grown on glass substrates at RT and 10 Pa (75 mTorr) oxygen pressure [4]. The small increase in crystallite size with film thickness reported in [6,28] is also observed in the present work. The general trend of a larger AZO crystallite size with decreasing pressure shown in [3,4] is generally followed here for AZO films on Zeonor substrates.

(b) Residual stress studies

The residual stress (σ) in the ZnO film plane is proportional to the strain along the *c*-axis in the biaxial strain model and can be estimated from equation (5.1)

$$\sigma = -4.54 \times 10^{11} \frac{(c - c_0)}{c_0} \text{ Nm}^{-2} \qquad \text{Eq (5.1)}$$

where c and c_0 are the *c*-axes length of the strained and relaxed ZnO crystal, respectively [29]. The *c*-axis length and stress values of all the samples are shown in Table 5.1 and Fig 5.7, respectively. As the films are grown at RT, thermal stress components are neglected. The experimental value of the *c*-axis length for the ZnO single-crystal wafer is taken as the c_0 value of 0.5207_2 nm. This is obtained from values of $2\theta_{(002)} = 34.45_1^{\circ}$ and $\lambda = 0.15425$ nm and matches accurately the ZnO *c*-axis length of 0.520690 nm (JCPDS card number 36-1451) when rounded off to the fourth decimal place (i.e. 0.5207 nm). This shows that the film stress values estimated from the measured change in the length of the *c*-axis are significant and reliable. A pointing error of ± 0.005º on the Bragg angle value yields an absolute error of ± 0.0002 nm on the *c*-axis length. The corresponding relative errors on the *c*-axis strain/film stress amount to about 5% and 15% for *c*-values of 0.5244 nm and 0.5220 nm, respectively. From equation (5.1), it is seen that this relative error gets larger as the *c*-axis length gets closer to c_0, while a negative σ value indicates a film in a compressive state of stress with its *c*-axis length larger than c_0.

Fig 5.7 shows that the ZnO and AZO films are in a compressive state of stress with σ values of – (2-3) GPa and – 0.5 GPa, respectively. The AZO films follow a similar trend. It is also seen that the stress has changed from compressive to tensile in the case of the AZO films grown at 300 mTorr (see below the discussion of

pole figures). For all the films, except the A9 sample, the stress values decrease linearly with film thickness at a given pressure indicating a relief of in-plane stress for the thicker films. Overall, the ZnO films grown at the lower oxygen pressure of 75 mTorr have less in-plane compressive stress than those grown at the higher pressures of 150 and 300 mTorr. These observations are consistent with our previous conclusions on both crystalline quality and growth mechanisms.

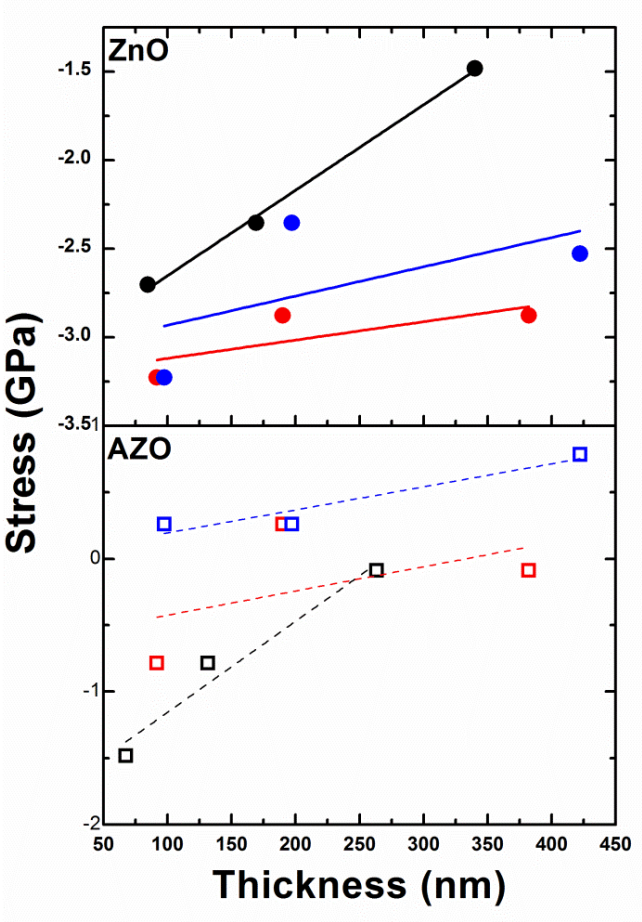

Figure 5.7: In-plane film stress (GPa) as a function of film thickness for *c*-axis oriented ZnO and AZO thin films deposited by pulsed-laser on Zeonor substrates at ambient oxygen pressures of 75 (black), 150 (red) and 300 mTorr (blue).

The compressive stress values for the ZnO films on Zeonor substrates are comparable with those (~ – 2 GPa) in the work of Maniv et al. [29] in which RT glass substrates were used, but differ from those of Zhu et al. [5] and Novotny et al. [30] in which tensile stress values of ~ 0.3 and 0.9 GPa were found for ZnO deposited on glass. Deposition temperatures of ~ 350 ºC were used in these last two works as well as a 750 ºC oxygen anneal in [30]. Thus, deposition and processing

temperatures significantly larger than RT can lead to different mechanical states for a ZnO film. For AZO films, the compressive stress is smaller than for ZnO due to the smaller ionic radius of Al^{3+} substituting on the Zn^{2+} sites. The σ or *c*–axis length values obtained here for AZO on Zeonor substrates are similar with comparable works quoted previously [4,7,28].

(c) Pole figure studies

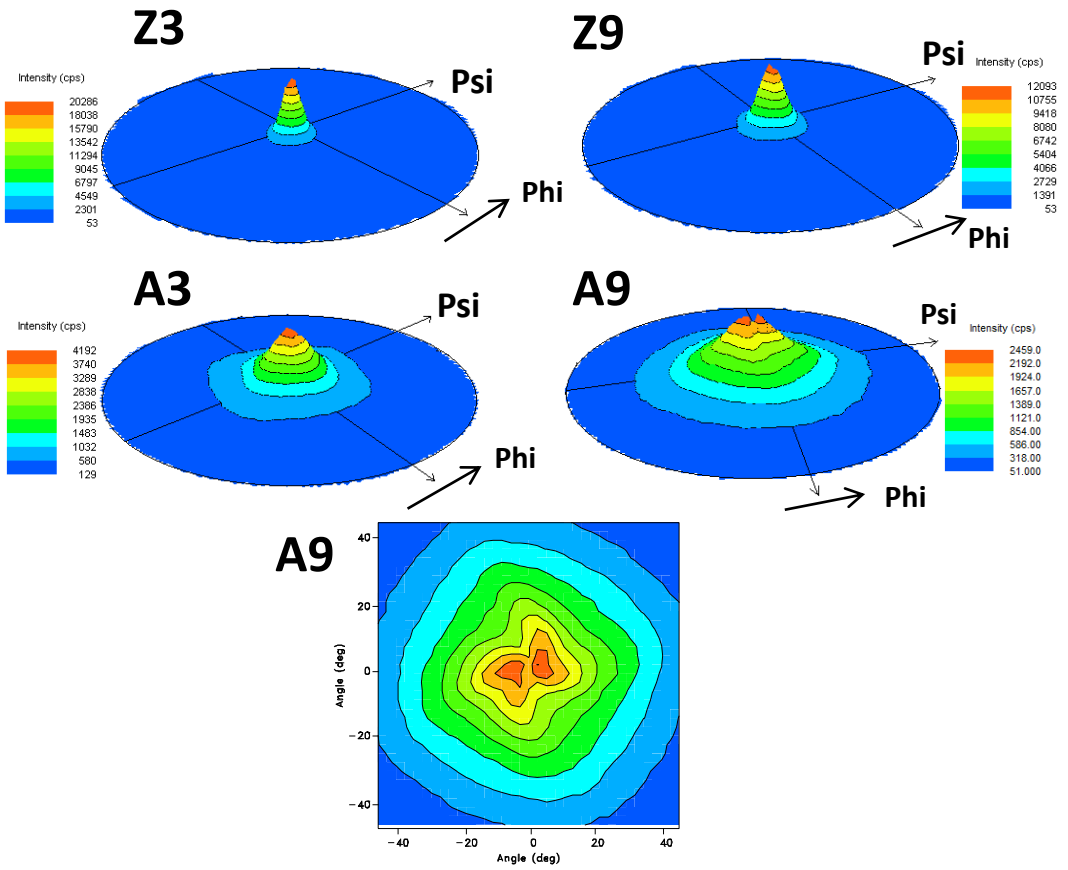

Figure 5.8: Perspective view of the (002) x-ray pole figure for a selection of ZnO (upper row) and AZO (middle row) films obtained in this work (samples Z3, Z9, A3 and A9). The films were grown by PLD on Zeonor substrates using 20,000 laser shots at ambient oxygen pressures of 75 mTorr (left-hand column) and 300 mTorr (right-hand column). The psi scale varies between -90° and 90°. The lower panel is a planar projection of the A9 figure on an enlarged psi scale to show the details of the peak splitting.

In order to investigate further the effects of deposition pressure on the texture and *c*-axis orientation of our ZnO and AZO thin films, we have measured the corresponding (002) pole figures for the selected samples Z3, Z9, A3 and A9 (same

as in Fig 5.2). The results are shown in Fig 5.8. The ZnO pole figures show high circular symmetry with narrow widths of 20° (75 mTorr) and 22° (300 mTorr) indicating a uniform alignment of the *c*-axis with small angular distribution about the substrate surface normal. The narrower width (20°) and more intense (20286 counts) pattern for sample Z3 suggests that the 75 mTorr deposition pressure creates better textured ZnO films. Kim et al. [19] have reported similar observations for Al and Ga doped ZnO films grown by RF sputtering. The AZO films appear to also follow this trend although the pole figures are much broader with widths of 34° (75 mTorr) and 54° (300 mTorr) indicating large variations of the *c*-axis orientation about the surface normal in the doped films. For sample A9 (AZO, 300 mTorr) the pole figure intensity maximum is split and off-centered indicating an overall tilt of the *c*-axis by about 5° with respect to the normal to the substrate surface. It has been shown that the state of stress in this sample was uniquely tensile as opposed to compressive for all the other ZnO and AZO films. From the pole figure study, we can conclude that both Al-doping and deposition pressure have noticeable effects (see Figure 5.5(b): presence of (101) plane in AZO samples) on the *c*-axis orientation of thin ZnO films deposited on Zeonor substrates indicating the sensitivity of the growth mode to these two parameters. We note here that Takayanagi et al. [31] have shown recently that tilted *c*-axis ZnO layered structures can be used as ultrasonic transducers and our work thus shows an experimental route for the fabrication of such structures.

5.1.2.5 Optical properties

The effect of deposition pressure on the optical properties/quality of the ZnO and AZO films of different thickness has been studied using UV-Vis absorption spectroscopy and low temperature photoluminescence spectroscopy.

(a) Transmission studies

The transmission spectra of the ZnO and AZO samples, referenced to the bare Zeonor substrate (visible transmission of 90%), are shown in Fig 5.9. All the spectra show the absorption onset behaviour characteristic of the direct band gap of ZnO consisting of almost complete transparency in the visible region followed by a sharp cut off in the near ultraviolet, around 370 nm for ZnO and 350 nm for AZO, and almost complete absorption at the shorter wavelengths. All the samples are characterised by a visible transparency of at least 85-90% and this can even be

greater than 95% for some samples (for particular wavelengths). The enhancement effect of multiple interferences due to multiple reflections at the air/ZnO-AZO/Zeonor/air interfaces is clearly present and indicative of the sharpness of these interfaces.

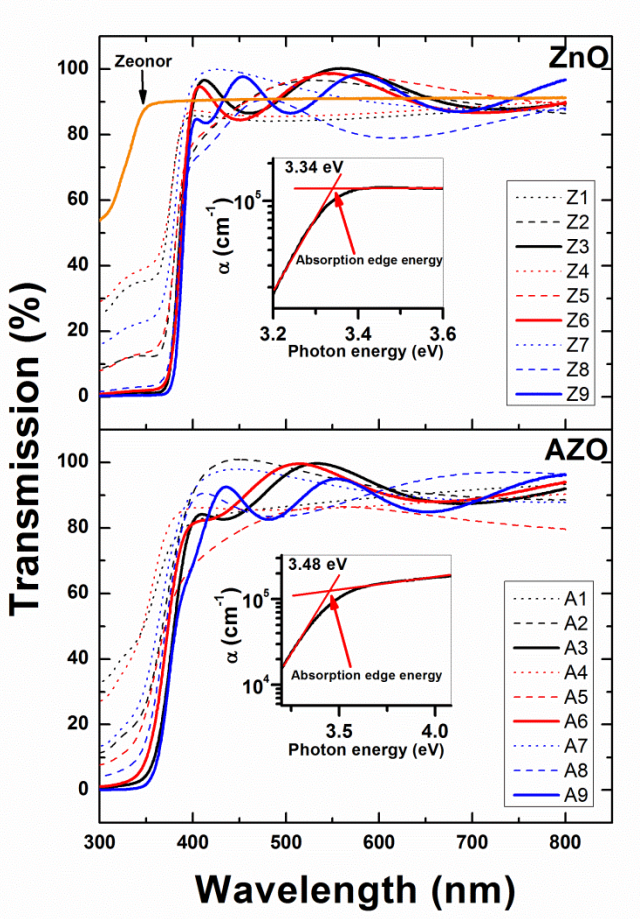

Figure 5.9: Optical transmission spectrum in the 300 – 800 nm wavelength range for ZnO and AZO thin films deposited by pulsed-laser on Zeonor substrates with 5000 (dotted lines), 10000 (dashed lines) and 20000 (solid lines) laser shots at ambient oxygen pressures of 75 (black), 150 (red) and 300 mTorr (blue). The insets show the absorption coefficient as a function of photon energy in the immediate vicinity of the ZnO (Z3 sample) and AZO (A3 sample) fundamental absorption edges and the graphical method employed in this work to determine the value of the latter.

It has been shown by several authors [30,32] that the commonly used method for determining the "optical band gap" E_g^{opt} based on an extrapolation to $\alpha = 0$ of the linear part of the α^2 vs $h\nu$ graph (Tauc plot), where α and $h\nu$ are the absorption coefficient and photon energy respectively, systematically underestimates the value

of E_g^{opt}, due to the presence of excitonic and other effects (e.g. broadening and stress effects), in ZnO which the Tauc model does not take into account. In addition, this method can lead to significant absolute errors for thick films (100 nm or greater) as the transmission values at the higher photon energies are then much less than a few percent and contain significant noise. We have thus evaluated the absorption edge energy from the transmission spectra using the following procedure to ensure a consistent approach allowing discussion of systematic trends. In the vicinity of the absorption edge, the ZnO and AZO layers are heavily absorbing and the transmittance assumes a simple exponential form from which the value of the absorption coefficients can be estimated with the knowledge of the layer thickness [7,33]. Typical results, showing α (cm^{-1}) as a function of $h\nu$ in eV on a semi-log plot, are shown in the insets of Fig 5.9 (for Z3 and A3 samples). It is seen (for ZnO) that the value of α is around 1.3×10^5 cm^{-1} near the edge without any distinct excitonic structure as would be expected in un-annealed samples [34]. For all the other samples, we found values of α in the $(0.9-2.0)\times10^5$ cm^{-1} range near the absorption edge which, thus, fall in the expected domain [32]. The value of the absorption edge can be estimated from semi-log plots of α vs $h\nu$ [35,36]. We have applied the graphical method depicted in the insets of Fig 5.9 systematically to all the ZnO and AZO samples data to estimate their fundamental absorption edge energy (with ±1% relative error). In the following, we treat these absorption edge values as our best estimation of the optical band gap values although we cannot properly take into account the 60 meV exciton binding energy and thus we still slightly underestimate the band gap. The results are shown in Fig 5.10 from which it is seen that the absorption edge energy of all the ZnO films is almost constant near an average value of 3.34 eV. This is just slightly less than the 3.37 eV band gap energy of bulk ZnO at room temperature [32] and thus confirms the validity of our method of estimation of the band gap energy. The variations of the ZnO optical band gap energy as a function of thickness and deposition pressure are observed to be relatively small. This behaviour of the band gap energy is compatible with the relatively small variations of the stress and grain size values with deposition pressure and thickness that we have discussed in the previous sections. In the comparable PLD works of Zhu et al. [2,5] and Novotný et al. [30], “Tauc band-gap” energies of

3.25 eV and 3.28 eV for ZnO films of similar thickness are reported and discussed by the authors.

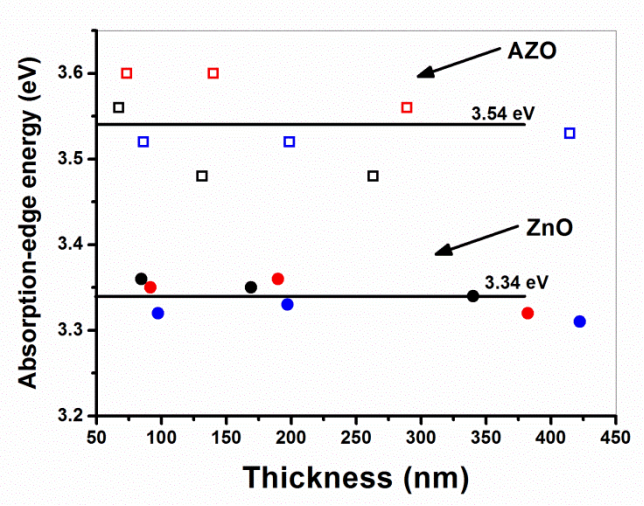

Figure 5.10: Fundamental absorption edge energy as a function of film thickness for ZnO and AZO thin films deposited by pulsed-laser on Zeonor substrates at ambient oxygen pressures of 75 (black), 150 (red) and 300 mTorr (blue).

For the AZO films a more dispersed pattern is observed in Fig 5.10 with values varying between 3.48 eV and 3.60 eV about a mean of 3.54 eV, larger than ZnO, as expected, as a result of the increased n-type dopant concentration. As the electron carrier densities measured (see section 5.1.2.6 below) are typically much lower than the ZnO critical density of ~10^{19} cm^{-3}, the observed band gap widening for AZO can be largely attributed to the Burstein-Moss shift [7,37,38]. Use of the Tauc plot method to determine E_g^{opt} in AZO (2 wt% Al_2O_3) gave values of 3.68 eV for RT deposition on PET substrates [28], 3.4 eV for RT deposition on glass substrates [3] and 3.45 eV for 400 ºC deposition on fused quartz substrates [7]. Our data lies within this spread of literature values. From Fig 5.10, the band gap energies for the 300 mTorr AZO films are seen to be consistently lower than for AZO films grown at the lower pressures and this can be related to our previous observation of a significant compressive to tensile change in the in-plane stress for 300 mTorr AZO films. This behaviour is similar to that reported by Mohanty et al. [39]. A trend whereby the AZO optical band gap slightly decreases in a linear fashion with film thickness is just discernable above the error margin in Fig 5.10. Again, this could be related to the corresponding grain size/stress behaviours discussed above.

(b) Photoluminescence studies

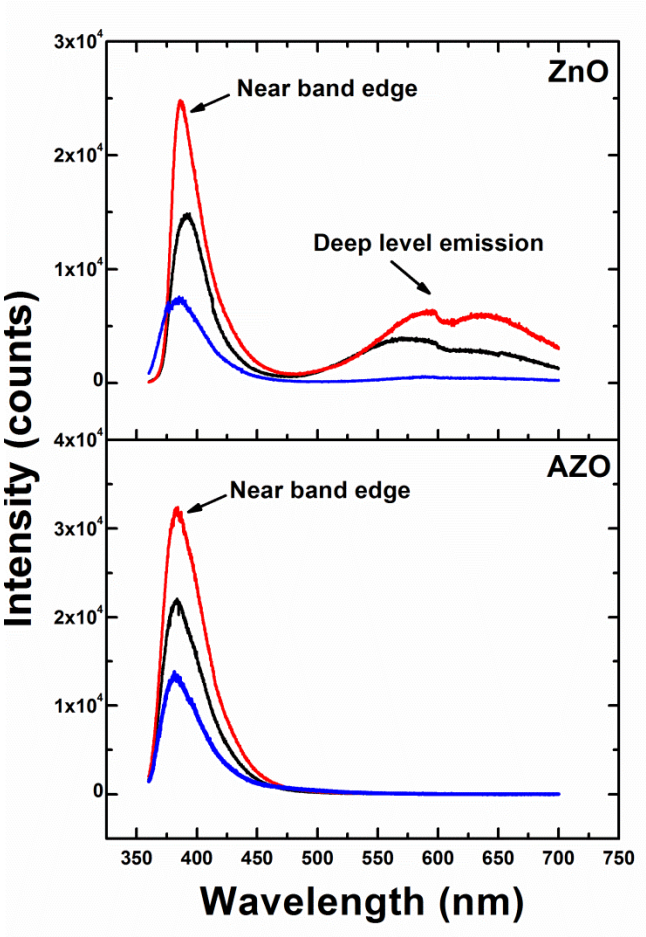

Figure 5.11: Low temperature (13 K) photoluminescence spectra for ZnO and AZO thin films deposited by pulsed-laser with 20000 laser shots on Zeonor substrates at ambient oxygen pressures of 75 (black), 150 (red) and 300 mTorr (blue).

Fig 5.11 shows the low temperature (13 K) photoluminescence spectra of the thickest (20,000 laser shots) of our ZnO and AZO thin films (samples Z3, Z6, Z9 and A3, A6, A9) for the three pressures of 75 mTorr, 150 mTorr and 300 mTorr used in this work. The spectra of the ZnO films show the characteristic near band edge (NBE) emission in the near UV emission and the deep-level emissions (DLE) in the visible spectrum composed of the yellow (2.2 eV) and orange/red (1.9 eV) bands. The NBE band is due to shallow bound excitonic recombinations while the yellow and orange/red DLE emissions are defect bands usually attributed to oxygen interstitials [40-42]. The NBE bands are significantly more intense than the defect bands at any deposition pressure, testifying to the good optical quality of the ZnO

material in the films. It is seen that the NBE peak emission wavelength shifts from 392 nm to 385 nm when the oxygen pressure increases from 75 mTorr to 300 mTorr. As this 7 nm wavelength shift is small, it cannot be conclusively correlated with the equally small differences in energy gap seen in Fig 5.10 for these samples.

For the AZO films, a strong NBE band is observed for all the oxygen pressures with a complete quenching of the deep level emissions. This effect is known and several reasons have been invoked in the literature to explain the absence of DLE in AZO films, see e.g. [43], though, to the best of our knowledge no consensus has yet been reached. We put forward one plausible explanation for the quenching of the DLE band in AZO. Native defects in ZnO, such as the oxygen interstitials responsible for the DLE, have higher formation energy in AZO than in ZnO due to the presence of aluminium which has a very strong chemical affinity for oxygen. Thus, oxygen displacement from its normal binding site is energetically less favorable in AZO compared to undoped ZnO. The concentration of oxygen interstitials may then be reduced when Al is incorporated during growth and hence no DLE is observed in AZO films. The AZO NBE peak emission wavelengths have blue-shifted to around 380 nm which is consistent with our previous observation of an increased band gap energy for AZO. Finally, we note that the NBE emission intensity is significantly reduced for the 300 mTorr AZO sample indicating that the optical quality of the material is highly sensitive to the oxygen deposition, in agreement with the markedly different structural and mechanical properties already noted for this particular sample.

5.1.2.6 Electrical properties

Fig 5.12 shows that the electrical properties of the ZnO and AZO samples in the form of the variations of Hall mobility and carrier concentration with film thickness for the various deposition pressures while the resistivity values are given in Table 5.1. It is worthwhile recalling here that all the measurements were carried out on the as-grown films without any thermal annealing or carrier activation treatments. For the ZnO films deposited at 75 mTorr, high resistivity values of 5×10^5 Ω cm (85 nm film), 2×10^4 Ω cm (169 nm film) and 4×10^5 Ω cm (340 nm film) and carrier concentrations $\leq 10^9$ cm^{-3} were typically obtained. Hall effect measurements on these highly resistive samples turned out to be too noisy and unreliable. The 75 mTorr

ZnO samples typically exhibit semi-insulating behaviour. For the ZnO samples grown at the higher pressures of 150 mTorr and 300 mTorr, resistivity values tend to drop by 2-3 orders of magnitude, down to 1.5×10^{2} Ω cm (92 nm thick sample at 150 mTorr), although some remain high, for example 2×10^{4} Ω cm (209 nm thick sample at 300 mTorr). Hall mobility values for these samples are all around 1 cm^2/V-s, whereas *n*-type carrier concentration values vary between 5×10^{14} cm^{-3} and 5×10^{16} cm^{-3}. Overall, the electrical behaviour of the ZnO/Zeonor samples varies significantly from semi-insulating to *n*-type semiconducting as a function of the oxygen deposition pressure. This pattern for ZnO thin films deposited by PLD under similar oxygen pressure conditions has been observed by many workers; see for example, Grundmann et al. [44].

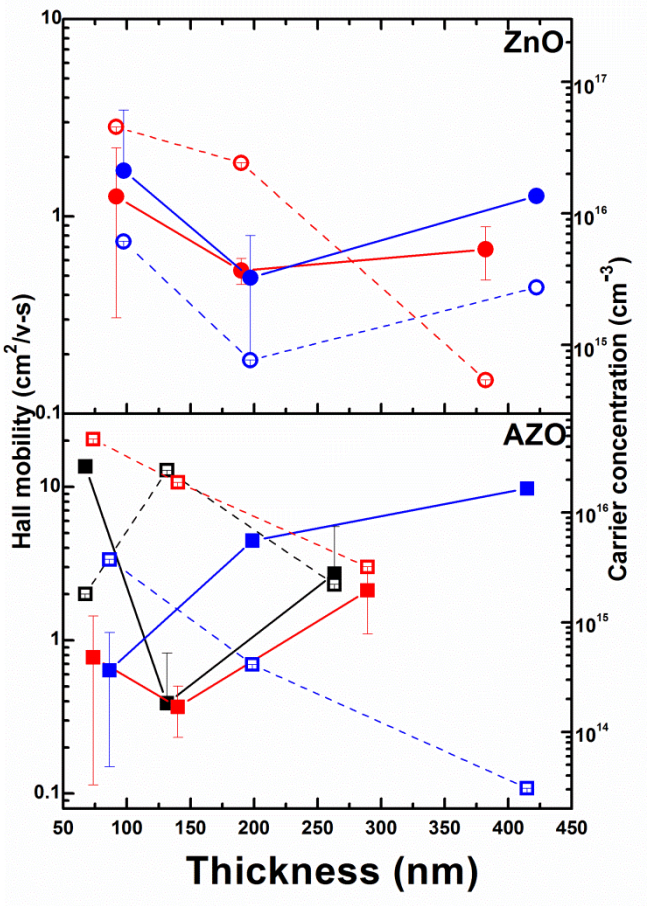

Figure 5.12: Hall mobility (closed symbols, solid lines) and carrier concentration (open symbols, dashed lines) as a function of film thickness for ZnO and AZO thin films deposited by pulsed-laser on Zeonor substrates at ambient oxygen pressures of 75 (black), 150 (red) and 300 mTorr (blue).

As expected, the electrical properties of the AZO thin films tend to show an improved conductive behaviour compared to ZnO. Notably, the resistivity values have all dropped significantly at all growth pressures and are mostly found in the range 4×10^{2} Ω cm - 2×10^{3} Ω cm for the lower pressures of 75 mTorr and 150 mTorr and around 9×10^{3} Ω cm for the films grown at 300 mTorr. Hall mobility values are significantly increased in AZO compared with ZnO, with the bulk of the values found in the range 4 - 14 cm^2/V-s with *n*-type carrier concentrations in the range 10^{15} cm^{-3} - 5×10^{16} cm^{-3}. The data of Table 5.1 shows that resistivity values tend to increase with both pressure and film thickness. The strong dependence of the resistivity of as-deposited AZO films grown by PLD at RT on glass with oxygen pressure was shown in ref [3], with the resistivity tending to insulator values at pressures of 10 Pa (75 mTorr) and greater. This behaviour is also verified in our work. Lu et al. [7] have also shown that the AZO electrical properties depend critically on the Al concentration with increase in resistivity from 10^{-3} Ω cm to 100 Ω cm when the concentration drops from about 3 at% to 1.5 at%. The AZO Hall mobility, resistivity and carrier density values reported in the present work are generally compatible with those of ref [7]. The 4-14 cm^2/V-s Hall mobility values for the AZO films obtained here could be suitable for use in transparent flexible thin film transistor applications, as reported by Nomura et al. [45] with 6-10 cm^2/V-s Hall mobility values. For applications requiring transparent conductive oxide (TCO) properties, the AZO resistivity would be significantly lowered (by a couple of orders of magnitude) and match that of other works on plastic substrates [17,28,46], by (i) carrying out the depositions at oxygen pressures in the 0.1 – 1 Pa (0.75 mTorr- 7.5 mTorr) range and (ii) non-thermal post-processing of the films using laser annealing [47].

5.1.3 Conclusions

In this high oxygen pressure work, we have shown for the first time that ZnO and Al-doped ZnO (AZO) nanocrystalline thin films with high material quality can be reproducibly grown on flexible Zeonor plastic substrates using pulsed laser deposition (PLD) at room temperature. We have also systematically studied the effects of oxygen in a selected pressure range on the growth rate, surface morphology, hydrophobicity and the structural, optical and electrical properties of

films having different thicknesses, and shed light on the aspects of the growth mechanisms.

All the films were observed to have the same nanostructured morphology. This was shown to be compatible with existing film growth models based on the capture by the Zeonor substrate of nanoclusters that have condensed in the expanding ablation plume. Highly linear growth rates were obtained showing that ZnO and AZO films with identical properties can be reproducibly deposited using the PLD technique. The deposition of ZnO or AZO films was shown to enhance the hydrophobicity of the Zeonor plastic surface. All the films were nanocrystalline (wurtzite structure) with high texture (*c*-axis orientation) and good crystallinity. Their optical quality was good: All the ZnO and AZO films displayed high visible transparency, greater than 95% in some cases, while their low temperature photoluminescence spectra showed intense near band edge emission. A considerable spread from semi-insulating to *n*-type conductive was observed in the ZnO and AZO films electrical behaviour, with marked dependences on film thickness and oxygen deposition pressure. The resistivity values of typically around 10^3 Ω cm and Hall mobility values in the range 4 - 14 cm^2/Vs showed that the ZnO and AZO films would be suitable for applications in flexible sensors, transducers and transparent thin film transistors.

5.2 Low oxygen growth pressures: 1-75 mTorr

In this section, we report the effects of oxygen growth pressures ≤ 75 mTorr, and show its very strong influence on ZnO and AZO thin films properties.

5.2.1 Growth details

	Sample labels	Oxygen pressure (mTorr)	Thickness (nm)	Plane	2θ (deg)	FWHM (deg)	Crystallite (or grain) size (nm)	*c*-parameter (nm)	Stress (GPa)
ZnO	Z_1	1	310	100	31.48	1.26	6.31	-	-
	Z_{10}	10	314	002	34.25	1.55	5.14	0.5237	-2.63
	Z_{25}	25	321	002	33.87	1.71	4.66	0.5294	-7.58
	Z_{40}	40	328	002	34.13	0.93	8.51	0.5256	-4.27
	Z_{75}	75	340	002	34.34	0.44	19.65	0.5225	-1.53
AZO	A_1	1	181	100	31.50	1.11	7.17	-	-
	A_{10}	10	188	100	31.48	1.11	7.18	-	-
	A_{25}	25	201	002	34.15	2.59	3.07	0.5252	-3.92
	A_{40}	40	214	002	33.78	1.19	6.65	0.5308	-8.80
	A_{75}	75	263	002	34.45	0.49	17.13	0.5208	-0.09

Table 5.2: Oxygen pressures used for PLD of ZnO and AZO films on Zeonor substrates. The resulting thickness, XRD 2θ angular position of the (002) and (100) Bragg reflection, XRD 2θ FWHM of the (002) and (100) Bragg reflection, crystallite size corresponding to the (002) and (100) Bragg reflection, value of the *c*-axis length and in-plane compressive stress are given for the films. "Z" indicates ZnO and "A" indicates AZO films.

The films were grown in a standard PLD apparatus with the substrate at room temperature. The details of laser specifications and growth parameters used in this section were kept the same as in the previous section 5.1. Growths were carried out in oxygen pressures in the PLD chamber of 75 mTorr (10 Pa), 40 mTorr (5.33 Pa), 25 mTorr (3.33 Pa), 10 mTorr (1.33 Pa) and 1 mTorr (0.13 Pa). In this section, all growths were carried out with a constant number of laser shots i.e. 20000 shots. The details of growth parameters, sample labelling, and some sample data are listed in Table 5.2.

5.2.2 Results and discussions

5.2.2.1 Surface morphology studies

Fig 5.13 shows AFM images for all the ZnO and AZO thin films grown at various oxygen pressures (75, 40, 25, 10 and 1 mTorr) on Zeonor substrates. The deposited films show micro and nanostructures for oxygen pressures above 25 mTorr. However, when the oxygen pressure in the PLD chamber decreased below 25 mTorr, a significant change was observed in both ZnO and AZO films. At lower oxygen pressures (10 mTorr and 1 mTorr), the deposits show a continuous film-like morphology, as shown in Fig 5.13. The change in the morphology may be due to the effects of the interaction of the ablated species with the background oxygen gas molecules on the cold and amorphous substrate, as suggested in previous works [1,3,4]. Fig 5.13 also shows that the films have no cracks when deposited at higher oxygen pressures i.e. 75 mTorr and that clear evidence of film cracking is seen at lower oxygen pressures (see below explanation). The surface roughness (rms) of the films was measured from the AFM data using WSXM software and is shown in Fig 5.14 (a). It is observed that, as oxygen pressure decreases from 75 mTorr to 1 mTorr, the surface rms roughness (calculated over an area of ~ 5 μm x 5 μm with a fixed resolution of 512 pixels × 512 pixels) increases dramatically from 5 nm to 60 nm for both ZnO and AZO films, due to the cracks observed in the lower oxygen pressure samples. However, the lower oxygen pressure samples appear smoother when the rms roughness is calculated over smaller areas (~ 1 μm x 1 μm) not including cracks, because of the depth (~ 150 nm) of the cracks which increases the overall surface roughness significantly.

We note that ZnO and ZnO:In (IZO) films grown by sputtering (growth at 150 ^{o}C) and PLD (growth at room temperature and similar oxygen pressures) on PEN and PET plastic substrates also show cracks [17,18]. By contrast, when using similar growth conditions (room temperature and similar oxygen pressures) AZO films grown by PLD on Si and glass substrates show no cracks in their morphology [3]. This indicates that the plastic substrates are key factors leading to the cracking, and this may be related to the substrate properties when interacting with high kinetic energy ablated species at lower oxygen pressures.

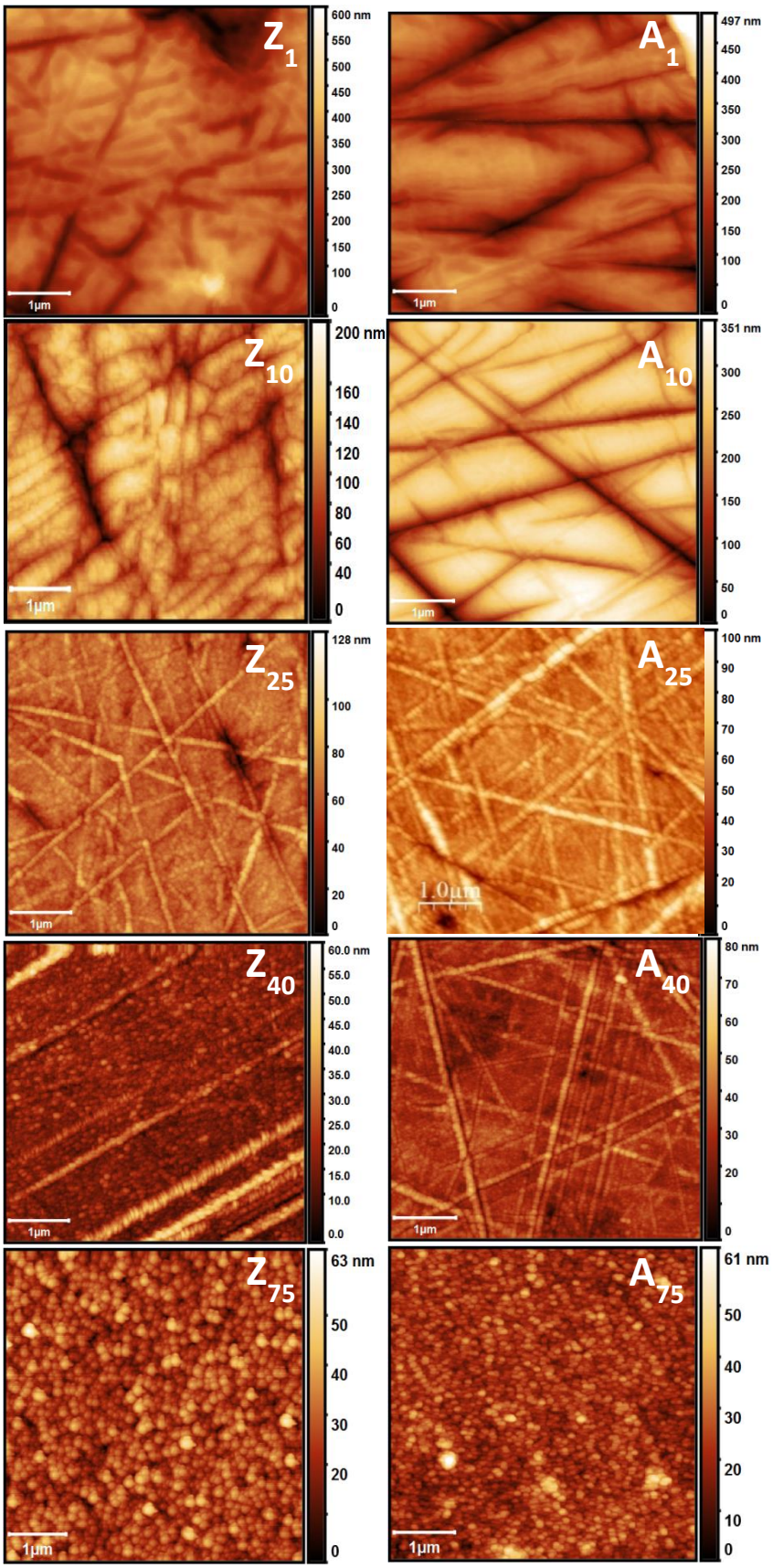

Figure 5.13: AFM images showing the surface morphologies of samples grown with various oxygen pressures (1 to 75 mTorr) for ZnO (left hand side column) and AZO (right hand side column) thin films (top to bottm).

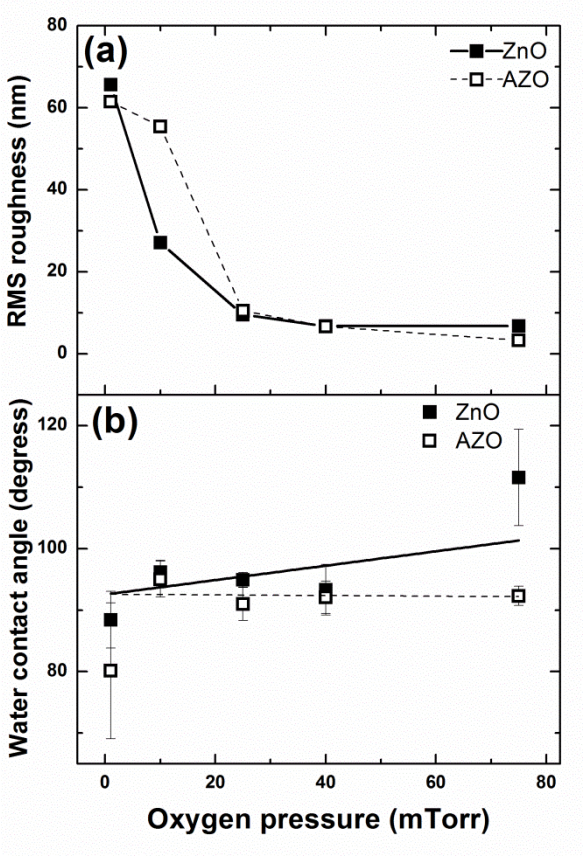

Figure 5.14: (a) Surface roughnesses (rms) obtained from AFM images of ZnO (closed symbols with solid lines) and AZO (open symbols with broken lines) thin films grown using various oxygen pressures (1-75 mTorr), (b) Water contact angle (WCA) for ZnO films (closed symbols with solid lines) and AZO thin films (open symbols with broken lines) grown using various oxygen pressures (1-75 mTorr).

Our surface roughness values are comparable with previous PLD reports on plastics substrates [17]. Overall, these findings indicate a significant effect of oxygen pressure on the surface morphology and surface roughness of films grown on Zeonor substrates.

5.2.2.2 Water contact angle (WCA) studies

The variation of water contact angle (WCA) as a function of oxygen pressure in the growth chamber for ZnO and AZO thin films are shown in Fig 5.14 (b) (see above Fig). The results are the average of several measurements (typically around 10) on different locations over the entire surface of the sample and the error bar represents the standard deviation of these measurements. The WCA for the bare hydrophobic substrate 1060 R Zeonor was measured at 92.0° [8]. As the oxygen

pressure decreases, the degree of hydrophobicity also decreases from 111° to 88° (for ZnO) and from 92° to 80° (for AZO). However, most of the films show a hydrophobic behaviour except the samples grown at 1 mTorr oxygen pressure. Thus, oxygen pressure during growth modifies the surfaces rendering them more hydrophobic, which may be related to the reduction in oxygen vacancy sites on the surface due to the higher oxygen pressure. The surface wetting properties generally depend on surface texture and roughness, as well as crystal structure [26,48,49]. As mentioned above, the surface roughness increases with decreasing oxygen pressure while the surface texture and grain size decrease with decreasing oxygen pressure (see below XRD data). These observations are consistent with our WCA results that hydrophobicity decreases with decreasing oxygen pressure. The relationship of hydrophobicity to the surface structure can be explained in terms of the number of trapped air spaces observed on surface of the films [26,48,49]. The trapped air pressure counteracts gravity as well as the surface tension of the water droplets and, as a result, the water droplets maintain a spherical shape (indicating greater hydrophobicity). Therefore, large numbers of air traps on the surface increase the hydrophobic behaviour [28]. This is consistent with the present work as the number of air traps is likely to be greater for the films with nanostructured grains, i.e. those formed at high oxygen pressures (≥ 25 mTorr). Furthermore, the degree of hydrophobicity seems greater for ZnO than AZO samples, although for many samples the difference is within the error bars, and this is consistent with previous works, e.g. [26].

5.2.2.3 Structural properties

Fig 5.15 shows 2θ-ω XRD scans for ZnO (Fig 5.15(a)) and AZO (Fig 5.15(b)) thin films grown by PLD on Zeonor plastic substrates, deposited at various oxygen pressures. Broad peaks associated with the amorphous Zeonor substrate were observed at around 2θ ≈16º and 41º [8]. The ZnO films grown at oxygen pressures above 1 mTorr (Z_{75}, Z_{40}, Z_{25}, Z_{10}) show evidence of wurtzite structure with dominant (002) and (004) peaks, and the Z_1 film deposited at an oxygen pressure of 1 mTorr shows a change in orientation of the crystalline fraction with the (100) peak being dominant, although the reduction in overall signal intensity may indicate an increased amorphous deposit fraction. Zhu et al. [2] also observed a reduction in

(002) peak intensity of ZnO films grown by PLD on glass substrates with decreasing oxygen pressure, consistent with the present work.

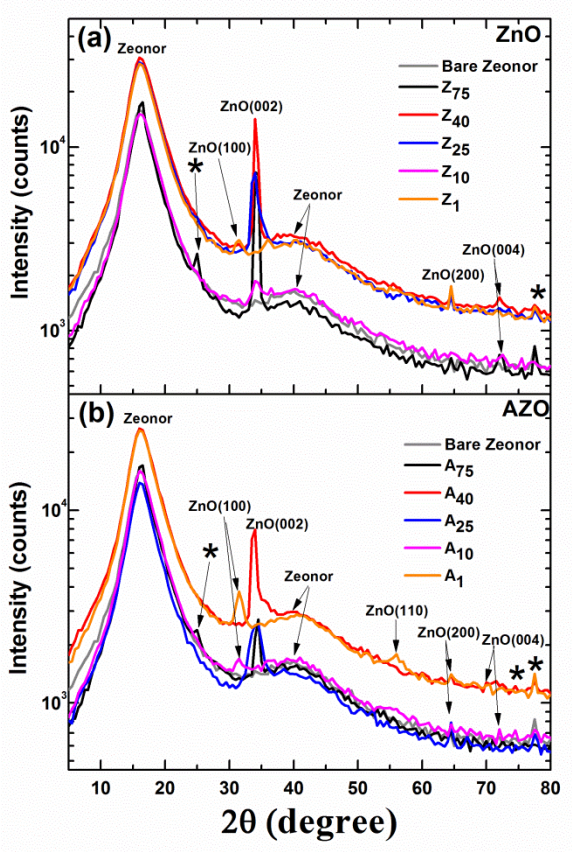

Figure 5.15: 2θ-ω XRD scans for (a) ZnO, (b) AZO thin films on Zeonor substrates. The features marked '*' are due to the adhesive mounting tape used.

The AZO films grown at oxygen pressures above 10 mTorr (A_{75}, A_{40} and A_{25}) also show dominant (002) and (004) peaks, whereas the AZO films grown at oxygen pressures below 25 mTorr (A_{10} and A_1) show a complete absence of the (002) peak and the growth of the (100) peak, although again the reduction in overall signal intensity may indicate an increased amorphous deposit fraction at lower oxygen pressures [50]. We note that AZO and IZO films grown by room temperature PLD on PET substrates also show an amorphous structure [17]. At high oxygen pressures (≥ 25 mTorr) both ZnO and AZO films on Zeonor substrates show a crystalline deposit fraction with (002) orientation (see above section 5.1), which changes to (100) orientation at low growth pressures (≤ 25 mTorr), i.e. from *c*-plane to *m*-plane. This crystalline fraction orientation shift correlates with our previously discussed

AFM surface morphology, where significant changes in surface morphology from nanocrystalline to film-like morphology occur in the same oxygen pressure region.

In order to study the effect of oxygen pressure on the crystalline quality, we have measured 2θ angular values and FWHM and have deduced the value of the *c*-axis length and in-plane stress of the films, as well as the average crystallite (or grain) size corresponding to the (002) and/or (100) Bragg reflection. These results are listed in Table 5.2. As mentioned earlier in Chapter 3.2 (see equation 3.2), measurement of the *a*-parameter is possible only from a measurement of the angular position of the (100) diffraction peak and hence no *c*-parameter value can be shown for the (100) oriented sample. For reference, we have also measured a *c*-axis oriented ZnO single crystal wafer of thickness 0.5 mm (Tokyo Denpa) with the same apparatus. The corresponding 2θ and *c*-parameter values are 34.45º and 0.5207 nm respectively. It is observed from Table 5.2 that the 2θ angular value reduces and diverges from the bulk ZnO value of 34.45º as oxygen pressure decreases for both ZnO and AZO films, for oxygen pressures above 25 mTorr. However, for samples grown at oxygen pressures of 25 mTorr and 10 mTorr, this trend does not hold and the 2θ angular value increases towards the bulk ZnO value for both ZnO and AZO films at low oxygen pressures (< 25 mTorr). This relaxation towards the bulk crystal value at low oxygen pressures is consistent with the evidence of cracks appearing in the low oxygen pressure samples (Z_1, A_1 and A_{10} samples). In all cases the 2θ angular values of ZnO and AZO films are smaller than the ZnO wafer value. From the known $2\theta_{(002)}$ angular values, we calculate the *c*-axis length of the samples using Bragg's Law and the residual stress in the films. It is observed (Table 5.2) that the films are compressively stressed in the *c*-axis direction (i.e. elongated in the substrate plane). This is consistent with our previous observations of ZnO and AZO films grown at oxygen pressures above 75 mTorr on Zeonor substrates (see above section 5.1). As mentioned in the previous section 5.1, the compressive stress values for AZO samples are also smaller than the ZnO samples due to the smaller ionic radius of Al^{3+} substituting on the Zn^{2+} sites [28].

From the experimental full width half maximum (FWHM) of the (002) peak, we have evaluated the average crystallite size using the Scherrer equation (see above section 5.1 for calculation details). The results are shown in Table 5.2. It is observed

from the data that, as oxygen pressure decreases the (002) FWHM increases (therefore, crystalline quality decreases), which can be taken to represent a proxy measure of the crystalline quality which seems to improve for samples grown at higher oxygen pressures. Similar results were reported previously for ZnO films grown by PLD on amorphous glass substrates [2]. The average crystallite size in our samples is in the range 2-12 nm for ZnO films and 3-18 nm for AZO films. We note that crystallite sizes reported in this work are comparable with previous reports of thin films on other plastic and glass substrates deposited by PLD (with similar oxygen growth pressures) [2,3], sputtering [28], and cathodic vacuum arc technology [51].

5.2.2.4 Optical properties

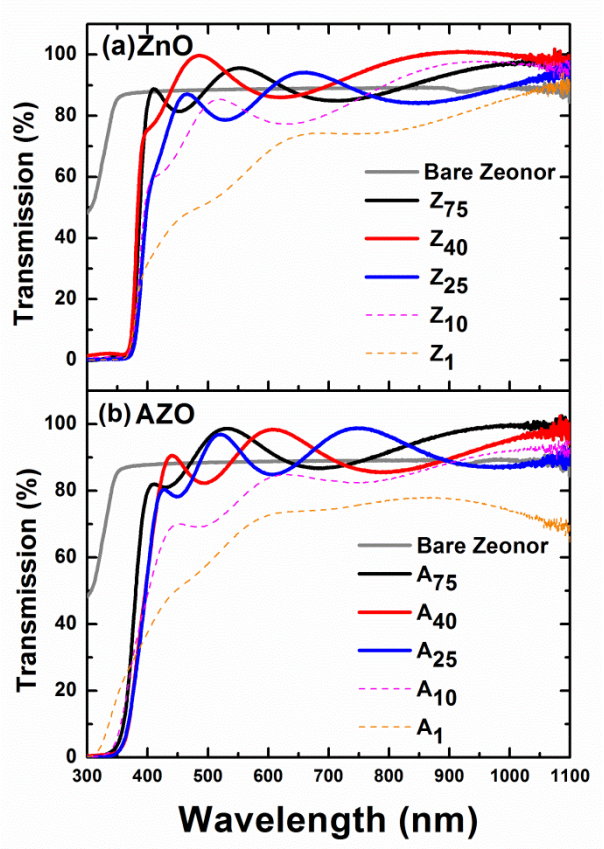

Figure 5.16: Transmission spectra in the 300 nm-1100 nm wavelength range for (a) ZnO and (b) AZO thin films grown by PLD at various oxygen pressures between 1 mTorr and 75 mTorr.

Transmission spectra of ZnO and AZO thin films in the range 300 -1100 nm are shown in Fig 5.16 (a) and (b), respectively. For reference, the transmission of a bare Zeonor substrate is also shown in Fig 5.16 (a and b), which has a transmission of 90 %. For both ZnO and AZO films, it is observed that the transmission is higher (85-95 %) with a sharp onset and clear evidence of interference fringes at higher oxygen pressures (75, 40 and 25 mTorr), whereas at low-oxygen pressures (10 and 1 mTorr) the transmission drops to 70-85 % with fewer fringes and a less sharp onset in transmission. These data are consistent with our AFM data (Fig 5.13 and Fig 5.14) where surface (rms) roughness increases (due to the formation of large cracks) with decreasing oxygen pressure. This roughness is very likely to lead to increased scattering, giving rise to the optical properties seen in Fig 5.16 (a) and (b) for these samples. We note that Gondoni et al. [3,4] have also observed this type of behaviour for samples grown under similar oxygen pressures by room temperature PLD on soda-lime glass substrates. We also note that the transmittance of our samples (with similar thicknesses) on Zeonor substrates at oxygen pressures ≥ 25 mTorr is higher than those reported previously on other plastic and glass substrates [18,28,52]. For example, Sierros et al. [18] have reported a 80 % transmission for ZnO films grown on PET substrates while Guillén et al. [28] have reported a 85-90 % transmission for AZO films grown on PET substartes. Also, Gong et al. have reported a 80 % transmission for GZO (ZnO:Ga) films grown on PC substrates.

5.2.2.5 Electrical properties

Fig 5.17 shows the electrical properties of the ZnO and AZO films grown on Zeonor substrates (resistivity, Hall mobility and carrier concentration). For ZnO films, the LHS of Fig 5.17 (a) shows that the resistivity value (black coloured symbols) is ~ 10^5 Ω cm at higher oxygen pressures (75, 40 and 25 mTorr), and the films are semi-insulating. It is worth recalling here that all the films were deposited at room temperature, i.e without any annealing or activation treatments. The resistivity of the films dropped sharply to 10^{-2}-10^{-3} Ω cm at low oxygen pressures (10 and 1 mTorr). Furthermore, the decrease in the resistivity with decreasing oxygen pressure is mainly attributed to the increasing oxygen vacancy concentration in the films, although the morphology transition of the samples to a thin film-like deposit from the nanocrystalline form (see Fig 5.13) may be of importance in explaining the behaviour of the Hall mobility at the lowest values of oxygen pressure, as discussed

below. Decreasing the oxygen pressure is expected to increase the number of oxygen vacancies, leading to an increase in carrier concentration and conductivity [1,2]. A similar correlation between resistivity and oxygen growth pressure has been reported by many authors [1,3]. The inner right hand side of Fig 5.17 shows that Hall mobility increases initially to 35 cm^2/V-s and then decreases to ~ 2 cm^2/V-s as oxygen pressure decreases, again correlating with the morphology and crystallinity behaviours observed previously. The Hall mobility variation can be explained in terms of grain boundary scattering as well as defect scattering [2]. As the oxygen pressure decreases the grain size of the film decreases (see Table 5.2), leading to an increase in grain boundary scattering. Simultaneously, the defect scattering also increases with decreasing oxygen pressure because of the increasing defect population (oxygen vacancies) at low pressures [1,2,3]. We observed the Hall mobility of the ZnO samples deposited at 75 mTorr were quite noisy and thus deemed unreliable. Hence we have not shown Hall mobility values for these samples. The carrier concentration increases sharply from 10^9 cm^{-3} to 10^{21} cm^{-3} as the oxygen pressure decreases from 75 mTorr to 1 mTorr, which we attribute to the oxygen vacancies created at lower oxygen growth pressures [1,2,3]. Our electrical resistivity, Hall mobilities and carrier concentration results for ZnO films are comparable with previous reports on other plastic substrates such as PET [51].

The AZO films generally show improved electrical behaviour compared to ZnO films in terms of resistivity, particularly at higher oxygen pressures. The resistivity decreases almost linearly with decreasing oxygen pressure and the maximum resistivity is ~ 10^3 Ω cm at an oxygen pressure of 75 mTorr and the minimum resistivity is in the range of 10^{-3}-10^{-4} Ω cm at an oxygen pressure of 1 mTorr. The overall decrease in the resistivity of AZO compared to ZnO films is attributed to an increase in the free carrier concentration for AZO for all growth conditions, due to the ubiquitous donor electrons from the Al dopant [1]. In terms of Hall mobilities for the AZO films, as the oxygen pressure decreases the Hall mobility value increases initially to 18 cm^2/V-s until an oxygen growth pressure of 40 mTorr and then a sudden drop is observed to a value of 1 cm^2/V-s at an oxygen pressure of 25 mTorr. As discussed above, the sudden decrease in the Hall mobility at 25 mTorr is again associated with the decrease in grain size of the AZO film (see Table 5.2). At the lowest oxygen pressures (1 mTorr) in both ZnO and AZO

samples, the Hall mobility increases slightly which may be related to the morphology transition of the samples to a film-like deposit (albeit with cracks) from the nanocrystalline form (see Fig 5.13). In terms of carrier concentrations in the AZO films, the concentration increases almost linearly from 10^{15} cm^{-3} to 10^{21} cm^{-3} as the oxygen pressure decreases from 75 mTorr to 1 mTorr.

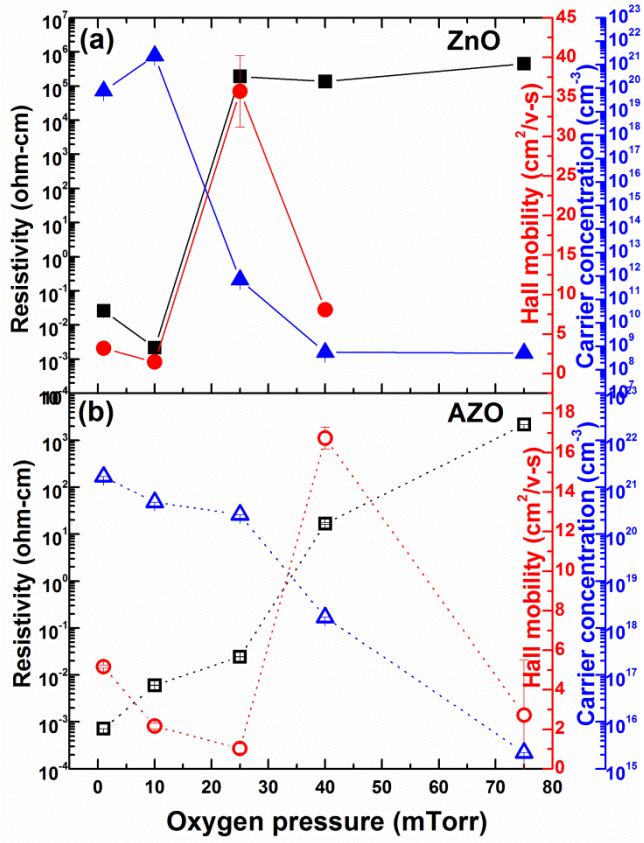

Figure 5.17: Resistivity (black coloured square symbols and left-hand scale), Hall mobility (red coloured circle symbols and inner right hand scale) and carrier concentration (blue coloured triangle symbols and outer right hand scale) of (a) ZnO and (b) AZO thin films grown by PLD at various oxygen pressures (mTorr).

Overall, the electrical properties of both the ZnO and AZO samples improve significantly at low oxygen growth pressures and all the films show *n*-type conductivity. By contrast, ZnO films grown at high oxygen pressures show a semi-insulating behaviour.

5.2.3 Conclusions

The effect of oxygen pressure on the surface morphology, structural, optical and electrical properties of as-grown ZnO and AZO thin films grown on Zeonor plastic substrates were studied. As the oxygen pressure decreases from 75 mTorr to 1 mTorr (i) the surface morphology changes from nanocrystalline to a film-like form and the surface rms roughness increases significantly from 4 nm to 65 nm, primarily due to the appearance of deep surface cracks (see Fig 5.13); (ii) the degree of hydrophobicity of the samples decreases. All the films show a hydrophobic behaviour (but WCA is very close to 90 °) except the 1 mTorr oxygen pressure sample; (iii) the orientation of the crystalline fraction (with possibility of large amorphous fraction at low oxygen pressures) of the deposit shifts from *c*-plane to *m*-plane for the ZnO material; (iv) the visible optical transmittance decreases significantly from 95 % to 70 % (or even less) while the band-edge onset becomes much less sharp and the interference fringes are obscured, most likely all due to increased scattering; (v) the electrical properties are significantly improved overall e.g. the resistivity of the ZnO films decreases from 10^{6} Ω cm to 10^{-3} Ω cm and the carrier concentration increases from 10^{9}-10^{15} cm^{-3} to 10^{21} cm^{-3}. Overall, the effect of oxygen pressure on the structure and properties of ZnO and AZO films has been shown to be an important factor. Researchers will benefit from this work for the control and tailoring of the properties of ZnO and AZO films on plastic substrates. Thin films such as these grown on flexible Zeonor substrates may find applications in flexible optoelectronics in the first instance, but also, because Zeonor plastics are used in many healthcare and medical applications, the outcomes from our work could also be used in microfluidic, bio-sensing or biofuel-cell energy applications amongst others.

5.3 Ageing effect study

In this section, we present a study of the ageing effect of ZnO and AZO thin films grown at oxygen pressures < 75 mTorr on Zeonor substrates. We observe the effect over a six month period. The samples grown in section 5.2 (low-oxygen pressure grown films) were used to study the ageing effect.

We now briefly review the literature on the ageing of ZnO thin films. Li et al. [53] have reported the effect of ageing time of ZnO sol on the properties of ZnO thin films grown by sol-gel method on glass substrates, while Shan et al. [54] have reported the ageing and annealing effects on ZnO films grown by PLD on GaN substrates. In those reports, the authors focused on the surface and PL properties. Shan et al. have also reported similar works on glass and sapphire substrates, respectively in refs [55,56]. Karamdel et al. [57] have reported an ageing study of nitrogen-doped ZnO films grown by RF sputtering on Si substrates, while Guillén-Santiago et al. [58] have done similar work on fluorine-doped ZnO films grown by chemical spray technique on glass substrates. Furthermore, Vidor et al. [59] and Pearton et al. [60] have reported an ageing study on ZnO and InGaZnO thin films grown on plastic substrates based TFTs, respectively. To the best of our knowledge, no report has been published on the ageing effect study of ZnO and AZO thin films grown on Zeonor plastic substrates. We present the effect of ageing on the optical transmittance, electrical and hydrophobic properties of the ZnO and AZO thin films grown by room temperature PLD on flexible Zeonor plastic substrates. The samples placed in transparent polycarbonate boxes were aged in a transparent desiccator cabinet at constant room temperature. Ageing studies were performed without any surface treatments or exposure to light.

5.3.1 Effect of ageing on optical properties

Figure 5.18 shows the ageing effect on the transmission properties of the ZnO and AZO thin films grown by PLD at various oxygen pressures between 1 and 40 mTorr on Zeonor substrates. The six-months ageing study shows that the transmission properties of the ZnO and AZO thin films are stable, including the features associated with the absorption edge. This means that the optical band gap properties also remain stable with ageing over the time period studied. Interference

fringes observed for the high oxygen pressure (25 and 40 mTorr) samples are not affected by ageing. Overall, the ageing effect on the transmission properties of the films is very minor and thus, the properties appear to be very stable.

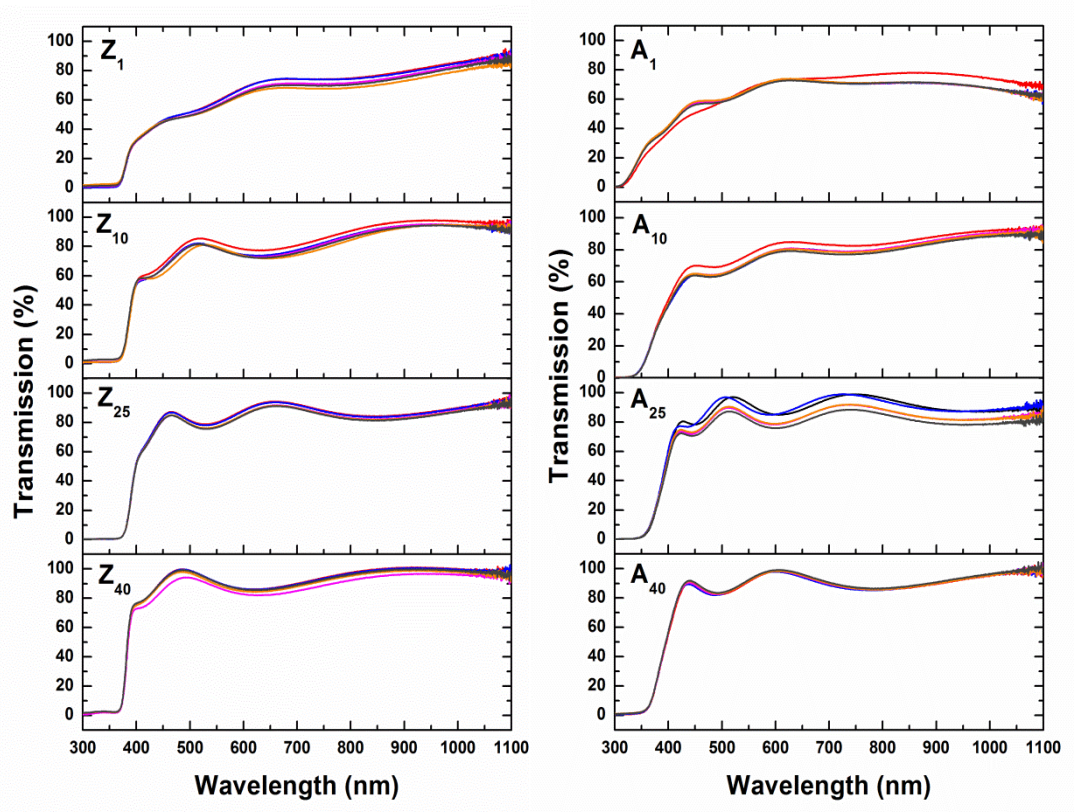

Figure 5.18: Ageing effect study on transmission spectra in the 300 nm-1100 nm wavelength range for ZnO and AZO thin films grown by PLD at various oxygen pressures between 1 mTorr and 40 mTorr on Zeonor substrates. Black lines- fresh sample, red line- 2 months, blue lines- 3 months, magenta lines- 4 months, orange lines- 5 months, and grey lines- 6 months.

5.3.2 Effect of ageing on electrical properties

The ageing effect study of the ZnO and AZO films on the resistivity and carrier concentrations is shown in Fig 5.19. For ZnO, the resistivity values of Z_1 and Z_{10} samples increase almost linearly with ageing time. For example, the resistivity of Z_1 increases from 0.02 Ω cm to 0.5 Ω cm, whereas, the resistivity of Z_{10} increases from 0.002 Ω cm to 1.26 Ω cm. The electrical measurements on the samples Z_{25} and Z_{40} are not shown here. This is due to the films becoming highly resistive with ageing and the data was too noisy and unreliable.

Interestingly, in the case of AZO, the resistivity of the films remains stable over the 6 month ageing. However, A_{40} sample shows a slight decrease in resistivity (from 15 to 3 Ω cm) with the ageing, but the other AZO samples such as $A_{1,}$ A_{10} and A_{25} show a slight increase in their resistivity. This could be correlated with the nanostructured morphology of the A_{40} sample (see above Fig 5.13). We believe that the film like morphology of the $A_{1,}$ A_{10} and A_{25} films is the reason for this stable behaviour with ageing time. Overall, the carrier concentration for AZO samples shows a stable behaviour i.e. followed the similar trend of the resistivity trend. The stable behaviour of the AZO samples with ageing could possibly be explained in terms of chemical differences affecting the ZnO lattice stability with or without the aluminium dopant.

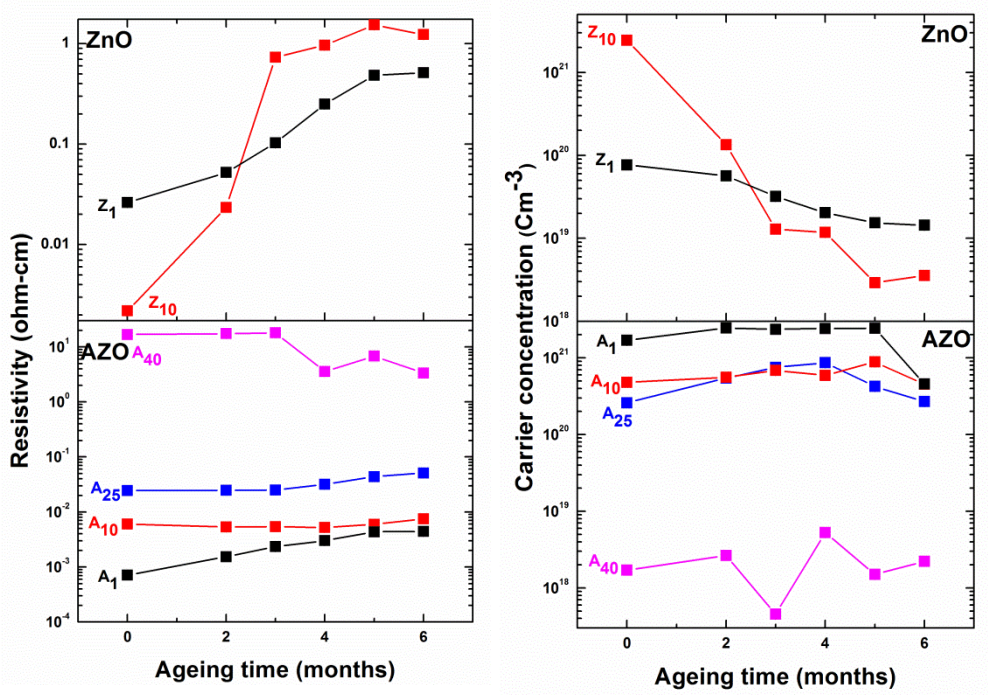

Figure 5.19: Ageing effect study on the resistivity (left hand side column) and carrier concentration (right hand side column) for ZnO and AZO thin films grown by PLD at various oxygen pressures between 1 mTorr and 40 mTorr on Zeonor substrates.

Fig 5.20 shows Hall mobilities for ZnO and AZO films grown by PLD on Zeonor substrates. We note that we have repeated all the electrical measurements for several times and the standard deviation of those measurements were taken as an error bar length. In case of Hall mobility values of ZnO samples, the error bar length

was observed to be large. Hall mobility for ZnO samples appear to be constant with ageing time, with values within the error bars. In case of AZO, except A_{40} the remaining samples show a constant behaviour for Hall mobility with ageing time. This is again correlated with nanostructured morphology of A_{40} sample. Overall, the ZnO films seem affected with ageing, whereas the AZO films seem almost stable with ageing.

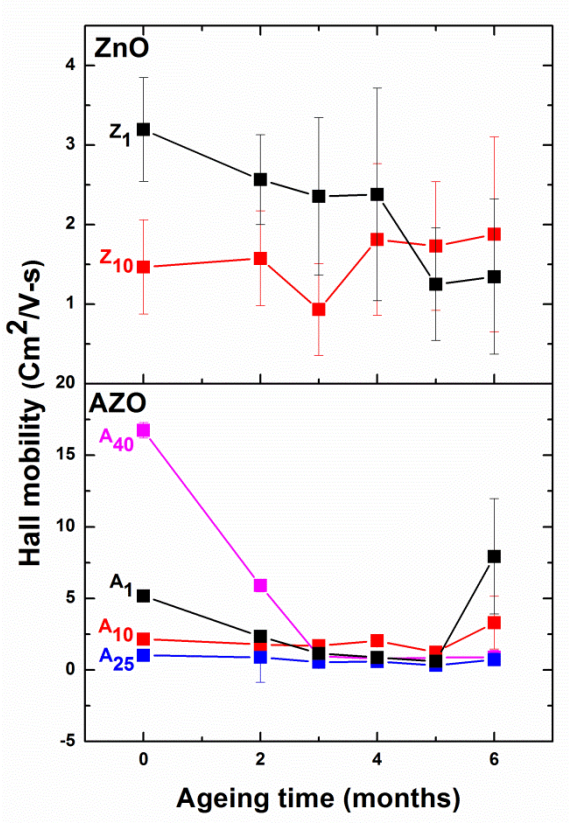

Figure 5.20: Ageing effect study on Hall mobility for ZnO and AZO thin films grown by PLD at various oxygen pressures between 1 mTorr and 40 mTorr on Zeonor substrates.

5.3.3 Effect of ageing on hydrophobic properties

The variation of water contact angle (WCA) as a function of ageing time for ZnO and AZO thin films are shown in Fig 5.21. The figure shows the linear fit of the respective data points. The size of some of the error bars in this figure reflects the large variations of several degrees which were occasionally found between successive measurements on the same sample. This is compatible with the high sensitivity of the ZnO surface wettability on both exposure to near ultraviolet radiation [23] and chemical contamination [24]. In ZnO, the films (except Z_1 sample)

are observed to be reducing in their hydrophobicity with ageing time by lowering WCA by a several degrees. Overall, the ZnO films show a reduced degree of hydrophobicity with the ageing. In the case of AZO, the A_1 film shows an increased degree of hydrophobic behaviour from 80° to 92°, whereas the remaining films showing a reduced hydrophobic behaviour. However, the reduction in hydrophobicity is observed to be smaller.

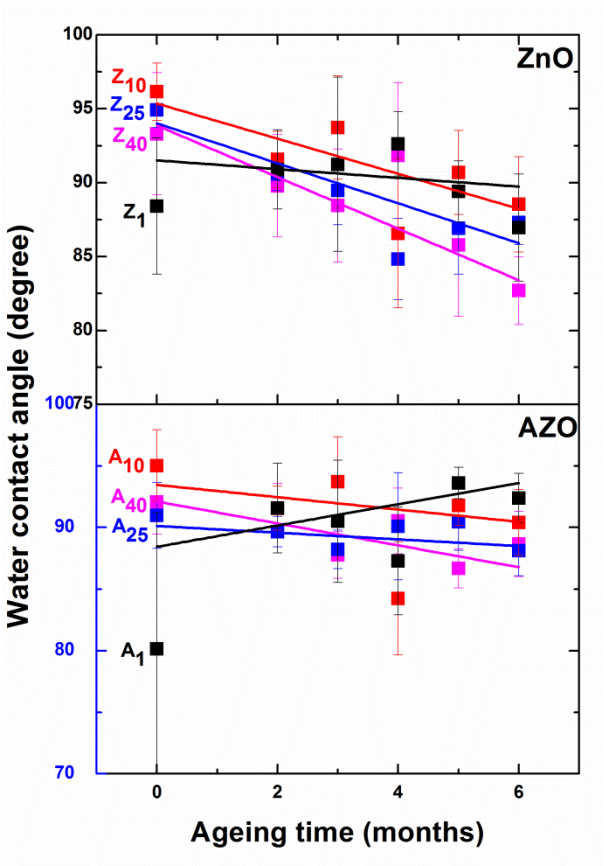

Figure 5.21: Ageing effect study on water contact angles for ZnO and AZO thin films grown by PLD at various oxygen pressures between 1 mTorr and 40 mTorr on Zeonor substrates.

5.3.4 Conclusions

We have studied the ageing effect over a period of 6 months on the optical transmittance, electrical and hydrophobic properties of the ZnO and AZO thin films. These films were grown by room temperature PLD on Zeonor substrates. Our studies confirmed that the AZO films have more stability against ageing in terms of optical, electrical and hydrophobic properties than the ZnO films. This is due to a very strong chemical affinity of the aluminium for the oxygen atoms, which may not affected by

ageing. However, the optical transmittance properties for both ZnO and AZO showed a stable behaviour with ageing. In terms of electrical properties, the resistivity, carrier concentration and Hall mobilities are observed to be affected by the ageing for ZnO samples. In case of AZO samples, the electrical properties appeared to be stable. In terms of hydrophobic properties, the degree of hydrophobicity is reduced for the both ZnO and AZO samples with ageing. However, the WCA of 1 mTorr samples (Z_1 and A_1) in both ZnO and AZO show a different behaviour from the other samples. Overall, the AZO thin films grown by room temperature PLD on Zeonor substrates show a stable behaviour with the ageing time for the period of 6 months. The stable behaviour of the films is important for a long term based device performance.

5.4 References

[1] R. Eason (Eds.), *Pulsed Laser Deposition of Thin films: Applications-Led growth of Functional Materials*, John Wiley and Sons Inc., New Jersey, 2007, pp.278-285.

[2] B.L. Zhu, X.Z. Zhao, S. Xu, F.H. Su, G.H. Li, X.G. Wu, J. Wu, R. Wu, J. Liu, Oxygen pressure dependences of structure and properties of ZnO films deposited on amorphous glass substrates by pulsed laser deposition, *Jpn. J. Appl. Phys.*47 (2008) 2225-2229.

[3] P. Gondoni, M. Ghidelli, F. Di Fonzo, M. Carminati, V. Russo, A.L. Bassi, C.S. Casari, Structure-dependent optical and electrical transport properties of nanostructured Al-doped ZnO, *Nanotechnology* 23 (2012) 365706.

[4] P. Gondoni, M. Ghidelli, F. Di Fonzo, V. Russo, P. Bruno, J. Marti-Rujas, C.E. Bottani, A.L. Bassi, C.S. Casari, Structural and functional properties of Al:ZnO thin films grown by Pulsed Laser Deposition at room temperature, *Thin Solid Films* 520 (2012) 4707-4711.

[5] B.L. Zhu, X.H. Sun, S.S. Guo, X.Z. Zhao, J. Wu, R. Wu, J. Liu, Effect of thickness on the structure and properties of ZnO thin films prepared by pulsed laser deposition, *Jpn. J. Appl. Phys.* 45 (2006) 7860-7865.

[6] C. Guillen, J. Herrero, Optical, electrical and structural characteristics of Al:ZnO thin films with various thicknesses deposited by DC sputtering at room temperature and annealed in air or vacuum, *Vacuum* 84 (2010) 924-929.

[7] J.G. Lu, Z.Z. Ye, Y.J. Zeng, L.P. Zhu, L. Wang, J. Yuan, B.H. Zhao, Q.L. Liang, Structural, optical, and electrical properties of (Zn,Al)O films over a wide range of compositions, *J. Appl. Phys.* 100 (2006) 073714.

[8] S. Inguva, R.K. Vijayaraghavan, E. McGlynn, J.-P. Mosnier, Highly transparent and reproducible nanocrystalline ZnO and AZO thin films grown by room temperature pulsed-laser deposition on flexible Zeonor plastic substrates, *Mater. Res. Express* 2 (2015) 096401.

[9] Web reference: Zeon Corporation, Available at: www.zeon.co.jp (last accessed 2nd May 2015)

[10] T. Okada, K. Kawashima, Synthesis of a variety of ZnO nanostructured crystals by nanoparticle-assisted pulsed-laser deposition, *Proc. SPIE Japan* 5662 (2004) 420 (doi:10.1117/12.596394).

[11] A.B. Hartanto, X. Ning, Y. Nakata, T. Okada, Growth mechanism of ZnO nanorods from nanoparticles formed in a laser ablation plume, *Appl. Phys. A* 78 (2004) 299-301.

[12] R. O'Haire, E. McGlynn, M.O. Henry, J.-P. Mosnier, ZnO nanostructured thin films grown by pulsed laser deposition in mixed O_2/Ar background gas, *Superlat. Microstruct.* 42 (2007) 468-472.

[13] T. Okada, B.H. Agung, Y. Nakata, ZnO nano-rods synthesized by nano-particle-assisted pulsed-laser deposition, *Appl. Phys. A* 79 (2004)1417-1419.

[14] W. Marine, L. Patrone, B. Luk'yanchuk, M. Sentis, Strategy of nanocluster and nanostructure synthesis by conventional pulsed laser ablation, *Appl. Surf. Sci.* 154 (2000) 345-352.

[15] S. Inguva, S.K. Marka, R.K. Vijayaraghavan, E. McGlynn, Vadali V.S.S. Srikanth, J.-P. Mosnier, Crystalline ZnO/Amorphous ZnO Core/Shell Nanorods: Self-Organized Growth, Structure, and Novel Luminescence, *J. Phys. Chem. C* 119 (2015) 4848-4855.

[16] P. Jensen, Growth of nanostructures by cluster deposition: Experiments and simple models, *Rev. Mod. Phys.* 71 (1999) 1695-1735.

[17] G. Socol, M. Socol, N. Stefan, E. Axente, G. Popescu-Pelin, D. Craciun, L. Duta, C.N. Mihailescu, I.N. Mihailescu, A. Stanculescu, D. Visan, V. Sava, A.C. Galca, C.R. Luculescu, V. Craciun, Pulsed laser deposition of transparent conductive oxide thin films on flexible substrates, *Appl. Surf. Sci.* 260 (2012) 42-46.

[18] K.A. Sierros, D.A. Banerjee, N.J. Morris, D.R. Cairns, I. Kortidis, G. Kiriakidis, Mechanical properties of ZnO thin films deposited on polyester substrates used in flexible device applications, *Thin Solid Films* 519 (2010) 325-330.

[19] J.-P. Kim, J.-S. Bae, T.-E. Hong, M.-S. Won, J.-H. Yoon, B.-S. Lee, H.-J. Lee, Optical and electrical properties of ZnO films, codoped with Al and Ga deposited at room temperature by an RF sputtering method, *Thin Solid Films* 518 (2010) 6179-6183.

[20] C. Volcke, R.P. Gandhiraman, V. Gubala, J. Raj, Th. Cummins, G. Fonder, R.I. Nooney, Z. Mekhalif, G. Herzog, S. Daniels, D.W.M. Arrigan, A.A. Cafolla, D.E. Williams, Reactive amine surfaces for biosensor applications, prepared by plasma-enhanced chemical vapour modification of polyolefin materials, *Biosens. Bioelectron.* 25 (2010)1875-1880.

[21] (a) D. Han, W. Wang, J. Cai, L. Wang, Y. Ren, Y. Wang, Z. Shengdong, Flexible Thin-Film Transistors on Plastic Substrate at Room Temperature, *J. Nanosci. Nanotechnol.* 13 (2013) 5154-5157; (b) D. Han, C. Zhuofa, N. Zhao, W. Wang, F. Huang, S. Zhang, X. Zhang, Y. Wang, Flexible aluminum-doped zinc-oxide thin-film transistor fabricated on plastic substrates, *Proc. SPIE USA* 8987 (2014) 89871L (doi: 10.1117/12.2044554).

[22] J. Connolly, A. Jain, G. Pastorella, S. Krishnamurthy, J.-P Mosnier, E. Marsili, Zinc oxide and indium tin oxide thin films for the growth and characterization of Shewanella loihica PV-4 electroactive biofilms, *Virulence* 2 (2011) 479-482.

[23] M. Sun, Y. Du, W. Hao, H. Xu, Y. Yu, T. Wang, Fabrication and Wettability of ZnO Nanorod Array, *J. Mater. Sci. Technol.* 25 (2009) 53-57.

[24] M. Guo, P. Diao, S. Cai, Highly hydrophilic and superhydrophobic ZnO nanorod array films, *Thin Solid Films* 515 (2007) 7162-7166.

[25] P.G. De Gennes, Wetting -Statics and Dynamics, *Rev. Mod. Phys.* 57 (1985) 827-863.

[26] D.P. Subedi, D.K. Madhup, A. Sharma, U.M. Joshi, A. Huczko, Study of the Wettability of ZnO Nanofilms, *Int. Nano Lett.* 1 (2011)117-122.

[27] V.D. Mote, Y. Purushotham, B.N. Dole, Williamson-Hall analysis in estimation of lattice strain in nanometer-sized ZnO particles, *Journal of Theoretical and Applied Physics* 6 (2012)1-8.

[28] C. Guillen, J. Herrero, Structure, optical and electrical properties of Al:ZnO thin films deposited by DC sputtering at room temperature on glass and plastic substrates, *Phys. Status Solidi A* 206 (2009) 1531-1536.

[29] S. Maniv, W.D. Westwood, E. Colombini, Pressure and angle of incidence effects in reactive planar magnetron sputtered ZnO layers, *J. Vac. Sci. Technol.* 20 (1982)162-170.

[30] M. Novotny, J. Cizek, R. Kuzel, J. Bulir, J. Lancok, J. Connolly, E. McCarthy, S. Krishnamurthy, J.-P. Mosnier, W. Anwand, G. Brauer, Structural characterization of ZnO thin films grown on various substrates by pulsed laser deposition, *J. Phys. D: Appl. Phys.* 45 (2012) 225101.

[31] S. Takayanagi, T. Yanagitani, M. Matsukawa, Wideband Multimode Transducer Consisting of c-Axis Tilted ZnO/c-Axis Normal ZnO Multilayer, *Jpn. J. Appl. Phys.* 51 (2012) 07GC08.

[32] C.F. Klingshirn, B.K. Meyer, A. Wagg, A. Hoffman, J. Geurts, Intrinsic Linear Optical Properties Close to the Fundamental Absorption Edge, in: R. Hull, C. Jagadish, R.M. Osgood, Jr., J. Parisi, Z. Wang, H. Warlimont (Eds.), *Zinc Oxide-From Fundamental Properties Towards Novel Applications*, Springer, Berlin, vol.120, 2010, pp.149-150.

[33] O.S. Heavens, *Optical Properties of Thin Solid Films*, Dover, New York, 1991, Chapter 4, pp.77.

[34] J.F. Muth, R.M. Kolbas, A.K. Sharma, S. Oktyabrsky, J. Narayan, Excitonic structure and absorption coefficient measurements of ZnO single crystal epitaxial films deposited by pulsed laser deposition, J. Appl. Phys. 85 (1999) 7884-7887.

[35] P.Y. Yu, M. Cardona, *Fundamentals of semiconductors: Physics and Materials Properties*, third ed., Springer, Berlin, 2010, Chapter 6, pp. 270.

[36] E.J. Johnson, H.Y. Fan, Impurity and Exciton Effects on the Infrared Absorption Edges of III-V Compounds, *Phys. Rev.* 139 (1965) A1991-A2001.

[37] J.G. Lu, S. Fujita, T. Kawaharamura, H. Nishinaka, Y. Kamada, T. Ohshima, Z.Z. Ye, Y.J. Zeng, Y.Z. Zhang, L.P. Zhu, H.P. He, B.H. Zhao, Carrier concentration dependence of band gap shift in n-type ZnO:Al films, *J. Appl. Phys.* 101 (2007) 083705.

[38] B.E. Sernelius, K.-F. Berggren, Z.-C. Jin, I. Hamberg, C.G. Granqvist, Band-Gap Tailoring of Zno by Means of Heavy Al Doping, *Phy. Rev. B* 37 (1988)10244-10248.

[39] B.C. Mohanty, Y.H. Jo, D.H. Yeon, I.J. Choi, Y.S. Cho, Stress-induced anomalous shift of optical band gap in ZnO:Al thin films, *Appl. Phys. Lett.* 95 (2009) 062103.

[40] A.B. Djurisic, Y.H. Leung, K.H. Tam, L. Ding, W.K. Ge, H.Y. Chen, S. Gwo, Green, yellow, and orange defect emission from ZnO nanostructures: Influence of excitation wavelength, *Appl. Phys. Lett.* 88 (2006)103107.

[41] A.B. Djurisic, Y.H. Leung, K.H. Tam, Y.F. Hsu, L. Ding, W.K. Ge, Y.C. Zhong, K.S. Wong, W.K. Chan, H.L. Tam, K.W. Cheah, W.M. Kwok, D.L. Phillips, Defect emissions in ZnO nanostructures, *Nanotechnology* 18 (2007) 095702.

[42] C.H. Ahn, Y.Y. Kim, D.C. Kim, S.K. Mohanta, H.K. Cho, A comparative analysis of deep level emission in ZnO layers deposited by various methods, *J. Appl. Phys.* 105 (2009) 013502.

[43] Z.-q. Xu, H. Deng, Y. Li, H. Cheng, Al-doping effects on structure, electrical and optical properties of c-axis-orientated ZnO:Al thin films, *Mater. Sci. Semicond. Process* 9 (2006) 132-135.

[44] M. Grundmann, H.V. Wenckstern, R. Pickenhain, T. Nobis, A. Rahm, M. Lorenz, Electrical properties of ZnO thin films and optical properties of ZnO-based nanostructures, *Superlattices Microstruct.* 38 (2005) 317-328.

[45] K. Nomura, H. Ohta, A. Takagi, T. Kamiya, M. Hirano, H. Hosono, Room-temperature fabrication of transparent flexible thin-film transistors using amorphous oxide semiconductors, *Nature* 432 **(**2004) 488-492.

[46] D.H. Zhang, T.L. Yang, J. Ma, Q.P. Wang, R.W. Gao, H.L. Ma, Preparation of transparent conducting ZnO:Al films on polymer substrates by r. f. magnetron sputtering, *Appl. Surf. Sci.* 158 (2000) 43-48.

[47] Q. Xu, R.D. Hong, H.L. Huang, Z.F. Zhang, M.K. Zhang, X.P. Chen, Z.Y. Wu, Laser annealing effect on optical and electrical properties of Al doped ZnO films, *Opt. Laser Technol.* 45 (2013) 513-517.

[48] S.B. Kim, W.W. Lee, J. Yi, W.I. Park, J.-S. Kim, Simple, Large-Scale Patterning of Hydrophobic ZnO Nanorod Arrays, W. T. Nichols, *ACS Appl. Mater. Interfaces* 4 (2012) 3910-3915.

[49] E.L. Papadopoulou, M. Barberoglou, V. Zorba, A. Manousaki, A. Pagkozidis, E. Stratakis and C. Fotakis, Reversible Photoinduced Wettability Transition of Hierarchical ZnO Structures, *J. Phys. Chem. C* 113 (2009) 2891-2895.

[50] E. McCarthy, R.T. Rajendra Kumar, B. Doggett, S. Chakrabarti, R.J. O'Haire, S.B. Newcomb, J.-P. Mosnier, M.O. Henry, E. McGlynn, Effects of the crystallite mosaic spread on integrated peak intensities in 2 theta-omega measurements of highly crystallographically textured ZnO thin films, *J. Phys. D: Appl. Phys.* 44 (2011) 375401.

[51] R.-Y. Yang, M.-H. Weng, C.-T. Pan, C.-M. Hsiung and C.-C. Huang, Low-temperature deposited ZnO thin films on the flexible substrate by cathodic vacuum arc technology, *Appl. Surf. Sci.* 257 (2011) 7119-7122.

[52] L. Gong, J. Lu and Z. Ye, Transparent and conductive Ga-doped ZnO films grown by RF magnetron sputtering on polycarbonate substrates, *Sol. Energy Mater. Sol. Cells* 94 (2010) 937-941.

[53] Y. Li, L. Xu, X. Li, X. Shen, A. Wang, Effect of aging time of ZnO sol on the structural and optical properties of ZnO thin films prepared by sol–gel method, *Appl. Surf. Sci.* 256 (2010) 4543-4547.

[54] F.K. Shan, Z.F. Liu, G.X. Liu, W.J. Lee, G.H. Lee, I.S. Kim, B.C. Shin, Y.S. Yu, Aging and Annealing Effects of ZnO Thin Films on GaAs Substrates Deposited by Pulsed Laser Deposition, *J. Electroceram.* 13 (2004) 195-200.

[55] F.K. Shan, B.I. Kim, G.X. Liu, Z.F. Liu, J.Y. Sohn, W.J. Lee, B.C. Shin, Y.S. Yu, Blueshift of near band edge emission in Mg doped ZnO thin films and aging, *J. Appl. Phys.*, 95 (2004) 4772-4776.

[56] F.K. Shan, G.X. Liu, W.J. Lee, G.H. Lee, I.S. Kim, B.C. Shin, Aging effect and origin of deep-level emission in ZnO thin film deposited by pulsed laser deposition, *Appl. Phys. Lett.* 86 (2005) 221910.

[57] J. Karamdel, C.F. Dee, B.Y. Majlis, Characterization and aging effect study of nitrogen-doped ZnO nanofilm, *Appl. Surf. Sci.* 256 (2010) 6164-6167.

[58] A. Guillén-Santiago, M. de la L. Olvera, A. Maldonado, R. Asomoza, D.R. Acosta, Electrical, structural and morphological properties of chemically sprayed F-doped ZnO films: effect of the ageing-time of the starting solution, solvent and substrate temperature, *phys. stat. sol. (a)* 201 (2004) 952-959.

[59] F. F. Vidor, G. I. Wirth, U. Hilleringmann, Low temperature fabrication of a ZnO nanoparticle thin-film transistor suitable for flexible electronics, *Microelectron Reliab.* 54 (2014) 2760-2765.

[60] S. J. Pearton, W. Lim, E. Douglas, F. Ren, Y. W. Heo, D. P. Norton, Oxide thin film transistors on novel flexible substrates, *Proceedings of SPIE* 7603 (2010) 760315.

Chapter 6

Conclusions and Outlook

6.1 PLD growth of cr-ZnO/am-ZnO core/shell nanorods on ZnO-seeded Si substrates: Self-organised growth and 3.331 eV luminescence

In section 4.1 of this thesis, we have reported for the first time the self-organised crystalline (cr)-ZnO/amorphous (am)-ZnO core/shell nanorods by pulsed laser deposition (PLD) on ZnO-seeded Si (100) substrates. These core/shell nanorods were grown without using a metal catalyst seed and without the need for a separate growth stage for the shell region. The structural, morphological and luminescent properties of the ZnO core/shell nanorod samples were established and show that the core/shell nanorods are highly textured with their *c*-axis oriented normal to the substrate surface, but without epitaxial in-plane ordering. The core/shell nanorods have a closely packed morphology and they also have conical terminations with rounded/blunt tips. A ZnO emission band at 3.331 eV is seen and its origin linked to the defects observed at the crystalline/amorphous interface of the core/shell

structure, specifically that the 3.331 eV emission arises from a single electron-hole pair recombination involving deeply bound constituents likely associated with the structural defects at the core/shell boundary interface region. This emission feature appears to have a different origin compared to the emissions at this energy reported by other workers and thus to be a new contribution to the body of knowledge concerned with ZnO nanostructures and their PL properties.

In section 4.2, we have grown crystalline (cr)-ZnO/amorphous (am)-ZnO core/shell nanorods in interconnected architectures. These interconnected cr-ZnO/am-ZnO core/shell nanorods were grown by catalyst free-PLD on ZnO-seeded Si (100) substrates. These deposits were characterised using x-ray diffraction, electron microscopies, photoluminescence and Raman spectroscopy, and four point probe/Hall effect instruments. The interconnected core/shell nanorods have a similar morphology to the previously discussed cr-ZnO/am-ZnO core/shell nanorods with a high degree of *c*-axis orientation. These nanorods also exhibit the characteristic emission at 3.331 eV. This study strongly supports our previous assignment concerning this defect related emission. No substantial differences in optical properties are seen following annealing at 500 °C. In terms of the electrical properties, the results reveal that the nanorods show good ohmic behaviour.

This work contains important new results in the field of ZnO nanorod growth and optical properties. Detailed characterisations of the ZnO nanorod samples were carried out and their analyses provide a deep physical insight into the nature of the new data reported. The most important findings are: (a) the self-organised growth of highly *c*-axis oriented cr-ZnO/am-ZnO core/shell nanorods without the need for (i) a separate shell growth and (ii) the use of a metal catalyst; (b) the formation of a crystalline ZnO core and an amorphous ZnO shell achieved as part of a unique two-staged sequence of growths at different temperatures and a single ambient oxygen pressure and (c) importantly, the identification of a emission band at 3.331 eV in the low temperature photoluminescence spectrum of the cr-ZnO/am-ZnO core/shell nanorods and its relationship with the defect structure observed at the irregular interface of the core-shell region.

We confirmed the origin of this emission from the 'interconnected cr-ZnO/am-ZnO core/shell nanorods' work (section 4.2), where this interconnected core/shell nanorod sample also exhibits this emission band with the same characteristic broad and asymmetric profile. Furthermore, the complete absence of this emission for either PLD-grown ZnO seed layer or VPT-grown ZnO nanorod samples (see section 6.2 below) further supports and strengthens our previous assignment on the origin of this emission band. Our extensive investigations on this defect-related ZnO emission contributes to an important increase in understanding of the different optically-active defects which contribute to the near-UV band edge photoluminescence in ZnO nanostructures, and the relationship of these defects to the nanostructure morphology is key to the choice of the optimum deposition methods and conditions for a particular application.

We believe that these features and properties of the cr-ZnO/am-ZnO core/shell nanorods would be advantageous in a number of state-of-the art applications based on the core/shell architecture. Specifically, the unique architecture and properties of the core/shell cr-ZnO/am-ZnO nanorods produced in this work should prove useful in applications where the functionality arises from the presence of an amorphous shell on a ZnO crystalline nanorod core. Examples of such applications would be in ZnO supercapacitor electrodes for energy storage, the passivation of ZnO photoanodes in dye-sensitized solar cells, or the control of the emission properties of ZnO nanolasers.

6.2 High optical quality ZnO nanorods on ZnO-seeded Si substrates: 3.331 eV luminescence

In section 4.3 of this thesis, we have also reported the growth of vertically aligned ZnO nanorods with excellent optical quality by catalyst-free vapour phase transport (VPT) on the PLD prepared ZnO-seeded Si (100) substrates. We have mainly compared the near band edge emission of such VPT nanorod deposits to the previously discussed PLD core/shell nanorod deposits (where identical PLD-grown ZnO seed layers were used for both VPT- and PLD-grown nanorods), with a focus on the identification of the origin of the 3.331 eV emission feature. The main difference between the PLD- and VPT-grown nanorod samples is the presence of the

3.331 eV emission in the former, and its complete absence in the latter (as well as in continuous PLD-grown seed layers) which was discussed in light of the differing surface morphologies and which provides strong support for our previous assignment of the origin of this defect to structural defects at the nanorod interface region.

The most important findings of this work are: (a) the nanorods are well separated and show smooth, facetted surfaces with a high *c*-axis orientation; (b) the nanorods also have a very high surface coverage density of ~ 18 per μm^2, compared to the previous literature; (c) importantly, the nanorods have an excellent optical quality, revealed by their low-temperature PL analyses and (d) finally, this study allows us to confidently assign the 3.331 eV emission to recombination at structural defects at the core/shell boundary region as this emission band was not seen for either the PLD-grown seed layer or VPT-grown nanorod samples.

6.3 Transparent and conductive ZnO and AZO nanocrystalline thin films on flexible Zeonor plastic substrates

Zeonor (a brand of COP) plastics are highly versatile due to exceptional optical and mechanical properties which make them the choice material in many novel applications. In section 5.1 and 5.2 of this thesis, we have investigated for the first time, the use of Zeonor as a flexible substrate for the deposition of high quality ZnO and Al-doped ZnO (AZO: 3 at% Al) thin films. Films were prepared by PLD at room temperature in oxygen ambient pressures between 1 and 300 mTorr. The growth rate, surface morphology, hydrophobicity and the structural, optical and electrical properties of as-grown films with thicknesses in the range 65 nm - 420 nm were measured. The films obtained are highly reproducible, with high optical transparency (> 90%), and optically very smooth (rms roughness ~ 4-8 nm for ZnO and ~ 1-2 nm for AZO). The films are also highly crystalline (average crystallite size ~ 4-22 nm for ZnO and ~ 3-18 nm for AZO) with strong *c*-axis orientation, and in-plane residual compressive stress in the ranges 2-7 GPa and 0.5-4 GPa for ZnO and AZO, respectively. Their electrical properties show low resistivities (10^{-2}-10^{-3} Ω cm for ZnO and 10^{-3}-10^{-4} Ω cm for AZO), high carrier concentrations (10^{20}-10^{21} cm^{-3} for

ZnO and 10^{21}-10^{22} cm^{-3} for AZO) and reasonable Hall mobilities (4-35 cm^2/Vs for ZnO and 1-18 cm^2/Vs for AZO). All films display a marked hydrophobic behaviour (water contact angle > 90°). Overall, the film properties are found to depend strongly on oxygen growth pressure and mildly on film thickness. The possible applications for these films are suggested. Furthermore, the effect of ageing on the properties of these films was also investigated over a 6-month period. This ageing study shows that the AZO samples have greater stability than the ZnO samples.

The work reported in this thesis shows that the high-quality ZnO and AZO electrodes can be successfully deposited at room temperature on amorphous, flexible Zeonor plastic substrates using PLD. The most important findings of this work are: (a) for the first time, Zeonor (a flexible, highly transparent (> 90%), low water absorption (< 0.01%) and hydrophobic) was used as a substrate for the deposition of high quality ZnO and AZO nanocrystalline thin films by PLD at room temperature; (b) we have successfully grown high transmittance, optically smooth, low stress, highly reproducible ZnO and AZO thin films at room temperature, which show hydrophobic surfaces; (c) we have extensively investigated the film properties as a function of thickness and oxygen ambient pressure, and shed light on the aspects of the growth mechanisms and (d) the large variations of film properties with oxygen growth pressure (especially for 40 and 1 mTorr range) will attract significant attention from a wide range of scientists working in many disciplines, especially in flexible TCO-based optoelectronics, as well as the PLD community.

The work broadly discussed in the context of current literature in the field of TCO growth on plastics. This work contains new and important results in the field of flexible TCOs for the flexible optoelectronic applications. In addition, as Zeonor plastics are a widely used material in many healthcare and medical applications, the work could also find applications in the fields such as microfluidics, biosensors and biofuel-cells.

Appendix A:

Nanostructured ZnO and AZO thin films grown by PLD on polycarbonate plastic substrates for glucose oxidase (GOx)-biosensor applications

A.1 Motivation

ZnO is a well-established material for bio-sensing applications due to its unique features such as a high catalyst efficiency, bio-compatibility, strong adsorption ability, electrochemical activity, good source material availability and long term environmental stability [1-6]. Importantly, ZnO has a high iso-electric point* of 9.3, which provides a suitable interface for proteins with the iso-electric point at acidic pH [2]. We note that more details of the ZnO material properties are discussed in section 2.1.

In recent years, ZnO nanostructures have attracted great attention for biosensor applications due to their high specific surface area, faster response and high sensitivity [2,4,5] compared with continuous films. The high iso-electric point of ZnO combined with its excellent material properties at room temperature allows the study of the electron transfer mechanisms of the enzyme (GOx) [1-3,7]. Two strategies can be used to improve the enzyme-ZnO nanostructures interaction: (i) modification of the ZnO nanostructure to improve the surface area and (ii) n-type doping to improve the free carrier concentration [1-5]. Previous studies have shown slightly improved enzyme loading on modified ZnO nanostructures [5,8]. However, such uniform nanostructures have proven difficult to reproduce [9]. Moreover, production of these nanostructures requires high temperatures in stringent experimental conditions [10]. In this thesis (section 5.1 and 5.2), we reported a highly reproducible growth of ZnO and AZO nanostructured films by room temperature PLD on Zeonor plastic substrates. In a similar context, we report here high quality ZnO and AZO nanostructured films on polycarbonate (PC) plastic substrates.

*iso-electric point is the pH at which a particular molecule carrier has zero net electrical charge.

PC features high optical transparency (90 %), temperature compatibility (145 °C), low-water absorption (0.2 %) and relatively low cost [11,12]. Because of the glass transition temperature of PC plastics being close to 145 °C, the deposition of high quality films needs to be carried out around 100 °C. PLD seems a highly suitable technique for these conditions (see section 2.2 for more details on PLD).

We now review the importance of doping in ZnO to study the electron transfer mechanisms of the enzyme in GOx-based bio-sensing applications. Doping is a common method to alter the electronic properties of ZnO thin films [13]. Aluminium (Al) and gallium (Ga) n-type dopants increase the concentration of free electrons, thus improving the conductivity of ZnO films [11,12,14,15]. Although Ga-doping causes a smaller deformation of the lattice [14], Al-doped ZnO (AZO) has a higher reactivity [15]. Furthermore, AZO has better optical transmittance [16] and *n*-type electrical properties [17,18]. Biosensors normally need a conductive bottom electrode for the efficient transfer of the electrons produced by biochemical reactions, and indium tin oxide (ITO) has been used extensively in this regard. However, the drawbacks associated with ITO such as limited source of the material and hence high cost, and relative toxicity have limited its usage [3]. We note that Saha and Gupta [3] have reported an Al- and Fe- co-doped ZnO-based biosensor on glass substrates, thus, obviating the need for a bottom electrode. Therefore, AZO is a suitable material for studying enzyme-nanostructured film interfacial interaction, as the reaction kinetics depends on the charge transfer resistance at the film surface. However, the possible changes that doping brings about in regard of the enzyme immobilization and activity remain largely unexplored.

We report for the first time the use of high quality transparent and conductive ZnO and AZO nanostructured thin films, grown by PLD on PC substrates, for GOx-based biosensing application.

A.2 Growth details

We have used PLD apparatus (see section 2.2 for more details) to grow ZnO and AZO nanostructured thin films on 1 cm × 2 cm rectangular sheets of 1.2 mm thick polycarbonate (Lexan 9030) substrates. The deposition chamber was pumped

down to the base pressure of 3×10^{-5} mTorr (3.9×10^{-6} Pa) for all the depositions. The oxygen pressure in the chamber was kept at 10 mTorr and 30 mTorr for the ZnO and AZO thin films, respectively. The substrate temperature was raised to 100 °C and kept constant for the whole deposition. Ten thousand laser shots were used for the depositions of duration around 15 min, after which the substrate temperature was lowered to 30 °C.

The nanostructured thin films were characterised using X-ray diffraction (XRD), optical transmission and four point probe electrical measurements. The electro-kinetics and the charge transfer mechanisms at the GOx-ZnO/AZO thin films interface have been studied using cyclic voltammetry (CV), chronoamperometry (CA) and electrochemical impedance spectroscopy (EIS). The nature of the interfacial interactions was studied using x-ray photoelectron spectroscopy (XPS). This work was conducted in collaboration with the Department of Biotechnology, Indian Institute of Technology-Madras (IITM), Chennai, India. The samples were prepared by ourselves at the laboratories of the School of Physical Sciences, DCU and the characterisation experiments were conducted by our collaborators at the laboratories of IITM, India.

A.3 Results and discussions

Figure A.1 (a) shows the nanostructured morphologies of the ZnO and AZO films. For the AZO films, clear nanostructured grains were observed with typical sizes around 20-30 nm. Quite similar nanostructures were also seen for ZnO films grown by PLD on PC substrates, as shown in the inset. Previous works have shown that nanostructured ZnO films can be grown by PLD on glass [19], sapphire [20], Perspex (or PMMA) [21] and Zeonor [22] substrates with a similar nanostructured grain morphology. From the XRD pattern (Fig A.1 (b)), 2θ values for the ZnO and AZO films were seen at around $2\theta \approx 34.4^{o}$. These correspond to the (002) reflections of the wurzite structure showing a preferred *c*-axis orientation for the ZnO and AZO thin films. The crystallite sizes of the deposited films were measured using the Scherrer equation and the results were 38 nm and 23 nm for ZnO and AZO, respectively. Software analyses (Xpert high score) of the diffraction peak profiles

also indicated higher lattice strain for AZO than for ZnO thin film, likely due to aluminium lattice incorporation.

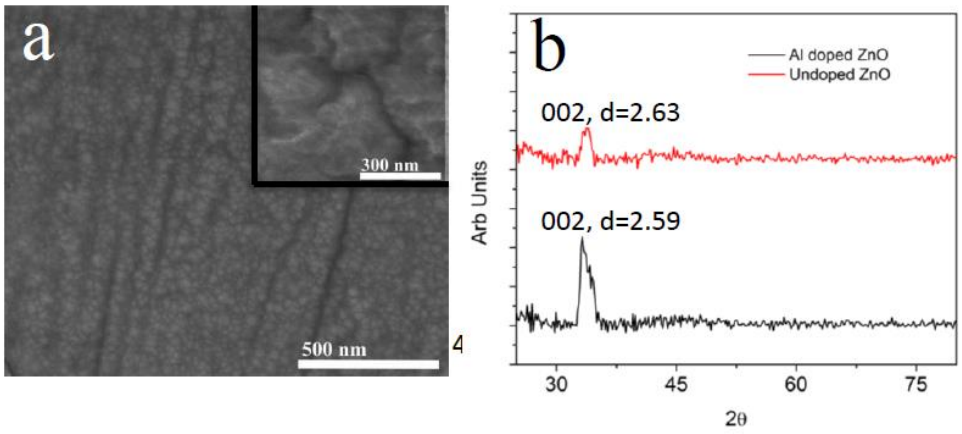

Figure A.1: (a) SEM morphology of the nanostructured AZO film, ZnO film is in the inset and (b) 2θ-ω XRD scans of the ZnO and AZO films (These experiments were performed at IITM laboratories).

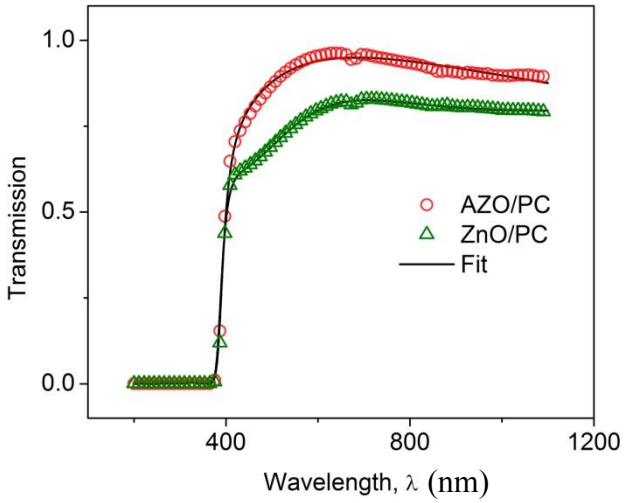

Figure A.2: Measured and fitted optical transmission spectra of undoped ZnO thin films and Al-doped ZnO (AZO) thin films (These experiments were performed at IITM laboratories).

In Figure A.2, the transmission spectra between 200 nm and 1100 nm of the ZnO and AZO films are presented. The thickness and the optical band gap of the deposited thin films were estimated by fitting the transmission spectra using the Scout 2 software [23]. A non-linear least square fitting algorithm was used to extract the optical constants of the films, from transmittance data alone, based on a

composite model for the complex dielectric function. The model assumes parabolic bands in the UV-vis region and a Drude model in the NIR region. The thicknesses thus obtained for the ZnO and AZO thin films were approximately 132 nm and 90-100 nm, respectively. The small difference observed for the lower visible transparency of the ZnO films can be accounted by the thickness difference and the oxygen pressure difference [24,25]. The fitted optical band gap for ZnO was 3.24 eV whereas for AZO it was estimated to be around 3.35 eV, which are comparable with the values of previous works [26,27].

The electrical measurements showed that both AZO and ZnO thin films have a sheet resistance in the range of 4000 Ω/sq corresponding to a bulk resistivity of about 0.04 Ω cm indicative of good conductive properties [17]. From the Hall measurements, *n*-type (electron) sheet concentrations of 1.44×10^{15} cm^{-2} and 6×10^{14} cm^{-2} for the AZO and ZnO thin films, respectively, were obtained.

Other characterisations such as XPS, CV, CA and EIS were performed to explore the nature of the electrical interactions of ZnO and AZO nanostructured thin films with the enzyme glucose oxidase (GOx) and performed by our collaborators. These results and analyses will be published later.

A.4 Conclusions

We have grown nanostructured ZnO and AZO thin films on polycarbonate plastic substrates by PLD at 100 °C substrate temperature. The films displayed *c*-axis orientation with good crystalline, optical and electrical quality. These films are used by our collaborators to immobilise the enzyme glucose oxidase (GOx) and assess the potential use of the GOx/AZO/PC material system for bio-sensing applications.

A.5 References

[1] S. Saha, M. Tomar, V. Gupta, Fe doped ZnO thin film for mediator-less biosensing application, *J. Appl. Phys.* 111 (2012) 102804.

[2] S.K. Arya, S. Saha, J.E. Ramirez-Vick, V. Gupta, S. Bhansali, S.P. Singh, Recent advances in ZnO nanostructures and thin films for biosensor applications: review, *Anal. Chim. Acta.* 737 (2012) 1-21.

[3] S. Saha, V. Gupta, Al and Fe co-doped transparent conducting ZnO thin film for mediator-less biosensing application, *AIP Adv.* 1 (2011) 042112.

[4] J. Wang, X.W. Sun, A. Wei, Y. Lei, X.P. Cai, C.M. Li, Z.L. Dong, Zinc oxide nanocomb biosensor for glucose detection, *Appl. Phys. Lett.* 88 (2006) 233106.

[5] Z. Dai, G. Shao, J. Hong, J. Bao, J. Shen, Immobilization and direct electrochemistry of glucose oxidase on a tetragonal pyramid-shaped porous ZnO nanostructure for a glucose biosensor, *Biosens. Bioelectron.* 24 (2009) 1286-1291.

[6] Y.Q. Fu, J.K. Luo, X.Y. Du, A.J. Flewitt, Y. Li, G.H. Markx, A.J. Walton, W.I. Milne, Recent developments on ZnO films for acoustic wave based bio-sensing and microfluidic applications: a review, *Sensors Actuat. B-Chem.* 143 (2010) 606-619.

[7] A. Janotti, Van de Walle, Chris G, Fundamentals of zinc oxide as a semiconductor, *Rep Prog Phys.* 72 (2009) 126501.

[8] S.U. Ali, M. Kashif, Z.H. Ibupoto, M. Fakhar-e-Alam, U. Hashim, M. Willander, Functionalised zinc oxide nanotube arrays as electrochemical sensors for the selective determination of glucose, *Micro Nano Lett.* 6 (2011) 609-613.

[9] D. Panda, T.-Y. Tseng, One-dimensional ZnO nanostructures: fabrication, optoelectronic properties, and device applications, *J. Mater. Sci.* 48 (2013) 6849-6877.

[10] Z.L. Wang, Zinc oxide nanostructures: growth, properties and applications, *J. Phys: Condens. Matter* 16 (2004) R829-R858.

[11] L. Gong, J. Lu, Z. Ye, Transparent and conductive Ga-doped ZnO films grown by RF magnetron sputtering on polycarbonate substrates, *Sol. Energy Mater. Sol. Cells* 94 (2010) 937-941.

[12] Y. Liu, Q. Li, H. Shao, Properties of ZnO: Al films deposited on polycarbonate substrate, *Vacuum* 83 (2009) 1435-1437.

[13] Y. Liu, Y. Li, H. Zeng, ZnO-based transparent conductive thin films: doping, performance, and processing, *J. Nanomater.* 2013 (2013) 196521.

[14] S. Chang, Post-annealed gallium and aluminum co-doped zinc oxide films applied in organic photovoltaic devices, *Nanoscale Res. Lett.* 9 (2014) 562.

[15] M.-C. Jun, S.-U. Park, J.-H. Koh, Comparative studies of Al-doped ZnO and Ga-doped ZnO transparent conducting oxide thin films, *Nanoscale Res. Lett.* 7 (2012) 639.

[16] H. Hagendorfer, K. Lienau, S. Nishiwaki, C.M. Fella, L. Kranz, A.R. Uhl, D. Jaeger, L. Luo, C. Gretener, S. Buecheler, Y.E. Romanyuk, A.N. Tiwari, Highly

Transparent and Conductive ZnO: Al Thin Films from a Low Temperature Aqueous Solution Approach, *Adv. Mater.* 26 **(**2014) 632-636.

[17] J.G. Lu, Z.Z. Ye, Y.J. Zeng, L.P. Zhu, L. Wang, J. Yuan, B.H. Zhao, Q.L. Liang, Structural, optical, and electrical properties of (Zn,Al)O films over a wide range of compositions, *J. Appl. Phys.* 100 (2006) 073714.

[18] J.G. Lu, S. Fujita, T. Kawaharamura, H. Nishinaka, Y. Kamada, T. Ohshima, Z.Z.Ye, Y.J. Zeng, Y.Z. Zhang, L.P. Zhu, H.P. He, B.H. Zhao, Carrier concentration dependence of band gap shift in n-type ZnO:Al films, *J. Appl. Phys.* 101 (2007) 083705.

[19] J.P. Mosnier, R.J. O'Haire, E. McGlynn, M.O. Henry, S.J. McDonnell, M.A. Boyle, K.G. McGuigan, ZnO films grown by pulsed-laser deposition on soda lime glass substrates for the ultraviolet inactivation of Staphylococcus epidermidis biofilms, *Sci. Techno. Adv. Mater.* 10 (2009) 045003.

[20] R. O'Haire, E. McGlynn, M.O. Henry, J.-P. Mosnier, ZnO nanostructured thin films grown by pulsed laser deposition in mixed O_2/Ar background gas, *Superlat. Microstruct.* 42 (2007) 468-472.

[21] J. Connolly, A. Jain, G. Pastorella, S. Krishnamurthy, J.-P Mosnier, E. Marsili, Zinc oxide and indium tin oxide thin films for the growth and characterization of Shewanella loihica PV-4 electroactive biofilms, *Virulence* 2 (2011) 479-482.

[22] S. Inguva, R.K. Vijayaraghavan, E. McGlynn, J.-P. Mosnier, Highly transparent and reproducible nanocrystalline ZnO and AZO thin films grown by room temperature pulsed-laser deposition on flexible Zeonor plastic substrates, *Mater. Res. Express* 2 (2015) 096401.

[23] Web ref- http://www.mtheiss.com/scout2.htm (last accessed on 5th Oct 2015).

[24] B.L. Zhu, X.Z. Zhao, S. Xu, F.H. Su, G.H. Li, X.G. Wu, J. Wu, R. Wu, J. Liu, Oxygen pressure dependences of structure and properties of ZnO films deposited on amorphous glass substrates by pulsed laser deposition, *Jpn. J. Appl. Phys.*47 (2008) 2225-2229.

[25] P. Gondoni, M. Ghidelli, F. Di Fonzo, M. Carminati, V. Russo, A.L. Bassi, C.S. Casari, Structure-dependent optical and electrical transport properties of nanostructured Al-doped ZnO, *Nanotechnology* 23 (2012) 365706.

[26] E.L. Papadopoulou, M. Varda, K. Kouroupis-Agalou, M. Androulidaki, E. Chikoidze, P. Galtier, G. Huyberechts, E. Aperathitis, Undoped and Al-doped ZnO

films with tuned properties grown by pulsed laser deposition, *Thin Solid Films* 516 (2008) 8141-8145.

[27] H. Kim, A. Pique, J.S. Horwitz, H. Murata, Z.H. Kafafi, C.M. Gilmore, D.B. Chrisey, Effect of aluminum doping on zinc oxide thin films grown by pulsed laser deposition for organic light-emitting devices, *Thin Solid Films* 377 (2000) 798-802.

Appendix B:

Atmospheric air plasma treatment of graphite and carbon felt electrodes to attach of *Shewanella* cells in a bio-fuel cell application

B.1 Motivation

We briefly review the background and importance of atmospheric air plasma treatments of graphite and carbon-felt (CF) electrodes for the attachment of *S. loihica* PV-4 cells in bio-fuel cell applications. The use of atmospheric air plasmas for surface treatment is well established [1,2]. The combination of the main plasma parameter values, such as discharge voltage (kV), power density (W cm^{-2}), discharge gap (mm) and treatment time (s), determines the nature of the possible plasma surface processes. These processes can be broadly classified as etching, cleaning, film deposition, ion implantation, oxidation or functionalisation. The last two processes are relevant to the present work and are also dependent on the nature of the surface e.g. metal, ceramic, polymer or glass. The formation of functional groups on the surface of electrodes results from chemical reactions between gaseous plasma active species, e.g. OH radicals, ozone and atomic oxygen species, and reactive surface species/sites over a depth of 1 nm. Functionalisation is known to significantly improve the wettability and adhesion properties of a plasma-treated surface as it generally increases the surface energy. The effects of atmospheric air and oxygen plasmas on graphite [3,4], carbon-based [5] e.g. carbon nanotubes [6-8] or carbon felt [9,10] and hydrocarbon polymer [11] surfaces, have been studied. All these works report significant oxidation of the surfaces with the formation of oxygen-rich polar groups like carbonyl, acetals or carboxyl groups, depending on the experimental conditions, e.g. relative humidity and plasma parameters [3-5,11]. A notable concomitant effect of plasma surface treatment is the increase in surface roughness [11,12]. The effects of plasma processing/treatment on biomaterials are similar to those just described [13].

Previous works have considered the effects of plasma treatment of surfaces or electrodes for increased adhesion of bacterial cells, notably in the context of biofuel

cell applications. Bax et al. [14] have applied plasma treatment to polymeric surfaces to improve eukaryotic biofilm formation and bio-adhesion, thus improving the tissue–polymer interface. Kamgang et al. [15] showed that treatment with atmospheric air plasma rendered the polymer surface more hydrophilic, thus improving bacterial cell attachment and electricity production at anodes, despite electrostatic repulsion between cells and the electrode. Radiofrequency generated-plasmas have also been beneficially used for electrode surface treatments. For example, Flexer et al. [16] demonstrated that radio-frequency oxygen and nitrogen plasma treatment of electrodes increased the initial anodic current from a mixed microbial consortium, with faster cellular adhesion on the electrode surface and higher biofilm growth. Using radio-frequency oxygen-plasma treatment, Okajima et al. [17] showed that surface functionalisation with hydrophilic groups on a carbon fiber surface also increased its surface capacitance by 28% for a specific oxygen gas feed concentration. To the best of our knowledge, this effect has not been reported in works using atmospheric air plasmas. Interestingly, He et al. [18] used plasma-based N^+ ion implantation to treat the carbon paper anode in a microbial fuel cell and showed significantly enhanced electricity production as a result. In spite of the promising results achieved with both radio-frequency plasma reactors and plasma-based ion implanters, atmospheric air plasma seems to be a more economically viable technique for the routine treatment of large electrodes as it does not require vacuum chambers/systems and gas manifolds, and thereby minimises the overall cost.

In our research [19], we investigate for the first time the effects of atmospheric air plasma treatment on surface roughness, water contact angle/wettability and the current output from attached *S. loihica* PV-4 cells on polished graphite and unpolished carbon felt electrodes. We demonstrate that plasma treatment increases the maximum current output and adsorption of microbially produced flavins is the main driver for electricity production. The results are presented below in section B.4. This work was conducted as part of a collaboration with the School of Biotechnology, DCU. We present only the physics related experiments performed by us as part of this thesis work.

B.2 Dielectric barrier discharge (DBD)

We have produced atmospheric air plasma using DBD experimental set up. In this section, we describe the background and experimental details of DBD set up.

B.2.1 Background on DBD

In 1857, a German scientist named Siemens first proposed an electrical discharge for "ozonizing" air. In detail, suppose atmospheric pressure air or oxygen gas passes through a narrow annular space in a double-walled cylindrical glass vessel constituting an electrode. Inside this cylindrical electrode, the outer tube is wrapped around the inner tube, similar to Figure B.1 (b). These were used to apply an alternating electrical field. If this electrical field has a sufficient energy (~ 1 eV), then it can caused a breakdown of the gases inside the annular discharge gap. Because of this discharge, a part of oxygen gas is converted into ozone. Here, the glass walls act as dielectric barriers (see ref [1] for more details on the DBD background) and have a strong influence on the discharge properties. This device is referred to as a dielectric barrier discharge (DBD). It produces non-equilibrium discharge plasma, in which chemical reactions happen among the electrons, ions and free radicals produced. The comprehensive details of the air plasma chemistry can be found in ref [1]. The control over the non-equilibrium atmospheric plasmas and their simple production methods are the main advantages of the DBD set up. DBD was used originally to generate ozone. However, DBD has many additional advantages in surface treatments, generation of UV radiation in excimer lamps, IR radiation in CO_2 lasers, flat plasma display panels, Hg-free fluorescent lamps and biomedical applications [1,20].

B.2.2 DBD experimental set up

The DBD apparatus (see Figure B.1) consists of two planar electrodes made up of two wooden formers covered by a dielectric material, and separated by a narrow air gap. DBD set up is operated at an atmospheric pressure with a high applied voltage to the electrodes in a range typically from 1 to 20 kV, and with the frequencies ranging from a few hundred Hz to a few kHz. In DBDs, the dielectric material (wooden former with turns of plastic (sheath around the cabling) act as the dielectric) placed between the electrodes plays an important role to keep the non-equilibrium nature of the discharge. As mentioned in the earlier section, when a

sufficiently high voltage is applied to the electrodes, the gas breaks down and ionisation occurs (plasma formation). This allows the flow of an electrical current in the gas. Because of the electrical current, the electrical charges start accumulates on the surface of the dielectric. This now creates an electrical potential between the electrodes in the DBD set up, which counteracts the externally applied voltage and limits the current flow [1].

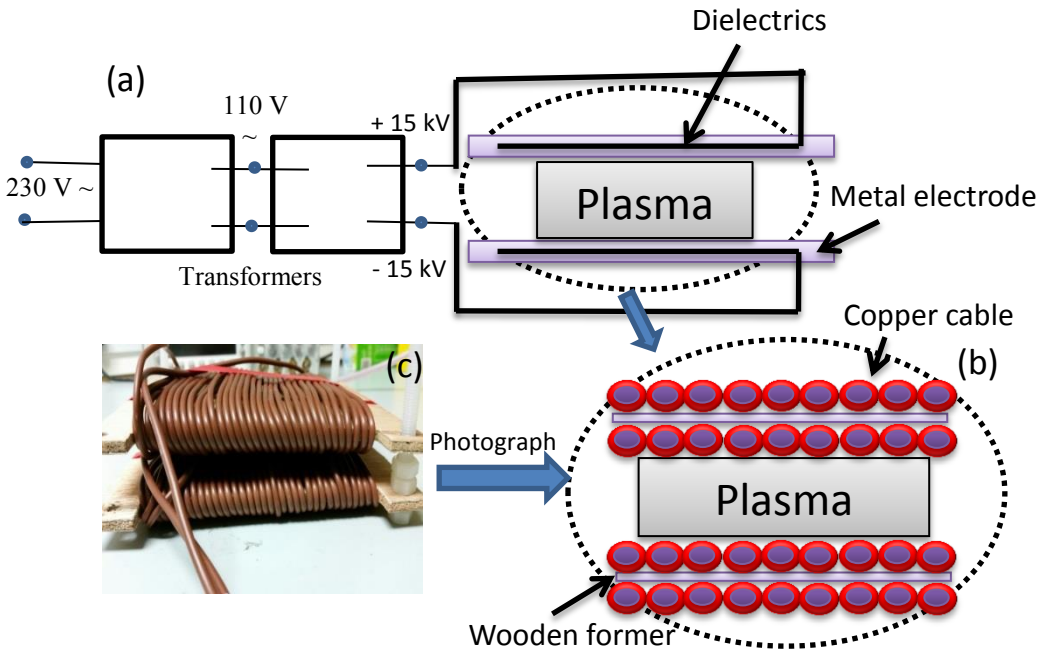

Figure B.1: (a) Schematic representation of DBD configuration, (b) close up view of electrode cross section, and (c) showing photograph view of (b).

The DBD apparatus used in this work is described (Figure B.1) in refs [20, 21]. DBD plasmas are out of equilibrium (non-thermal) plasmas characterised by electron temperatures of the order ~ 1 eV while the gas remains at room temperature. This is because of the abundant production of reactive oxygen species such as ozone and atomic oxygen. The samples were placed inside a 5 L commercial polyethylene zip-lock bag. The plastic package ensures containments of the active gaseous species during operation. The plastic bag was flushed with an ambient air, then zip-locked. This was kept in-between the two high-voltage discharge electrodes separated by a 1 cm gap. The high-voltage of 15 kV with a 50 Hz source frequency was switched on for 120 seconds. These treatment parameters were produced a discharge power of ~

0.1 Wcm^{-2}. These operation conditions including plasma treatment time are typical of those required for surface functionalisation using DBD air-plasma treatment [19].

B.3 Experimental details

The CF and graphite (isotropic graphite Grade 347 from Tokai Carbon Co. Japan) sheets were both cut into 2 × 1 × 0.2 cm electrodes, defining a total surface area of 5.2 cm^2. Current output values were normalised to the electrode surface area. The graphite electrodes were sanded with either P240 (grit diameter 58.5 μm), P400 (grit diameter 35 μm) or P600 (grit diameter 25.8 μm), P-graded sandpapers in order to obtain different surface roughness. The roughest graphite electrode surface was thus obtained by polishing with P240 sandpaper. All electrodes were cleaned overnight in 1 M of HCl and then stored in deionised water.

Atomic force microscopy (AFM) was used to determine the surface morphology of the P240, P400, and P600 graphite electrodes. CF electrodes could not be imaged with AFM, as the AFM tip remained entangled in the CF thin fiber. Images were taken in tapping mode, using standard aluminium coated silicon AFM probe (Tap 300Al-G, Budget Sensors, Bulgaria) with a force constant of 40 $N\text{-}m^{-1}$. The AFM images were acquired by scanning areas of dimensions 20 μm ×20 μm with a fixed resolution of 512 pixels × 512 pixels. The details of the AFM instrument were discussed earlier in section 3.3. Although a precise evaluation of the resolution would require the knowledge of the AFM tip shape and size, we can estimate, from the knowledge of standard AFM performance and the present acquisition conditions, the lateral and vertical (z-axis) resolutions to be at least 50 nm and greater than 1 nm, respectively. The latter value, quite lower than typical AFM performance, is due to the inherent roughness of the bare graphite electrode [22], which tends to blunt the tip during scans. Where possible, AFM scans for the electrodes were repeated several times at different locations over the electrode surface. The surface rms roughness (R_q) of each electrode was evaluated from image pixel data analyses using the WSXM software [23]. The R_q value is specified in this work, instead of the average roughness (R_a), as R_q is more sensitive to large differences in the surface peaks and valleys, which allows for the effects of plasma treatment at the sub-μm level to be better ascertained.

In order to investigate the wettability of the graphite and CF electrodes for before and after air plasma treatments, we have performed water contact angle (WCA) experiments. The WCA apparatus and procedures were discussed earlier in section 3.6.

B.4 Results and discussions

B.4.1 Effect of air plasma treatments on electrode roughness and current output in *S. loihica* PV-4 attached cells

Previous studies of Marsili et al. [24] with *G. sulfurreducens* biofilms have shown that the rougher surface obtained with sandpaper polishing treatment increased the current output in electrochemically active biofilms. Here we obtained similar results with P240, P400, and P600 sanded graphite electrodes. The lag phase increased with the P-grade of the sandpaper used, e.g., 240 < 400 < 600, from 2 to 6 hr and the maximum current density in the initial growth phase (approx. 15–20 hr) decreased from 104 ± 9 to 67±2 and 67±2 μA cm^{-2}, respectively (see Figure 1 in ref [19], i.e. our publication on this work). These results are consistent with slow attachment and growth of the biomass on smoother electrodes. Both surface topography and chemistry determine current output enhancement in electrochemically active biofilms [25]. The surface rms roughness of the polished graphite electrodes calculated from the AFM images (see Figure B.2 shown below) of the P240, P400 and P600 graphite electrodes were 0.74 ± 0.14, 0.86, and 1.14 μm, respectively. The relative uncertainty on the rms roughness for the P400 and P600 graphite is likely to be comparable to the P240 surface and thus at least 20%. Therefore, these differences in surface roughness are marked but not significant from the viewpoint of the sandpaper P-grade (see grit diameters quoted above). The surface roughness of P240 graphite electrodes increased by 75% to 1.301 μm after plasma treatment, as expected and in accordance with previous works [11,12]. The AFM results show the surface roughness at the nm scale level while the SEM images (see supplementary material in ref [19], i.e. our publication on this work) show surface topography details at the μm scale level.

Following plasma treatment, the lag phase on P240 graphite electrodes increased from approximately 1 to 5 hr and the current slope, roughly corresponding to cell attachment rate, increased by 45%, while the maximum current density did not change significantly (101±1.5 μA cm^{-2}, n=3) with respect to the untreated P240 graphite electrodes (see Figure 1 in ref [19], i.e. our publication on this work). Interestingly, the current stabilised sooner for the plasma treated electrode but decreased rapidly after the maximum (data not shown). This might be due to diffusional limitations at the interface cells/electrode caused by rapid cell attachment. We note that the current output experiments were performed by our collaborators at the School of Biotechnology, DCU.

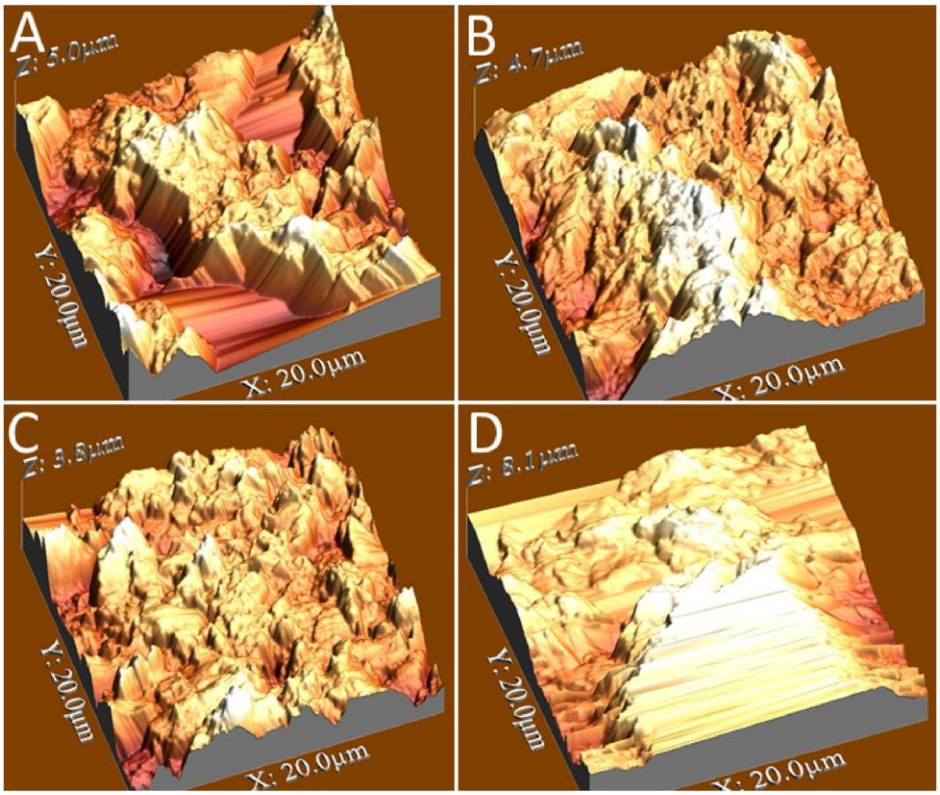

Figure B.2: AFM images of graphite electrodes. (A) P600, (B) P400, (C) P240 and (D) plasma treated P240 graphite electrodes.

B.4.2 Effect of air plasma treatments on the electrode wettability

The air plasma treatments are observed to be affected the WCA very significantly for the CF electrodes (see Figure B.3). Before the plasma treatments, the water was completely absorbed by the CF electrode and hence a WCA of 0° was

realised. Interestingly, after the plasma treatment the WCA of the same CF electrode is increased to 108°, indicating a hydrophobic behaviour. In case of graphite electrodes, the increase in WCA is not very significant, especially for P400 electrode, where its WCA increased from 55° to 68°. However, the WCA for the P240 and P600 electrodes increased significantly from 43° to 87° and 31° to 72°, respectively. We note that the WCA values for the graphite electrodes can be partially correlated with their grit diameters. As mentioned earlier, the grit diameter of P240 and P400 is greater than the P600 electrodes. Hence, the WCA of P240 and P400 electrodes is also greater than the P600 electrode by considering the error bars. All graphite electrodes show a hydrophilic behaviour.

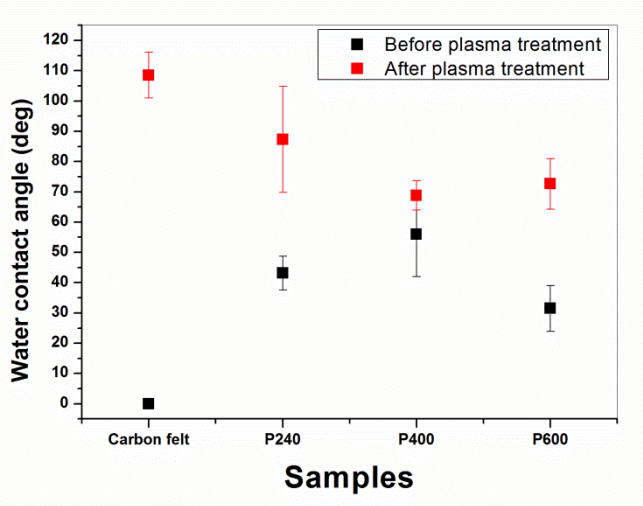

Figure B.3: WCA results of graphite (P600, P400 and P240) and CF electrodes for the before and after air plasma treatments.

The increase in WCA with plasma treatments has been observed previously by several authors. For example, Shiu et al. [26] have observed the increase in WCA with oxygen plasma treatments on Polystyrene nanospheres. Furthermore, Tsougeni et al. [27] have also observed the increase in WCA with oxygen plasma treatments on Polydimethylsiloxane (PDMS) surface coated with Teflon. The formation of functional groups result from chemical reactions between gaseous plasma active species, e.g. OH radicals, ozone and atomic oxygen species, and reactive surface species/sites over a depth of 1 nm is the reason for the WCA increase. Furthermore, we note that functionalisation is known to significantly improve the wettability and adhesion properties of a plasma-treated surface as it generally increases the surface

energy [1,19]. We also note that the increase in WCA with plasma treatment mainly depends on the duration of the plasma treatment and the type of the electrode or substrate used for the treatment. For example, Kamgang et al. [15] have observed the reverse behaviour compared to present work. They showed that the treatment with atmospheric air plasma render the surface of polymers (AISI stainless steel (SS), polytetrafluoroethylene (PTFE) and low density polyethylene (LDPE)) to more hydrophilic. However, their plasma treatment durations were very high (in a range of 0-300 sec) and hence their results were not accurately comparable with the present study. Overall, the WCA studies showed that the plasma treatments modified the CF electrode from a complete water absorption state to a good hydrophobic (WCA ~ 108°) behaviour. The plasma treatments improved the hydrophilic behaviour of the graphite electrodes at about 50 %.

B.5 Conclusions

In this appendix section and our publication based on this work [19], we have investigated the effects of atmospheric air plasma treatments on the surface roughness, wettability and the current output from electrochemically active biofilms formed by the model organism *S. loihica* PV-4 on polished graphite and carbon felt electrodes. The plasma treatments were shown to be improved the surface rms roughness and thus, improve the adhesion of the bacteria cells. The plasma treatments were also observed to be improved the wettability of the electrodes. This improvement was very significant in case of carbon felt electrodes. This work suggests that plasma treatment is a feasible option to increase power output in bioelectrochemical systems in the absence of microbially produced redox mediators.

The most important findings of this work are: (a) the work reported shows a low-cost, easily scaled-up and user friendly route of air plasma treatments to increase the current output in bio-electrochemical systems; (b) the work also shows that the air plasma treatments used marginally improves the maximum current output on graphite electrodes and significantly increases the maximum current output for carbon felt electrodes through increased cellular attachment (due to increased surface roughness) and not by adsorption of microbially produced flavins.

The atmospheric air plasma set up used in this work seems to be a more viable technique for the routine plasma treatment of large electrodes as it does not require vacuum chambers/systems and gas manifolds, and thereby minimises the overall cost significantly. Hence, this work opens up a new route for the low-cost air-plasma treatments based bio-fuel cells.

B.6 References

[1] K.H. Becker, U. Kogelschatz, K.H. Schoenbach, R.J. Barker (Eds.), *Non-Equilibrium Air Plasmas at Atmospheric Pressure, Institute of Physics Series in Plasma Physics*, IOP Publishing Ltd, 2005.

[2] J. Reece Roth, *Industrial plasma engineering, Applications to nonthermal plasma processing*, Vol. 2, *IOP Publishing Ltd*., Bristol, 2001.

[3] U. Cvelbar, B. Markoli, I. Poberaj, A. Zalar, L. Kosec, S. Spaic, Formation of functional groups on graphite during oxygen plasma treatment, *Appl. Surf. Sci.* 253 (2006) 1861-1865.

[4] M.K. Seo, S.J. Park, S.K. Lee, Influence of atmospheric plasma on physicochemical properties of vapor-grown graphite nanofibers, *J. Colloid Interface Sci.* 285 (2005) 306-313.

[5] R.J. Zaldivar, J. Nokes, G.L. Steckel, H.I. Kim, B.A. Morgan, The effect of atmospheric plasma treatment on the chemistry, morphology and resultant bonding behaviour of a pan-based carbon fiber-reinforced epoxy composite, *J. Compos. Mater.* 44 (2010) 137-156.

[6] M.V. Naseh, A.A. Khodadadi, Y. Mortazavi, F. Pourfayaz, O. Alizadeh, M. Maghrebi, Fast and clean functionalization of carbon nanotubes by dielectric barrier discharge plasma in air compared to acid treatment, *Carbon* 48 (2010) 1369-1379.

[7] Z. Hou, B. Cai, H. Liu, D. Xu, Ar, O_2, CHF_3 and SF_6 plasma treatments of screen-printed carbon nanotube films for electrode applications, *Carbon* 46 (2008) 405-413.

[8] T.I.T. Okpalugo, P. Papakonstantinou, H. Murphy, J. McLaughlin, N.M.D. Brown, Oxidative functionalization of carbon nanotubes in atmospheric pressure filamentary dielectric barrier discharge, *Carbon* 43 (2005) 2951-2959.

[9] J.-Z. Chen, W.-Y. Liao, W.-Y. Hsieh, C.-C. Hsu, Y.-S. Chen, All-vanadium redox flow batteries with graphite felt electrodes treated by atmospheric pressure plasma jets, *J. Power Sources* 274 (2015) 894-898.

[10] K.J. Kim, Y.-J. Kim, J.-H. Kim, M.-S. Park, The effects of surface modification of carbon felt electrodes for use in vanadium redox flow batteries, *Mater. Chem. Phys.* 131 (2011) 547-553.

[11] N.-Y. Cui, N.M.D. Brown, Modification of the surface properties of a polypropylene (PP) film using an air dielectric barrier discharge plasma, *Appl. Surf. Sci.* 189 (2002) 31-38.

[12] U. Cvelbar, S. Pejovnik, M. Mozetiè, A. Zalar, Increased surface roughness by oxygen plasma treatment of graphite/polymer composite, *Appl, Surf. Sci.* 210 (2003) 255-261.

[13] P.K. Chu, J.Y. Chen, L.P. Wang, N. Huang, Plasma-surface modification of biomaterials, *Mater. Sci. Eng. R* 36 (2002) 143-206.

[14] D.V. Bax, A. Kondyurin, A. Waterhouse, D.R. McKenzie, A.S. Weiss, M.M.M. Bilek, Surface plasma modification and tropoelastin coating of a polyurethane co-polymer for enhanced cell attachment and reduced thrombogenicity, *Biomaterials* 35 (2014) 6797-6809.

[15] J.O. Kamgang, M. Naitali, J.M. Herry, M.N. Bellon-Fontaine, J.L. Brisset, R. Briandet, Increase in the hydrophilicity and Lewis acid–base properties of solid surfaces achieved by electric gliding discharge in humid air: Effects on bacterial adherence, *Plasma Sci. Technol.* 11 (2009) 187-193.

[16] V. Flexer, M.Marque, B.C. Donose, B. Virdis, J. Keller, Plasma treatment of electrodes significantly enhances the development of anodic electrochemically active biofilms, *Electrochim. Acta* 108 (2013) 566-574.

[17] K. Okajima, K. Ohta, M. Sudoh, Capacitance behavior of activated carbon fibers with oxygen-plasma treatment, *Electrochim. Acta* 50 (2005) 2227-2231.

[18] Y.-R. He, X. Xiao, W.-W. Li, G.-P. Sheng, F.-F. Yan, H.-Q. Yu, H. Yuan, L.-J. Wu, Enhanced electricity production from microbial fuel cells with plasma-modified carbon paper anode, *Phys. Chem. Chem. Phys.* 14 (2012) 9966-9971.

[19] M. Epifanio, S. Inguva, M. Kitching, J.-P. Mosnier, E. Marsili, Effects of atmospheric air plasma treatment of graphite and carbon felt electrodes on the anodic current from Shewanella attached cells, *Bioelectrochemistry* 106 (2015) 186-193.

[20] J. Connolly, PhD thesis on "*On the uses of atmospheric and laser plasmas for biomedical applications*", DCU, (2013).

[21] J. Connolly, V.P. Valdramidis, E. Byrne, K.A. Karatzas, P.J. Cullen, K.M. Keener, J.P. Mosnier, Characterization and antimicrobial efficacy against *E. coli* of a helium/air plasma at atmospheric pressure created in a plastic package, *J. Phys. D: Appl. Phys.* 46 (2013) 035401.

[22] A. Jain, J. O'Connolly, R. Woolley, S. Krishnamurthy, E. Marsili, Extracellular electron transfer mechanism in Shewanella loihica PV-4 biofilms formed at indium tin oxide and graphite electrodes, *Int. J. Electrochem. Sci.* 8 (2013) 1778-1793.

[23] I. Horcas, R. Fernandez, J.M. Gomez-Rodriguez, J. Colchero, J. Gomez-Herrero, A.M. Baro, WSXM: a software for scanning probemicroscopy and a tool for nanotechnology, *Rev. Sci. Instrum.* 78 (2007) 013705.

[24] E. Marsili, J.B. Rollefson, D.B. Baron, R.M. Hozalski, D.R. Bond, Microbial biofilm voltammetry: direct electrochemical characterization of catalytic electrode-attached biofilms, *Appl. Environ. Microbiol.* 74 (2008) 7329-7337.

[25] Y. Fan, S. Xu, R. Schaller, J. Jiao, F. Chaplen, H. Liu, Nanoparticle decorated anodes for enhanced current generation in microbial electrochemical cells, *Biosens. Bioelectron.* 26 (2011) 1908-1912.

[26] J.-Y. Shiu, C.-W. Kuo, P. Chen, C.-Y. Mou, Fabrication of Tunable Superhydrophobic Surfaces by Nanosphere Lithography, *Chem. Mater.* 16 (2004) 561-564.

[27] K. Tsougeni, A. Tserepi, G. Boulousis, V. Constantoudis, E. Gogolides, Control of Nanotexture and Wetting Properties of Polydimethylsiloxane from Very Hydrophobic to Super-Hydrophobic by Plasma Processing, *Plasma Process. Polym.* 4 (2007) 398-405.